ABSTRACT

Title of Dissertation: A VISCOELASTOPLASTIC CONTINUUM DAMAGE MODEL FOR THE COMPRESSIVE BEHAVIOR OF ASPHALT CONCRETE

Nelson H. Gibson, Doctor of Philosophy, 2006

Dissertation directed by: Dr. Charles W. Schwartz, Associate Professor
Department of Civil and Environmental Engineering

Mechanistic performance prediction of asphalt concrete pavements has been a goal for the pavement industry for some time. A comprehensive material model is essential for such predictions. This dissertation illustrates the development, calibration and validation of a comprehensive constitutive material model for asphalt concrete in unconfined and confined compression.

A continuum damage-based viscoelastic model is extended with viscoplasticity. Thermodynamic principles, an elastic-viscoelastic correspondence principle and internal state variables quantify degradation by accounting for linear viscoelasticity and any non-linear viscoelasticity with cumulative damage. Viscoplastic effects are addressed separately. Two distinctly different strain-hardening viscoplastic models were investigated. A more capable multiaxial model with primary-secondary hardening improved upon the original uniaxial. These characteristics enable the whole model to decompose total strain into individual response components of viscoelasticity, viscoplasticity and damage.

Separate laboratory tests were required to measure and calibrate the individual response components. The calibration tests include small-strain dynamic modulus tests for undamaged viscoelastic properties, cyclic creep and recovery tests for viscoplastic properties, and constant rate of strain tests for damage properties. All tests were performed at appropriate temperatures and loading rates.

An extensive set of validation tests was used to confirm each model, which were very different from the calibration conditions to evaluate the models' capabilities. The predictions at these different conditions indicate that the comprehensive model can realistically simulate a wide range of asphalt concrete behavior. Recommendations are given based on lessons learned in the laboratory experiments and analyses of the data generated.

A COMPREHENSIVE MODEL FOR THE COMPRESSIVE BEHAVIOR OF ASPHALT CONCRETE

By

Nelson H. Gibson

Dissertation submitted to the Faculty of the Graduate School of the
University of Maryland at College Park in partial fulfillment
of the requirements for the degree of
Doctor Philosophy
2006

Advisory Committee:

Dr. Charles W. Schwartz, Chair
Dr. M. Sherif Aggour
Dr. Ahmet H. Aydilek
Dr. Dimitrios G. Goulias
Dr. Sung Lee

DEDICATION

To my wife Jenni. Your love gave me the support needed in this journey.

ACKNOWLEDGEMENTS

First and foremost, I would like to thank my advisor. It has been an extreme pleasure learning from and working with Dr. Charles W. Schwartz. He has guided my development in this research where clear paths to solutions do not exist.

This research was funded in part by the National Cooperative Highway Research Program under NCHRP Project 9-19, which originally began under a Federal Highway Administration initiative. Additional funding was provided from the Eisenhower Graduate Research Fellowship program at the National Highway Institute within the Federal Highway Administration.

Table of Contents

List of Figures

List of Tables

1. Introduction

1.1 Background

There are many existing methods that can be used to design and manage pavements. Trade industries, State Departments of Transportation and other governmental organizations offer various methods such as the American Concrete Pavement Association (ACPA) StreetPave, the Asphalt Institute SW-1 Asphalt Thickness Design, Washington DOT and Minnesota DOT pavement design manuals, the American Association of State Highway Transportation Officials (AASHTO) empirical 1993 Guide and the Federal Aviation Administration's LEDFAA methodology.

The universal objective when designing new pavements or managing existing infrastructure is to determine the likely performance or deterioration in the future and either change the design before being built or allocate the appropriate maintenance and rehabilitation funds. Naturally, the quality of any performance prediction will impact heavily on the quality of the corresponding life cycle analyses that consider optimal timing of pavement maintenance and rehabilitation activities. This is a critical concern

for transportation agencies and industries. Additional and recent needs include pavement warranties and or rational pay factor schemes for quality acceptance. This is a challenging task because it requires accurate distress models that are widely accepted in the state-of-the-practice and because pavements deteriorate in many different ways:

- Distributed cracking from fatigue (traffic related),
- Reflection of pre-existing cracks into newer layers (traffic and environment related),
- Localized cracking from thermal expansion and contraction (environment related),
- Permanent ruts in the wheel-path (traffic related),
- Distributed freeze/thaw deterioration (environment related),
- Hydraulic erosion of the unbound sub-layers (traffic and environment related),
- Stripping of the bituminous coating from the aggregate particles (environment related).

More complications arise because some of the above distresses can interact with one another and accelerate overall pavement deterioration. For example, surface cracks enable water to enter the pavement, causing stripping of the asphalt and softening and erosion of unbound and foundation materials, eventually producing a pothole. Additionally, variations of these major distresses are presented at different locations in the pavement structure and under different temperature regimes. For example, rutting primarily occurs during warmer seasons while fatigue cracks develop under moderate temperatures. Fatigue cracks may grow from the top to the bottom or from the bottom up depending on pavement temperature and stress conditions.

The state-of-the-practice for design and performance prediction of pavements in most of the United States is based on empirical methods developed from the results of large-scale tests of new highway pavements conducted in the late 1950's and early 1960's (National Research Council, 1962). Such empirical principles are becoming less and less appropriate as:

- The focus of pavement design and analysis shifts from new construction to maintenance and rehabilitation of distressed highways,
- Truck axle loads and configurations become heavier and traffic volumes increase,
- New materials such as geosynthetics and polymer modifications are incorporated in the pavement structure,
- Warranty and performance-based construction specifications become more and more attractive than method, end result and even performance-related specifications.

The net effect of such limitations in empirical design and performance prediction is less than optimal design, management and preservation of the country's highway infrastructure.

In response, the NCHRP 1-37A Guide for the Design of New and Rehabilitated Pavement Structures, intended to replace the 1993 AASHTO design method, has taken some steps to improve the state-of-the-practice by using a combined mechanistic-empirical analysis approach. The Guide emphasizes more realistic inputs for traffic, material properties and environmental characteristics that are more amenable to the mechanistic analysis of pavement response (e.g. stresses and strains) while the empirical techniques bridge the gap between pavement response and pavement distress (e.g. rutting

and fatigue cracking). National implementation and a thorough review are needed to ascertain the true benefits of the mechanistic-empirical approach, but it is clear that mechanistic-empirical engineering principles are not powerful enough to address the most complex of pavement distresses and configurations. The ultimate solution is to move away from empirical and mechanistic-empirical techniques and use fully mechanistic principles to understand pavements based on inherent material behavior. At present, practical fully mechanistic performance prediction is beyond the state-of-the-art, but recent advances in analysis tools and material characterization have moved this closer to realization.

1.2 Problem Statement

Mechanistic approaches for pavement design and performance prediction employ theories of mechanics to relate pavement structural behavior and performance to traffic loading and environmental influences. The mechanistic approach for flexible pavements has its roots in Burmister's development during the 1940's of multilayer elastic theory to compute stresses, strains, and deflections in pavement structures.

A key element of the mechanistic design approach is the accurate prediction of the response of the pavement materials—and thus of the pavement itself. The elasticity-based solutions by Burmister were an important first step toward a theoretical description of the response of flexible pavements under load. However, the linearly elastic material behavior assumption underlying these solutions is unable to simulate the nonlinear and inelastic cracking, permanent deformation, and other distresses of interest in pavement systems. This requires far more sophisticated material models and analytical tools. Much

progress has been made in recent years on isolated pieces of the mechanistic performance prediction problem. The Strategic Highway Research Program during the early 1990's made an ambitious but ultimately unsuccessful attempt at a fully mechanistic performance system for flexible pavements (Witczak, Von Quintus, and Schwartz, 1997).

Several years later, the National Cooperative Highway Research Program (NCHRP) Project 9-19 was charged with applying advanced material characterization techniques to develop the foundation for future mechanistic modeling of asphalt concrete mixtures in the Superpave mix design system. The ultimate goal for Superpave is accurate performance models that may have the ability to support performance based mix designs and specifications.

Pavement performance models in their most simple interpretation can be viewed as "black boxes" that relate a series of inputs such as geometry, environment, and traffic loads to a set of outputs such as cracking, and rutting as in Figure 1. Material properties such as the strengths and stiffness of the various layers of the pavement system are clearly one of the major inputs in these models. Consequently, adequate and accurate characterization of material behavior is vital if pavement performance is to be predicted with realism.

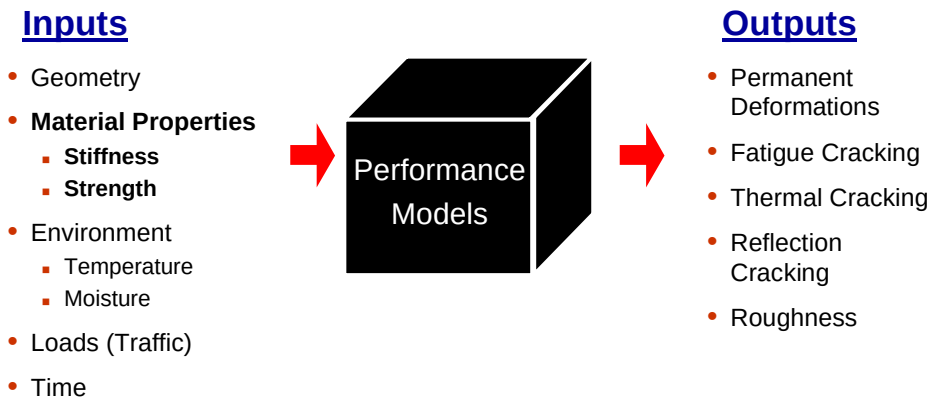

Figure 1. Conceptual view of pavement performance models.

One reason that material characterization is so important to pavement performance prediction is that it affects nearly all components of the system. As shown in Figure 2, major interactions between model components include:

- *Environmental Effects Model:* Material properties are required to predict pavement temperature and moisture distributions over depth and time as a consequence of environmental history. These temperature and moisture distributions in turn alter the material properties as used in other model components (e.g., decreasing AC stiffness with increasing temperature, decreasing subgrade strength with increasing moisture).
- *Primary Response Model:* Material properties are a major input into tools such as the finite element models used to compute the stresses and strains induced in the various layers by environmental and traffic loadings. These computed stresses and strains in turn alter the material properties (e.g., stress dependent stiffness, damage/failure of the materials).

- *Distress Models:* Material properties such as those for fatigue and fracture resistance and permanent deformation response are often major inputs into the models for predicting individual pavement distresses. These models are ultimately dependent on material properties beyond the familiar modulus and strength parameters.

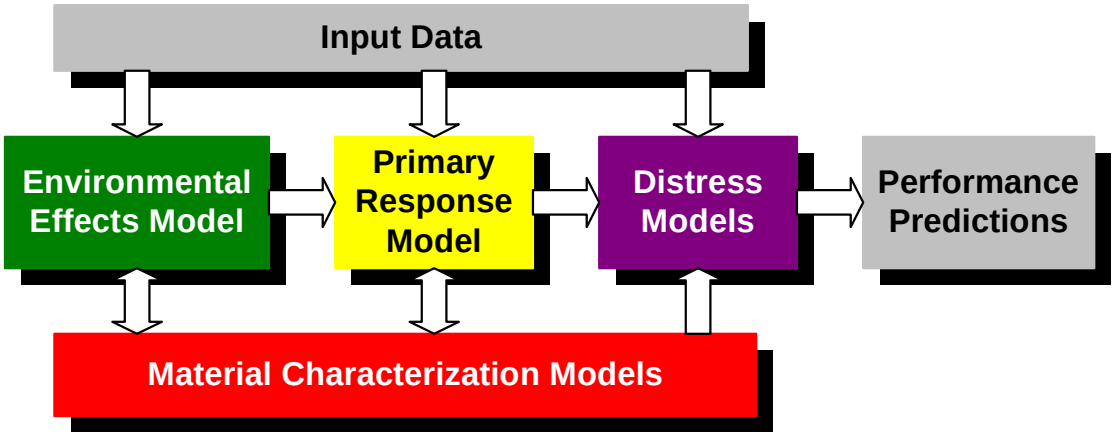

Figure 2. Components of a pavement performance prediction system.

The demands on material characterization models for pavement systems are severe. Not only does a pavement system contain many diverse materials (e.g., bound vs. unbound), but also the behavior of each of the materials is different and often quite complex. All of the pavement layer materials will generally exhibit some type of stress-strain nonlinearity as well as accumulated damage and/or permanent deformation under cyclic loading. In addition, temperature and loading rate effects will have an important effect on the behavior of the asphalt concrete layer. Furthermore, the behavior of the various layer materials will also be influenced by secondary phenomena such as aging and moisture effects. The extensive tests required to determine the material parameters will in general

include multiaxial stress-strain loading under controlled stress levels, loading rates, and temperatures.

1.3 Objectives

The research described in this dissertation focuses on material modeling for asphalt concrete that is based on solid mechanics but independent of specific mixture properties. An ideal model should be capable of predicting the stress and deformation response of asphalt concrete over the full range of temperatures, strain rates, and stress states of interest in flexible pavement systems. Heretofore, the model explicitly offers secondary asphalt distress prediction such as rutting and the onset of cracking

This dissertation describes the development, calibration, and validation of a comprehensive, fundamental material model for asphalt concrete. The model, which is based on an extended form of the Schapery continuum damage formulation (Ha and Schapery, 1998; Schapery, 1999) considers the viscoelastic, viscoplastic, and damage components of asphalt concrete behavior over the full range of temperatures, loading rates, and stress levels of interest in pavement engineering.

The work described in this focuses on asphalt concrete behavior in unconfined and confined compression. Although only one specific dense graded asphalt mixture was employed in this study, it is believed that the mechanistic nature of the model makes it applicable to other asphalt concrete materials as well. Secondary phenomena such as aging and moisture effects are outside the scope of this research.

1.4 Organization

This dissertation has directly contributed to the collective research performed by the NCHRP Project 9-19 Superpave Models Team. The Team consisted of the Arizona State University for test specimen production and the source of independent validation test results, Advanced Asphalt Technologies that documented specific Superpave mix design and binder characterization and the North Carolina State University that offered equivalent tensile characterization of the same mixture. The dissertation is organized as follows. The basic formulation of the material models is described in Chapter 2, and the details of the basic experimental protocols and equipment required to calibrate these models are provided in Chapter 3. Chapter 4 summarizes the conventional characterization of the small-strain linear viscoelastic response in terms of the complex modulus and time-temperature superposition concepts; Chapter 5 describes how the time-temperature superposition concept can also be extended into the large strain domain, a necessary step for this research. Characterization of a very useful initial viscoplastic model is given in Chapter 6. The damage components of the model are described in Chapters 7. Validation of the models is provided in Chapter 8. Chapter 9 describes efforts to adjust and then ultimately to re-formulate the viscoplastic model component to address some of the deficiencies of the initial viscoplastic approach. The overall summary, conclusions and recommendations from the work are found in Chapters 10 and 11.

2. Model Formulation

2.1 Introduction

The theoretical context for this modeling is the Schapery continuum damage model (Park and Schapery, 1997; Ha and Schapery, 1998) with extensions to viscoplasticity (Schapery, 1999). Key conceptual components of this model include the use of viscoelastic correspondence principles, microstructural damage functions based on a thermodynamics formulation and expressed in terms of rate-dependent internal state variables, and a strain hardening viscoplasticity relation. Note that a simplified form of the basic Schapery continuum damage model has been applied in the past to asphalt concrete under moderate temperature tension loading by Park *et al*. (1996) and Lee and Kim (1998a, 1998b); this earlier work neglected any viscoplastic response components.

The Schapery model explicitly separates the total strain ε_t into viscoelastic ε_{ve} and viscoplastic ε_{vp} components:

$$\varepsilon_t = \varepsilon_{VE} + \varepsilon_{VP} \qquad \textbf{Equation 1}$$

in which both ε_{VE} and ε_{VP} can include contributions from microstructural damage. For the present discussion it is helpful to separate the strain components even further:

$$\varepsilon_t = \varepsilon_{LVE} + \varepsilon_D + \varepsilon_{VP} \quad \textbf{Equation 2}$$

in which ε_{lve} is the linear viscoelastic strain, ε_d is the strain due to microstructural damage, and ε_{vp} is the viscoplastic strain. Note that the damage strain ε_d is actually included as a part of the viscoelastic strain ε_{ve} (and potentially as part of the nonlinear viscoplastic strain ε_{vp}) in the formal Schapery model, but this can be separated out conceptually (and mathematically, given some simplifying assumptions) for the present discussion.

There are four major factors assumed to influence the strain components for a given loading: loading rate, temperature, stress state (confining and/or shear stress), and material damage. The assumptions regarding the impact of these factors on each of the strain components in the model are as follows:

- *Linear viscoelastic strain* ε_{lve}: The viscoelastic strain is assumed to be linear and thus independent of stress state and damage. The viscoelastic strain is dependent upon rate of loading and temperature, but these may be interchanged using conventional time-temperature superposition:

$$\varepsilon_{lve} = f_{lve}(t,T) = f'_{lve}(t_R) \quad \textbf{Equation 3}$$

in which t is time, T is temperature (isothermal conditions), and t_R is the reduced time given by:

$$t_R = \frac{t}{a_{T\,lve}(T)} \quad \textbf{Equation 4}$$

in which $a_{Tlve}(T)$ is the temperature shift for linear viscoelasticity. Materials for which Equation 4 is valid are termed *thermorheologically simple* materials. Asphalt concrete

is commonly assumed to be thermorheologically simple under small strain (<~100με) linear viscoelastic conditions.

- *Damage strain* ε_d: The underlying damage functions for the material are assumed to be independent of loading rate, temperature, and stress state. However, loading rate, temperature, and stress state are expected to have a definite and direct effect on the magnitudes of the time-dependent computed internal state variables and thus on the magnitudes of ε_d computed from the underlying damage functions. It is provisionally assumed, however, that the effects of loading rate and temperature on damage strains can be interchanged using conventional time-temperature superposition:

$$\varepsilon_d = f_d(t,T) = f'_d(t_R) \qquad \textbf{Equation 5}$$

in which the reduced time t_R in this case is given by:

$$t_R = \frac{t}{a_{Td}(T)} \qquad \textbf{Equation 6}$$

where $a_{Td}(T)$ is the temperature shift for damage. Establishing the validity of this provisional assumption was one of the objectives of this study; this is described in more detail in Chapter 5.

- *Viscoplastic strain* ε_{vp}: It is provisionally assumed that the effects of loading time and temperature on viscoplastic strains can be interchanged using a generalized time-temperature superposition:

$$\varepsilon_{vp} = f_{vp}(t,T,\sigma) = f'_{vp}(t_R)g_{vp}(\sigma) \qquad \textbf{Equation 7}$$

in which $g_{vp}(\sigma)$ captures any influence of stress state[1] and the reduced time t_R in this case is given by:

$$t_R = \frac{t}{a_{Tvp}(T)} \qquad \textbf{Equation 8}$$

where $a_{Tvp}(T)$ is the temperature shift for viscoplasticity effects. Establishing the validity of this provisional assumption is one of the objectives of this study.

A key question for the Schapery model when applied to asphalt concrete is whether the same time-temperature superposition relationship exists for all of the strain components, i.e., whether

$$a(T)_{T-LVE} = a(T)_{T-D} = a(T)_{T-VP} \qquad \textbf{Equation 9}$$

Physically, Equation 9 implies that the same underlying rate process is governing the linear viscoelastic, damage, and viscoplastic responses of the material. If this can be demonstrated to be true, it enables great economies in the laboratory testing program needed to characterize the material parameters in the model. If the relationship in Equation 9 is not true, then a full factorial material characterization testing program may be required to span the full range of loading rates, temperatures, and stress levels of interest—a formidable task. Fortunately, the substudy described in Chapter 5 established that Equation 9 is sufficiently valid for practical engineering purposes.

[1] This could alternatively be formulated in terms of strain level and a corresponding function $h_{vp}(\varepsilon)$ for capturing the strain level influence.

2.2 Viscoelasticity

Linear viscoelastic materials have the properties of both linear elastic and viscous materials. When loaded, an elastic material deforms immediately and then continues to deform under constant load. As for linear elastic materials, viscoelastic displacement or strain is proportional to the load or stress at a given time. The definition of linearity also implies that stress and strain responses can be superimposed; responses from complex loading histories can be determined by superimposing the responses from multiple simplified loading histories. One of the simplest viscoelastic material models is the Maxwell model element consisting of spring and a dashpot as shown in Figure 3. The spring and dashpot give the element elastic and viscous properties respectively. A single Maxwell element rarely fits observed behavior of real viscoelastic materials, including asphalt concrete. A more useful formulation is a generalized Maxwell model consisting of n Maxwell elements placed in parallel as in Figure 4. The material constants E_i and μ_i correspond respectively to the stiffness of each Maxwell spring and the viscosity of each dashpot. The generalized Maxwell model provides an excellent fit to the observed behavior of a wide range of viscoelastic materials.

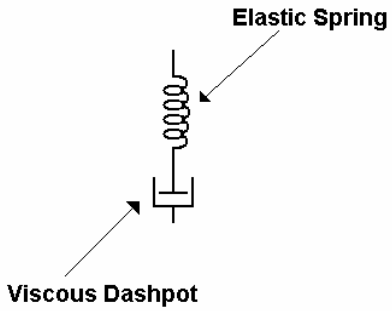

Figure 3 Simple Maxwell model.

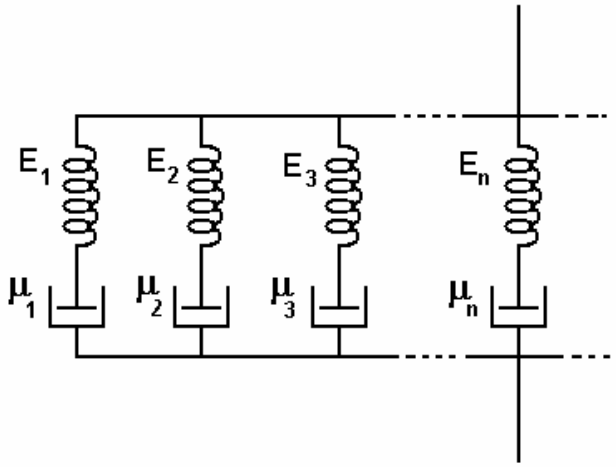

Figure 4. Generalized Maxwell model.

2.2.1 Dynamic Modulus

The behavior of viscoelastic materials can be characterized in terms of a relaxation modulus, creep compliance, or complex modulus. Because of laboratory testing convenience, complex modulus is commonly used to characterize the viscoelastic response of asphalt concrete. As shown in Figure 5, the complex modulus test consists of an applied sinusoidal axial stress that induces a sinusoidal axial strain response (Findley, Lai, and Onaran, 1989):

$$\sigma(t) = \sigma_0 \cos(\omega t) = \sigma_0 e^{i\omega t} \quad \textbf{Equation 10}$$

$$\varepsilon(t) = \varepsilon_0 \cos(\omega t - \phi) = \varepsilon_0 e^{i(\omega t - \phi)} \quad \textbf{Equation 11}$$

In Equation 10 and Equation 11, σ_o is the dynamic stress amplitude, ε_o is the dynamic strain amplitude, ω is the loading frequency, and the phase angle ϕ is the frequency-

dependent measure of the strain lag. For relevant conditions, the strain response will always lag behind the stress in time for a viscous material in this stress-controlled test.

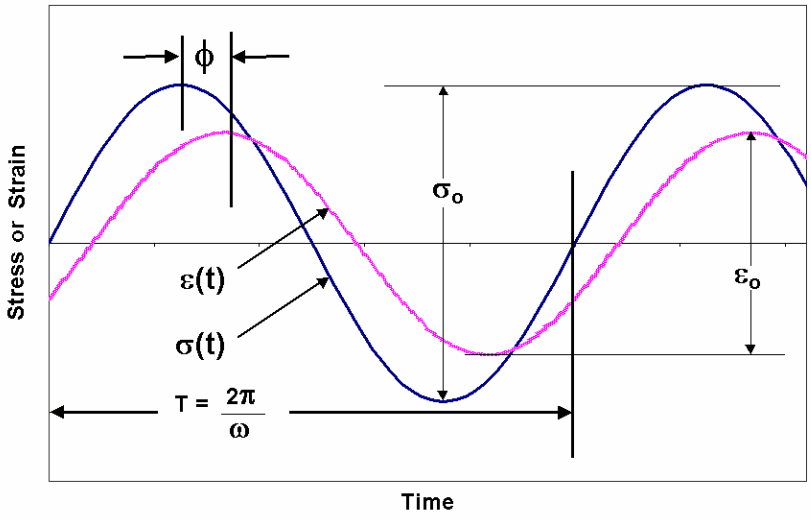

Figure 5. Schematic of complex modulus response.

The complex modulus, E^*, is defined as the ratio of the dynamic stress to dynamic strain:

$$E^* = \frac{\sigma_o}{\varepsilon_o} e^{i\phi} = \frac{\sigma_o}{\varepsilon_o}[\cos\phi + i\sin\phi] = E' + iE'' \qquad \textbf{Equation 12}$$

in which the storage modulus, E', and loss modulus, E'', represent the real and imaginary components of complex modulus (Findley, Lai, and Onaran, 1989). The dynamic modulus, $|E^*|$, is defined as the ratio of the dynamic stress amplitude to the dynamic strain amplitude:

$$|E^*| = \frac{\sigma_0}{\varepsilon_0} = \left|\sqrt{(E')^2 + (E'')^2}\right| \qquad \textbf{Equation 13}$$

Dynamic modulus can be related to the storage and loss moduli:

$$E'(\omega) = |E^*(\omega)|\cos\phi(\omega) \qquad \textbf{Equation 14}$$

$$E''(\omega) = |E^*(\omega)|\sin\phi(\omega) \qquad \textbf{Equation 15}$$

Dynamic modulus is a function of loading frequency. As shown in Figure 6, the dynamic modulus for asphalt concrete is stiffer at higher frequencies and softer at slower frequencies because of the viscoelastic nature of the material.

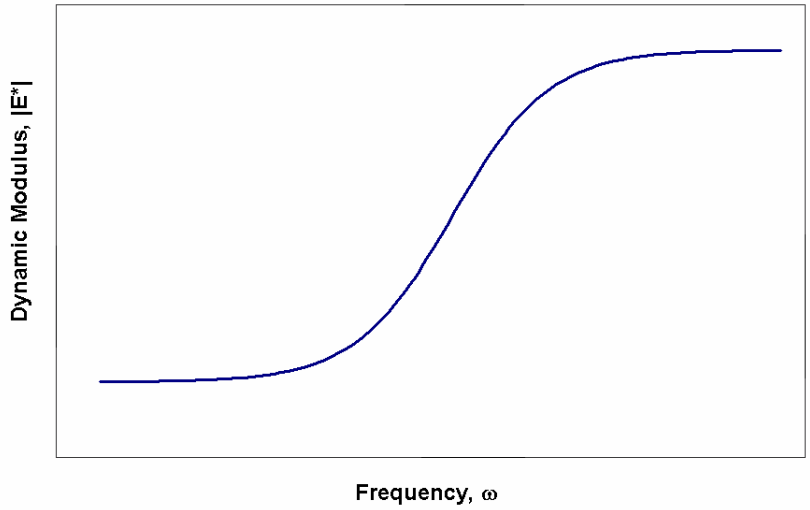

Figure 6. Dynamic modulus as a function of loading frequency.

The generalized Maxwell model can be fit to the storage and loss moduli in the frequency domain using a Prony series (Park and Schapery, 1999):

$$E'(\omega) = E_o + \sum_{i=1}^{m} \frac{\omega^2 \rho_i^2 E_i}{1 + \omega^2 \rho_i^2} \qquad \textbf{Equation 16}$$

$$E''(\omega) = \sum_{i=1}^{m} \frac{\omega \rho_i E_i}{1 + \omega^2 \rho_i^2} \qquad \textbf{Equation 17}$$

in which E_i are the elastic spring stiffnesses and ρ_i are the relaxation times for the elements in the generalized Maxwell model. The relationship between relaxation time, viscosity, and stiffness is:

$$\rho_i = \frac{\eta_i}{E_i} \qquad \textbf{Equation 18}$$

For practical purposes, a set of arbitrary ρ_i values spanning the relevant time range are selected and a corresponding set of E_o and E_i values are determined that minimizes the differences between the computed and measured $E'(\omega)$ and/or $E''(\omega)$ values.

2.2.2 Time-Temperature Superposition Principle

The viscoelastic behavior of asphalt concrete depends strongly on temperature as well as rate of loading. Consequently, complex modulus is most correctly expressed as $E^*(\omega, T)$, indicating dependence on temperature as well as frequency.

The effects of temperature and loading rate on the viscoelastic properties of certain materials can be unified using the time-temperature superposition principle. This principle allows for a master stiffness curve to be developed from test data at different loading rates and temperatures by 'shifting' the data along the loading time or frequency axis as a function of temperature. Figure 7 illustrates an example of this for dynamic modulus, $|E^*|$. Arrows show the direction and amount that the modulus data at each temperature is shifted horizontally to the single underlying master curve.

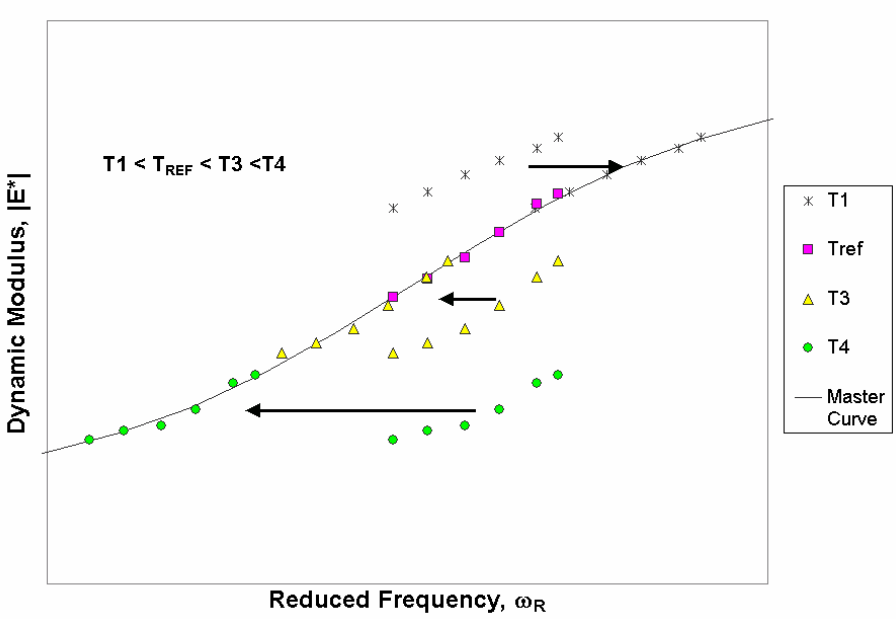

Figure 7. Time-temperature superposition schematic.

Using the principle of time temperature superposition, the material property is no longer dependent upon both absolute frequency and temperature but instead is a function only of reduced frequency defined as:

$$\omega_R = \omega \times a(T) \qquad \textbf{Equation 19}$$

or

$$\log \omega_R = \log \omega + \log a(T) \qquad \textbf{Equation 20}$$

in which ω is the actual loading frequency, $a(T)$ is temperature shift factor, T is temperature, and ω_R is reduced frequency. When loading time is used in the context of a time-domain viscoelastic material property (e.g. creep compliance), a reduced time instead of reduced frequency can be defined as:

$$t_R = \frac{t}{a(T)} \qquad \textbf{Equation 21}$$

or

$$\log t_R = \log t - \log a(T) \qquad \textbf{Equation 22}$$

in which t is the actual loading time, t_R is reduced time, and the other terms are as defined previously.

Temperature shifting requires the selection of an arbitrary reference temperature toward which the data from other temperatures is 'shifted'. Each temperature has an associated shift factor $a(T)$ as illustrated in Figure 8. The temperature shift factors are used to shift the data in Figure 7, where data at temperatures above the reference temperature are horizontally shifted in one direction (i.e., $a(T) < 1$) and data below the reference temperature are horizontally shifted in the other direction (i.e., $a(T) > 1$).

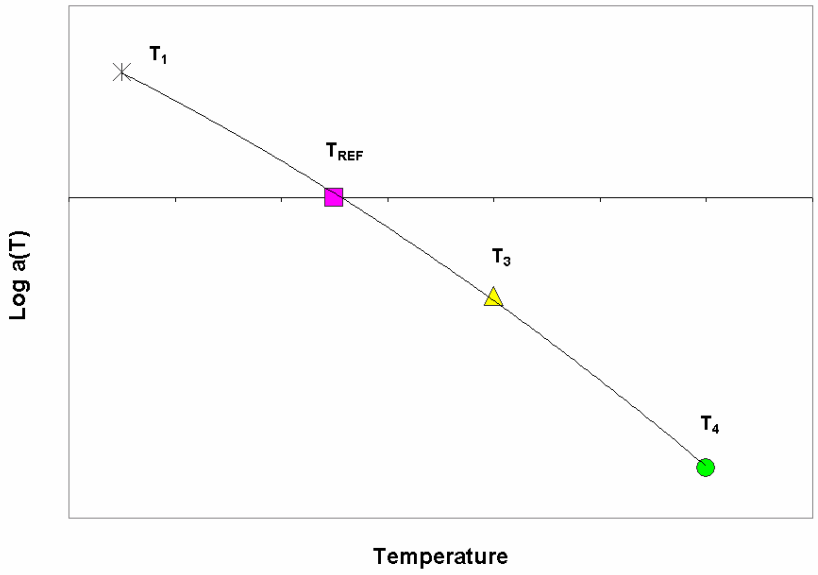

Figure 8. Temperature shift factors *a*(*T*) for time-temperature superposition.

Time-temperature superposition allows viscoelastic properties to be predicted at loading times or frequencies well outside the capable range of testing equipment. For example, dynamic modulus at a cold temperature and very slow loading rate is the same

as the dynamic modulus at some warmer temperature and faster loading rate. Time-temperature superposition can be advantageous because the very cold and slow test conditions (i.e.-corresponding to a truck stopped at an intersection) may be difficult or impractical to test in the laboratory; instead, this behavior can be captured at an equivalent warmer temperature and higher frequency that is easier to achieve in the laboratory.

Materials that follow time-temperature superposition are termed "thermorheologically simple," meaning that temperature and loading rate effects can be interchanged solely via the temperature shift factor. It is well established that asphalt concrete is a thermorheologically simple material under linear viscoelastic conditions at "small" strain levels. The linear viscoelastic limit is typically assumed to be on the order of 100 $\mu\varepsilon$ (e.g., Monismith *et al.*, 1966; Mehta and Christensen, 2000). A primary objective of the research described in this dissertation was to determine if asphalt concrete remains thermorheologically simple for strains exceeding the linear viscoelastic limit (i.e., at strains greater than 100 $\mu\varepsilon$); this is described in more detail in Chapter 5.

2.2.3 Relaxation Modulus and Creep Compliance

As described previously, the behavior of viscoelastic materials can alternatively be characterized in terms of its relaxation modulus or creep compliance. The relaxation modulus is commonly measured in a uniaxial relaxation test in which a fixed axial strain ε_o is applied instantaneously and the induced stress $\sigma(t)$ attenuates with time t. The relaxation modulus $E(t)$ is then defined as:

$$E(t) = \frac{\sigma(t)}{\varepsilon_o} \qquad \textbf{Equation 23}$$

Conversely, the creep compliance is commonly measured in a uniaxial creep test in which a constant stress σ_o is applied instantaneously and the induced strain $\varepsilon(t)$ increases with time. The creep compliance $D(t)$ is then defined as:

$$D(t) = \frac{\varepsilon(t)}{\sigma_o} \qquad \textbf{Equation 24}$$

The relaxation modulus $E(t)$ and the small-strain temperature shift function $a(T)$ are the principal linear viscoelastic properties needed in the Schapery continuum damage model. To determine the relaxation modulus, the linear viscoelastic strain response determined more conveniently from small strain complex modulus tests is used to develop a master curve for the storage modulus E'. As described previously by Equation 16, the variation of storage modulus E' with frequency ω can be approximated as a Prony series, corresponding to a generalized viscoelastic Maxwell model (Figure 4). A Prony series can then also be used to represent the relaxation modulus and creep compliance for the generalized Maxwell model (Park and Schapery, 1999):

$$E(t) = E_o + \sum_{i=1}^{m} E_i e^{\frac{-t}{\rho_i}} \qquad \textbf{Equation 25}$$

$$D(t) = D_o + \sum_{j=1}^{n} D_j (1 - e^{\frac{-t}{\tau_j}}) \qquad \textbf{Equation 26}$$

in which E_o is the long-term equilibrium modulus and the E_i and ρ_i terms are the same as for the storage modulus E' as given by Equation 16. The Prony series can be fit to complex modulus laboratory test data by means of a collocation method (Schapery, 1961) or other numerical technique.

The Prony series representation of creep compliance can be predicted from the Prony representation of relaxation modulus by using a technique developed by Park and Schapery (1999). The unknown compliance constants $\{D_o, \tau_j, D_j\ (j=1,2...n)\}$ can be solved in terms of the known relaxation constants $\{E_o, \rho_i, E_i\ (i=1,2...m)\}$ by means of the relationship:

$$[A]\{D\} = \{B\} \qquad \textbf{Equation 27}$$

or $A_{kj}D_j = B_k$ (summed on j; j = 1,2,...n; k = 1,2,...p) where:

$$A_{kj} = \begin{cases} E_o\left(1 - e^{\frac{-t_k}{\tau_j}}\right) + \sum_{i=1}^{m} \frac{\rho_i E_i}{\rho_i - \tau_j}\left(e^{\frac{-t_k}{\rho_i}} - e^{\frac{-t_k}{\tau_j}}\right) & \text{when } \rho_i \neq \tau_j \\ \text{or} & \\ E_o\left(1 - e^{\frac{-t_k}{\tau_j}}\right) + \sum_{i=1}^{m} \frac{t_k E_i}{\tau_j}\left(e^{\frac{-t_k}{\rho_i}}\right) & \text{when } \rho_i = \tau_j \end{cases} \qquad \textbf{Equation 28}$$

and

$$B_k = 1 - \frac{\left(E_e + \sum_{i=1}^{m} E_i e^{\frac{-t_k}{\rho_i}}\right)}{\left(E_e + \sum_{i=1}^{m} E_i\right)} \qquad \textbf{Equation 29}$$

and

$$D_o = \frac{1}{E_o + \sum_{i=1}^{m} E_i} \qquad \textbf{Equation 30}$$

The relaxation modulus and creep compliance are useful for computing stresses and strains from given strain and stress histories respectively using the following standard convolution integrals:

$$\sigma(t) = \int_0^t E(t-\tau)\frac{\partial \varepsilon}{\partial \tau} d\tau \qquad \textbf{Equation 31}$$

$$\varepsilon(t) = \int_0^t D(t-\tau)\frac{\partial \sigma}{\partial \tau} d\tau \qquad \textbf{Equation 32}$$

2.3 Continuum Damage

The continuum damage model described herein consists of constitutive equations and damage evolution equations for three-dimensional mechanical behavior of asphalt concrete and other particulate composites having low-modulus, time-dependent matrices. The damage and filler particles are assumed sufficiently well distributed that a composite material element can be viewed as a homogeneous continuum. This characterization for the local material behavior can be implemented in a finite element analysis to predict pavement stress, deformation, damage states, damage localization (including post-peak behavior), and growth of macro cracks. Analysis of crack propagation requires additional experimental information on fracture properties as determined from macro crack growth measurements in laboratory specimens; this is beyond the scope of the present research.

The theoretical context for the work described herein is the Schapery continuum damage model (Park and Schapery, 1997; Ha and Schapery, 1998). Key conceptual

components of this model include the use of elastic-viscoelastic correspondence principles, reduced time, microstructural damage functions based on a thermodynamics-based formulation and expressed in terms of rate-dependent internal state variables. A simplified form of the basic Schapery continuum damage model has been applied in the past to asphalt concrete under cyclic and monotonic tension at moderate temperatures by Park *et al*. (1996) and Lee and Kim (1998a, 1998b).

2.3.1 Uniaxial Formulation

The Schapery-based damage model is a nonlinear viscoelastic formulation with fully recoverable strains. Viscoelastic effects are treated using elastic-viscoelastic correspondence principles that transform the viscoelastic problem into a mathematically equivalent elastic case. Schapery (1984) proposed an extended elastic-viscoelastic correspondence principle applicable to linear and non-linear viscoelastic media. This correspondence principle states that the constitutive equations for viscoelastic material are the same as for an elastic material, but with actual stresses and strains replaced by pseudo stresses and pseudo strains determined using the following convolution integrals:

$$\varepsilon^R = \frac{1}{E_R}\int_0^{t_R} E(t_R - \tau)\frac{\partial \varepsilon_{ve}}{\partial \tau} d\tau \qquad \textbf{Equation 33}$$

$$\sigma^R = E_R \int_0^{t_R} D\left(t_R - \tau\right)\frac{\partial \sigma}{\partial \tau} d\tau \qquad \textbf{Equation 34}$$

in which σ, ε_{ve} = physical stress and viscoelastic strain component (which includes the elastic strain)

σ^R, ε^R = pseudo stress and pseudo strain

E_R = arbitrary reference modulus that is constant

$E(t)$ = relaxation modulus

$D(t)$ = creep compliance

t_R = reduced time—see Equation 21

This formulation is advantageous as compared to other methods that use Laplace or Fourier transforms, which can be difficult to evaluate analytically.

It is important to mention that Equation 33 is for applications in which the damage is constant or growing, as has been assumed in the present research. When the damage decreases (i.e. heals) then Equation 34 should be used instead. Although healing is an important concern for asphalt concrete, particularly for fatigue cracking, it is not considered in the present version of the model.

For the case of no damage, the axial pseudo strain is related to the uniaxial stress via the standard linear elasticity relation:

$$\sigma = E_R \varepsilon^R \qquad \textbf{Equation 35}$$

Damage is incorporated by replacing the reference modulus with a damage function $C(S)$ that is dependent upon an internal state variable S:

$$\sigma = C(S)\varepsilon^R \qquad \textbf{Equation 36}$$

The $C(S)$ function represents the degree of damage in the material. When the reference modulus is taken as unity for simplicity the damage function ranges between 1 for intact material to 0 for a completely damaged material. A strain energy density W^R in terms of pseudo strains (i.e., pseudo strain energy density) is defined as:

$$W^R = \frac{1}{2} C(S) \left(\varepsilon^R\right)^2 \qquad \textbf{Equation 37}$$

The nonlinear stress-strain relation in Equation 36 can then alternatively be generated from the strain energy density using the standard relation:

$$\sigma \equiv \frac{\partial W^R}{\partial \varepsilon^R} = C(S)\varepsilon^R \qquad \textbf{Equation 38}$$

A damage evolution law governs development of the damage internal state variable *S*:

$$\dot{S} = \frac{\partial S}{\partial t_R} = \left(-\frac{\partial W^R}{\partial S} \right)^{\alpha} \qquad \textbf{Equation 39}$$

in which $dt_R = \frac{dt}{a(T)}$, $a(T)$ is the temperature shift, and α is a material property.

2.3.2 Multiaxial Formulation

2.3.2.1 Undamaged Material

For a transversely isotropic material without damage, the strain energy density function can be written in terms of pseudo strains as follows (after Schapery, 1985):

$$W^R = \frac{1}{2}\left[A_{11}\left(e_V^R\right)^2 + A_{22}\left(e_3^R\right)^2 + 2A_{12}e_3^R e_V^R + A_{44}\left(\left(\gamma_{13}^R\right)^2 + \left(\gamma_{23}^R\right)^2\right) + A_{66}\left(\left(\gamma_{12}^R\right)^2 + \left(e_2^R\right)^2\right)\right]$$

Equation 40

in which x_3 is the axis of material symmetry and the pseudo strain terms are defined as:

$$\begin{aligned} e_2^R &\equiv \varepsilon_{22}^R - \varepsilon_{11}^R \\ e_3^R &\equiv \varepsilon_{33}^R - e_V^R/3 \\ e_V^R &\equiv \varepsilon_{11}^R + \varepsilon_{22}^R + \varepsilon_{33}^R \\ \gamma_{12}^R &\equiv 2\varepsilon_{12}^R \\ \gamma_{23}^R &\equiv 2\varepsilon_{23}^R \\ \gamma_{13}^R &\equiv 2\varepsilon_{13}^R \end{aligned} \qquad \textbf{Equation 41}$$

and the A_{ij} terms are the five elastic coefficients for a transversely isotropic material. For asphalt concrete test specimens, the x_3 axis is the axial direction (usually assumed to correspond to the vertical direction in the pavement) and a principal direction. For these

conditions, $\gamma_{13}^R = \gamma_{23}^R = \gamma_{12}^R = 0$, $\varepsilon_{11}^R = \varepsilon_1^R$, $\varepsilon_{22}^R = \varepsilon_2^R$, $\varepsilon_{33}^R = \varepsilon_3^R$ where ε_1^R, ε_2^R, and ε_3^R are principal strains, and Equation 41 can be simplified as:

$$W^{R\prime} = \frac{1}{2}\left(A_{11}\left(e_V^R\right)^2 + A_{22}\left(e_3^R\right)^2 + 2A_{12}e_3^R e_V^R + A_{66}\left(e_2^R\right)^2\right) \qquad \textbf{Equation 42}$$

The stress- pseudo strain relations are derived from the simplified pseudo strain energy density Equation 42 in terms of principal stresses as:

$$\sigma_i = \frac{\partial W^{R\prime}}{\partial \varepsilon_i^R} \qquad \textbf{Equation 43}$$

or:

$$\sigma_1 = \left(A_{11} - \frac{A_{12}}{3}\right)e_V^R + \left(A_{12} - \frac{A_{22}}{3}\right)e_3^R + A_{66}e_2^R$$

$$\sigma_2 = \left(A_{11} - \frac{A_{12}}{3}\right)e_V^R + \left(A_{12} - \frac{A_{22}}{3}\right)e_3^R - A_{66}e_2^R \qquad \textbf{Equation 44}$$

$$\sigma_3 = \left(A_{11} + \frac{2A_{12}}{3}\right)e_V^R + \left(A_{12} + \frac{2A_{22}}{3}\right)e_3^R$$

2.1.1.1 Damage

The inclusion of rate dependent irreversible damage in the model is based on Park and Schapery (1997) and (Ha and Schapery, 1998). For confined uniaxial monotonic loading of a time-dependent material with damage, the dual energy density function in terms of pseudo strains is given as:

$$W_D^R = C_{11}(S)\frac{\left(\varepsilon_1^r\right)^2}{2} + C_{12}(S)\varepsilon_1^R p + \frac{1}{2}C_{22}(S)p^2 \qquad \textbf{Equation 45}$$

in which p is the confining pressure (compression positive—i.e., $p = -\sigma_3$ for conventional triaxial test conditions), ε_1^R is the axial pseudo strain (tension positive), and C_{11}, C_{12}, and C_{22} are material damage functions defined in terms of internal state variable S, as will be described in more detail below.[2] Distributed damage due to this type of loading produces transverse isotropy (in an initially isotropic material) with the isotropy axis x_3 in the specimen's axial direction.

The stress-pseudo strain relations are expressed as:

$$\Delta\sigma \equiv \frac{\partial W_D^R}{\partial \varepsilon_1^R} = C_{11}(S)\varepsilon_1^R + C_{12}(S)p$$

$$e_V^R \equiv \frac{\partial W_D^R}{\partial p} = C_{12}(S)\varepsilon_1^R + C_2(S)p$$

Equation 46

in which $\Delta\sigma$ is the deviator stress (tension positive) and e_V^R is the volumetric pseudo strains (expansion positive). Comparing Equation 46 and Equation 44, the instantaneous elastic material constants A_{ij} can be expressed in terms of the damage functions C_{ij} as:

[2] Ha and Schapery's (1998) original formulation was for solid rocket propellant problems in which the material can be subjected to confining pressures having magnitudes approaching the elastic modulus. For these conditions, they included an additional damage function and a second internal state variable to capture damage effects under intense volumetric loading. These additional terms are not needed for asphalt concrete in pavement problems.

$$A_{11} = \frac{1}{9}\left(C_{11} - \frac{\left(C_{12} - 3\right)^2}{C_{22}} \right)$$

$$A_{12} = \frac{C_{11}}{3} + \frac{C_{12}}{C_{22}}\left(1 - \frac{C_{12}}{3}\right) \qquad \textbf{Equation 47}$$

$$A_{22} = C_{11} - \frac{C_{12}^2}{C_{22}}$$

Note that the material constant A_{66} cannot be determined from Equation 47. Schapery (1991) used micromechanical model arguments to show that A_{66} should be relatively insensitive to microstructural damage, and therefore A_{66} can be taken as the initial shear modulus G_{init}, of the undamaged material:

$$A_{66} = G_{init} = \frac{E_{init}}{2\left(1 + \nu_{init}\right)} \qquad \textbf{Equation 48}$$

The internal state variable S in the C_{ij} damage functions accounts for changes in the internal structure of the material such as caused by micro cracking. The internal state variable is again defined via an evolution law:

$$\frac{\partial S}{\partial t_R} = \left(-\frac{\partial W_D^R}{\partial S} \right)^{\alpha} \qquad \textbf{Equation 49}$$

in which $dt_R = \frac{dt}{a(T)}$, $a(T)$ is the temperature shift, and α is a material property. Park *et al.* (1996) describe the characterization process for determining the material damage functions C_{ij}.

2.4 Uniaxial Viscoplasticity

The axial viscoplastic strain rate for uniaxial constant-stress loading is assumed to follow a strain-hardening model of the form:

$$\dot{\varepsilon}_{vp} = \frac{g(\sigma)}{A\varepsilon_{vp}^{p}} \qquad \textbf{Equation 50}$$

in which $\dot{\varepsilon}_{vp}$ is the viscoplastic strain rate, ε_{vp} is the total viscoplastic strain, $g(\sigma)$ is the uniaxial stress loading function, and A and p are material constants. Equation 50 can be rearranged and integrated:

$$\varepsilon_{vp}^{p+1} = \frac{p+1}{A}\int_0^t g(\sigma)dt \qquad \textbf{Equation 51}$$

or:

$$\varepsilon_{vp} = \left(\frac{p+1}{A}\right)^{\frac{1}{p+1}}\left(\int_0^t g(\sigma)dt\right)^{\frac{1}{p+1}} \qquad \textbf{Equation 52}$$

For constant stress creep conditions, $g(\sigma)$ is independent of time and Equation 51 becomes:

$$\varepsilon_{vp} = \left(\frac{p+1}{A}\right)^{\frac{1}{p+1}} g(\sigma)^{\frac{1}{p+1}} t^{\frac{1}{p+1}} \qquad \textbf{Equation 53}$$

Assuming a power law of the form $g(\sigma) = B\sigma^{q}$ in which B and q are material properties, Equation 53 reduces to:

$$\varepsilon_{vp} = \left(\frac{p+1}{A}\right)^{\frac{1}{p+1}} \left(B\sigma^{q}\right)^{\frac{1}{p+1}} t^{\frac{1}{p+1}} \qquad \textbf{Equation 54}$$

or more simply:

$$\varepsilon_{vp} = \left(\frac{p+1}{Y}\right)^{\frac{1}{p+1}} \left(\sigma^{q}\right)^{\frac{1}{p+1}} t^{\frac{1}{p+1}} \qquad \textbf{Equation 55}$$

in which $Y=A/B$. For conditions where stress is not constant over time, the viscoplastic model is expressed in a more general form as:

$$\varepsilon_{vp} = \left(\frac{p+1}{Y} \right)^{\frac{1}{p+1}} \left[\int_0^t [\sigma(t)]^q \, dt \right]^{\frac{1}{p+1}} \qquad \textbf{Equation 56}$$

The total or physical strain is the sum of the viscoelastic (adjusted for damage) and viscoplastic strains:

$$\varepsilon_{total} = \varepsilon_{vp} + \varepsilon_{ve} \qquad \textbf{Equation 57}$$

Extensions to more general stress states may be accomplished as described by Schapery (1999).

3. Test Specimen Preparation

3.1 Test Material

The material used in the experimental program is a dense graded unmodified asphalt concrete mixture meeting Superpave requirements that is used by the Maryland State Highway Administration (MDSHA) as a surface course mixture. The mixture is a 12.5 millimeter nominal maximum aggregate size based on MDSHA specifications for 3-10 million 80 kN equivalent single axle loads (ESALs). The mixture properties were altered slightly from the MDSHA standard design for this study. New optimum gyration levels, asphalt contents, and mineral filler contents were determined in a separate study by the Superpave Models Team (1999a). The mixture was not short-term oven aged in order to save time. Short-term oven aging was not necessary since the material was being used only for experimental research.

Different aggregate stockpiles from Redland Genstar's Frederick, Maryland quarry were blended by the percentages shown in Table 1. The aggregate is a hard,

durable crushed limestone with low Los Angeles abrasion and meets Superpave gradation requirements as shown in Figure 9.

Table 1. Aggregate stockpile blend percentages.

Aggregate Stockpile	Blend Percentage by Weight
#7	28 %
#8	15 %
#10	17 %
Washed #10	40 %

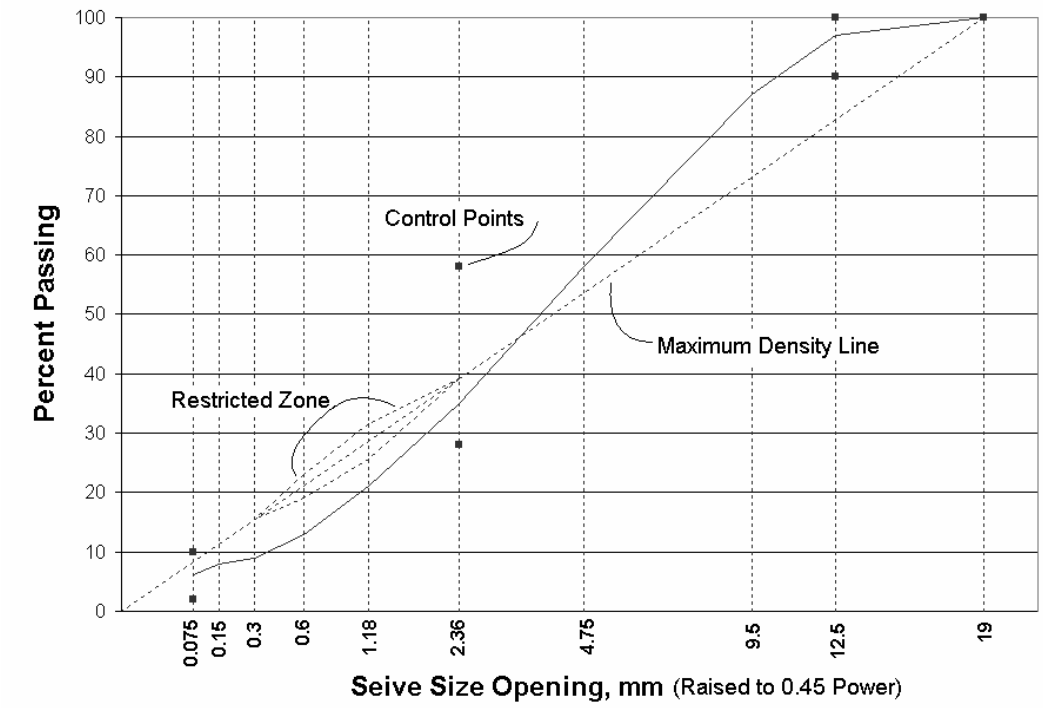

Figure 9. 12.5 mm aggregate gradation used in asphalt mixture for model calibration.

The unmodified asphalt binder used in the mixture is rated as a performance grade PG 64-22. Extensive tests were performed by others on the asphalt binder to characterize it over a wide range of temperatures and rates. Superpave and conventional binder tests were performed for tank, rolling thin film oven (RTFO) aged, pressure aging vessel

(PAV) aged, and recovered conditions. Detailed results from the individual aggregate, binder, and mixture material tests can be found in a report prepared by the Superpave Models Team (1999a). The final properties of the mixture are shown in Table 2.

Table 2. 12.5 mm asphalt concrete mixture design.

Property	**Design**	**Superpave Criteria**
Gradation 19.0 mm	(% Passing) 100	100
12.5 mm	97	100 – 90
9.5 mm	87	
4.75 mm	58	
2.36 mm	35	58 – 28
1.18 mm	21	
0.600 mm	13	
0.300 mm	9	
0.150 mm	8	
0.075 mm	6.1	10 – 2
Asphalt Content, %	5.2	
G_{mm}	2.492	
G_{sb}	2.674	
Air Voids, %	4.0	>= 4.0
VMA, %	15.5	>14.0
VFA, %	74	65-75
Filler/Effective Asphalt Ratio	1.26	0.6-1.2
% G_{mm} at $N_{initial}$	84.8	>89.0
%G_{mm} at $N_{maximum}$	97.6	<98
Coarse Aggregate Angularity	100/100	95/90
Fine Aggregate Angularity	46	>45
Flat and Elongated	8.3	<10
Sand Equivalent	91	>45
Binder Mixing Temperature, ^{o}C	153-159	
Compaction Temperature, ^{o}C	142-147	

3.2 Test Specimens

All test specimens were fabricated at Arizona State University and shipped to the other laboratories (NCSU and UMD) participating in this joint study to eliminate lab-to-lab variability in specimen manufacture. The geometry and instrumentation of the test specimens followed recommendations from the Superpave Models Team (1999b). The study recommends height to diameter ratios for different types of loading and boundary conditions. For unconfined uniaxial compression of 12.5 mm mixtures, the recommended test geometry is a cylindrical specimen 150 mm tall and 100 mm in diameter (height to diameter ratio of 1.5). For unconfined uniaxial tension or tension/compression tests, the recommended test geometry is a cylindrical specimen 150 mm tall and 75 mm in diameter (height to diameter ratio of 2.0). The larger aspect ratio is required for the tension specimens to minimize end effects at the bonded interfaces between the test specimen and the top and bottom loading platens.

Gyratory plugs 170 mm tall and 150 mm in diameter were compacted at Arizona State University using an IPC Servopac Superpave gyratory compactor. The test specimens were then cored from the gyratory plugs and the ends cut smooth and parallel. The target air void content for the cored and trimmed test specimens was 4.0% with a tolerance of ±0.5% to minimize air void content effects. To reduce the effects of aging, all specimens were placed in plastic bags and stored at temperatures between 5^{o}C and 25^{o}C before testing.

Linear variable differential transformers (LVDTs) were used for axial strain measurements. The axial LVDTs had spring-loaded gage heads and had a physical range of ±5.0 mm, although they were calibrated and used only over a reduced range of ±2.5

mm. The axial gage length for the LVDTs was 100 mm over the center of the specimen. All strain measurements reported are the average of four axial LVDTs located at 90 degree intervals around the specimen circumference. Averaging the four axial LVDTs removes specimen bending effects and reduces the overall variability of strain measurements on the specimen.

The axial LVDTs were attached to the specimen by means of glued studs to which brackets are affixed to hold the LVDTs in place. A gluing jig facilitates the process of attaching the studs. A cradle large enough for three to four specimens was constructed to hold the specimens horizontally. This cradle was used in conjunction with small Lexan© strips having holes drilled at the predetermined gage lengths. The studs were attached to the Lexan© strips to ensure the studs were aligned and glued at the correct gage length. Schematics of the LVDT brackets are shown in Figure 10. A photo of an instrumented compression specimen is provided in Figure 10. This axial LVDT setup allows for unhindered radial dilation of the specimen. Latex membranes may be used with this setup for triaxial confined testing. The membranes are placed over of the specimen and the glued brass studs. At each brass stud, the membrane is punctured by the screw and then sealed with a washer and liberal amounts of vacuum grease. The ends of the membrane are sealed on the top and bottom platen edges with O-rings and vacuum grease.

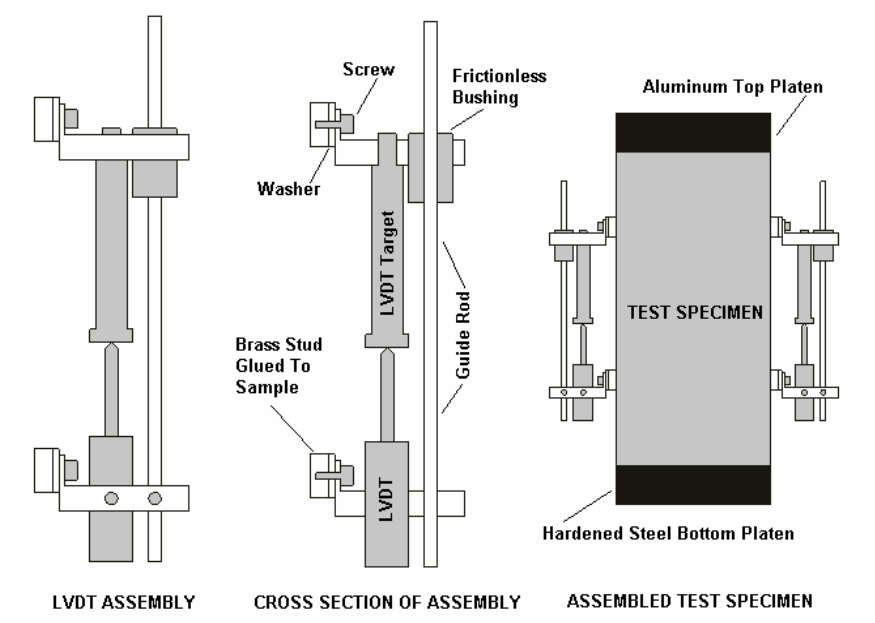

Figure 10 On-specimen LVDT instumentation.

Figure 11. Photo of instrumented specimen.

The ends of the test specimens for compression testing are lubricated to allow for uniform dilation and minimum end effects. Lubrication was achieved through greased rubber membrane sandwiches placed between the specimen ends and the top and bottom loading platens. The sandwich consists of two 100-mm diameter disks made from scrap latex

membranes with a thin layer of silicone grease in between. Trial and error was required to find the correct amount of grease. The specimens will shift between the loading platens if there is too much grease because it is very difficult to obtain perfectly parallel ends. Too little grease will create larger end effects by preventing free dilation of the specimen.

The top loading platen is lightweight aluminum to reduce the effect of its own weight on the material under soft conditions at high temperatures. The bottom is hardened steel for durability.

3.3 UTM-100 Testing System

IPC Global of Victoria, Australia manufactured the UTM-100 testing machine used for this study[3]. The machine is a servohydraulic feedback controlled testing machine capable of performing load and displacement controlled tests. A photo of the UTM-100 system is provided in Figure 12. The axial load capacity of the machine is 100 kN. Gain switches can be used to reduce the load range to 50 kN, 20 kN, or 10 kN for more sensitive tests. The machine is outfitted with an environmental temperature cabinet and confining pressure cell for confined tests. Control and data acquisition is achieved through a Control and Data Acquisition System (CDAS) unit interfaced with a PC via two serial cables. Two forms of test control software available from the manufacturer were used in this study. The first software package (UTM 3) utilized pre-programmed test templates for dynamic modulus, uniaxial strain rate, and other standard tests. More sophisticated tests were performed with the second user-defined program (UTM 100),

[3] More details about IPC products can be found at www.ipcglobal.com.au.

which gives the operator much greater flexibility in specifying loading and data acquisition settings.

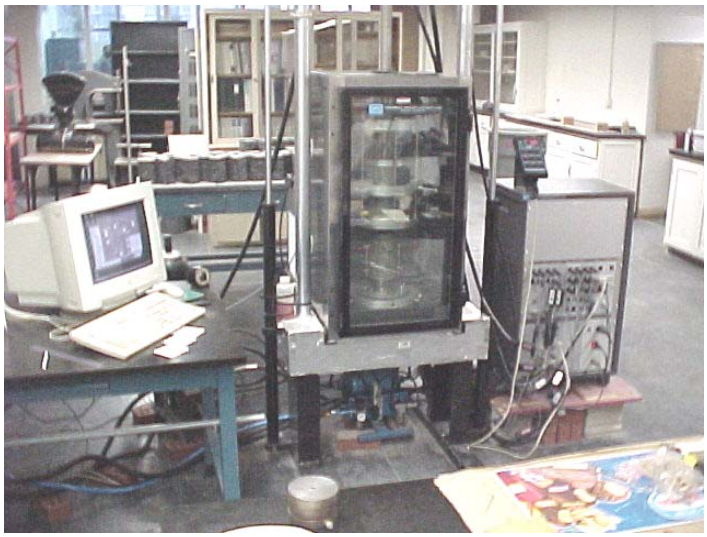

Figure 12. UTM-100 testing system.

4. Linear Viscoelasticity Characterization

4.1 Introduction

Small-strain frequency sweep tests were used to determine the linear viscoelastic complex modulus and the temperature shift factors of the material for small-strain response. Conventional dynamic modulus tests were performed in unconfined compression at four temperatures and five frequencies at each temperature. Dynamic modulus and phase angle data are then converted to relaxation modulus for use in the Schapery continuum damage model formulation.

4.2 Testing Details

Draft test protocols developed as part of NCHRP Projects 1-37A and 9-19 formed the basis for the dynamic modulus testing in compression for this project. These data are obtained from uniaxial compression frequency sweep tests performed just prior to the

constant strain rate tests used to evaluate time-temperature superposition at large strains (Chapter 5) and to calibrate the uniaxial damage model (Chapter 7). A summary of the test conditions is found in Table 3. Testing was performed at 5, 25, 40, and 60^{o}C. These temperatures, which deviate somewhat from the NCHRP 1-37A and 9-19 dynamic modulus test protocols, were selected based on the target temperatures for the constant strain rate tests performed immediately after the frequency sweep. The test temperatures approximate the range of temperatures a pavement would experience, except for perhaps the coldest temperatures.

The frequencies used in this research also deviated a bit from NCHRP 1-37A and 9-19 complex modulus protocols. At each temperature the material was loaded sinusoidally at frequencies of 20 Hz, 10 Hz, 3 Hz, 1 Hz, 0.3 Hz, and 0.1 Hz. These frequencies approximate the full range of loading rates pavements experience from highway speeds down to very slow traffic. As will be described later, multiple frequencies ensure complete development of a complex modulus master curve for the material. An overlap between dynamic modulus isothermal curves is desirable (although not essential) when creating master curves. In other words, the modulus at the highest frequency at a given temperature should be similar to the modulus at the neighboring lowest frequency at a colder temperature.

Preconditioning was performed at 10 Hz using one half the stress level applied in the normal 10 Hz loading. Preconditioning is intended to seat any loose aggregates in the specimen and remove any other anomalous strain measurements before the formal frequency testing. The duration of loading for each compressive frequency sweep is summarized in Table 4 and varied between 25 to 100 seconds depending on what was

feasible and what the pre-programmed IPC software would allow. The specimen was allowed to recover under a very small contact stress for five minutes between each frequency. The data acquisition software acquired the last six cycles of data for analysis purposes. The last six cycles are used to determine the linear viscoelastic properties of the material on the assumption that the dynamic strain response has reached steady state at this point.

It was assumed that limiting the dynamic strains to less than 100με ensured linear viscoelastic behavior and negligible microstructural damage of the material. This required the applied stress to vary with frequency at each temperature, with higher stresses being applied at the higher frequencies. Typical compressive stresses applied in the dynamic modulus tests are shown in Table 5.

Table 3. Summary of small strain dynamic modulus test conditions.

Test Temperatures	5, 25, 40, 60 °C (41, 77, 100, 140 °F)
Frequencies in Frequency Sweep	0.1, 0.3, 1, 3, 10, 20 Hz
Cycles per Frequency	10, 15, 40, 100, 250, 600 cycles respective to the above frequencies
Dynamic Strain Limit	Stress levels controlled such that dynamic strains were no greater than 100 με (but large enough to analyze)
Preconditioning	200 cycles at 10 Hz Using ½ the Stress Applied in the Regular 10Hz Sweep

Table 4. Details of loading for small-strain dynamic modulus tests.

Loading Cycle	**10Hz** Preconditioning	**20Hz**	**10Hz**	**3Hz**	**1Hz**	**0.3Hz**	**0.1Hz**
Number of Cycles	100	600	250	100	40	15	10
Total Time, sec	10	30	25	33.3	40	50	100

Table 5. Typical stresses applied in small-strain dynamic modulus tests.

Temperature (°C)	Typical Stresses Applied (kPa)					
	20 Hz	10 Hz	3 Hz	1 Hz	0.3 Hz	0.1 Hz
5	1192	1041	895	756	609	501
25	601	525	374	274	211	169
40	259	213	149	113	94	83
60	65	58	43	35	32	29

Note that in a conventional dynamic modulus test, frequency sweeps would be performed at all test temperatures on a single test specimen. Testing usually begins with the coldest temperature, with frequency varied from the highest to lowest values under constant temperature conditions. The temperature in the environmental chamber is then increased, the specimen is allowed to reach thermal equilibrium, and the frequency sweep is repeated at this new temperature. This process is repeated for all temperatures in the test protocol. The modified protocol used in the present study is slightly different in that it tests a different specimen at each test temperature; this is necessary because the subsequent constant strain rate test is run to failure.

As indicated in Table 3, the stress was varied so that the magnitudes of the dynamic strains were limited to a maximum of 100με at all frequencies in order to minimize specimen damage and ensure linear behavior. This goal was achieved with an average strain of about 60με. Sacrificial specimens were required to determine the appropriate stress settings for the formal production tests. It is useful to note the current specifications for the Simple Performance Tester from NCHRP Project 9-29 have removed this iterative trial and error (Bonaquist et al., 2002). The control software for the Simple Performance Tester is required to automatically adjust the target stresses in the

stress-control test such that the measured dynamic strains are always within a user defined tolerance, typically 75με to 125με.

A typical trace of dynamic strain vs. time from the frequency sweep tests is shown in Figure 13. Histograms summarizing the distribution of dynamic strain magnitudes at each test temperature are provided in Figure 14. There was considerable amount of signal noise in the strain measurements. Possible causes include the large capacity of the load cell and the large amount of inherent noise in the LVDT signals. The magnitude of the noise can be seen in Figure 13. The noise amplitude in the LVDTs was on the order of 24$\mu\varepsilon$, as compared to dynamic strain amplitudes on the order of 60 to 70$\mu\varepsilon$. Although much effort was put into troubleshooting the noise, the source was not isolated nor its magnitude reduced during this study. A faulty electronic signal conditioner was eventually detected and repaired at a later date.

For various reasons, about eight specimens (five more than the required three) were typically tested at each temperature in this study. The added benefit from these additional samples is increased confidence in the mean |E*| values.

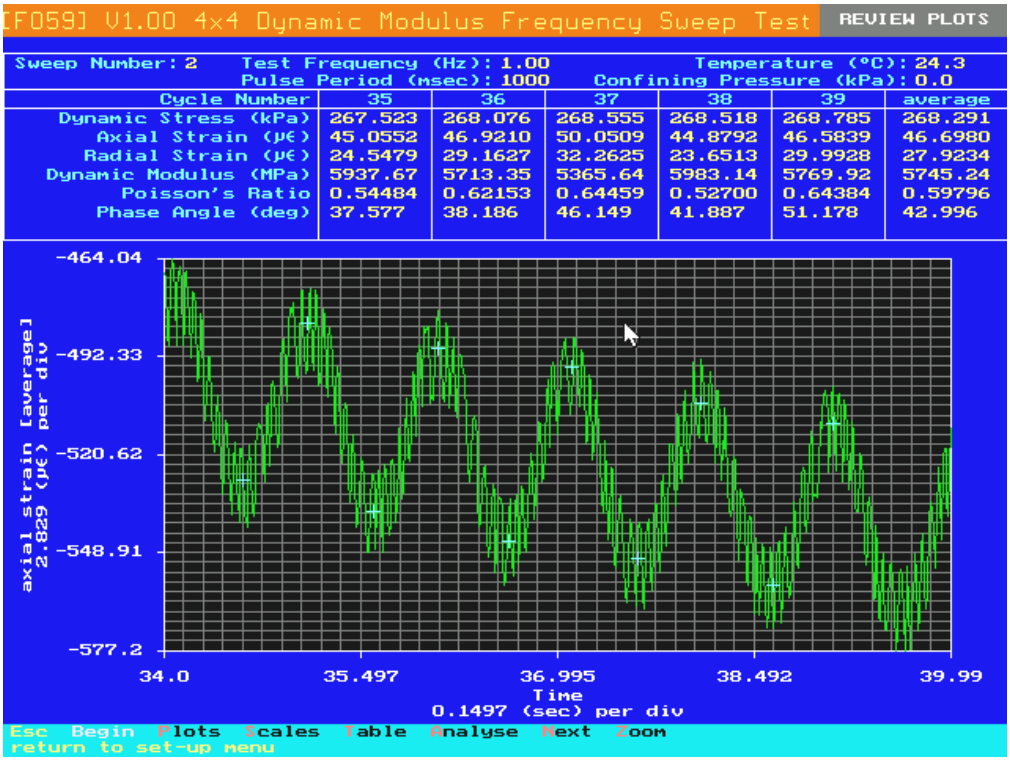

Figure 13 Typical trace of dynamic strains from pre-programmed IPC |E*| software.

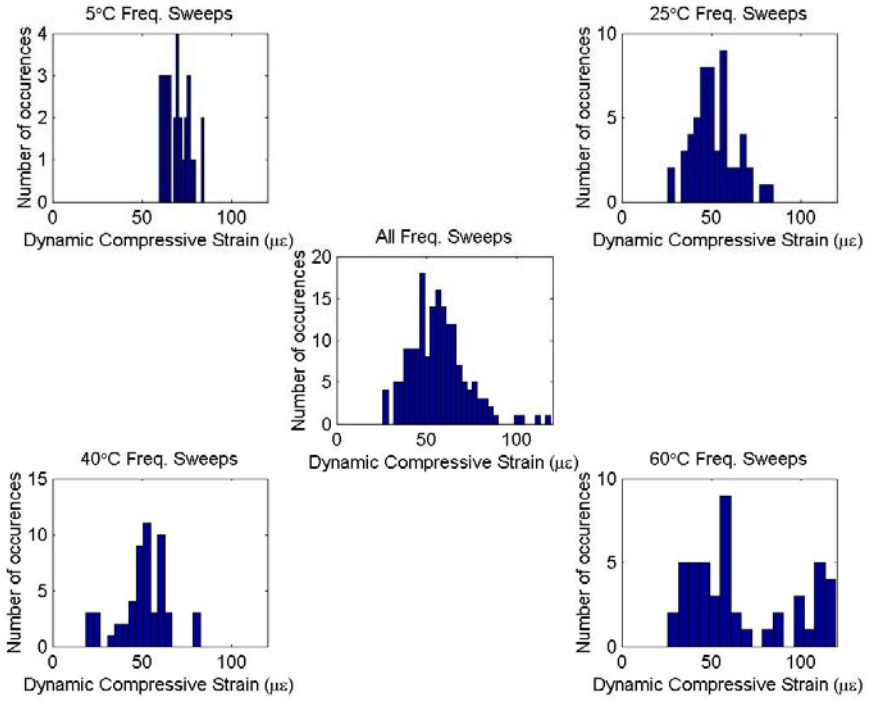

Figure 14 Dynamic strain magnitudes from dynamic modulus frequency sweeps.

4.3 Dynamic Modulus Test Results

The magnitude of the dynamic modulus, $|E^*|$, and the time lag or phase angle, ϕ, between the stress and strain at each temperature and frequency were the primary objectives for the data analysis. For the compression tests, determination of $|E^*|$ and phase angle was performed using the built-in algorithms in the pre-programmed IPC software controlling the test and data acquisition. For a given cycle of stress and strain data, the algorithm fits a second order polynomial over 25% of the period on either side of the peak or valley to determine the peak-to-peak dynamic strain, peak-to-peak dynamic stress, and lag time between the stress and strain peaks. Typical results from this pre-programmed software are shown in Figure 13.

4.3.1 Isothermal Dynamic Modulus and Phase Angle

Dynamic modulus and phase angle values versus loading frequency for each replicate at each temperature are shown in Figure 15 through Figure 22. These data were collected and analyzed using the methods described earlier in the testing details subsection.

Dynamic modulus and phase angle values generally followed expected trends. Phase angle increases with loading frequency at the warmer temperatures and decreases with frequency at the colder temperatures. The only unusual results were for the phase angle the two warmest temperatures, in that the phase angle at 40^{o}C was unexpectedly

very similar to the phase angle at 60°C. Dynamic modulus increases with increasing loading frequency and increases as temperature decreases in all cases.

Coefficients of variation were computed to assess the variability of the measured values. Coefficient of variation CV is defined as:

$$CV = \frac{s}{\bar{x}} \times 100\% \qquad \textbf{Equation 58}$$

in which s is standard deviation and $\bar{x}$ is the mean value. Coefficients of variation for measured dynamic modulus at each temperature and frequency are summarized in Table 6. Coefficients of variation for measure phase angle at each temperature and frequency are listed in Table 7.

The coefficients of variation for both phase angle and dynamic modulus increase with increasing temperature, in large part because the material properties are more difficult to measure as the asphalt binder becomes softer. Pellinen (2001) reported dynamic modulus coefficients of variation of 12.8%, 14.2%, 14.5%, and 28.1% and phase angle coefficients of variation of 10.2%, 5.0 %, 4.6%, and 9.5% at temperatures of 4.4, 21.1, 37.8, and 54.4°C, respectively. The values for the present study listed in Table 6 and Table 7 are a bit higher than Pellinen's. It is believed that the reasons for the larger variations in the present study are the higher capacity of the UMD testing machine and the larger than desirable noise in the strain measurement signals. The tests were particularly difficult to control at 60°C; this is reflected in the large coefficients of variation for both dynamic modulus and phase angle at 60°C. The gain setting on the 100 kN load cell was set to the 10 kN range for the 60°C tests in an effort to improve the data quality. However, this only slightly improved the signal to noise ratio, and the very small

loads (average load of 0.75 kN) applied to the specimens at 60°C were still only about 7.5% of the 10kN load cell range.

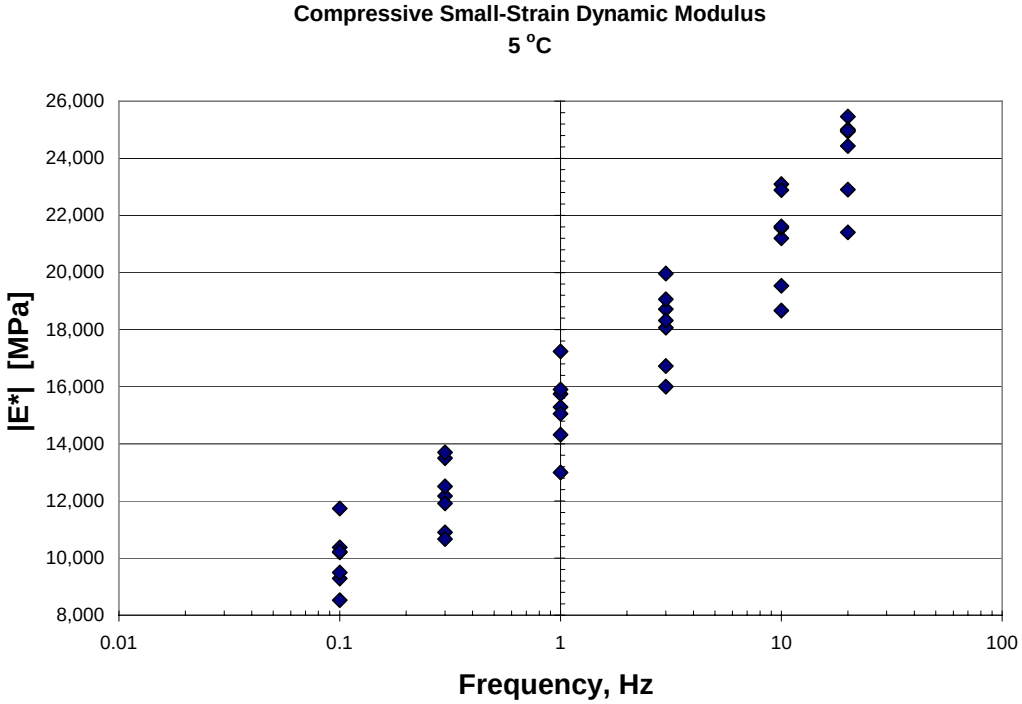

Figure 15. Dynamic modulus in compression at 5°C.

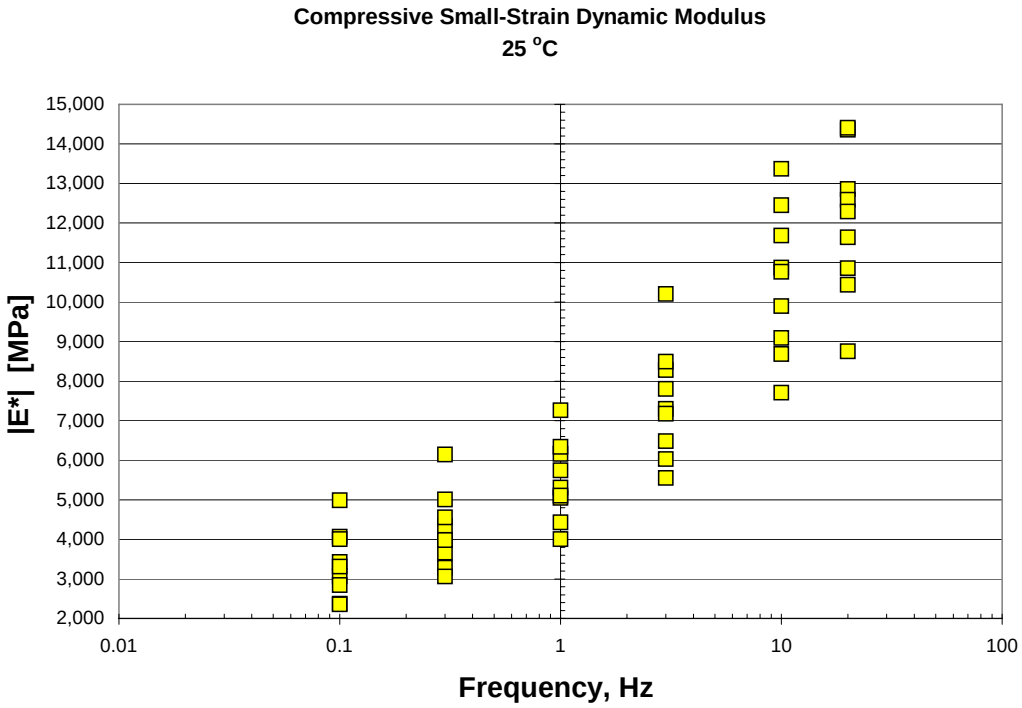

Figure 16. Dynamic modulus in compression at 25°C.

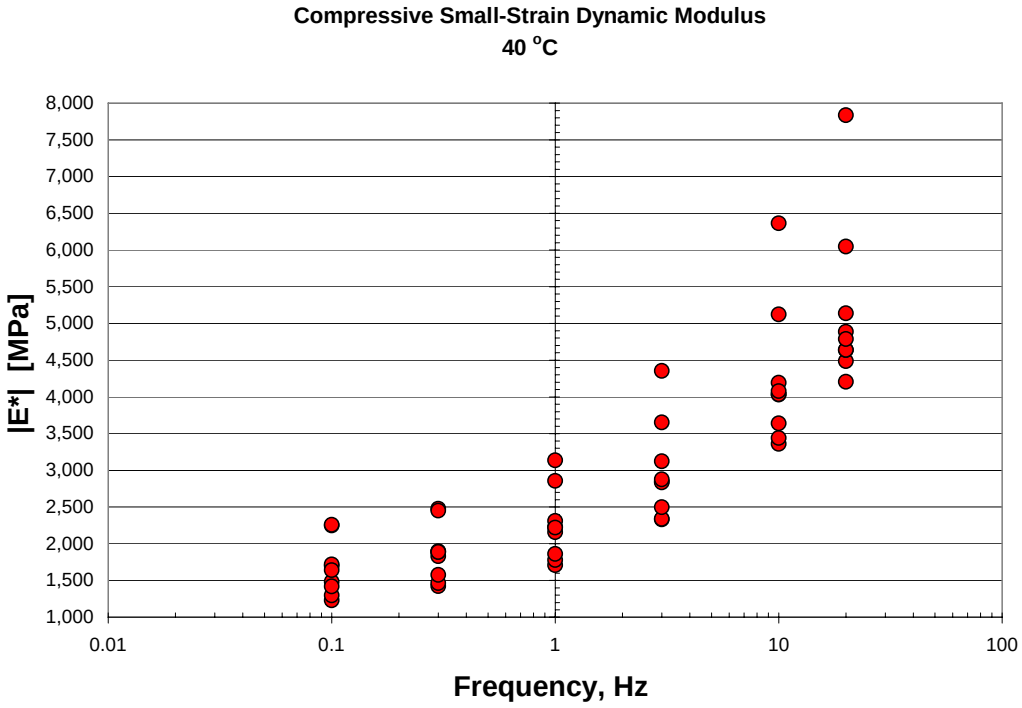

Figure 17. Dynamic modulus in compression at 40°C.

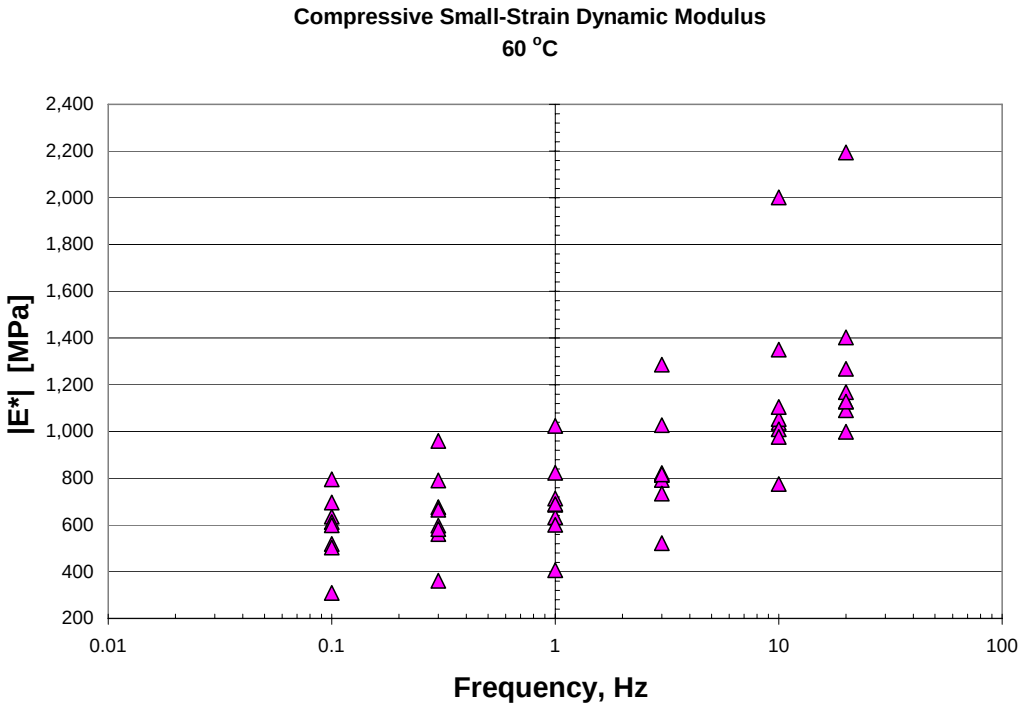

Figure 18. Dynamic modulus in compression at 60°C.

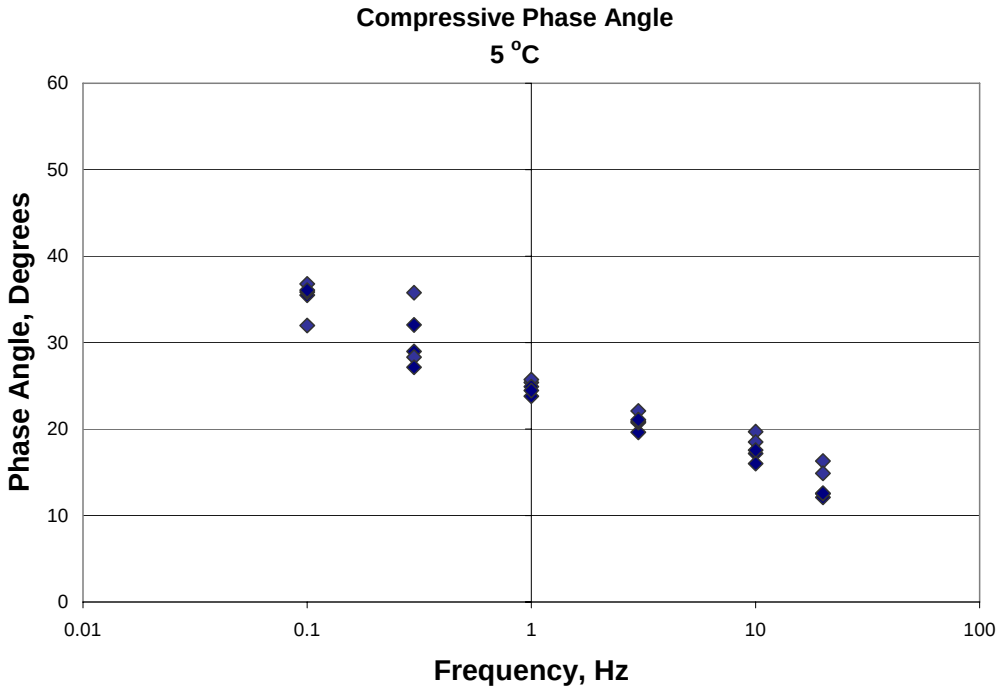

Figure 19. Phase angle in compression at 5°C.

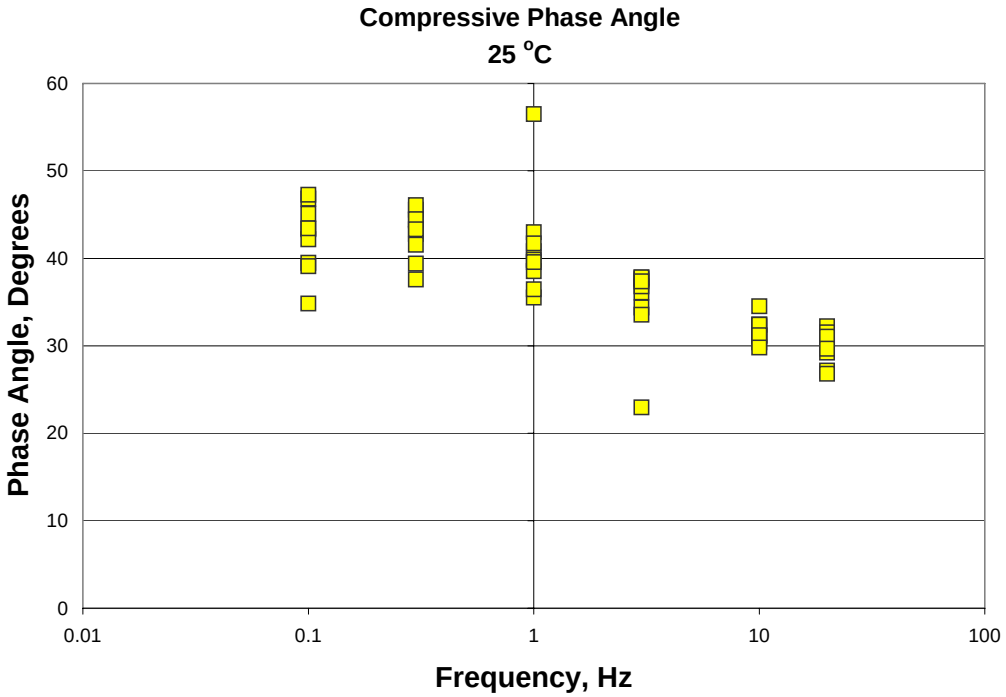

Figure 20. Phase angle in compression at 25°C.

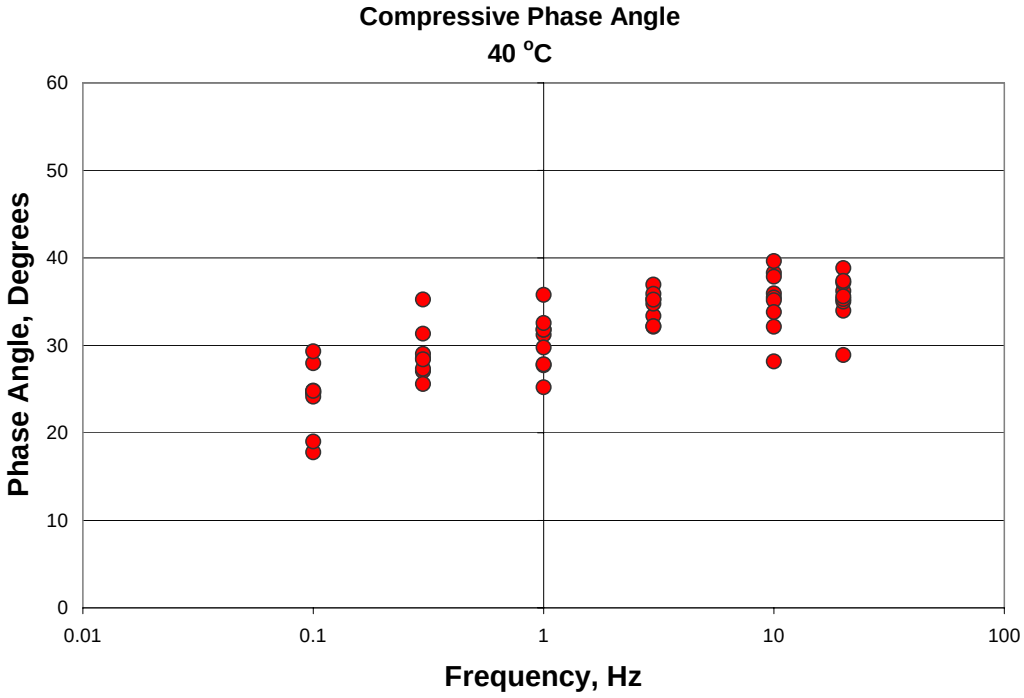

Figure 21. Phase angle in compression at 40°C.

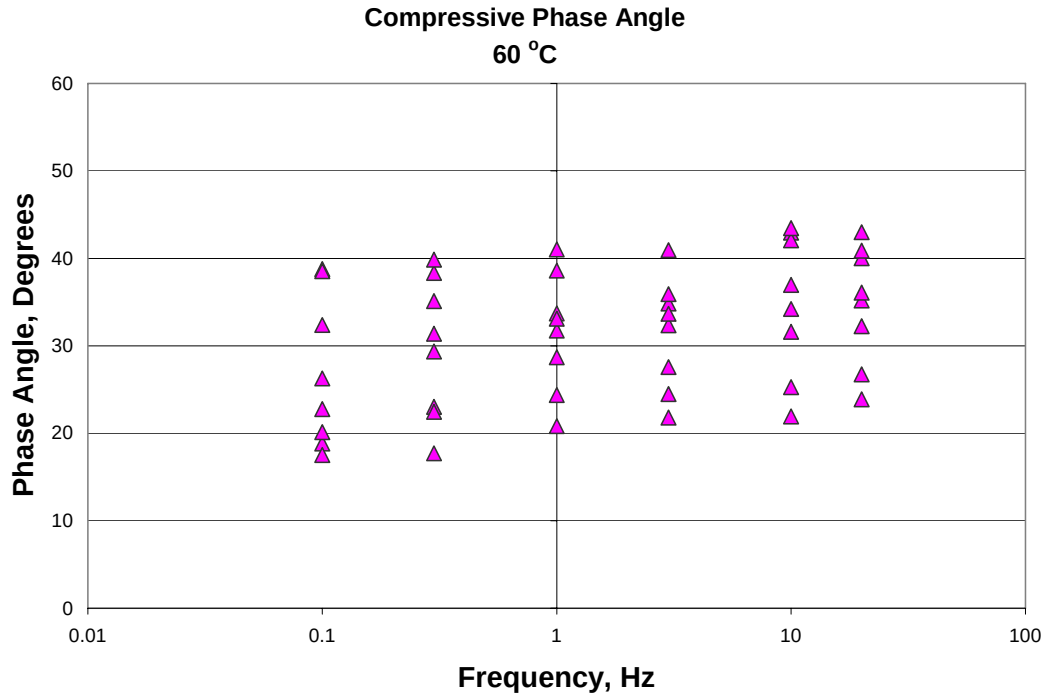

Figure 22. Phase angle in compression at 60°C.

Table 6. Coefficients of variation for compressive dynamic modulus.

Temperature, °C	Dynamic Modulus Coefficients of Variation (%)						
	Avg. of All Freq.	20 Hz	10 Hz	3 Hz	1 Hz	0.3 Hz	0.1 Hz
5	**9.7**	7.0	8.4	8.8	10.5	11.6	12.1
25	**19.6**	15.3	17.5	19.0	18.3	22.3	25.4
40	**21.6**	21.6	22.3	22.1	21.3	20.3	22.4
60	**27.5**	29.4	32.1	26.2	25.5	27.0	24.8

Table 7. Coefficicents of variation for compressive phase angle.

Temperature, °C	Phase Angle Coefficients of Variation (%)						
	Avg. of All Freq.	20 Hz	10 Hz	3 Hz	1 Hz	0.3 Hz	0.1 Hz
5	**7.5**	13.3	7.8	4.2	3.1	11.4	5.3
25	**9.2**	6.3	4.4	13.6	14.9	6.6	9.5
40	**7.9**	4.3	6.8	5.1	8.5	10.4	12.2
60	**24.0**	19.6	23.4	20.2	21.5	27.1	32.1

4.3.2 Dynamic Modulus and Phase Angle Master Curves

Following work by Pellinen (2001), the underlying shape for the dynamic modulus master curve was assumed to be a sigmoidal function in the following form:

$$\log|E^*| = c_1 + \frac{c_2}{1+e^{(-c_3*\log\omega_R - c_4)}} \qquad \textbf{Equation 59}$$

The sigmoidal function in log-log space is an appropriate shape for the dynamic modulus master curve of asphalt concrete; it can be applied equally well to characterize the storage modulus master curve. The sigmoidal function is characterized by high and low temperature shelves where the dynamic modulus becomes relatively insensitive to further change in temperature. The high and low temperature shelves are typically approached at temperatures of about 60°C and -10°C, respectively. Temperatures colder than 5°C were not considered here because it was determined in advance that the capacity of testing machine was insufficient to fail the specimens in the constant strain rate portion of the tests immediately following the frequency sweeps.

The method for calibrating the master curve proposed by Pellinen (2001) uses the nonlinear optimization tool Solver in Microsoft Excel to determine the best-fit master curve. The four coefficients for the sigmoidal function are optimized in Solver simultaneously with the individual $a(T)$ shift factors for each temperature. The results from this optimization are shown in Figure 23 and Figure 24, which summarize the individual temperature-shifted dynamic modulus data, the underlying fitted master curve, and the $a(T)$ temperature shift factor relationship. Each data point in the dynamic modulus master curve is the average of at least eight replicates. The measured dynamic modulus values begin to approach their respective shelves at the high and low temperature extremes.

The average phase angle was shifted at each temperature using the same $a(T)$ temperature shift factors developed for the dynamic modulus; the shifted phase angles are shown in Figure 25. It is more reasonable to use the temperature shift factors from dynamic modulus to shift phase angle than to optimize a phase angle master curve separately because of the larger variability in the phase angle data.

The key results from the dynamic modulus master curve development are the individual temperature shift factors and the coefficients that characterize the underlying sigmoidal master curve. These are summarized in Table 8 and Table 9, respectively.

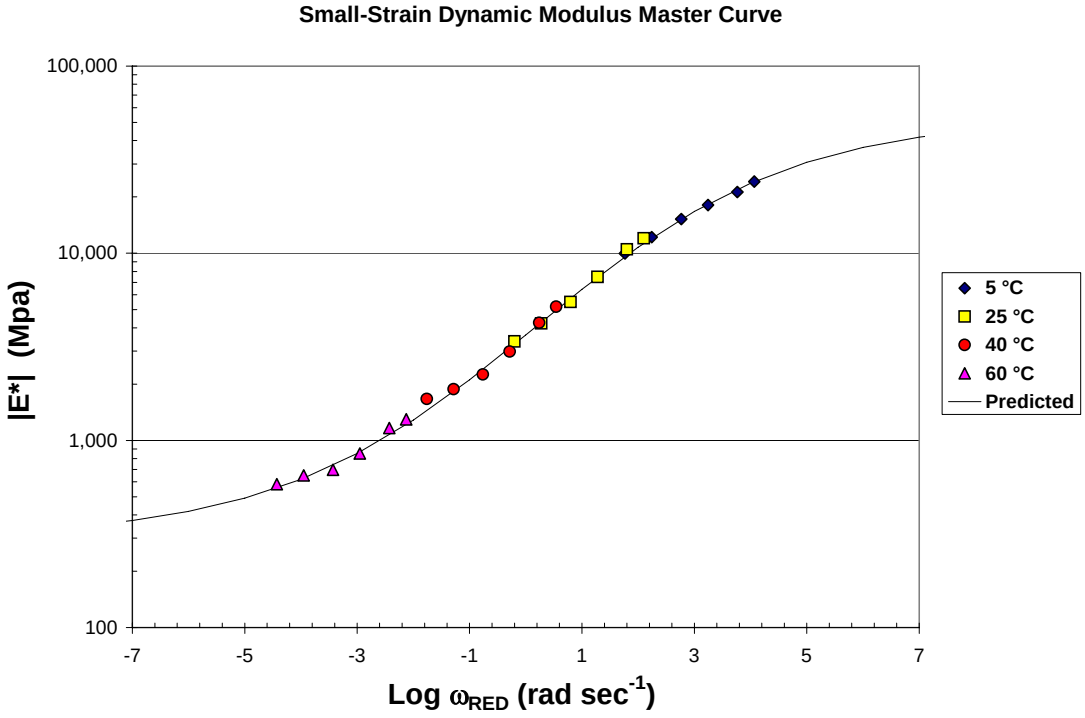

Figure 23. Small-strain dynamic modulus master curve. Average of replicates at each temperature shown.

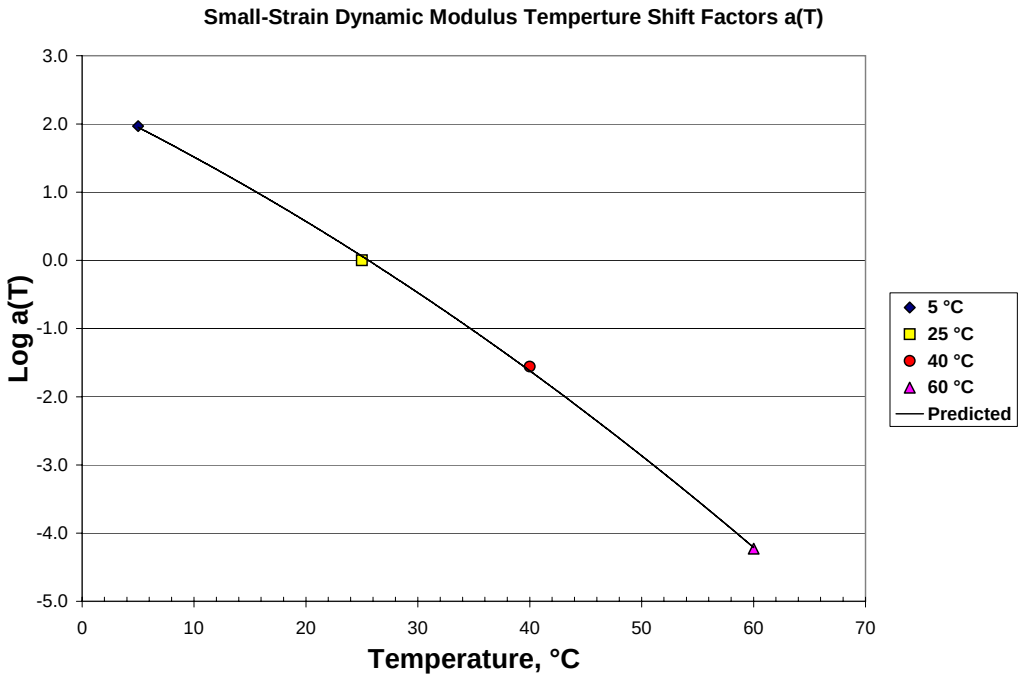

Figure 24. Small-strain dynamic modulus temperature shift factors.

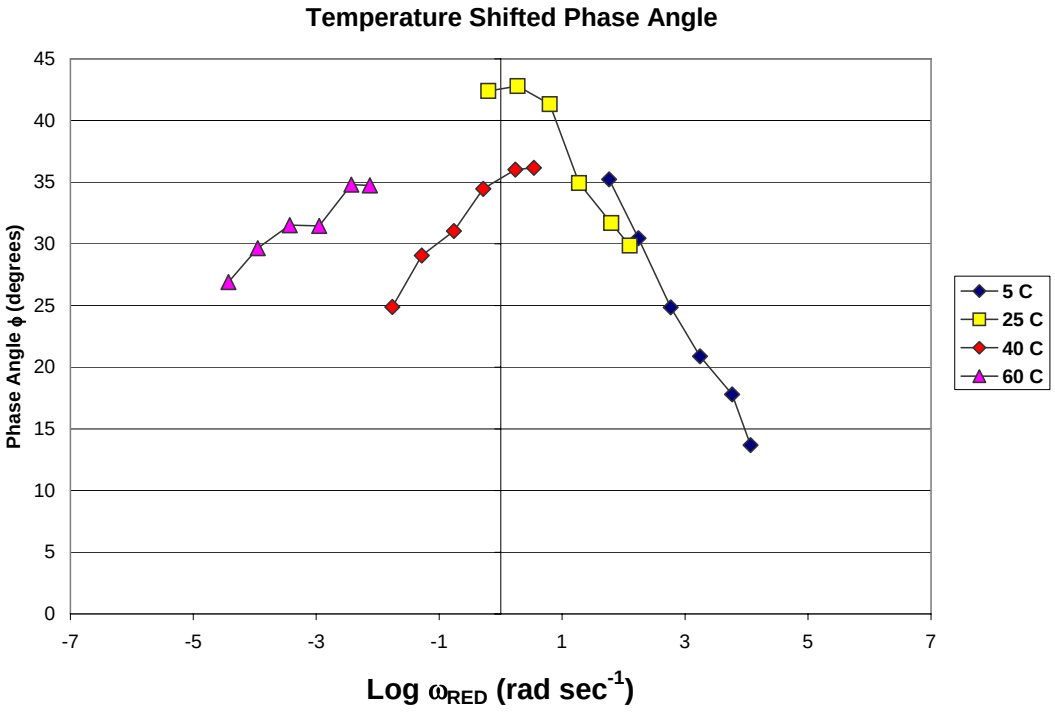

Figure 25. Temperature shifted phase angle.

Table 8. Small-strain dynamic modulus *a*(*T*) shift factors.

Temperature, ^{o}C	5	25	40	60
a(T)	$10^{1.9670}$	0	$10^{-1.5587}$	$10^{-4.2267}$

Table 9. Coefficients for dynamic modulus master curve Equation 58 in units of MPa with frequency units of radians per second.

c_1	c_2	c_3	c_4
2.4479	2.2510	0.4369	-0.0706

4.3.3 Effect of Accumulated Strain on Dynamic Modulus

Significant amounts of accumulated strain ranging up to 0.45% were observed during some of the warmer compressive dynamic modulus frequency sweeps. This accumulated strain is caused by the non-zero mean stress from the compressive haversine loading over all of the frequencies. It was of interest to determine if this accumulated strain had any effect on the measured dynamic modulus as a consequence of induced damage or viscoplasticity.

To address this concern, an exploratory test was conducted at about 40^{o}C with a modified frequency sweep applying the standard suite of frequencies from preconditioning through 0.1 Hz followed by this same frequency sweep in reverse order. The dynamic modulus and phase angle at each frequency were examined to determine if there were any significant differences between the forward and reverse frequency sweeps.

The measured strain versus time throughout this exploratory test is shown in Figure 26. Strain clearly increases due to the mean compressive stress during loading at each frequency; only a portion of this strain is recovered during the rest periods. The majority of the accumulated strain develops during the 10 Hz preconditioning and the 20

Hz initial loading phase. Dynamic modulus and phase angle values measured at each frequency during the forward and reverse passes are plotted in Figure 27 and Figure 28.

The dynamic modulus measured at 20 Hz in the forward pass was identical to the value measured in the reverse pass after about 0.3% strain had accumulated (recall that the small strain limit is conventionally assumed to by 100$\mu\varepsilon$ or 0.01%). The phase angle values varied slightly more between the two passes, but this is likely due at least in part to the larger inherent variability of the phase angle measurements. The dynamic modulus did not appear to be affected by the accumulated strain.

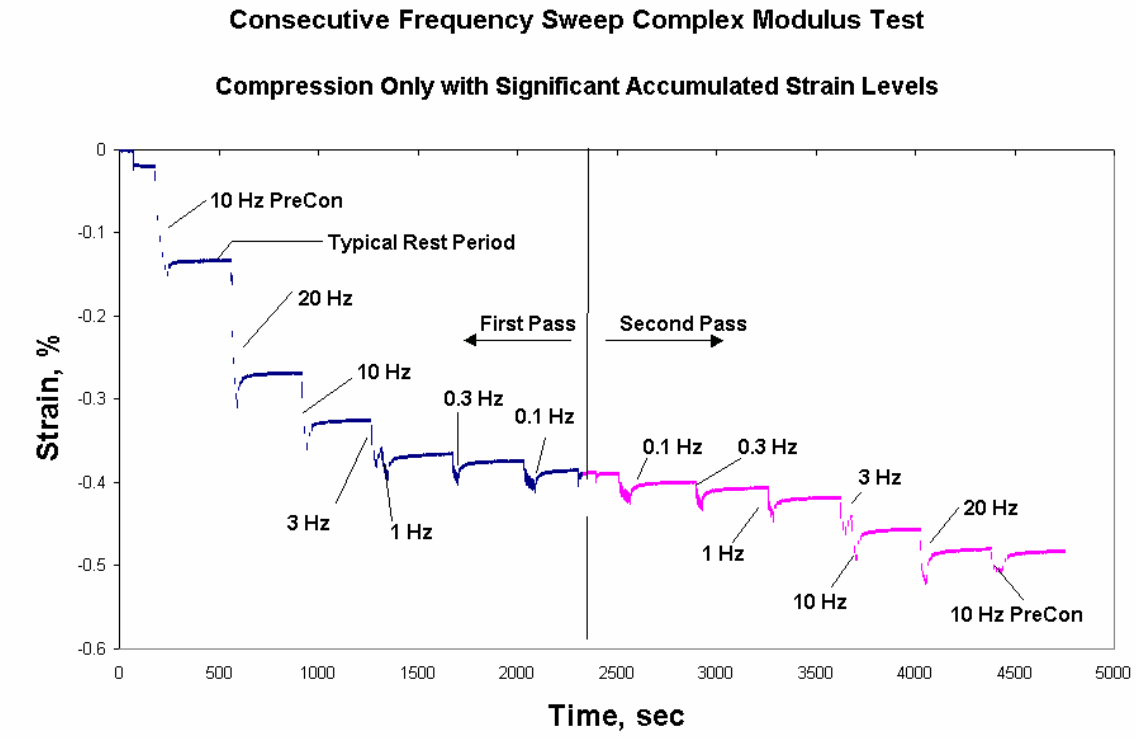

Figure 26. Back-to-back compressive frequency sweep with accumulated strain.

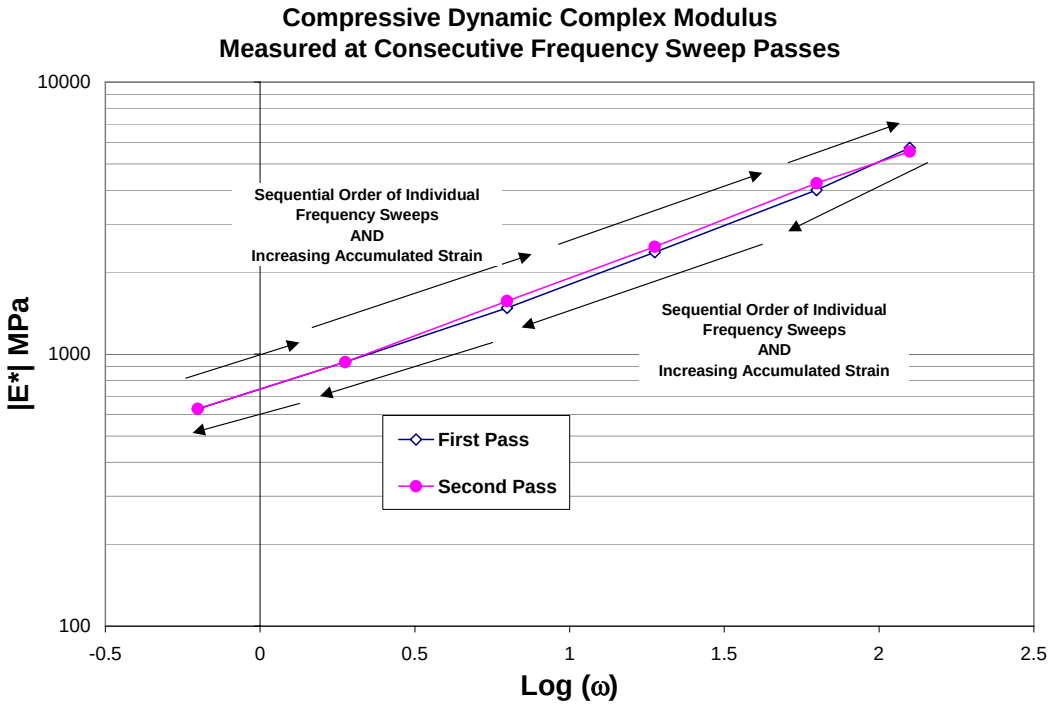

Figure 27. Compressive dynamic modulus with different amounts of accumulated strain.

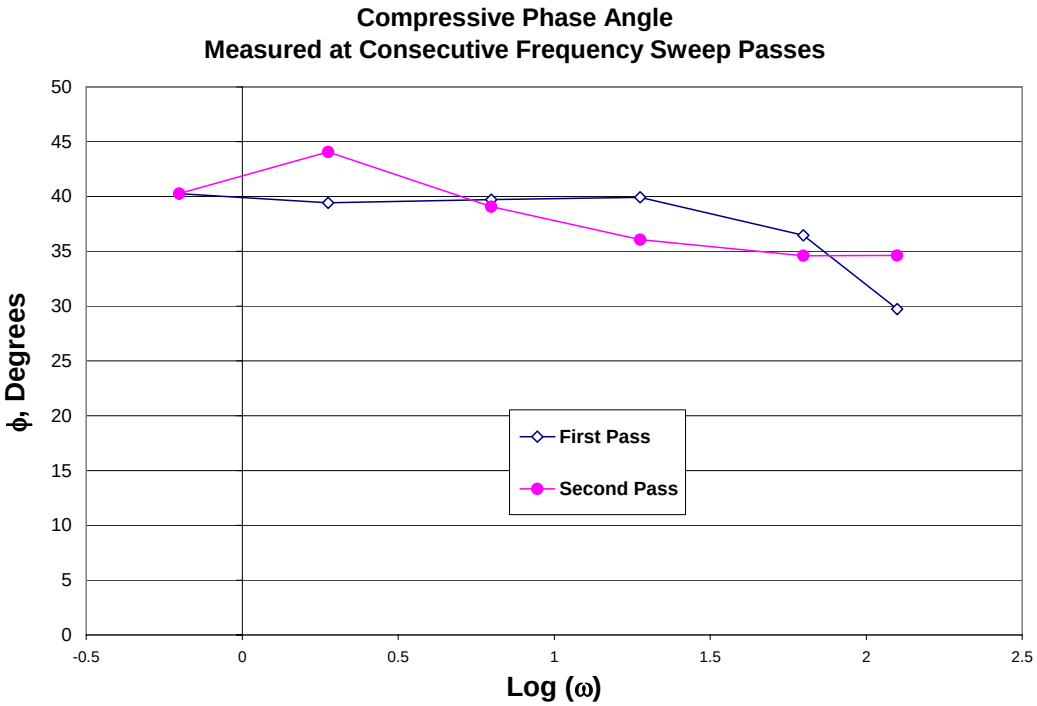

Figure 28. Compressive phase angle with different amounts of accumulated strain.

4.4 Relaxation Modulus and Creep Compliance

As described earlier in Chapter 2, the complex modulus can be alternatively modeled using a generalized Maxwell viscoelastic model. In this case, the storage $E'(\omega)$ and loss modulus $E''(\omega)$ components of E^* can be expressed mathematically in terms of the following Prony series:

$$E'(\omega) = E_o + \sum_{i=1}^{m} \frac{\omega^2 \rho_i^2 E_i}{1 + \omega^2 \rho_i^2} \qquad \textbf{Equation 60}$$

$$E''(\omega) = \sum_{i=1}^{m} \frac{\omega \rho_i E_i}{1 + \omega^2 \rho_i^2} \qquad \textbf{Equation 61}$$

in which E_i are the elastic spring stiffness and ρ_i are the relaxation times for the elements in the generalized Maxwell model. The relaxation modulus $E(t)$ and creep compliance $D(t)$ can then be evaluated as:

$$E(t) = E_o + \sum_{i=1}^{m} E_i e^{\frac{-t}{\rho_i}} \qquad \textbf{Equation 62}$$

$$D(t) = D_o + \sum_{j=1}^{n} D_j (1 - e^{\frac{-t}{\tau_j}}) \qquad \textbf{Equation 63}$$

in which the E_i and ρ_i terms in Equation 62 are the same as in Equation 60 or Equation 61 and the D_j and τ_j terms in Equation 63 are derived from the E_i and ρ_i terms using the techniques previously described in Chapter 2.

The expression for storage modulus in Equation 60 was used to determine the Prony series terms. However, a problem was discovered during analysis of the 5°C constant strain rate test data. The constant strain rate tests, which immediately followed the frequency sweep tests, are described more fully in Chapters 5. The initial assumption

for these tests was that the damage strains were very small at the very beginning of the test and that the viscoplastic strains were negligible throughout. Consequently, the initial portion of the test response should be almost entirely viscoelastic. However, when the linearly viscoelastic stresses were computed from the measured strains via the relaxation convolution integral (see Chapter 2), the computed stresses were higher (from 0 to 70%) than the measured stresses. A worst-case example of this is shown in Figure 29.

The hypothesized cause of this problem was that the relaxation modulus as derived from the storage modulus was too large at very early times. Very early relaxation times correspond to the upper shelf of the complex modulus master curve and in hindsight the frequency sweep tests performed in this study had insufficient low temperature data to define the magnitude of the upper shelf of the storage modulus with adequate precision. The following scheme was therefore developed to correct this problem:

1. The very early portions of the 5^{o}C constant strain rate tests were assumed to have negligible damage and viscoplastic strains. (This is not quite correct, as will be discussed later, but is sufficiently accurate for the present purposes.)
2. The very early portions of the 5^{o}C constant strain rate tests are dominated by the early-time relaxation modulus, which is in turn related to the upper shelf of the storage modulus master curve.
3. Through a process of trial and error, a correction factor was determined by which the early-time relaxation modulus must be reduced so that the predicted response for the very early portions of the 5^{o}C constant strain rate tests approximately

matched the measured values. This correction factor in was in general different for each replicate, so an average correction factor was determined.

4. The "corrected" relaxation modulus was extrapolated to time=0; this value corresponds to the constrained upper shelf of the storage modulus curve. For the data measured in this study, this upper shelf value was determined as 30.8 GPa.
5. The storage modulus master curve was re-fit using the procedures described but with the additional constraint that the upper shelf not exceed the value from step 4. Figure 30 summarizes the storage modulus master curves both with and without the upper shelf constraint. Both curves fit the measured data with approximately equal fidelity and differ only in their extrapolations of the data. The effect of the upper shelf constraint on the master curve temperature shift factors was negligible, as shown in the inset of Figure 30. Figure 31 highlights the upper and lower shelves of the storage modulus in relation to the measured data by plotting in log-log space.

One additional correction was implemented in the comparisons of predicted versus measured early period response for the 5^{o}C constant strain rate tests. Although the viscoplastic strains were assumed to be negligibly small, estimates using the calibrated viscoplasticity model (see Chapter 6) suggested these strains even at 5^{o}C were still on the order of 10% of the total strain near the peak stress; typical results are shown in Figure 32. The viscoplastic strains during the very early portion of the controlled strain rate response are still negligible. Nevertheless, faithful computations of the hardened viscoplastic strains that occurred during the preceding |E*| tests were calculated because they influenced the subsequent monotonic tests. These computed viscoplastic strains

were therefore subtracted from the measured total strains before making the comparisons with the computed LVE strains. Typical results are shown in Figure 33 and at an expanded scale in Figure 34. The results in Figure 34 clearly show that the computed LVE stress versus strain response is nearly identical to the net measured (total strain less viscoplastic component) response for the first several hundred microstrains. This in addition to the back-to-back frequency sweeps suggests that little damage is developing during this early portion of the response.

After incorporating all of these corrections the final, best estimate terms for a 12-term Prony series for the relaxation modulus and creep compliance and the corresponding temperature shift functions at a reference temperature of 25^{o}C are summarized in Table 10, Table 11, and Figure 35.

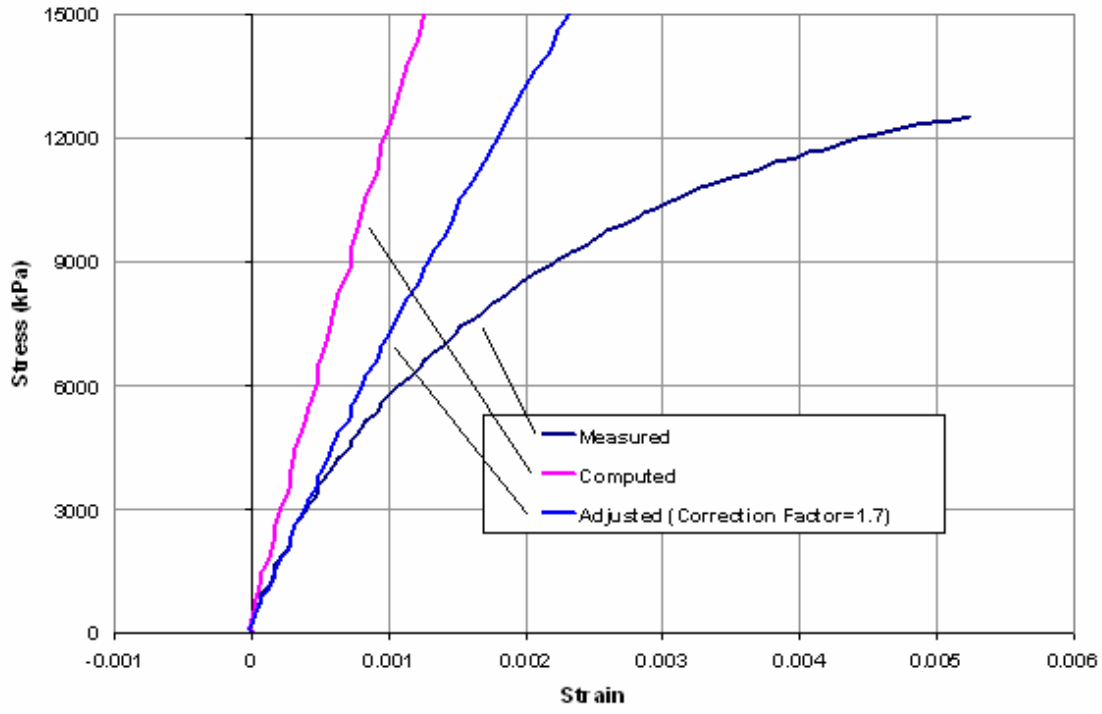

Figure 29. Worst-case discrepancy between measured and LVE computed stress versus strain response for 5^{o}C constant strain rate test (specimen 5STOA12).

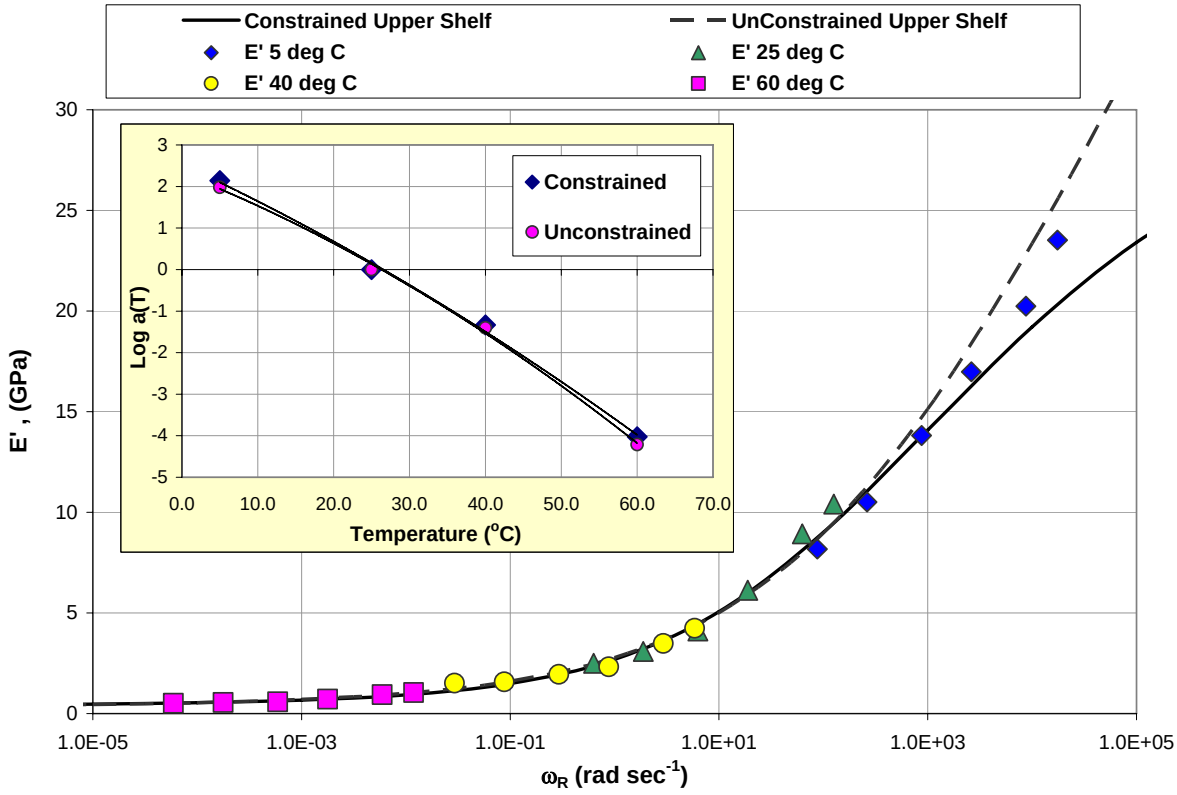

Figure 30. Storage modulus master curve with constrained upper shelf.

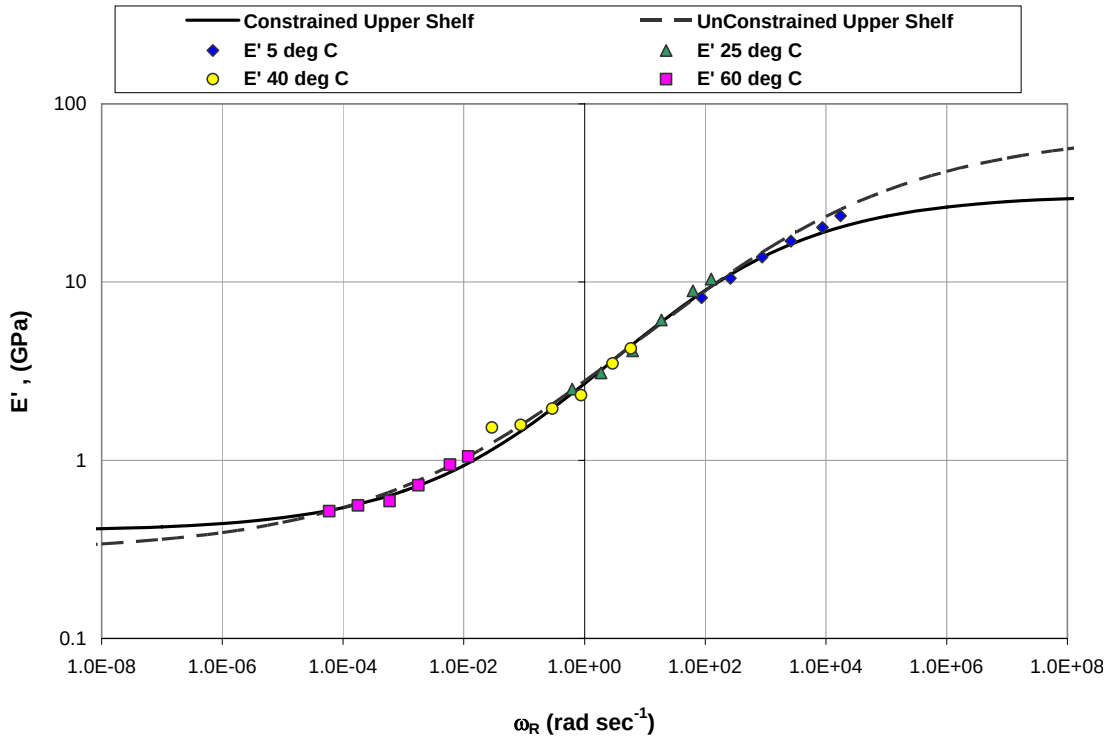

Figure 31. Storage modulus in log-log space to illustrate the upper and lower shelves.

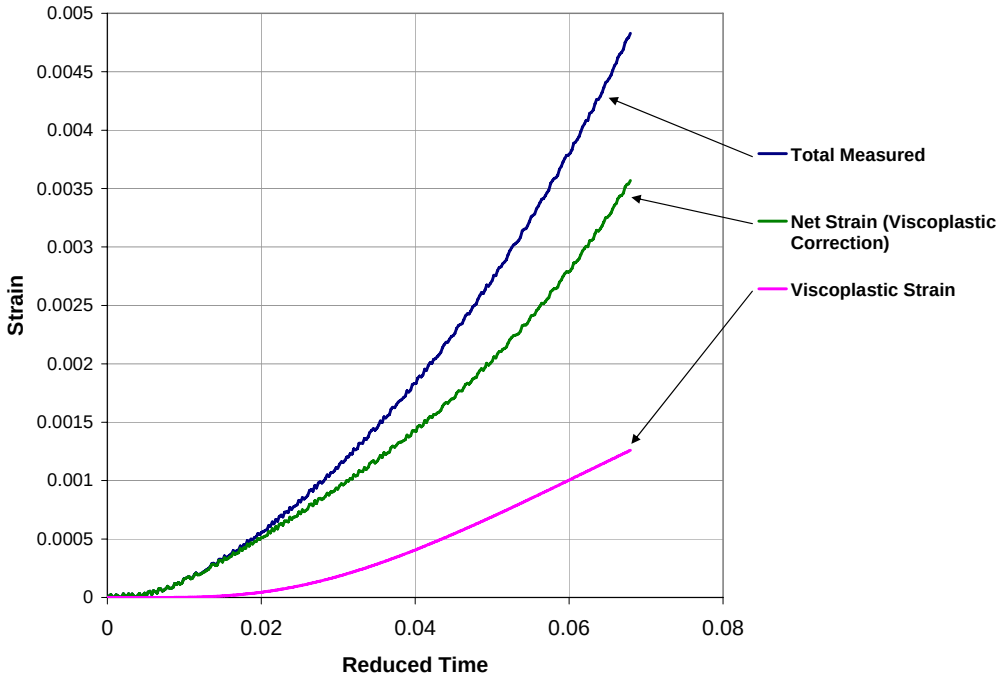

Figure 32. Typical computed viscoplastic strain for 5°C constant strain rate test.

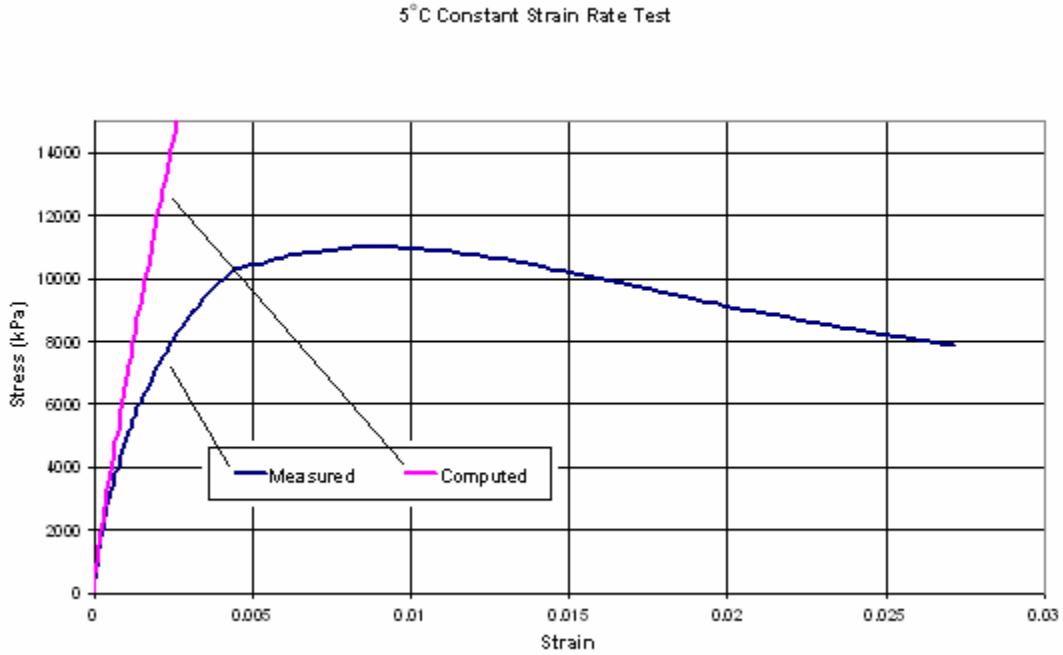

Figure 33. Comparison of stress versus strain response: computed LVE versus net measured (total less viscoplastic).

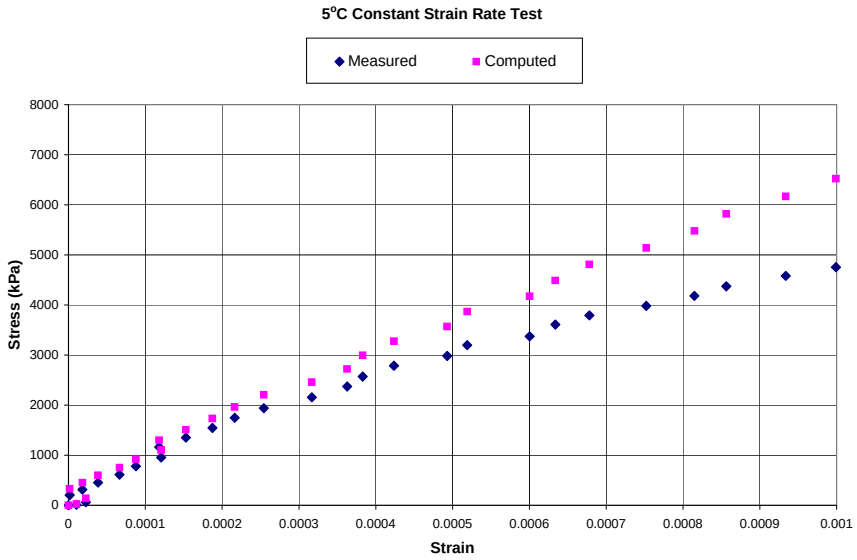

Figure 34. Comparison of stress versus strain response: computed LVE versus net measured (total less viscoplastic)—expanded scale.

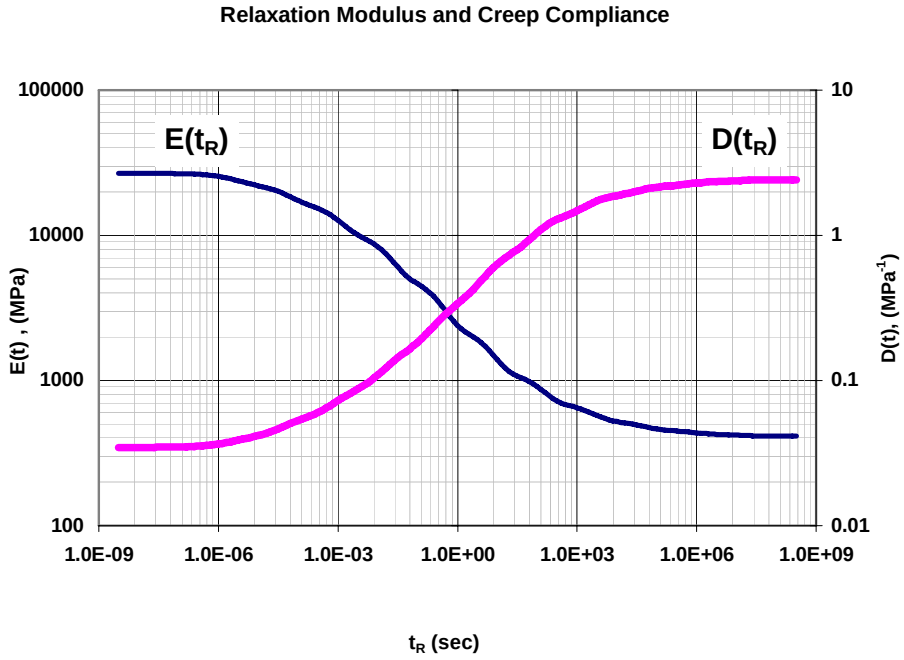

Figure 35. Creep compliance and relaxation modulus functions found from dynamic modulus tests.

Table 10. Prony series terms for relaxation modulus and creep compliance.

i	E_i (MPa)	ρ_i (sec)	D_i (MPa^{-1})	τ_i (sec)
0	412.8	--	3.459E-05	--
1	1.430E+01	1.500E+07	9.042E-05	1.125E+07
2	3.210E+01	8.005E+05	1.885E-04	6.004E+05
3	7.420E+01	4.272E+04	3.525E-04	3.204E+04
4	1.796E+02	2.280E+03	5.769E-04	1.710E+03
5	4.588E+02	1.217E+02	5.955E-04	9.125E+01
6	1.232E+03	6.493E+00	3.396E-04	4.870E+00
7	2.956E+03	3.465E-01	1.405E-04	2.599E-01
8	5.286E+03	1.849E-02	5.670E-05	1.387E-02
9	6.531E+03	9.869E-04	2.367E-05	7.402E-04
10	5.727E+03	5.267E-05	1.172E-05	3.950E-05
11	3.848E+03	2.811E-06	4.222E-06	2.108E-06
12	2.160E+03	1.500E-07	-6.095E-08	1.125E-07

Table 11. Time-temperature superposition shift functions.

Temperature	5°C	25°C	40°C	60°C
Log a(T)	1.9595	0	-1.5669	-4.1774

4.5 Comparison of Compression-Only and Tension/Compression Linear Viscoelastic Properties

As part of the collaborative research for this project, investigators at North Carolina State University (NCSU) performed small-strain reversed tension and compression dynamic modulus tests to find the corresponding linear viscoelastic master curves of the same mixture the University of Maryland (UMD) tested in direct compression. It is of interest to make direct comparisons of this and the other linear viscoelastic properties from these tests. It is well known asphalt concrete behaves differently in tension vs. compression in the large strain nonlinear region; however, these

differences may be absent and/or insignificant in the small-strain region assumed to be linear and undamaged. Similar small-strain properties in tension and compression would enable more economical material characterization in the laboratory.

Storage modulus E' master curve data points, relaxation modulus $E(t_R)$ Prony series terms (E_i and ρ_i), temperature shift functions $a(T)$, and phase angle ϕ data were exchanged between the two laboratories. The tension-compression data from NCSU was interpreted at a 10^{o}C reference temperature while the compression-only data from UMD was characterized at a 25^{o}C reference temperature. To be compatible with the tension/compression data, the compression-only temperature shift function was adjusted to reflect a common reference temperature of 10^{o}C, as shown in Figure 36. Another minor discrepancy was that reduced frequency for the tension/compression linear viscoelastic analysis was quantified in terms of Hz rather than in radians per second as for the compression-only test data. This was easily corrected by multiplying Hz by 2π to convert to radians per second.

The two sets of storage moduli data were plotted on the same graph with the same x-axis units. As shown in Figure 37, there is very good agreement in the overlapping range where both sets of data were collected. The compression-only fitted curve is inside the tension/compression error bars representing one standard deviation; conversely, the tension/compression curve is inside the compression-only one standard deviation error bars. There are different levels of variability in the NCSU and UMD data at different temperatures and frequencies, which is to be expected given that the data were measured using different machines with different specimen geometries, transducers, load capacity, loading fixtures, and environmental chambers. There is a marked difference in measured

response at extreme low reduced frequencies (Figure 37 inset), which corresponds to very warm temperatures in the context of time-temperature superposition. The compression-only tests give a higher modulus than the reversed tension and compression, suggesting that loading mode is important under these conditions. This is reasonable considering that the influences from the aggregate skeleton become more pronounced and the influence from the bituminous binder is reduced at warm temperatures and/or long loading times.

Regarding the $a(T)$ temperature shift functions, the compression-only function was determined using a unified procedure that fit a single curve to all the storage modulus data simultaneously whereas the approach employed in the tension/compression analysis was to fit individual shift functions to each replicate and then average. The means and differences between the temperature shift functions from the two laboratories are very small, as shown in Figure 38. Although the NCSU and UMD tests were performed for slightly different temperatures ranges, there are very small differences in the overlapping temperature range and both sets of data combine to form a relatively smooth relationship (although the compression-only values probably do not all lie within one standard deviation of the tension/compression points).

There are significant differences between tension/compression and compression-only mean values and variability of the phase angle as shown in Figure 39 for individual temperature and frequency conditions. The differences are particularly large for the 40^{o}C compression-only data. It should be remembered, however, that phase angle is most always more variable than dynamic or storage modulus. In addition, NCSU corrected the measured phase angle for any phase lag that may occur within the loading train (actuator,

load cell and shafts) and UMD did not. This may cause a systematic difference between the two labs.

The compression-only relaxation modulus was compared to the tension/compression relaxation modulus in two ways. The first was a direct comparison of the two Prony series solutions. A slight additional correction was required to shift the NCSU tension/compression data from a 5^{o}C to a 10^{o}C reference temperature. The second approach was a recalibration of the Prony series fit that started with the tension/compression storage modulus master curve data points that were then fit with a new Prony series using a different total number of terms and ρ_i constants. Figure 40 shows the overall the agreement of the UMD compression-only and the NCSU tension/compression relaxation modulus from both the direct and recalibration comparisons is excellent over the intermediate portion of the relaxation modulus master curve. There is a noticeable difference in the upper shelves (Figure 40 inset) at very small values of reduced time. Then at about $t_R = 0.005$ seconds the relaxation moduli converge and remain in agreement before diverging at about $t_R = 100$ seconds and settling into two different lower shelf stiffness – about 0 kPa for the NCSU tension-compression and about 520 kPa for the UMD compression only data. This is a direct a reflection of the corresponding storage modulus behavior.

For demonstrational purposes, the UMD compression-only data were re-fit with another Prony series, but this time without a constraint on the upper shelf (see discussion in preceding subsection). It can be seen in Figure 40 that the upper shelf for this re-analysis was larger than both tension/compression and the constrained compression-only

cases, reinforcing the need for the data at cooler temperatures or a constrained analysis for the UMD compression-only data.

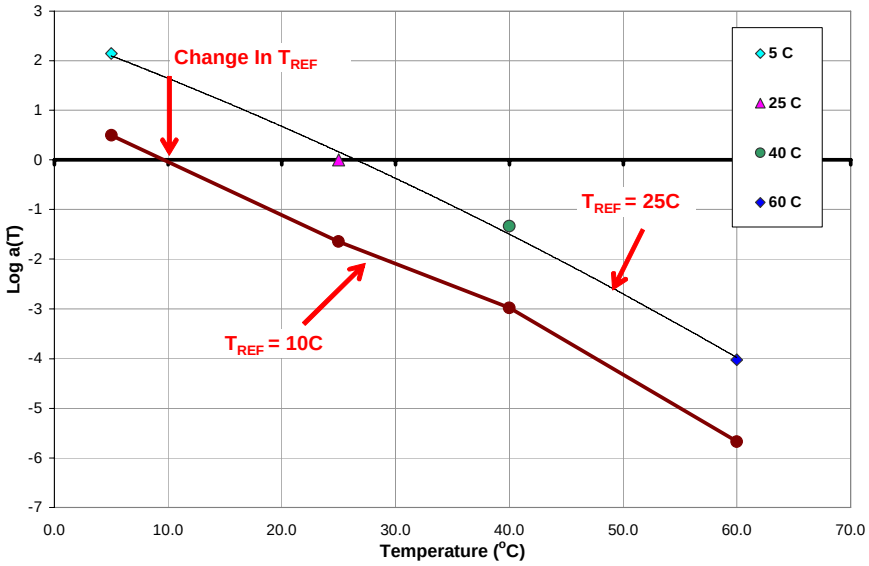

Figure 36. Compressive storage modulus temperature shift function at 25°C reference temperature adjusted for comparison to NCSU reversed tension and compression at 10°C reference temperature.

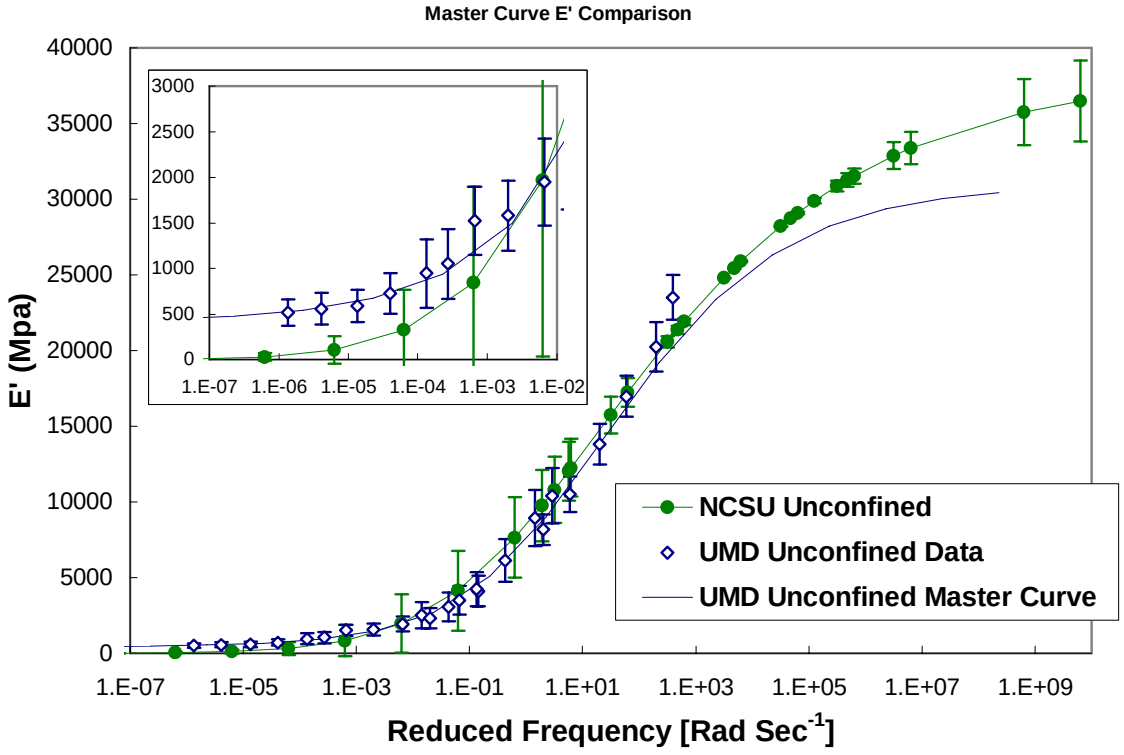

Figure 37. Storage modulus measured at UMD (compression) and NCSU (tension and compression) at 10°C reference temperature.

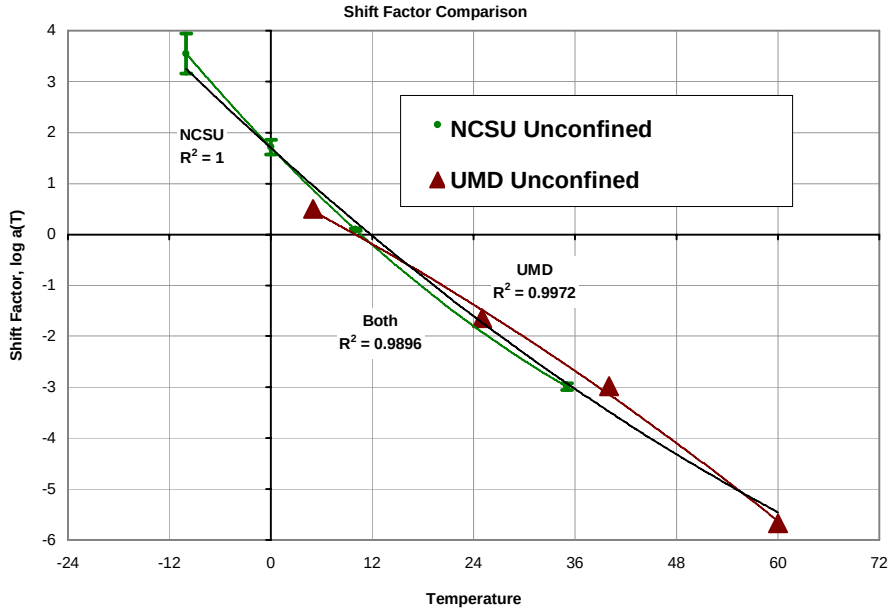

Figure 38. Shift factors determined in master curve development at UMD and NCSU at 10°C reference temperature.

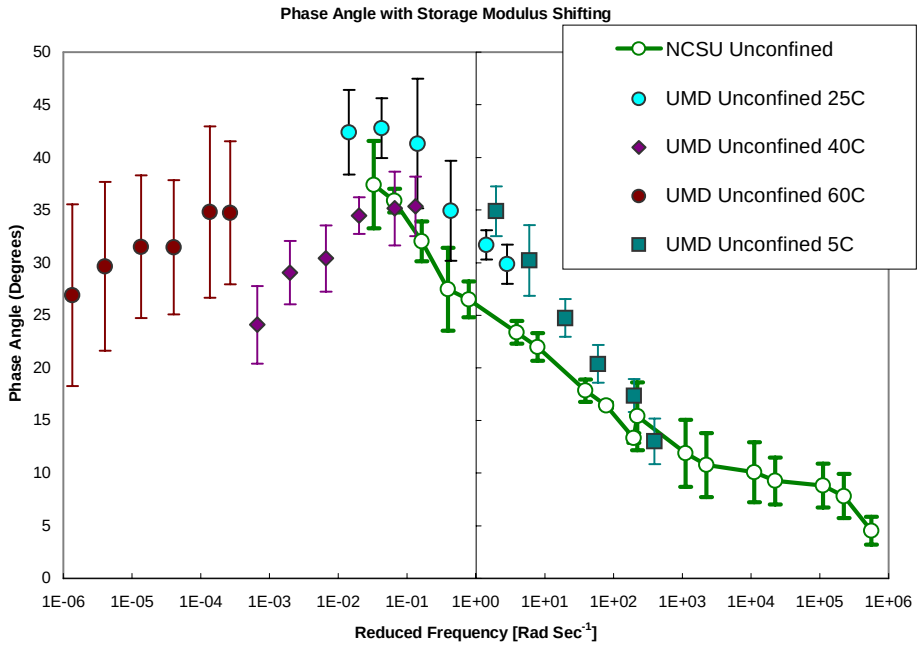

Figure 39. Temperature shifted phase angle from UMD and NCSU with one standard deviation error bar at 10°C reference temperature.

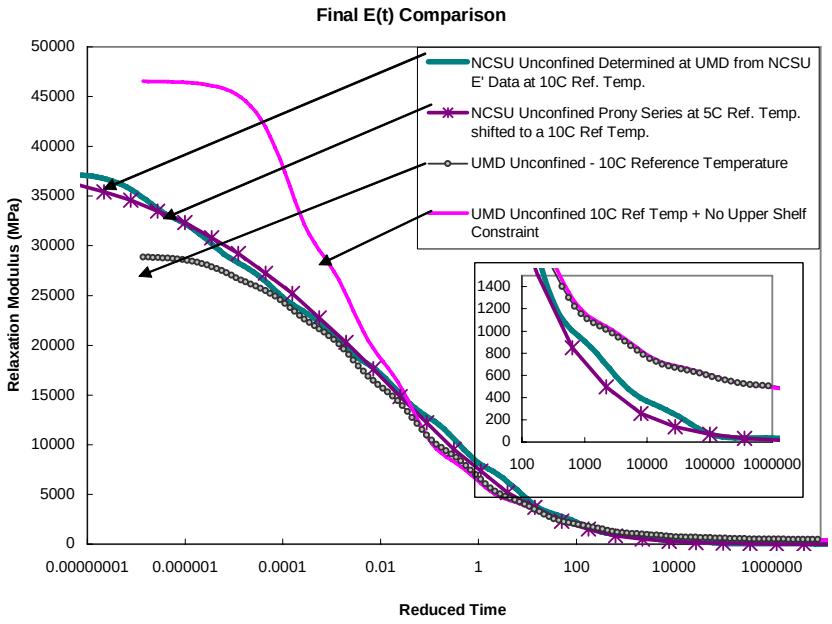

Figure 40. Various NCSU and UMD relaxation modulus master curves from different analyses at 10°C reference temperature.

4.6 Comments on Confining Pressure Effects on Linear Viscoelastic Properties

In the light of the comments made on loading mode effects, some comments are offered on the effect of confining pressure on the linear viscoelastic properties of asphalt concrete. No confined frequency sweep tests were performed at UMD and only confined tension/compression tests were performed at NCSU. The confining stress levels in the NCSU tests were 250 and 500 kPa. Some additional confined test data were exchanged for the loading mode comparisons. First, one must understand confined tension or reversed tension/compression tests are very difficult to perform and is challenging even for the most seasoned researcher because the specimen is connected to the loading shaft. This complicates controlling the test machine about the actual zero-force condition.

The relaxation modulus upper shelf is ultimately determined by upper shelf of the storage modulus, as shown in Figure 41 under various levels of confinement. One might expect higher confining pressure to increase the stiffness and raise the upper shelf as with frictional materials. However, this was not clearly observed here. The upper shelf storage modulus for the highest confining stress case (500 kPa) is about the same as for unconfined conditions at the highest reduced frequencies. The intermediate 250 kPa case has an upper shelf below both the 500 kPa confined and unconfined cases, but it is hypothesized that this is simply an artifact attributable to measurement variability inherent at each condition. It is most likely that all three confining pressures have the same upper shelf and thus that confining stress has no effect on the upper shelf; binder rather than aggregate stiffness controls at these low temperatures/short loading times, and binder stiffness is not sensitive to confining pressure.

Another unexpected effect was seen on the lower shelf at warmer temperatures where it is more likely that asphalt concrete will behave like a frictional soil and exhibit increasing stiffness with increasing confining stress. Under warm temperatures and/or slow loading rates, the material's stiffness is largely governed by the aggregate structure and not by the binder. The 0 and 500 kPa confinement cases plotted in Figure 41 follow this reasoning, but the 250 kPa case diverges and has a higher lower shelf than the other two cases. This is more apparent when plotting in log-log scale, as shown in the inset in Figure 41. However, this may be an artifact of extrapolating the fitted master curves outside the measured range of reduced frequencies. As a practical matter, the modulus on the lower shelf is orders of magnitude smaller than the upper shelf and intermediate

values, and therefore small differences in these very small moduli may not have much physical significance.

The phase angle data in Figure 42 still exhibit quite a bit of variability, but this is expected for this property. There is fairly good agreement between all three confining stresses; the 0 and 500 kPa confinement cases are almost identical while the 250 kPa case shows a slightly but consistently smaller phase angle. As was the case for the UMD compression-only data, the phase angle-reduced frequency behavior for the confined tension/compression condition shows a peak at about $1x10^{-3}$ reduced Hz.

Finally, the temperature shift functions shown in Figure 43 appear to be the most insensitive to confining pressure. This is sensible physically; the temperature shift functions should be most strongly related to the binder behavior, and this behavior is relatively insensitive to confining pressure.

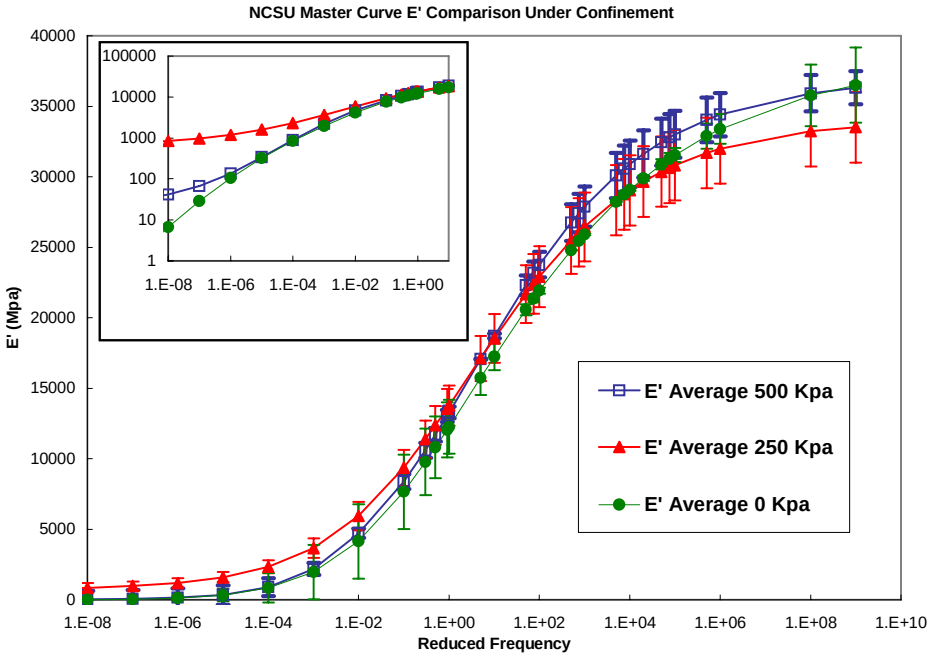

Figure 41. Tension/compression storage modulus master curves measured at NCSU under different levels of confinement.

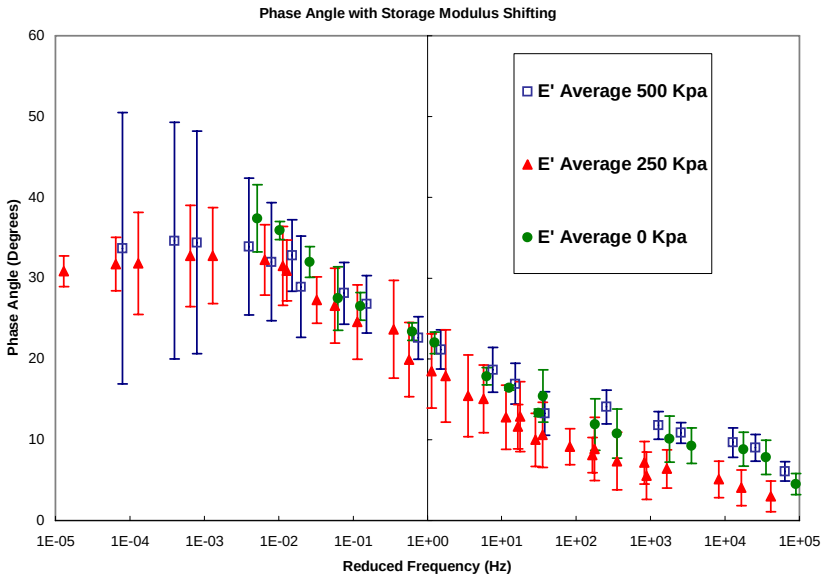

Figure 42. Tension/compression phase angle measured at NCSU under different levels of confinement.

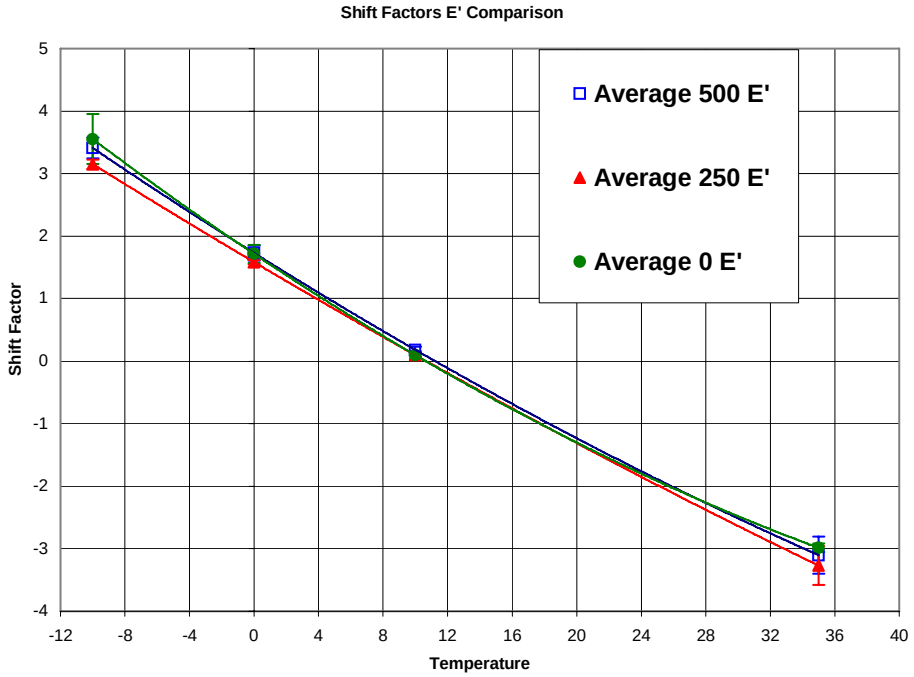

Figure 43. Tension/compression temperature shift functions for storage modulus measured at NCSU under different levels of confinement.

4.7 Conclusions

This linear viscoelastic characterization in this chapter, while not groundbreaking, is thorough and illustrates in detail the steps that can be taken to derive an inherent viscoelastic material property for asphalt concrete from convenient testing conditions. The linear viscoelastic relaxation modulus of asphalt concrete is relatively easy to calibrate using simple small-strain dynamic modulus tests and mathematical principles. The compression-only tests at UMD were not cold enough to determine accurately the upper shelf of the storage and relaxation modulus master curves. Temperatures no warmer than 60^{o}C are required, but data at temperatures cooler than 5^{o}C such as -10^{o}C are needed to obtain a more accurate characterization of the complete master curve. Thus, the upper shelf was found by imposing artificial limits and checking the agreement between the predicted versus measured response. The upper shelf determined by that constraint was about 30 GPa. The unconstrained compression only upper shelf was about 39 GPa reinforcing the need for test data in the very cold temperature range. The accumulated strain during the frequency sweeps was found to have little impact on measured dynamic modulus values, but it is recommended this behavior be at least checked for any other mixture being studied in the future, i.e. an SMA.

Comparisons of the compression-only (UMD) and tension/compression (NCSU) test data show little difference in the storage modulus values within the overlapping temperature range; the storage modulus master curves are generally within one standard deviation of each another. The lower shelf for the tension-compression relaxation modulus was smaller than the compression only case, suggesting mode of loading appears to have an effect on stiffness at very long loading times and/or high temperatures.

Physical reasoning would suggest that the compression-only tests should be stiffer under these conditions because asphalt concrete is a geo-material that tends to have lower stiffness in tension than compression. However, for locations other than the lower shelf, all of the viscoelastic properties—storage modulus, relaxation modulus, creep compliance, phase angle, and temperature shift—are essentially insensitive to the mode of loading.

Confinement stress effects were examined using some exchanged confined tension/compression data from NCSU. The phase angle measured at three different confining stresses (0, 250 and 500 kPa) appears to be only very slightly changed by the confining stress. There is a practically no effect of confining stress on the storage modulus stress in the measured range, although some influence may exist in the extrapolated lower shelf region. The practical conclusion drawn from the data in this study is that the linear viscoelastic properties of asphalt concrete may be assumed largely insensitive to confining stress based on measurements at up to 500 kPa of confinement.

The comparison of confined and unconfined dynamic modulus and phase angle demonstrated linear viscoelastic material properties for asphalt concrete were essentially similar between 0 and 500 kPa of confinement. Importantly, this means that a linear viscoelastic constitutive relation measured in uniaxial tests can be applied to multiaxial stress conditions, for example as required for damage model calibration as described later in Chapter 7.

5. Validation of Time-Temperature Superposition at Large Strains

5.1 Theoretical Justification

Strategic planning in the early stages of the project identified the time-temperature superposition principle as potential means to reduce the set of calibration tests required. Time-temperature superposition removes temperature as an explicit variable. However, in order to reduce the set of tests required for calibrating the viscoplastic and continuum damage components of the model, the validity of time-temperature superposition under large strain conditions had to be established. This was the objective of the work described in this chapter.

Temperature shifted dynamic modulus of asphalt concrete demonstrates conventional time-temperature superposition when the dynamic strain is kept at or below $100\mu\varepsilon$. The behavior of asphalt concrete at these magnitudes is primarily linear viscoelastic. Nonlinear response components such as plasticity, viscoplasticity, structural

adjustments/physical damage, and others come into play at higher strains for asphalt concrete. These other nonlinear responses can be expected to be dependent upon temperature and loading rate as well. It is not hard to imagine the very large laboratory testing factorial that would be required to individually characterize each of these nonlinear responses at multiple loading rates and temperatures. The laboratory effort required to characterize nonlinear responses can be significantly reduced if time-temperature superposition can be shown to be applicable at large strain levels. Laboratory tests could be economized through the use of the temperature shift relationship to predict other nonlinear responses at different temperatures and/or loading rates. There is some rationale that time-temperature superposition can be extended to the large strain region because all rate and temperature dependent processes should be intrinsically related to the viscous properties of the bituminous binder.

Appendix B of Chehab *et al.* (2002) gives detailed justification of the underlying theory for determining the thermorheologic simplicity of materials. Key details are summarized here. Strain and stress tensors $\boldsymbol{\varepsilon}$ and $\boldsymbol{\sigma}$ are related via the Gibbs free energy as:

$$\boldsymbol{\varepsilon} = -\frac{\partial G}{\partial \boldsymbol{\sigma}} \qquad \textbf{Equation 64}$$

where G = G($\boldsymbol{\sigma}$, **S**, T) is the Gibbs free energy dependent upon stress, temperature, and a set of thermodynamic internal state variables, **S**. The internal state variables address, on all scales, the molecular motions, micro-deformations, micro-cracking, and macro-cracking (if any). The evolution law that defines how **S** evolves is stated as:

$$\frac{d\mathbf{S}}{dt} = \mathbf{f}(\boldsymbol{\sigma}, \mathbf{S}, T) \qquad \textbf{Equation 65}$$

The fundamental viscous behavior of asphalt is expressed by $\mathbf{f}(\boldsymbol{\sigma},\mathbf{S},T)$.

For thermorheologically simple materials, time t and temperature T can be combined into an equivalent reduced time, ξ by:

$$\xi = \int_0^t \frac{dt}{a_T} \qquad \textbf{Equation 66}$$

S can then be expressed in terms of stress and reduced time histories, reducing Equation 65 to:

$$\frac{d\mathbf{S}}{d\xi} = \mathbf{F}(\boldsymbol{\sigma},\mathbf{S}) \qquad \textbf{Equation 67}$$

Since temperature effects in Equation 64 can be assumed to induce thermal expansion strains $\boldsymbol{\varepsilon}_\mathbf{T}$ only, the strain due to stress ε_σ can be written as:

$$\boldsymbol{\varepsilon}_\boldsymbol{\sigma} = \boldsymbol{\varepsilon} - \boldsymbol{\varepsilon}_\mathbf{T} = -\frac{\partial G_\sigma}{\partial \boldsymbol{\sigma}} \qquad \textbf{Equation 68}$$

in which $G_\sigma = G_\sigma(\boldsymbol{\sigma},\mathbf{S})$.

For uniaxial conditions, a power law in time can describe the strain due to stress as:

$$\varepsilon_\sigma = k' t^n \qquad \textbf{Equation 69}$$

in which n is a material constant and k' is a variable related to the imposed strain rates. Rewriting Equation 69 in terms of reduced time yields:

$$\varepsilon_\sigma = k \xi^n \qquad \textbf{Equation 70}$$

where $k = k' a_T^n$ is the "reduced strain rate" when $n = 1$. Note that when $n \neq 1$, k is not precisely equal to the reduced strain rate, but it will be treated as such for the ease of discussion here.

Under uniaxial stress-strain conditions, Equation 68 can be inverted giving conceptually:

$$\sigma = g\left(\varepsilon_\sigma, \mathbf{S}\right) \qquad \textbf{Equation 71}$$

and using Equation 71 in Equation 67 gives:

$$\frac{\partial \mathbf{S}}{\partial \xi} = h\left(\varepsilon_\sigma, \mathbf{S}\right) \qquad \textbf{Equation 72}$$

Taking Equation 70 and solving Equation 72 in concept for **S**, stress is obtained from Equation 71 in the form:

$$\sigma = \bar{g}\left(\xi, k, n\right) \qquad \textbf{Equation 73}$$

where ξ and k are "reduced" variables. The parameter k can be eliminated and replaced by ε_σ:

$$\sigma = \bar{f}\left(\varepsilon_\sigma, \xi, n\right) \qquad \textbf{Equation 74}$$

Equation 74 provides the theoretical basis for analyzing stress-strain data for thermorheologically simple behavior for strain history data in the form of Equation 69. Plots of stress σ versus log t at any given constant strain level ε_σ for a given temperature may be shifted by corresponding temperature dependent shift factors $a(T)$ to give a single curve of stress vs. log ξ (Equation 74). This is the same as stating that at a given strain level ε_σ, the material's dependence on time and temperature is the same as for a linear viscoelastic material.

The relationship in Equation 74 allows for a cross-plotting procedure to be developed to analyze constant rate of strain [i.e. n = 1 in Equation 69] to failure tests for asphalt concrete using time-temperature superposition. The cross-plotting procedure is illustrated schematically in Figure 44 and can be described as follows: First, a given

magnitude of axial strain is selected (ε_1 in Figure 44a). For this strain magnitude at a given temperature, the corresponding axial stresses and response times are determined for each of the strain rates tested (points A,B,C in Figure 44a for $T=T_1$, e.g.). These values are used to construct a stress versus log-time plot for the given strain magnitude and temperature (points A, B, C in Figure 44b for $T=T_1$, e.g.). Note that since strain magnitude is fixed, this plot is similar in concept to a modulus versus log frequency curve for linear viscoelastic dynamic modulus. This procedure is repeated for each test temperature. The final set of stress versus log time curves (one for each temperature at a given strain magnitude) are then temperature shifted (Figure 44b) to produce a master curve and temperature shift function (Figure 44c) using the same procedures as for the dynamic modulus master curve analysis in the frequency sweep tests. This entire process is then repeated for other fixed strain levels. Master curves of stress at multiple discrete strain levels are produced instead of the one single master curve for the case of dynamic modulus.

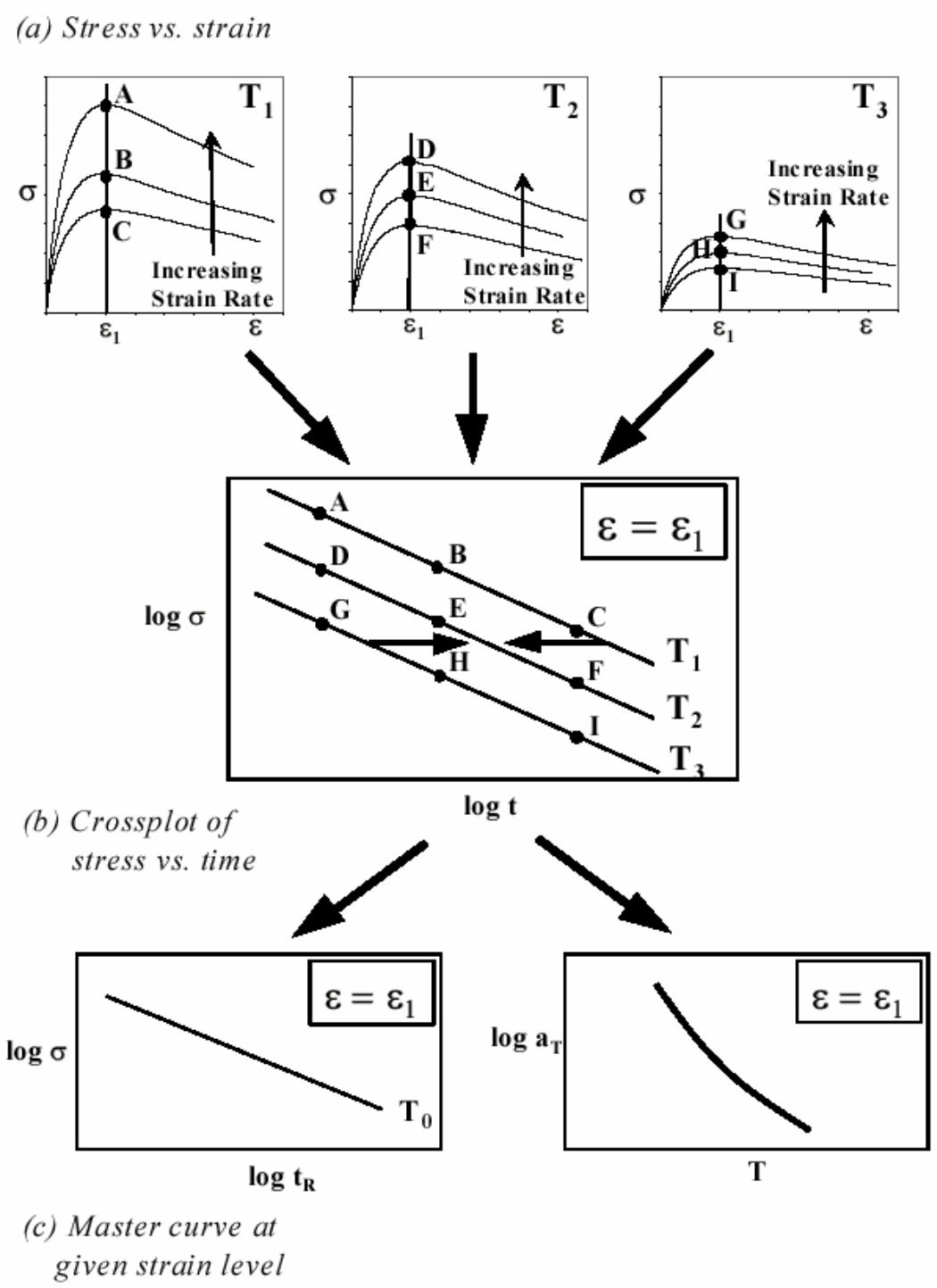

Figure 44. Schematic Illustration of the Cross-Plotting Procedure.

5.2 Uniaxial Constant Rate of Strain to Failure Tests

5.2.1 Test Procedure

These tests were carried out on the dynamic modulus specimens immediately after the frequency sweep tests (described previously in Chapter 4). The LVDT instrumentation and specimen geometry were therefore the same as for the dynamic modulus test and the temperatures were fixed at the compression-only dynamic modulus temperatures: 5, 25, 40, and 60^{o}C. For some of the warmer tests at 40 and 60^{o}C, the axial LVDTs needed to be readjusted to the beginning of their range to maximize data collection due to some residual permanent deformation from the dynamic modulus frequency sweeps. The specimens were allowed to rest for 30 minutes immediately after the dynamic modulus frequency sweeps before being loaded to failure at a constant strain rate in strain (displacement) control. During this time only partial recovery was observed, indicating that some permanent strains were induced, the effects of these permanent strains on the analysis procedure are discussed below.

The strain rate control was limited to the actuator LVDT instead of the on-specimen LVDTs. A method to control the strain rate by the average of the four on-specimen LVDTs was investigated, but the equipment upgrade costs were deemed not worth the benefit. Furthermore, controlling strain with the LVDTs mounted on the specimen can be very dangerous. The feedback control loop using the on-specimen LVDT signal can become extremely unstable if one or more on-sample LVDTs fail (e.g., due to debonding of one of the attachment mounts).

One test parameter that needed to be addressed was the magnitude of the fastest strain rate to be applied. This strain rate needed to be similar to observed rates in real

pavements. A literature search was performed to determine the fastest nominal strain rates measured or estimated for real pavements. Data from the Danish Road Testing Machine (Krarup, 1994) of a wide base tire traveling about 12 mi/hr (20km/hr) indicated a strain rate of 0.0125 ε/sec measured at the bottom of the AC layer in the longitudinal direction of travel. Data from a falling weight deflectometer at the same location induced a strain rate of about 0.00686 ε/sec. Strain rates on this order of magnitude were supported by results from simulated pavement strain response studies using numerical analysis programs VESYS (Gillespie *et al*., 1993) and DYNAPAVE (Zafir *et al*. 1994). Nominal strain rates from these studies were estimated as 0.0165, 0.0066, and 0.0115 ε/sec at the bottom of the AC layer in the longitudinal direction of travel for pavements having an AC layer thickness on the order of 150mm to 200mm. The strain path for all reported strain measurements was typically from compression to tension to compression as the truck tire passed. Based on these data from the literature, the strain rate targets for the constant strain rate tests were set at 0.0005, 0.0015, 0.0045 and 0.0135 ε/sec. At least two replicates were tested at each strain rate. Table 12summarizes the original testing factorial. Additional replicates were added at some temperatures and strain rates when deemed necessary.

Table 12. Original constant rate of strain test factorial.

Target Strain Rates (ε/s)	Test Temperatures (^{o}C)	Test Replicates	Total Tests
0.0005 ε/s, 0.0015 ε/s 0.0045 ε/s, 0.0135 ε/s (4)	5^{o}C, 25^{o}C, 40^{o}C, 60^{o}C (4)	(2)	(32)

5.2.2 Test Results

The results for the entire set of uniaxial strain to failure tests can be seen in Figure 45 to Figure 52. Measured stress versus strain and strain versus time is shown for each temperature and target strain rate. The stress-strain curves for each strain rate are clearly distinct from one another for all but the highest temperature of 60^{o}C, with the fastest rate on the top (highest stresses) and the slowest rate on the bottom (lowest stresses) – see Figure 48, e.g. the initial portions of the stress-strain curves are fairly linear, then the curves become nonlinear, reach peak strength, and descend into the post peak region. The stress-strain agreement between replicates is excellent. As would be intuitively expected, the peak strengths increase as the strain rate increases. Remarkably, the strain at the peak stress is consistently about 1% strain for all rates and temperatures. The tests end at about 4% strain where the axial LVDTs reach the end of their range.

Overall, the targeted strain rates were nominally achieved. For every temperature and strain rate there is a small nonlinear start-up response evident in the strain-time curves at the beginning of loading. The strain rate eventually becomes fairly linear and reaches the nominal target strain rate. The nonlinear start-up response is due primarily to a combination of actuator acceleration limits and small amounts of compliance in the machine and loading shaft. The strain rate input from the actuator LVDT (the control signal) is always linear, but as stress increases the loading shaft and testing machine deform and flex. The result is a nonlinear strain rate measured from the on-specimen LVDTs. The amount of nonlinearity was sufficiently negligible in most cases that the input strain rate from the actuator did not need to be corrected to achieve the target on-specimen strain rate. In many tests there is also some nonlinearity at the very end of the

strain-time record. This occurs when one or more of the averaged axial LVDTs reaches the end of its linear calibrated range.

Few testing problems were experienced at intermediate temperatures, but there were some difficulties at the extreme high and low temperatures. At 60°C the nominal target rates were easily achieved (Figure 47), but the measured stress was quite variable (Figure 46). For individual replicates at 60°C, it was difficult to distinguish which stress-strain curve corresponds to its unique strain rate. This is in contrast to the other temperatures where the stress-strain curves clearly correlated with strain rate, the replicates agreed well with each other, and the stress-strain curves became stiffer as strain rate increased. It is believed that the variability at 60°C is due to the extreme softening of the asphalt binder at this high temperature, and thus the underlying stiffness of the aggregate is controlling the stress-strain response.

A completely different problem was encountered at 5°C. The 100-kN testing machine had insufficient load capacity to fail the specimen at the 0.0015 ε/sec strain rate or faster. The testing machine was able to fail the specimen at the slowest strain rate (0.0005 ε/sec), but the nonlinear start-up effects were much larger because of the increased straining of the loading shaft and testing machine at the larger loads at this temperature. In fact, the initial trial tests at 5°C induced measured on-specimen strain rates that were orders of magnitude smaller than the input actuator strain rate. Additional trial tests used larger actuator input strain rates to correct for compliance with some success, but the nonlinear start-up response was no longer negligible. The final solution to this problem was to use two input strain rates. The initial rate was much faster than the target to account for the nonlinear start-up response. This rate was followed by a slightly

slower input from the actuator as the response approached a steady rate. The result gave on-specimen strain rates comparable to those achieved at the other temperatures. Unfortunately the measured stress was not smooth at the point where the input strain rate changed (Figure 52 at $\varepsilon \cong 0.004$).

A second problem was also encountered at 5^{o}C. Although the 100-kN testing machine had insufficient load capacity to fail the specimens at the 0.0015 ε/s strain rate, tests were attempted at this rate to capture the response prior to peak. Testing was discontinued at this strain rate, however, after a catastrophic failure occurred while attempting to get satisfactory results. A localized failure at the bottom end of one specimen quickly caused the specimen to bend and abruptly fail on one side. As a result, a section of the loading shaft was bent and an axial LVDT was destroyed. Fortunately, enough data were still collected for the time-temperature superposition analysis.

As mentioned earlier, irrecoverable strains were observed after a 30 minute recovery period from the |E*| tests. The LVDTs were essentially re-zeroed after exiting the control software for the |E*| tests and before entering the control software for the uniaxial constant strain rate tests. Table 13 highlights the results of the uniaxial constant strain rate tests showing the individual replicate target strain rates, peak stress, peak strain, measured linear strain rate approximation, and a statistical measure of the linear strain rate approximation. A straight line is fit through the most linear portion of the strain-time curve to estimate the measured strain rate. About 10-15% of the initial nonlinear strain-time record was excluded when estimating the measured linear strain rate. The nonlinear portion at the end where LVDTs reach the end of their range was also excluded. An example of this is shown in Figure 53.

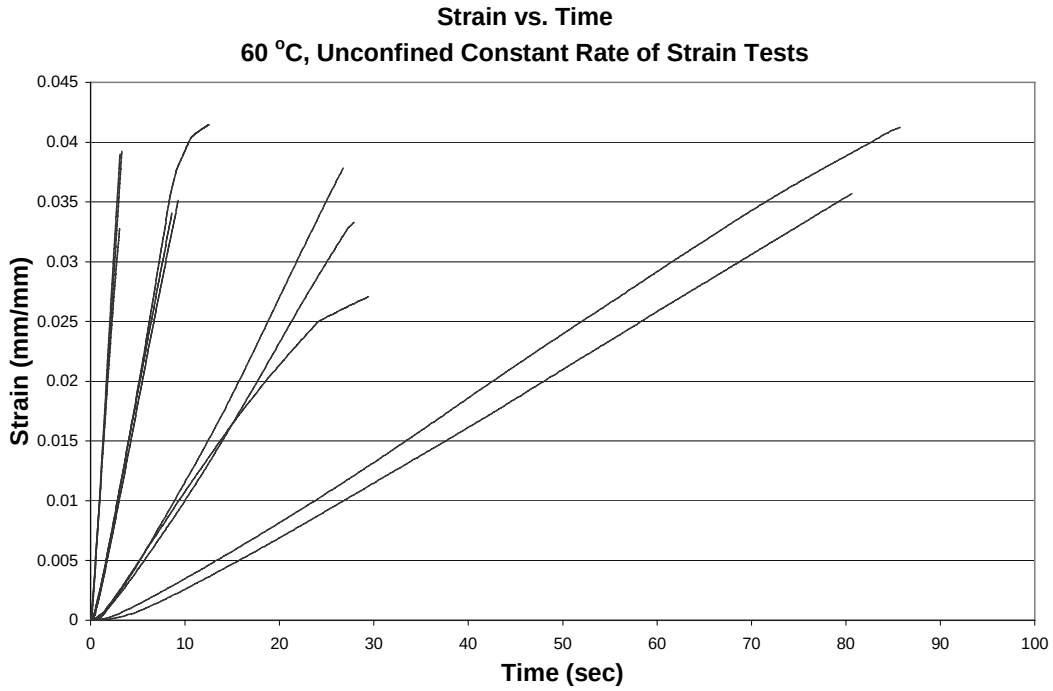

Figure 45. Axial strain-time for 60°C strain rate tests. Two replicates at 0.0005ε/sec and three replicates each at 0.0015, 0.0045, and 0.0135ε/sec.

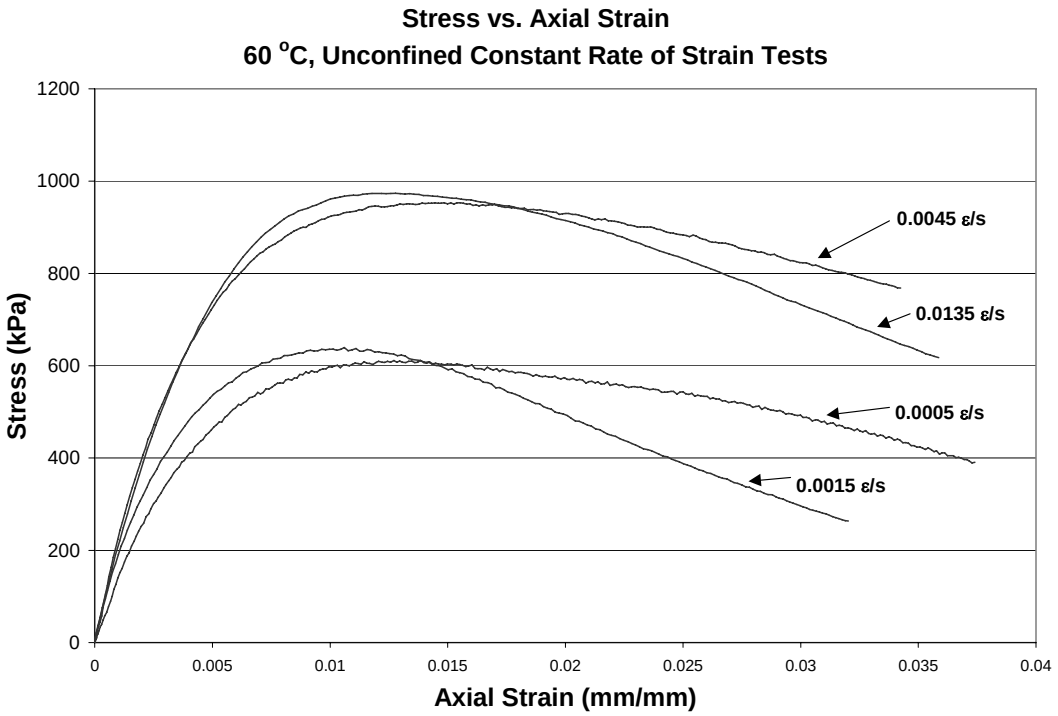

Figure 46. Stress-axial strain for 60°C strain rate tests. Results plotted are the averages of two replicates at 0.0005ε/sec and three replicates at 0.0015, 0.0045, and 0.0135ε/sec strain rates.

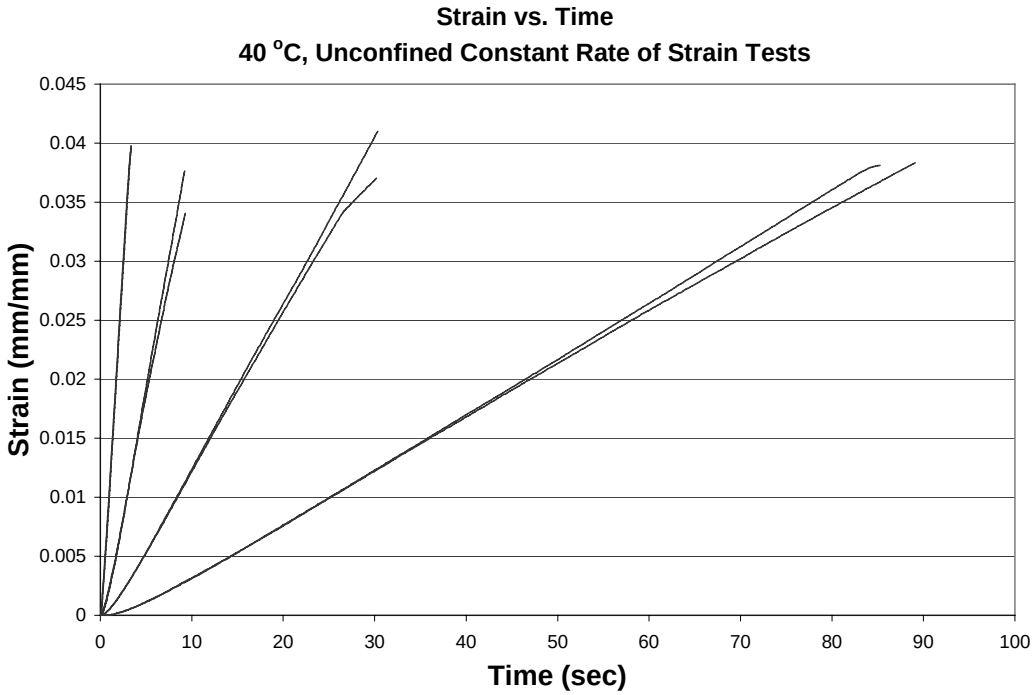

Figure 47. Axial strain-time for 40°C strain rate tests. Two replicates each at 0.0005, 0.0015, 0.0045, and 0.0135ε/sec.

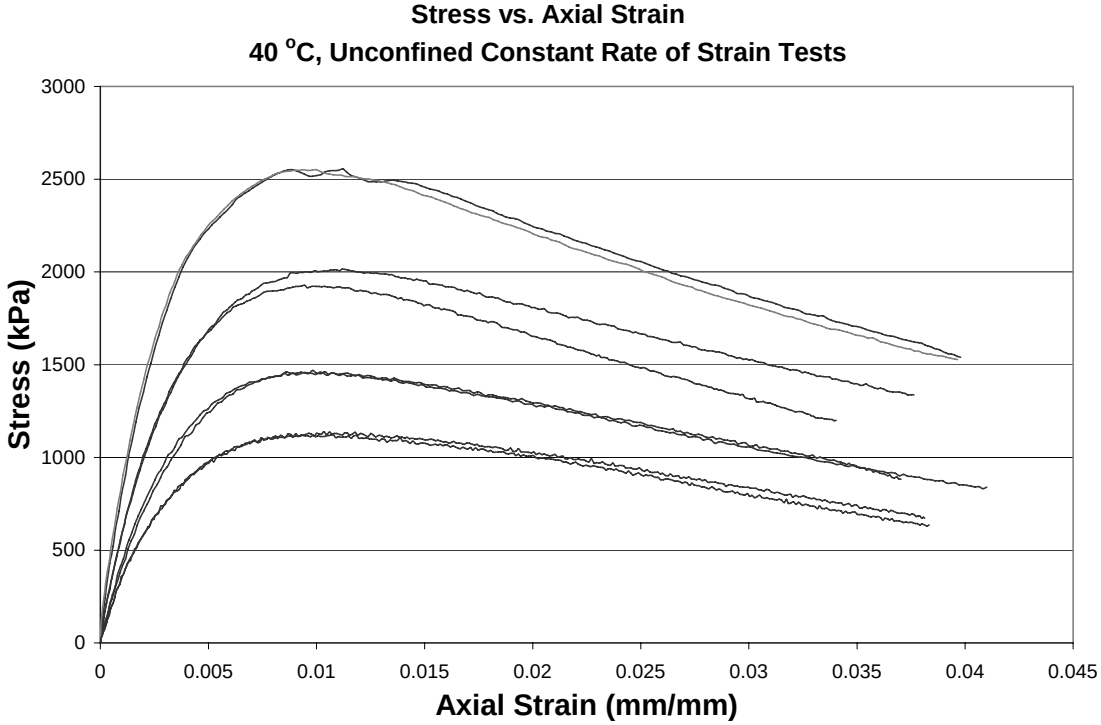

Figure 48. Stress-axial strain for 40°C strain rate tests. Two replicates each at 0.0005, 0.0015, 0.0045, and 0.0135 ε/sec.

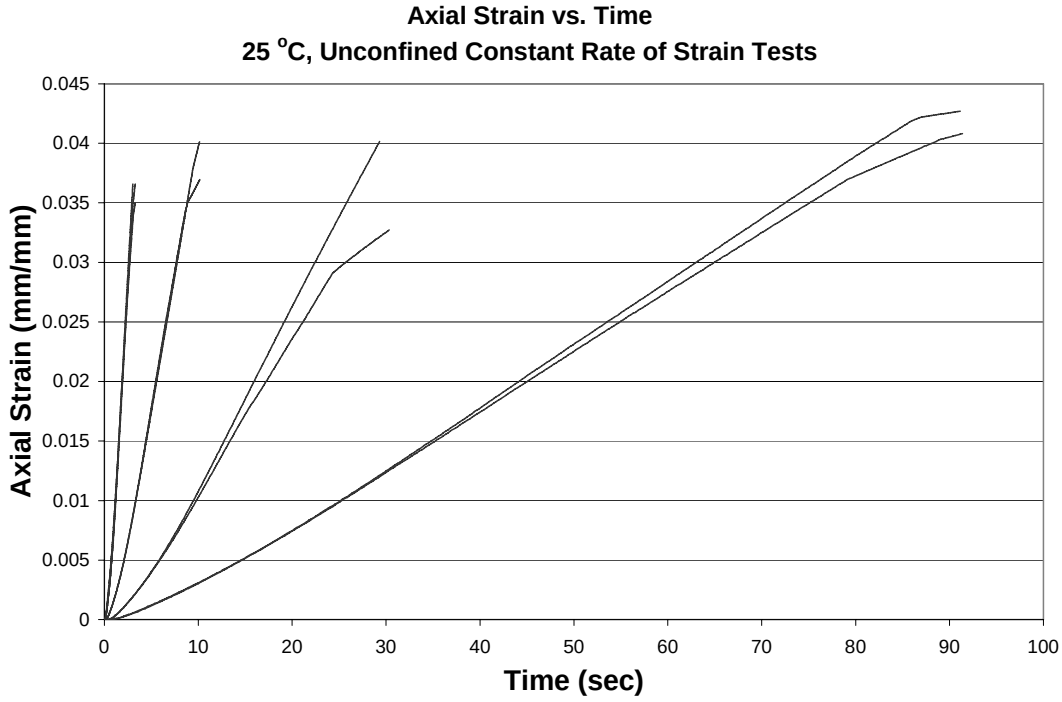

Figure 49. Axial strain-time for 25°C strain rate tests. Two replicates each at 0.0005, 0.0015, 0.0045ε/sec and three replicates at 0.0135ε/sec.

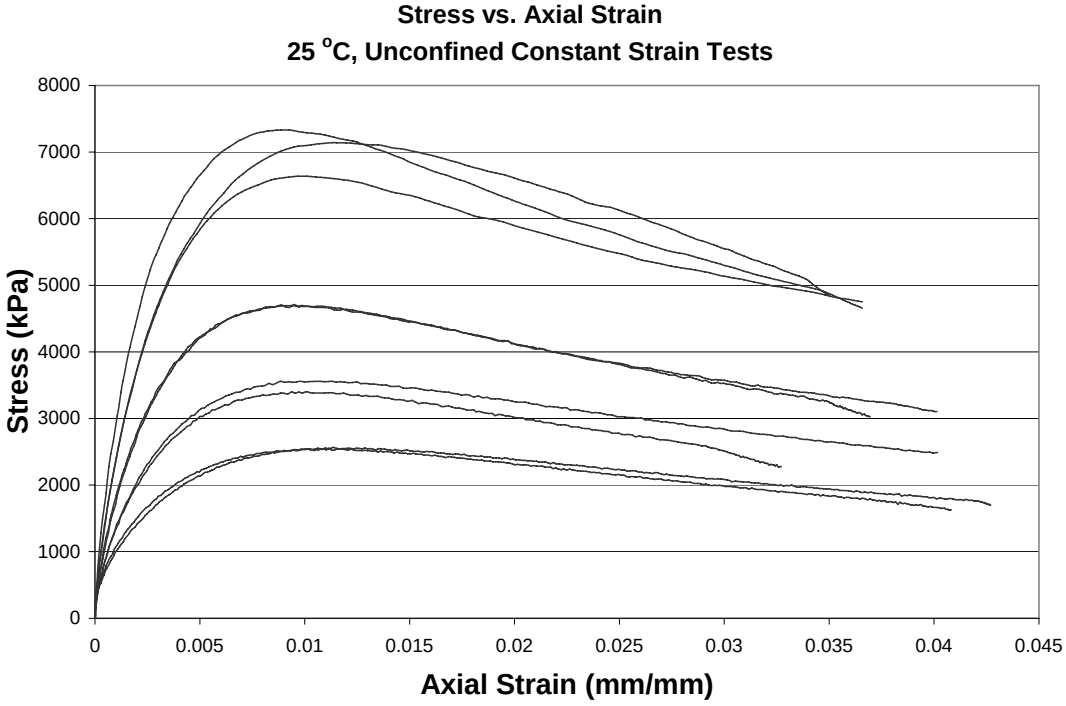

Figure 50. Stress-axial strain for 25°C strain rate tests. Two replicates each at 0.0005, 0.0015, 0.0045ε/sec and three replicates at 0.0135ε/sec.

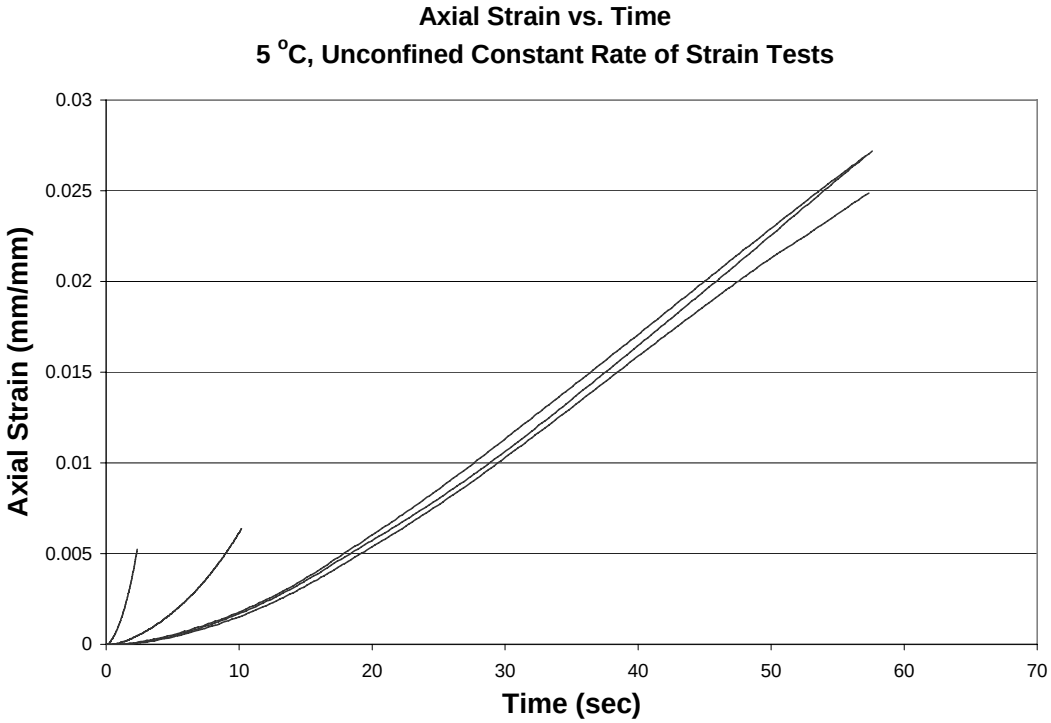

Figure 51. Axial strain-time for 5°C strain rate tests. Three replicates at 0.0005ε/sec and two replicates each at 0.0015ε/sec.

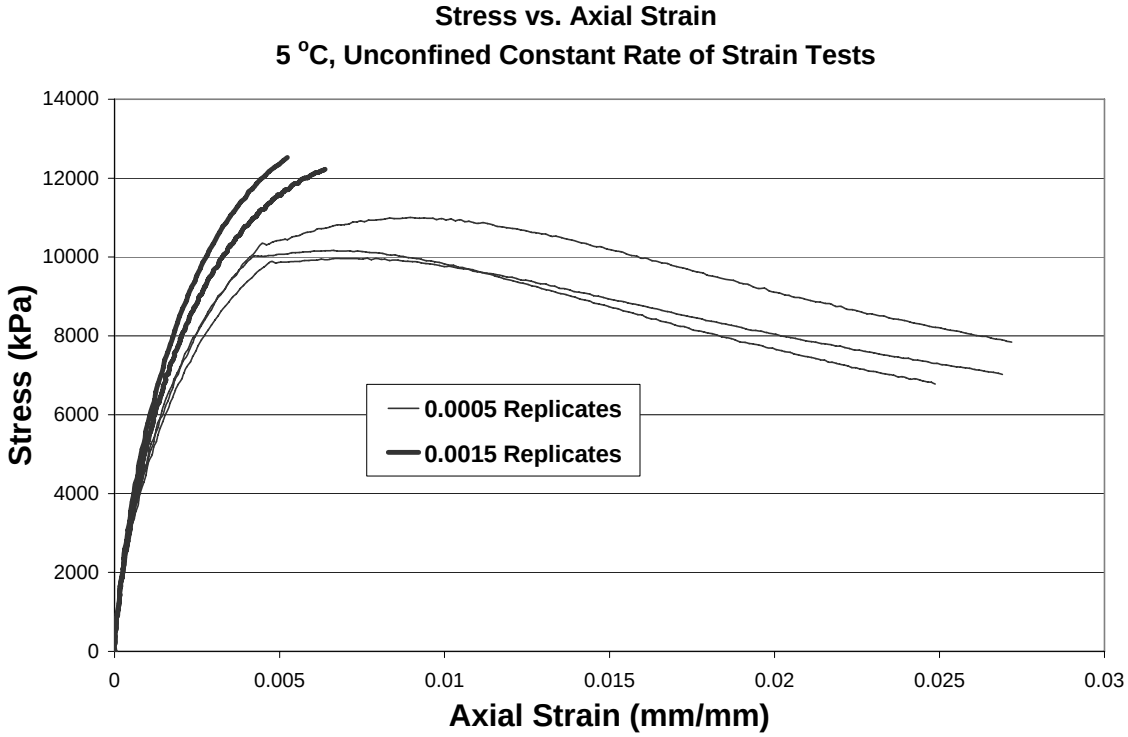

Figure 52. Stress-axial strain for 5°C strain rate tests. Three replicates at 0.0015 ε/s and two replicates at 0.0005ε/sec.

Table 13. Result Summary for Uniaxial Constant Strain Rate Tests.

Temp (^{o}C)	Target Rate (ε/s)	Replicate	Linear Fitted Rate (ε/s)	R^2 of Linear Fit	Peak Stress (kPa)	Peak Strain (%)
5	0.00050	1	0.00057	0.99754	10999.9	0.90%
5	0.00050	2	0.00053	0.99920	10163.7	0.66%
5	0.00050	3	0.00057	0.99943	9969.1	0.77%
5	0.00150	1	0.00285	0.98471	n/a	n/a
5	0.00150	2	0.00081	0.98542	n/a	n/a
25	0.00050	1	0.00050	0.99959	2552.2	1.12%
25	0.00050	2	0.00052	0.99934	2563.8	1.14%
25	0.00150	1	0.00131	0.99962	3401.5	1.01%
25	0.00150	2	0.00151	0.99941	3558.1	1.06%
25	0.00450	1	0.00448	0.99942	4709.1	0.95%
25	0.00450	2	0.00453	0.99938	4702.8	0.89%
25	0.01350	1	0.01334	0.99823	7333.1	0.91%
25	0.01350	2	0.01339	0.99824	6636.6	0.99%
25	0.01350	3	0.01256	0.99888	7142.2	1.13%
40	0.00050	1	0.00047	0.99994	1137.8	1.03%
40	0.00050	2	0.00045	0.99981	1120.4	1.07%
40	0.00150	1	0.00135	0.99987	1468.3	0.98%
40	0.00150	2	0.00140	0.99997	1458.9	1.02%
40	0.00450	1	0.00388	0.99869	1928.1	0.94%
40	0.00450	2	0.00429	0.99869	2014.6	1.12%
40	0.01350	1	0.01257	0.99964	2554.4	1.12%
40	0.01350	2	0.01260	0.99989	2551.3	1.00%
60	0.00050	1	0.00046	0.99859	751.6	1.49%
60	0.00050	2	0.00051	0.99918	484.8	1.22%
60	0.00150	1	0.00109	0.99780	630.5	1.05%
60	0.00150	2	0.00126	0.99739	649.1	0.98%
60	0.00150	3	0.00148	0.99646	637.5	1.24%
60	0.00450	1	0.00397	0.99926	1085.3	1.88%
60	0.00450	2	0.00413	0.99940	1003.3	1.73%
60	0.00450	3	0.00435	0.99768	802.6	1.20%
60	0.01350	1	0.01309	0.99902	980.4	1.20%
60	0.01350	2	0.01110	0.99911	980.3	1.21%
60	0.01350	3	0.01231	0.99962	971.5	1.32%

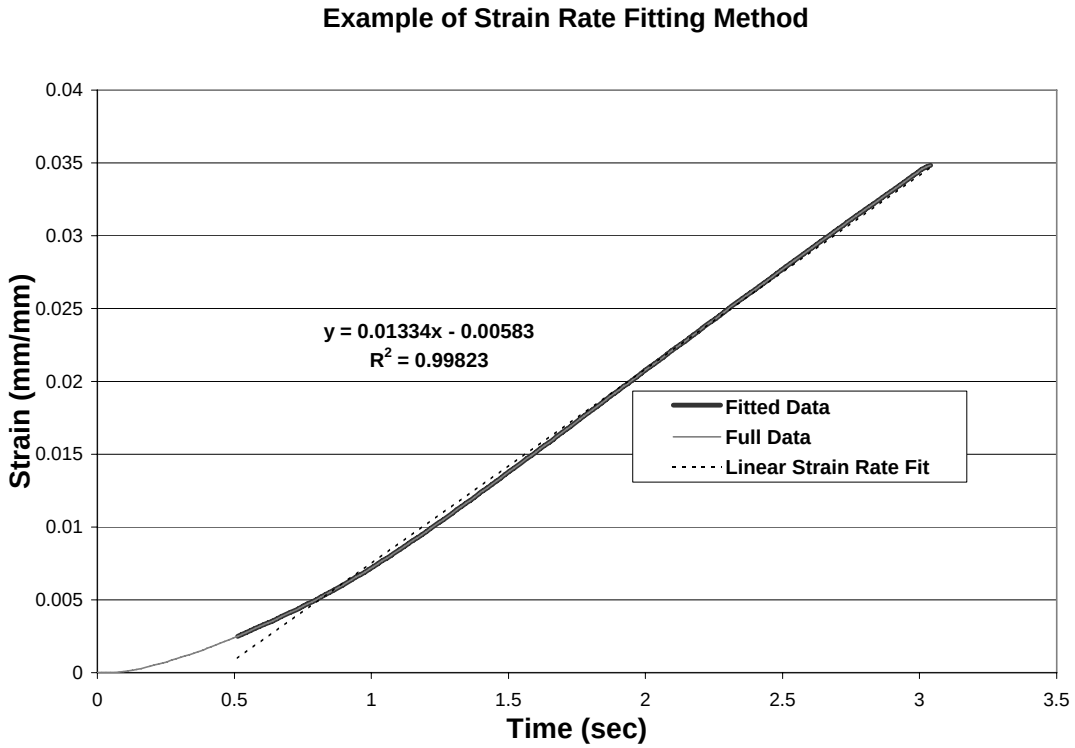

Figure 53. Example of strain rate estimation procedure.

5.3 Time-Temperature Superposition Analysis

The stress versus strain data from the previous section were cross-plotted to produce stress versus reduced time master curves at strain magnitudes ranging from 0.0025 to 0.0250 in 0.0025 intervals. Corresponding temperature shift functions at various strain levels were also produced from this cross plotting procedure to determine how far into the response the material remains thermorheologically simple—i.e., a material for which time-temperature superposition is valid. The results from this analysis procedure are presented in Figure 54 through Figure 63 Note that this range begins at about one-quarter of the way to the peak and ends well within the post-peak region. A sigmoidal function was assumed for the basic shape of the master curves, and the

isothermal curves were then shifted using the same Solver techniques (Pellinen, 2001) as for the small-strain dynamic modulus master curve analysis procedure. As is clearly evident in Figure 54 through Figure 63, the stress versus log reduced time points for all three temperatures form smooth and continuous master curves for all of the strain magnitudes considered. While there is only slight overlap among the data from the different temperatures, it is nevertheless very clear that these data all follow the same trend line. The best-fit sigmoidal master curves are summarized in Figure 64 for the strain magnitudes considered in this analysis. The master curves in Figure 64 are roughly parallel for all strain magnitudes; the curves shift upward and to the right at increasing strain magnitudes up to the peak condition. The master curves are all essentially the same from the peak strain magnitude and beyond.

The corresponding temperature shift factors from the time-temperature superposition analysis at various strain levels are summarized in Figure 65. Also included in Figure 65 is the temperature shift factors from the small-strain dynamic modulus master curve presented previously in Chapter 4. The temperature shift factors in Figure 65 are similar across all strain magnitudes at low to moderate temperatures, but there are some deviations with strain level at the highest temperature.

The implications of Figure 64 and Figure 65 are extremely important. These results indicate that asphalt concrete in compression is a thermorheologically simple material – i.e., time temperature superposition is valid – well into the post peak region. The master curves have a similar shape but a vertical offset as a function of strain level. The temperature shift function, however, is only slightly sensitive to strain level.

Given that significant cracking is observed post-test in the specimens, this further implies that time-temperature shifting is also valid for the fracture processes in the severely damaged material. Although fracture in the compression tests reported here is either vertical or shear cracking, Chehab et al. (2002) found similar results for uniaxial tension tests to failure.

The results in Figure 65 further suggest that although asphalt concrete remains thermorheologically simple throughout its full response range, the temperature shift function $a(T)$ may be a weak function of strain level. The temperature shift curves are a bit steeper for small strain conditions where linear viscoelastic strains are dominant and less steep where nonlinear strains (nonlinear viscoplastic and damage strains) are dominant. Put another way, the temperature shift curves tend to diverge slightly at higher temperatures where viscoplasticity and damage become more important relative to viscoelasticity.

For practical engineering purposes, however, the differences between the small strain and large strain temperature shift relations may be of negligible importance for many phenomena. With regard to overall stiffness, for example, the differences between small- and large-strain $a(T)$ values at the highest temperatures occur in the region in which the material is already very soft and thus relatively insensitive to the differences in the temperature shift factors. Figure 66 compares the $a(T)$ temperature shift factors developed out of the small strain dynamic modulus tests and the large-strain uniaxial constant rate of strain tests for a strain value of 0.0100. Figure 67 compares complex modulus master curves shifted using both the small strain and large strain $a(T)$ relations. As is clearly evident in the figure, the largest discrepancies occur in the high temperature

region where the differences between the master curves using the two $a(T)$ relations is on the same order as the variability in the underlying complex modulus test data.

A limited investigation into this discrepancy was completed towards the end of the project. It was suspected the confining cell induced a significant temperature gradient that could be remedied by disassembling the cell to expose the specimen to the ambient conditions in the temperature cabinet. Small-strain |E*| tests were performed on two specimens. The same specimen was tested at all temperatures and frequencies Temperature was verified at the center of the specimen as previously done. The *a(T)* shift functions for 5^o, 25^o and 40^o were essentially unaltered, but the small-strain *a(T)* shift function at 60^oC was much more similar to that determined in the large strain TTS analysis above. The conclusion reached from this small investigation was that vertical temperature gradient in the original |E*| tests was most likely equally uniform in the 5^o, 25^o and 40^o test, but not in the 60^oC tests. Essentially, removing the confining cell produced an equally acceptable temperature gradient at 60^oC. The results from this second set of |E*| tests do suggest that the large strain temperature shift function for temperatures between 40^o and 60^oC is perhaps closer to reality, and as a consequence the large strain temperature shift function was used for all model calibrations and prediction for the project. The differences between the small or large strain functions at cooler ranges of temperatures are negligible for all practical purposes.

Other research into extended time temperature superposition supports this study's findings. Zhao and Kim (2003) revisited compressive large strain testing and cross plotting with fresh specimens, but analyzed the data with a different approach. The small strain |E*| shift function was applied in a forward manner instead of back calculating the

a(T). The findings reinforced the conclusions that small strain TTS shift factors can be used to accurately shift the large strain response of asphalt concrete. Pellinen and Zhao (2005) give an independent validation of the extended time temperature superposition principle to large strains and failure. Mohr-Coulomb failure envelopes were compared. The envelopes were found equivalent between indirect tension (IDT) tests at a relatively cool temperature and confined triaxial tests at a relatively warm temperature. The loading rates in addition to the temperature were also different, but made thermorheologically equivalent with time temperature superposition. This was not done for test economization, but for convenience because IDT specimen preparation and testing is more attractive than triaxial tests. However, IDT cannot be used for high temperature rutting characterization because the geometry lends itself to very weak and unstable specimens. This validation is important for two reasons. The first is this study is an independent confirmation of the time temperature superposition principle with many mixtures. The second is that the phenomenon was shown valid in the IDT testing mode that induces complex stress states.

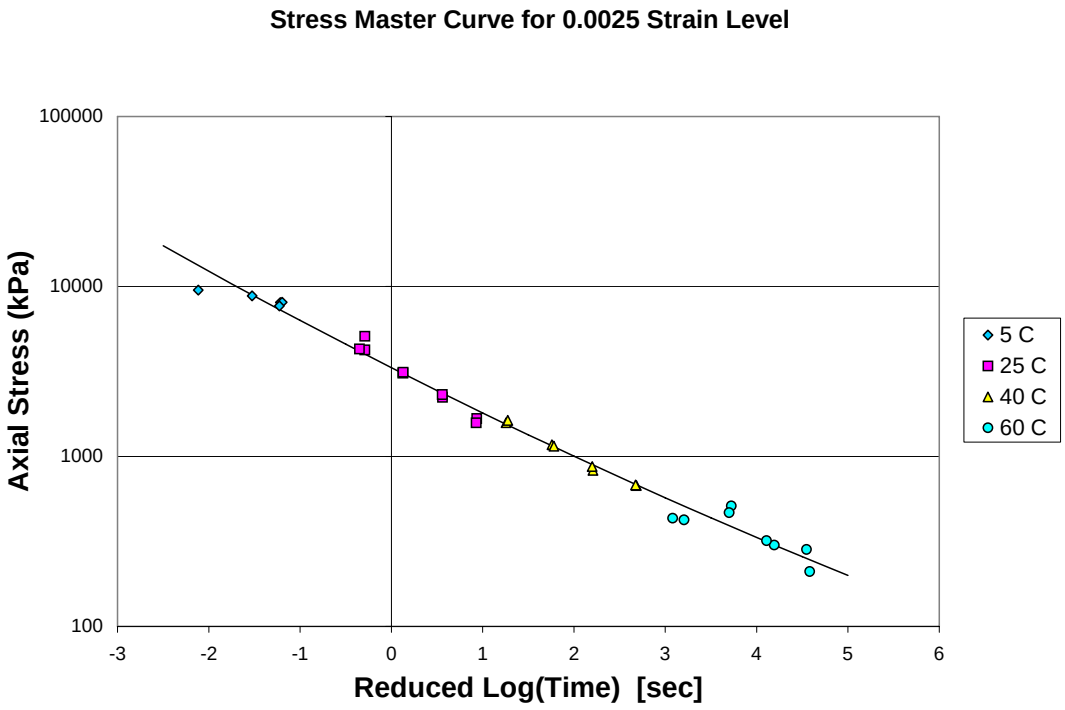

Figure 54. Stress vs. reduced time master curve for 0.0025ε from strain rate tests.

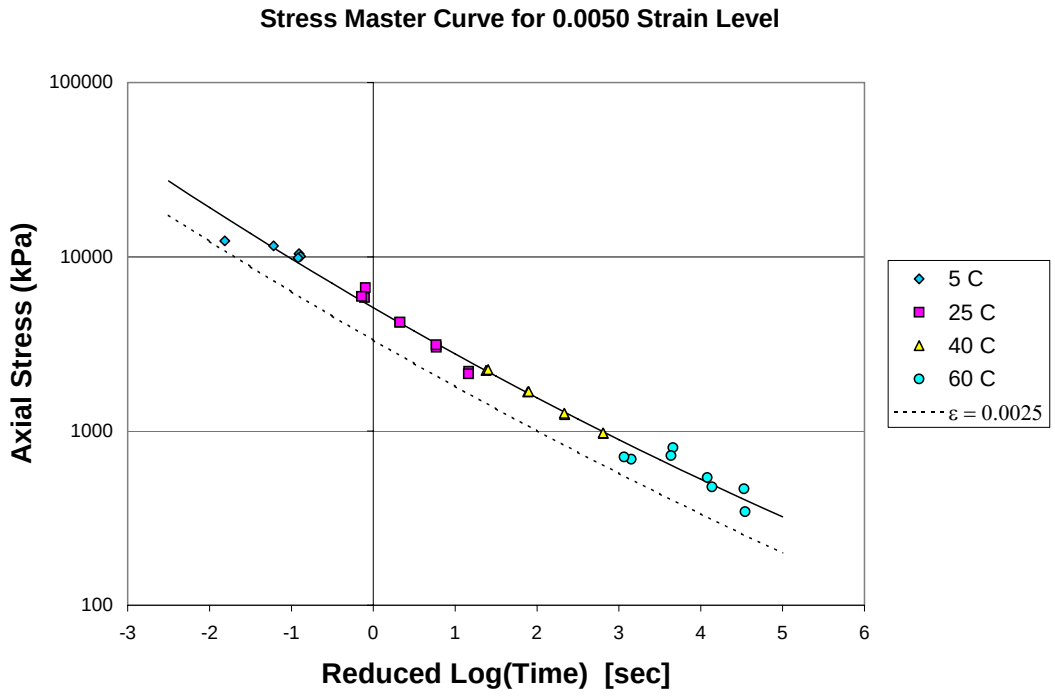

Figure 55. Stress vs. reduced time master curve for 0.0050ε from strain rate tests.

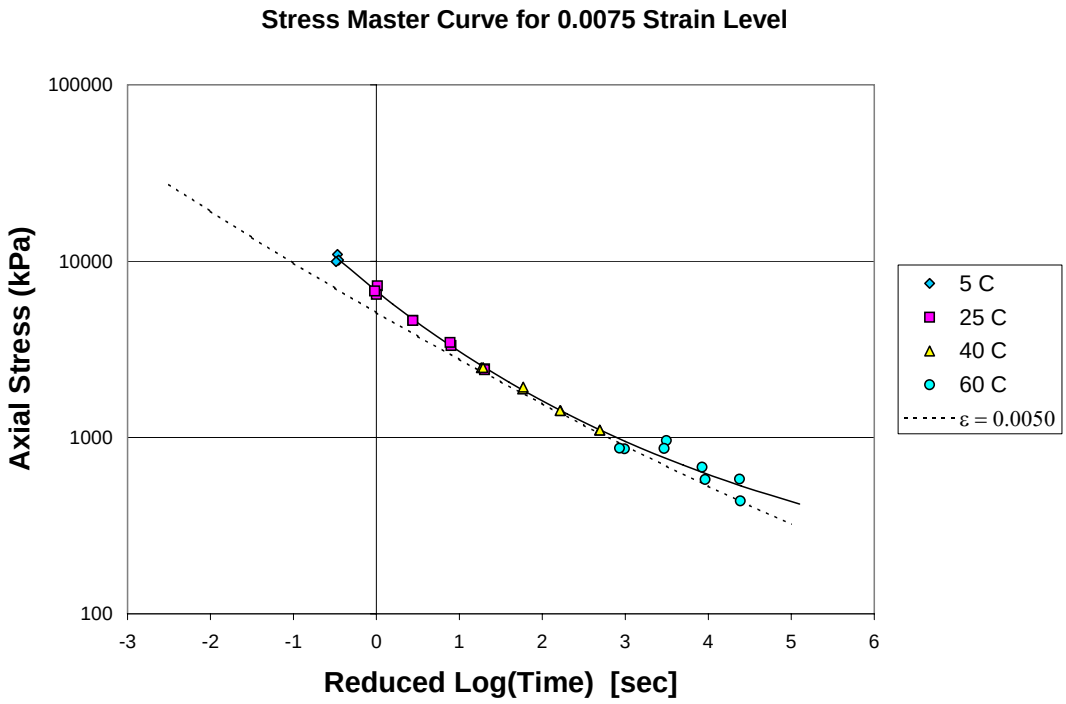

Figure 56. Stress vs. reduced time master curve for 0.0075ε from strain rate tests.

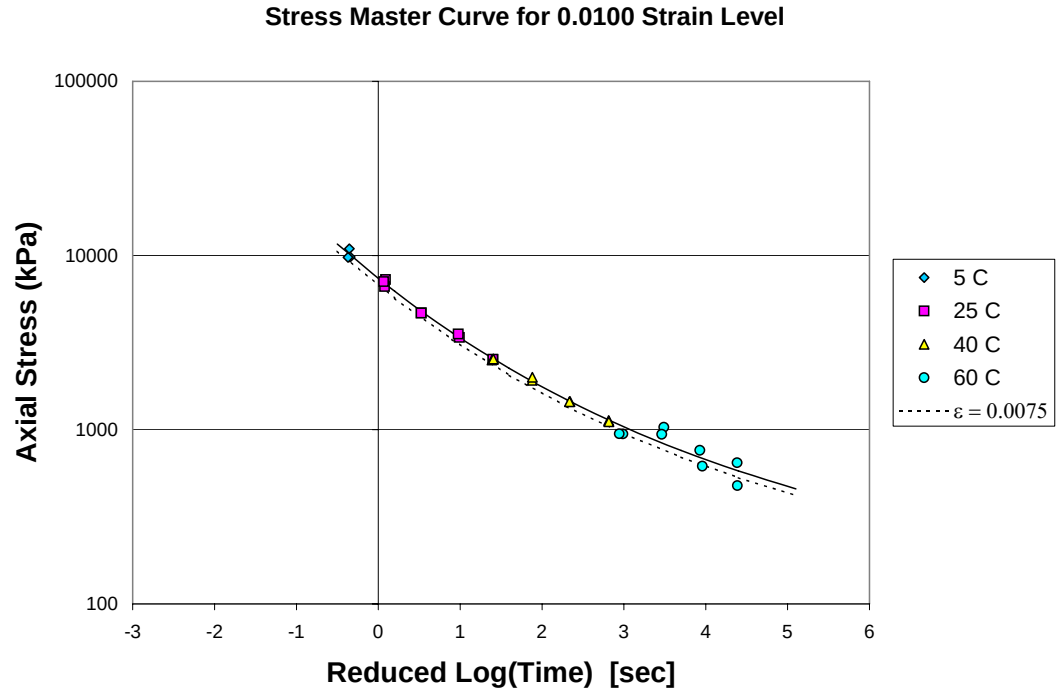

Figure 57. Stress vs. reduced time master curve for 0.0100ε from strain rate tests.

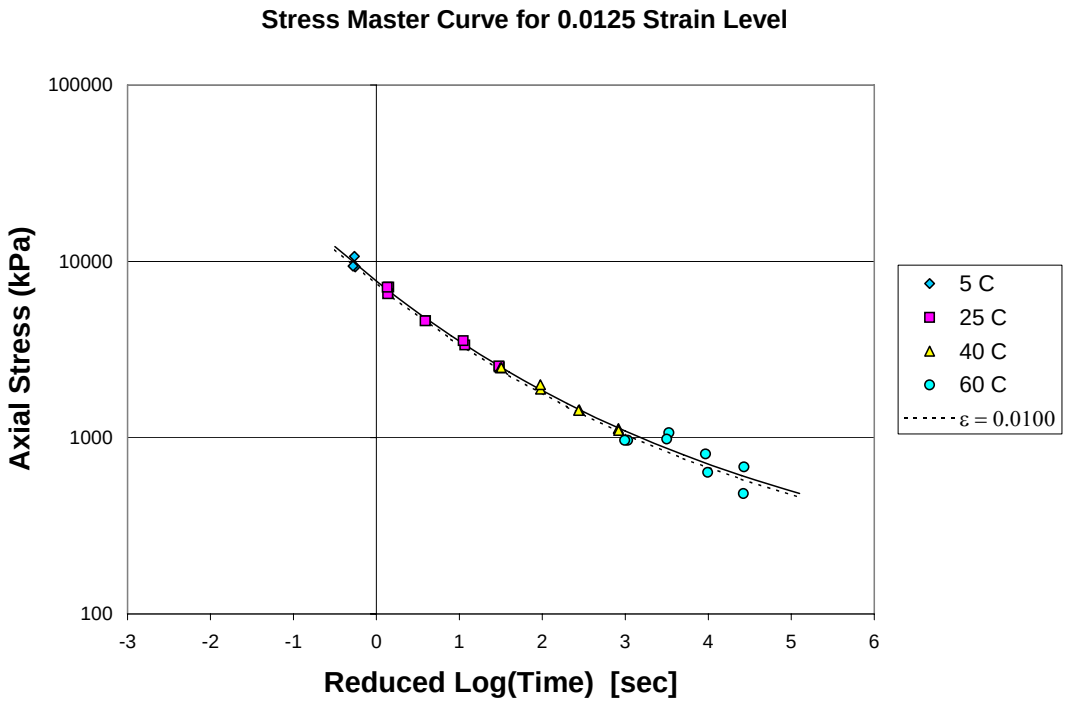

Figure 58. Stress vs. reduced time master curve for 0.0125ε from strain rate tests.

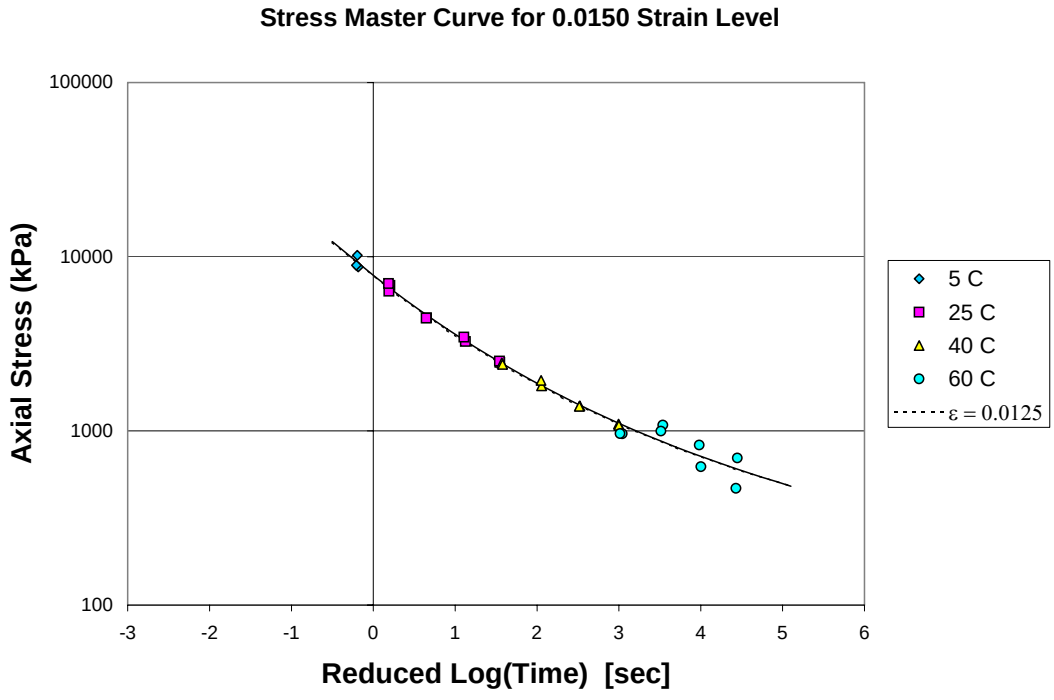

Figure 59. Stress vs. reduced time master curve for 0.0150ε from strain rate tests.

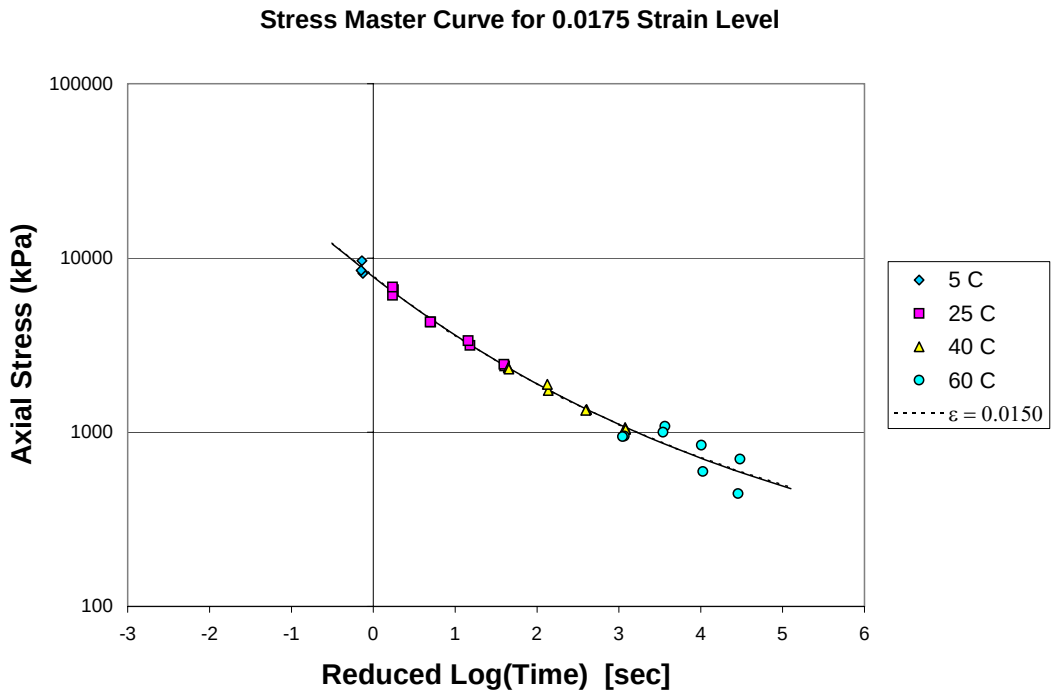

Figure 60. Stress vs. reduced time master curve for 0.0175ε from strain rate tests.

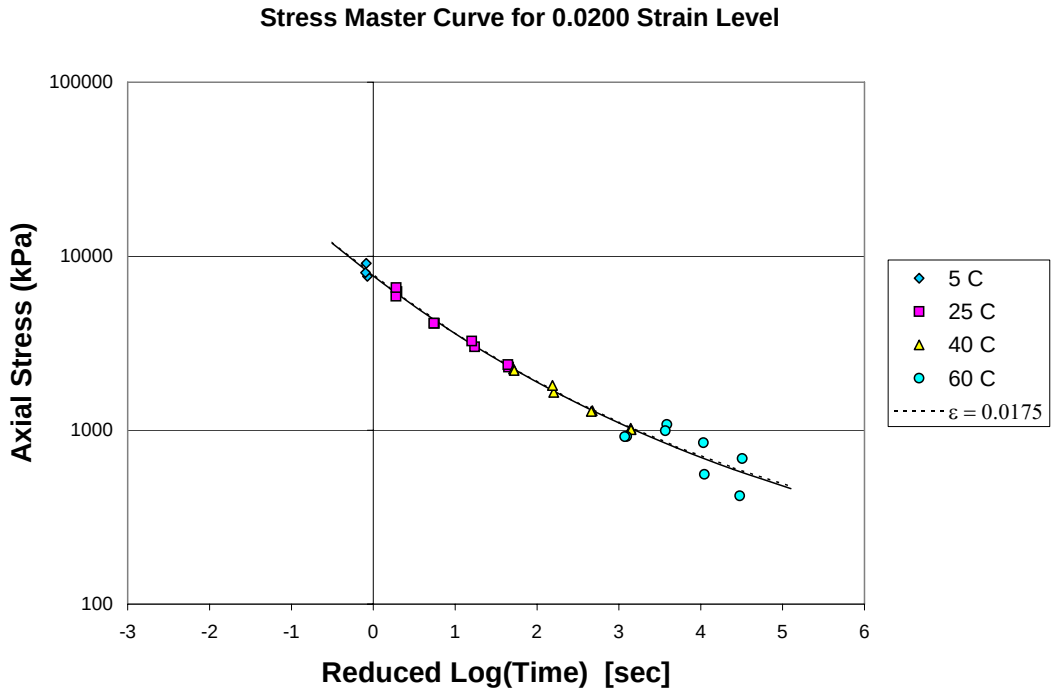

Figure 61. Stress vs. reduced time master curve for 0.0200ε from strain rate tests.

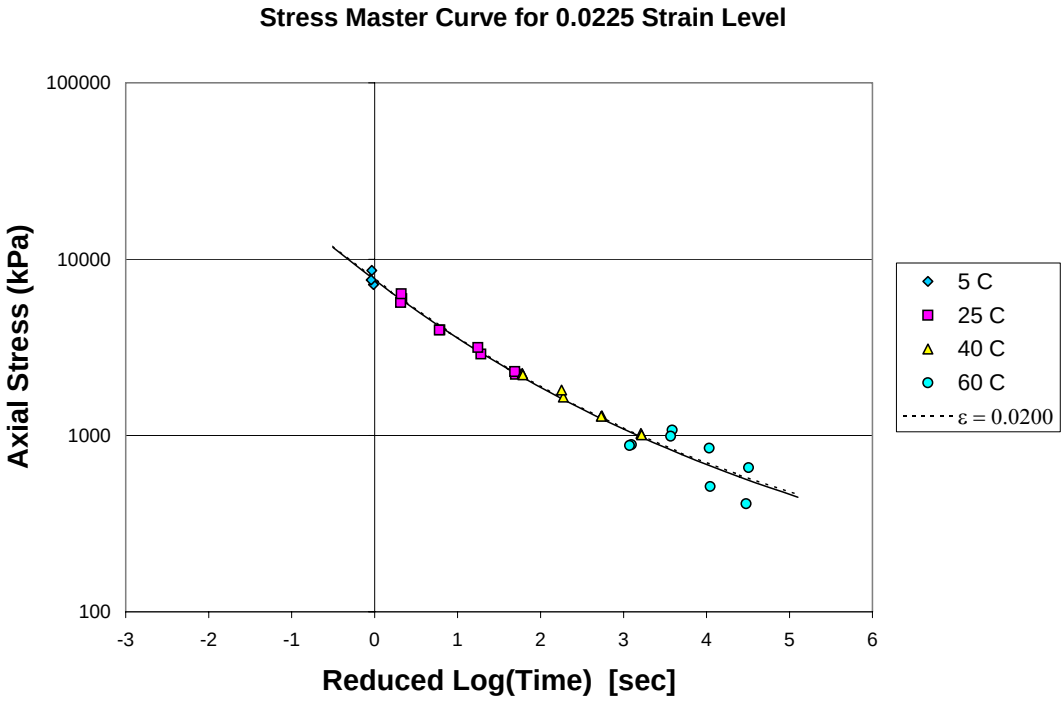

Figure 62. Stress vs. reduced time master curve for 0.0225ε from strain rate tests.

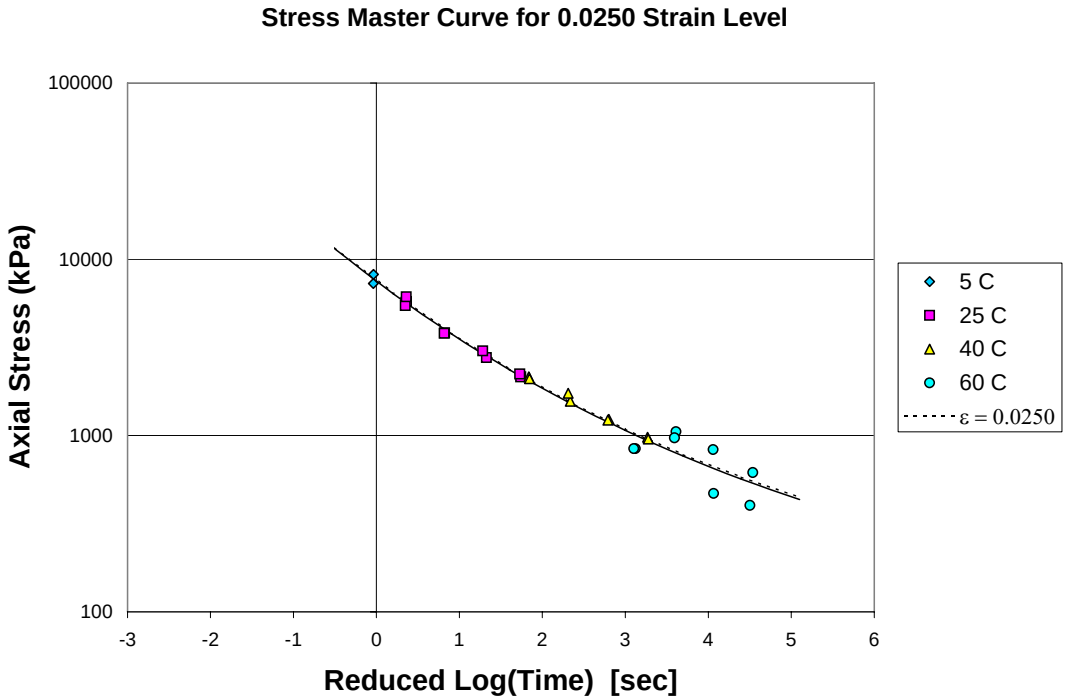

Figure 63. Stress vs. reduced time master curve for 0.0250ε from strain rate tests.

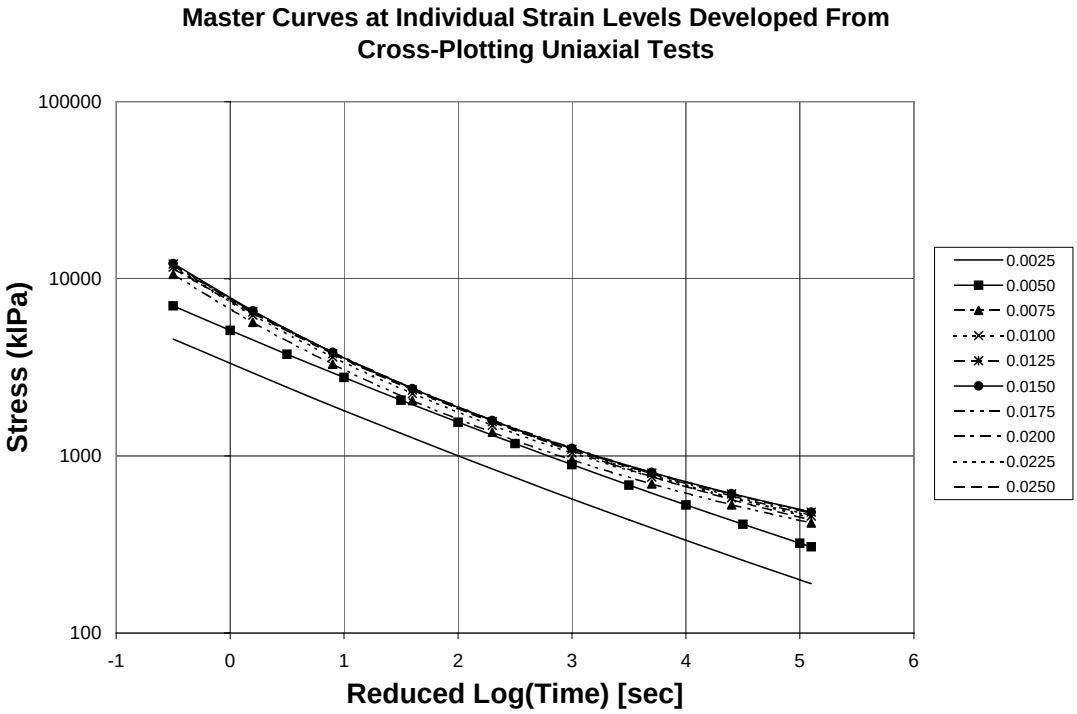

Figure 64. Master curve summary for strain rate tests.

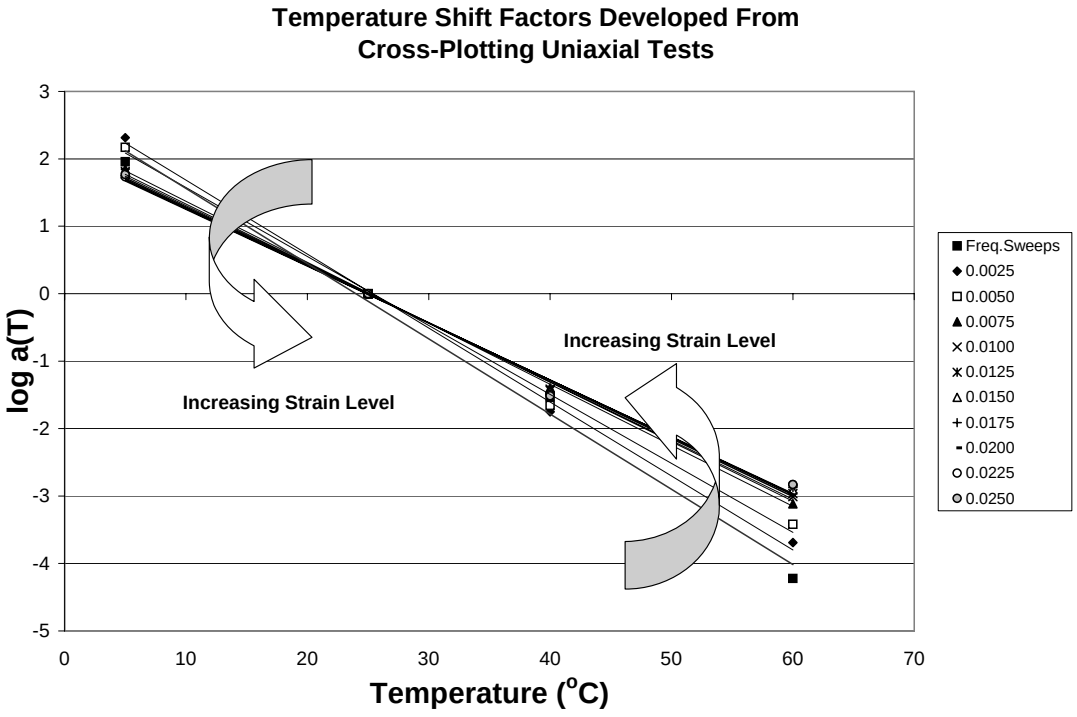

Figure 65. a(T) temperature shift factors for strain rate tests.

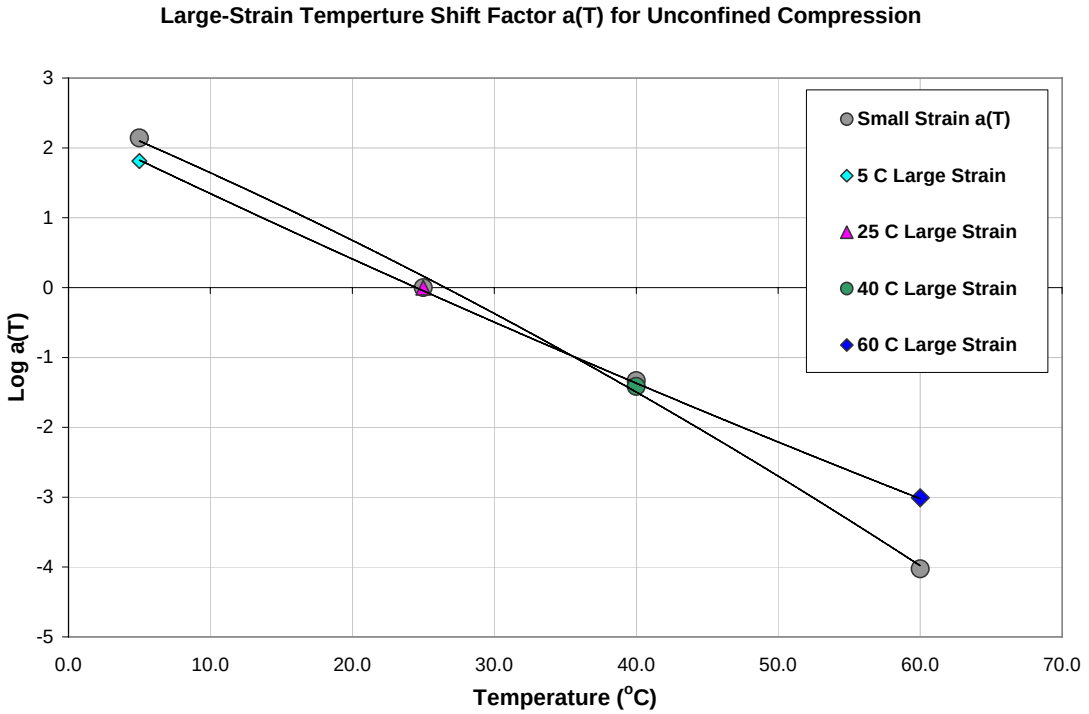

Figure 66. Small and large strain temperature shift factors with second order polynomial fit.

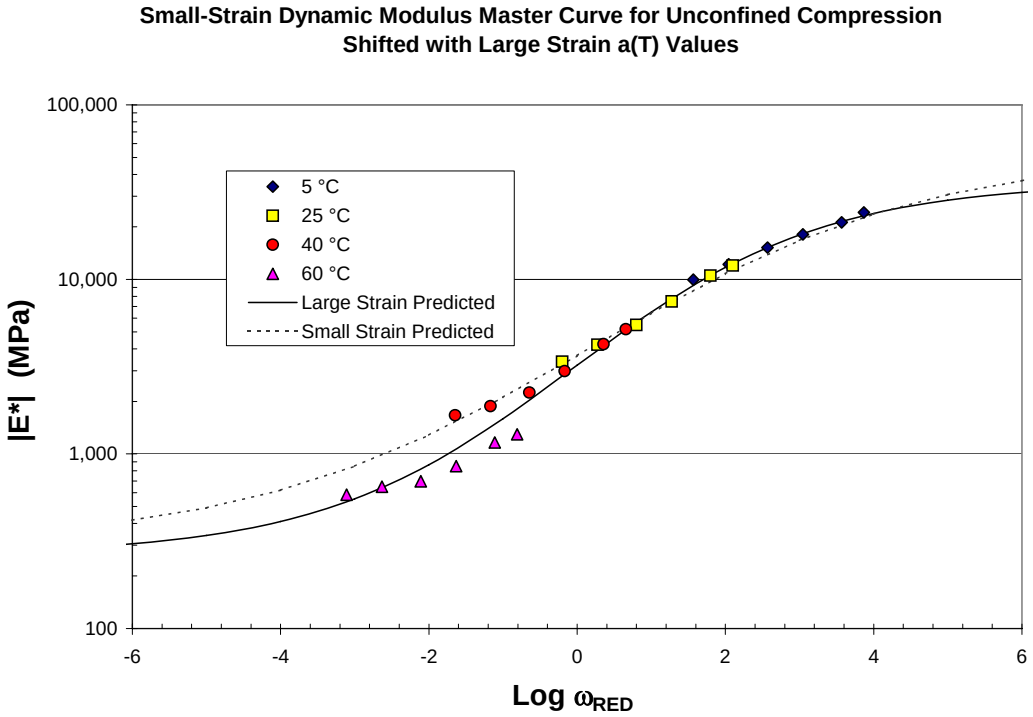

Figure 67. Master curve developed with large strain *a*(*T*) temperature shift factors.

5.4 Validation Tests for Extended Time Temperature Superposition

5.4.1 Rationale

The constant rate of strain to failure tests demonstrated the validity of large-strain time-temperature superposition and showed the $a(T)$ temperature shift factors from the large strain analysis were similar to the small-strain $a(T)$ temperature shift factors. Two series of creep and recovery tests were performed to verify these findings. These creep and recovery tests were performed at different temperatures but were designed such that the loadings were equivalent in reduced time. Theoretically, the response should also be equivalent if time-temperature superposition is valid.

It must also be noted these tests served dual purposes, as did the small-strain dynamic modulus tests. These tests and another type of cyclic creep and recovery tests were used to calibrate the viscoplastic model discussed in more detail later in Chapter 6 of this dissertation.

5.4.2 Validation Testing Details

Cyclic creep and recovery tests were performed in compression on previously unloaded specimens. Small-strain dynamic modulus frequency sweeps and preconditioning methods were omitted in these tests to avoid any undesirable initial permanent strain in the specimens. Instead, the general test procedure started with the application of a very small contact stress. The contact stress keeps the actuator from

drifting away from the specimen during zero stress control and then impacting the specimen once loading begins. The contact stress was not a function of the load in the tests but was simply the smallest load the testing machine could apply. This was about 0.05 kN, inducing a stress of about 7 kPa on the specimens.

Following the application of the contact stress the specimens were cyclically loaded with creep stress pulses that produced larger and larger total strains including larger and larger unrecoverable strains with each cycle. The specimens were allowed to recover over time (under the contact stress) after the end of each creep stress pulse. Three replicates were tested for each test condition.

These validation tests applied multiple cycles of near-square stress pulses that varied in duration but had a constant stress magnitude. For analysis purposes, it is desirable for the stress pulses to be as square as possible. Unfortunately, all servo-hydraulic testing machines are limited in the speed at which stress can be applied. It was accepted that the some cycles (not all) would have significant ramp-up and ramp-down times when compared to the time that the stress was constant.

Two sets of creep and recovery tests were carried out. The first set of tests was performed at intermediate and warm temperatures of 25^{o}C and 35^{o}C respectively. The second set of tests was performed at warm and high temperatures of 35^{o}C and 45^{o}C respectively. The loading duration for each subsequent cycle increased exponentially. This produced larger and larger strains due to increased duration of loading even though stress did not change. Complete viscoelastic recovery at the end of the rest periods was desired to enable direct measurement of permanent viscoplastic strains. The ratio of rest

time to loading time was 10:1 in order to maximize strain recovery. A schematic of the test procedure is shown in Figure 68.

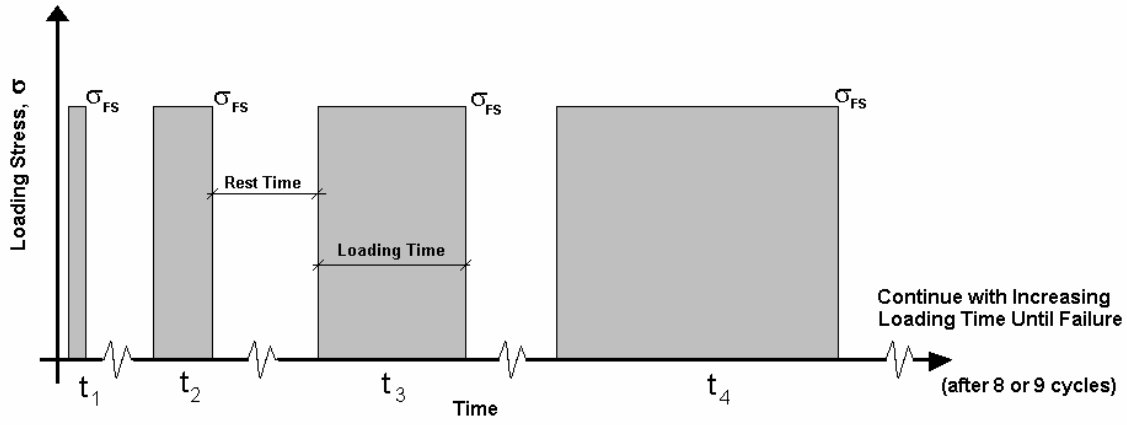

Figure 68. Schematic of cyclic creep and recovery tests.

The loading histories for each paired set of validation tests were designed to be equivalent in reduced time using time-temperature superposition. The loading histories for the 35°C tests were temperature shifted back to a 25°C reference temperature in order for the loading histories for the 25°C tests to match those for the 35°C tests in reduced time. A similar shifting was done for the 35/45°C validation tests where the 45°C tests were shifted back to a 35°C reference temperature. In other words, the tests at the higher temperature for each pair had shorter load cycle durations than the tests at the lower temperature in real time but identical load cycle durations in reduced time.

The initial cycles of the creep and recovery tests had trapezoidal stress waveforms because the ramp up and down times were significant when compared to the time the stress was held constant. However, as long as the stress waveform at the complimentary temperature has the same trapezoidal loading in reduced time, the time-temperature superposition validation objectives of the tests could still be achieved.

The speed with which the UTM-100 hydraulic testing machine could reach the target stress defined the loading history for the 35°C tests in the 25/35°C tests. The slower loading at 25°C made the tests easier to control. This strategy was used again for the 35/45°C validation tests. Tests were carried out at the warmer temperatures first to obtain the resulting load history in absolute time. Then the absolute time load history for the cooler temperatures was computed from the warmer temperature load history and an assumed temperature shift factor. The temperature shift factor used to develop the matched loading sequence in reduced time for the 25°C creep and recovery tests was interpolated from the small-strain temperature shift factor relationship (Figure 66), although the differences between the small and large-strain shift factors are negligible at this temperature.

Due to the loading limitations in the testing machine, the 35°C results from the 25/35°C test set could not be used in conjunction with the new 45°C tests. This was because the loading rate required to have the tests at 45°C match the tests at 35°C in reduced time would be much faster than the machine could apply. Therefore, a completely new set of creep and recovery tests at 35°C was conducted.

The original testing plan called for the use of the small-strain temperature shift factors for all temperature shifting. As will be detailed in this section, this was changed after poor agreement was observed in some trial tests in the 35/45°C set. Instead, the large-strain temperature shift factor was used to make the 45°C and 35°C tests equivalent in reduced time at the 35°C reference temperature.

The final loading histories in absolute time for the validation tests are in Table 14 to Table 17. Stress magnitudes for the two test conditions were selected to give large strains and eventually failure in the eighth or ninth cycle.

Table 14. Target loading for 35°C creep and recovery tests in the 25/35°C set.

Cycle	Ramp-Up Time, sec	Constant Loading Time, sec	Ramp-Down Time, sec	Loading Stress, kPa
1	0.040	0.040	0.040	1525
2	0.040	0.060	0.040	1525
3	0.040	0.125	0.040	1525
4	0.040	0.250	0.040	1525
5	0.040	0.500	0.040	1525
6	0.040	1	0.040	1525
7	0.040	2	0.040	1525
8	0.040	4	0.040	1525
9	0.040	8	0.040	1525

Table 15. Target loading for 25°C creep and recovery tests in the 25/35°C set.

Cycle	Ramp-Up Time, sec	Constant Loading Time, sec	Ramp Down Time, sec	Loading Stress, kPa
1	0.570	0.570	0.570	1525
2	0.570	0.855	0.570	1525
3	0.570	1.780	0.570	1525
4	0.570	3.561	0.570	1525
5	0.570	7.121	0.570	1525
6	0.570	14.243	0.570	1525
7	0.570	28.486	0.570	1525
8	0.570	56.972	0.570	1525
9	0.570	113.944	0.570	1525

Table 16. Target loading for 45°C creep and recovery tests in the 35/45°C set.

Cycle	Ramp-Up Time, sec	Constant Loading Time, sec	Ramp Down Time, sec	Loading Stress, kPa
1	0.032	0.032	0.032	936
2	0.032	0.064	0.032	936
3	0.032	0.128	0.032	936
4	0.032	0.256	0.032	936
5	0.032	0.512	0.032	936
6	0.032	1.009	0.032	936
7	0.032	2.018	0.032	936
8	0.032	4.041	0.032	936
9	0.032	8.072	0.032	936
10	0.032	16.119	0.032	936

Table 17. Target loading for 35°C creep and recovery tests in the 35/45°C set.

Cycle	Ramp-Up Time, sec	Constant Loading Time, sec	Ramp Down Time, sec	Loading Stress, kPa
1	0.232	0.232	0.232	936
2	0.232	0.464	0.232	936
3	0.232	0.928	0.232	936
4	0.232	1.856	0.232	936
5	0.232	3.713	0.232	936
6	0.232	7.317	0.232	936
7	0.232	14.634	0.232	936
8	0.232	29.304	0.232	936
9	0.232	58.536	0.232	936
10	0.232	116.890	0.232	936

5.4.3 Validation Tests Results and Analysis

The strain vs. time responses measured for the 25/35°C set of cyclic creep and recovery tests are shown in Figure 69 to Figure 70. At both of these temperatures, two of the replicates gave nearly identical response while the third gave somewhat different strains. Figure 71 shows the average response of the three replicates at each temperature in terms of reduced time. The agreement in the tests between the total strain including recoverable, irrecoverable, and damage responses over the full range of reduced time confirms that time-temperature superposition is valid in the large-strain region. Failure is reached in the ninth cycle for both temperatures.

Trial validation tests for the 35/45°C set using the small-strain temperature shift yielded results that did not temperature-shift together. The cooler 35°C tests gave consistently larger strain values at all reduced times than did the warmer 45°C tests in reduced time as seen in Figure 72. This implies that the load duration in the reduced time

loading history at 45°C was perhaps too short or the loading history at 35°C was perhaps too long.

After reviewing the results of the preliminary tests it was decided that the large-strain temperature shift factors from the uniaxial strain rate tests might be more appropriate than the small-strain temperature shift factors from the dynamic modulus tests for developing the matched loading in reduced time. This concurs with the previous discussed findings of temperature shift functions with and without the confining cell assembled. The difference between these shift factors is shown in Figure 73. The 45°C test results were kept and the 35°C tests were repeated with the new loading sequence (Table 17). The axial strain results for the higher temperature tests using the large-strain temperature shift factors can be seen in Figure 74 to Figure 76. Three replicates were tested at each temperature. As in the first series of tests, two of the replicates were in very close agreement, and a third replicate differed by a small to moderate amount. Failure was reached in the ninth cycle.

The results from these validation tests are alternately shown in Figure 77 and Figure 78 in a format more similar to un-shifted and shifted dynamic modulus data. In these plots only the un-recovered strain (of interest in the viscoplastic model calibration in Chapter 6) is shown at the end of each cycle. This strain is plotted against the absolute (unshifted) and reduced (shifted) cumulative loading time that ignore the recovery times in a log-log space. Again these plots show time-temperature superposition is valid because the responses are equivalent in reduced time and form smooth overlapping curves. One may notice the data points from the two temperatures in a set do not lie at the same reduced time position.

In summary, very good overall agreement of total, unrecovered, and recovered strain vs. reduced time was observed between both pairs of tests performed at two different temperature combinations. These test results confirm the validity of time-temperature superposition at large strain magnitudes having large degrees of viscoplasticity and other nonlinear components.

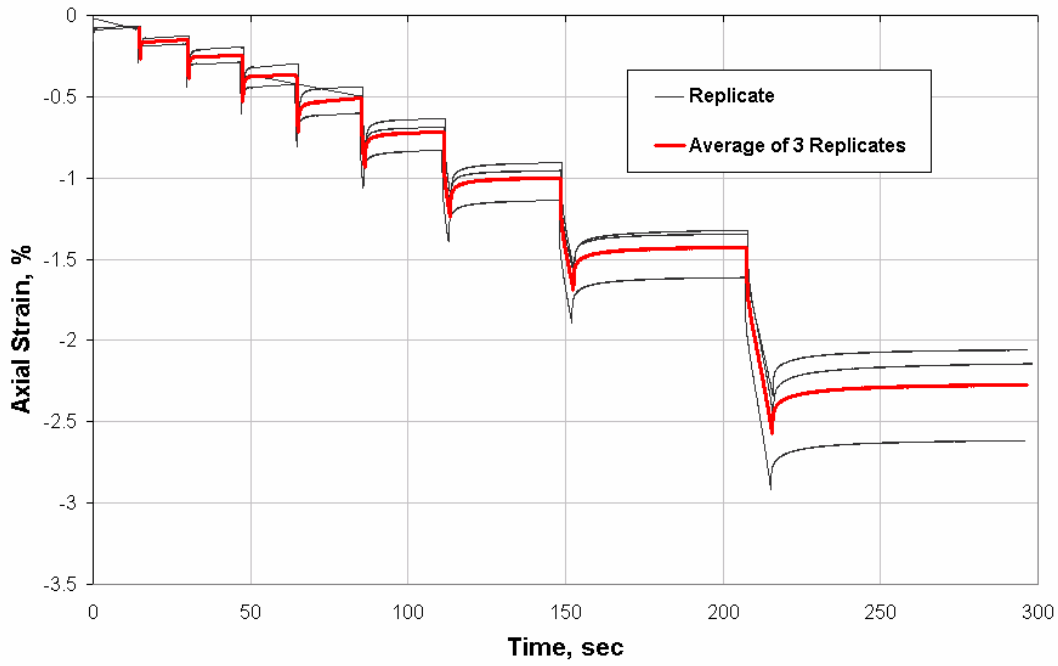

Figure 69. 35°C axial strain of three replicates for 25/35°C creep and recovery tests. Straight lines represent a data acquisition faliure over an entire loading cycle.

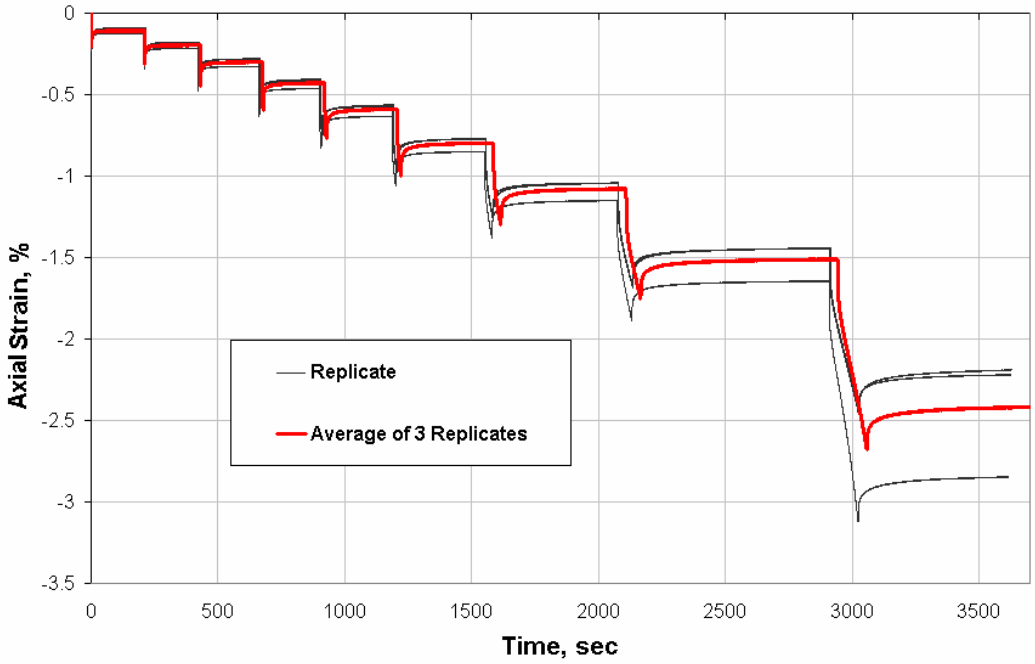

Figure 70. 25°C axial strain of three replicates for 25/35°C creep and recovery tests.

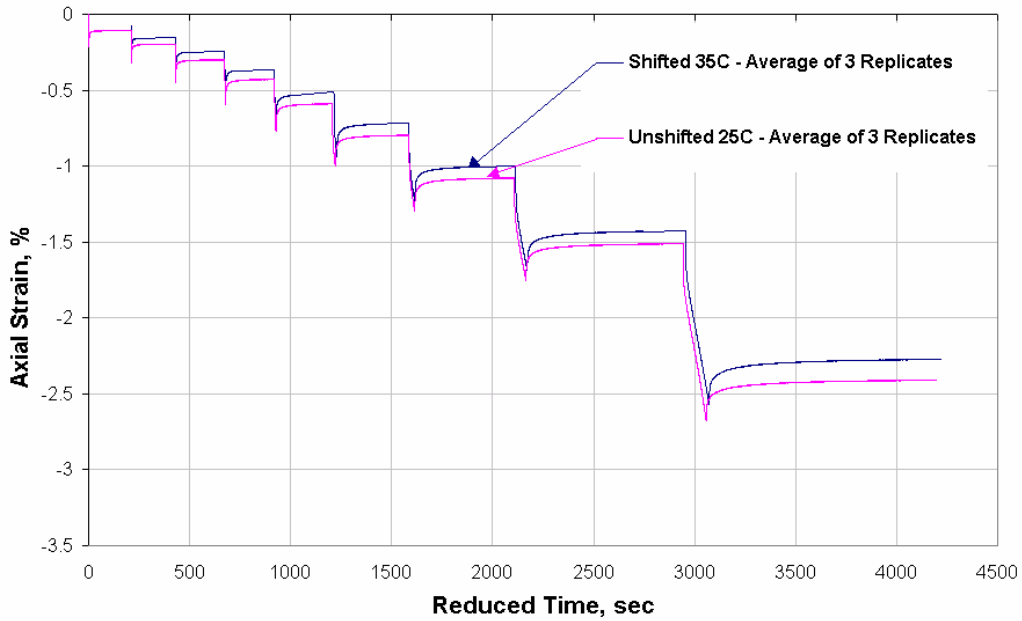

Figure 71. Shifted average of axial strain for 3 replicates for 25/35°C creep and recovery tests.

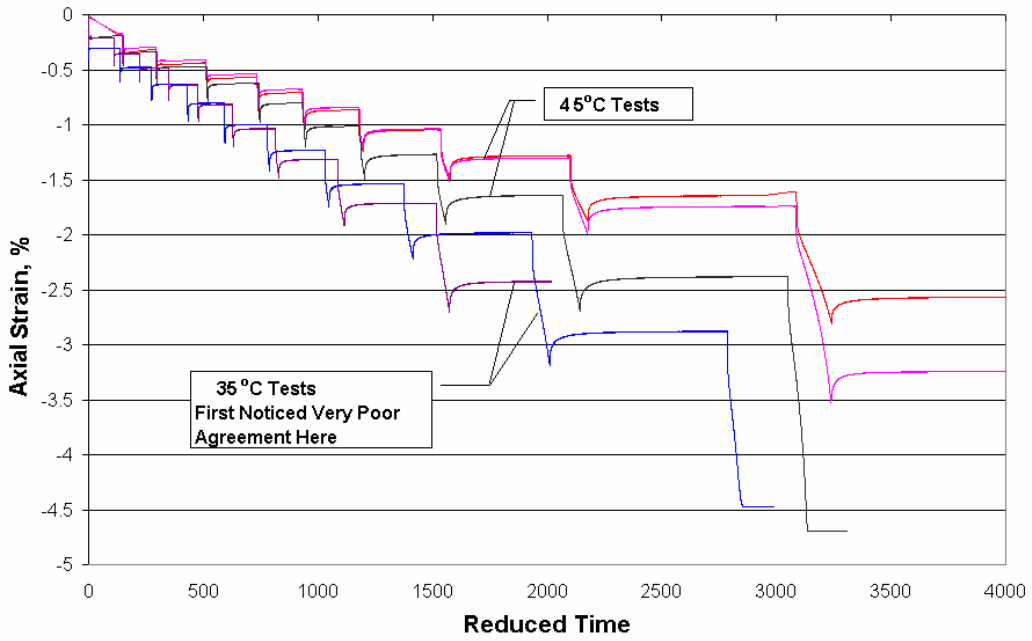

Figure 72. Preliminary results for 35/45°C creep and recovery tests series using the small-strain temperature shift factors. Straight lines represent a data acquisition failure over an entire cycle.

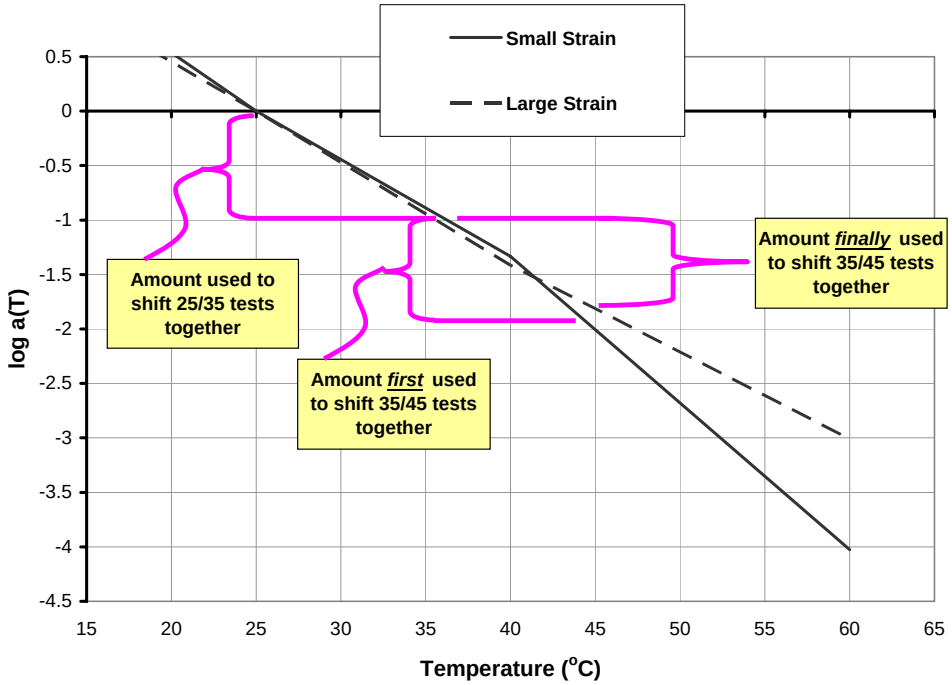

Figure 73. Large and small strain temperature shift factors used in cyclic creep and recovery tests.

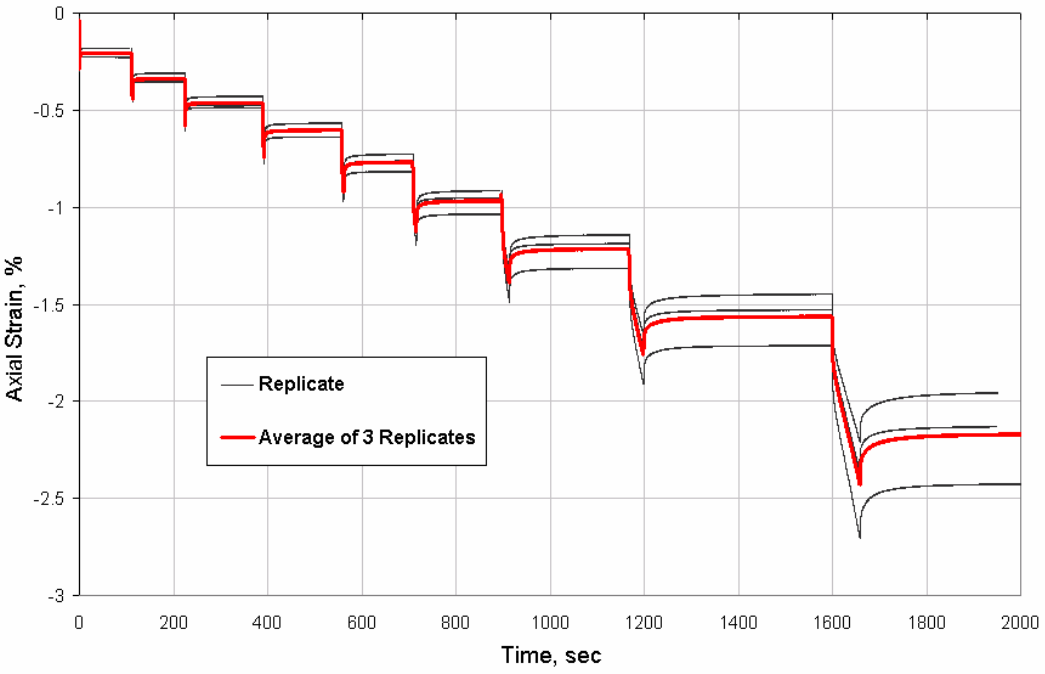

Figure 74. 35°C axial strain of three replicates for 35/45°C creep and recovery tests.

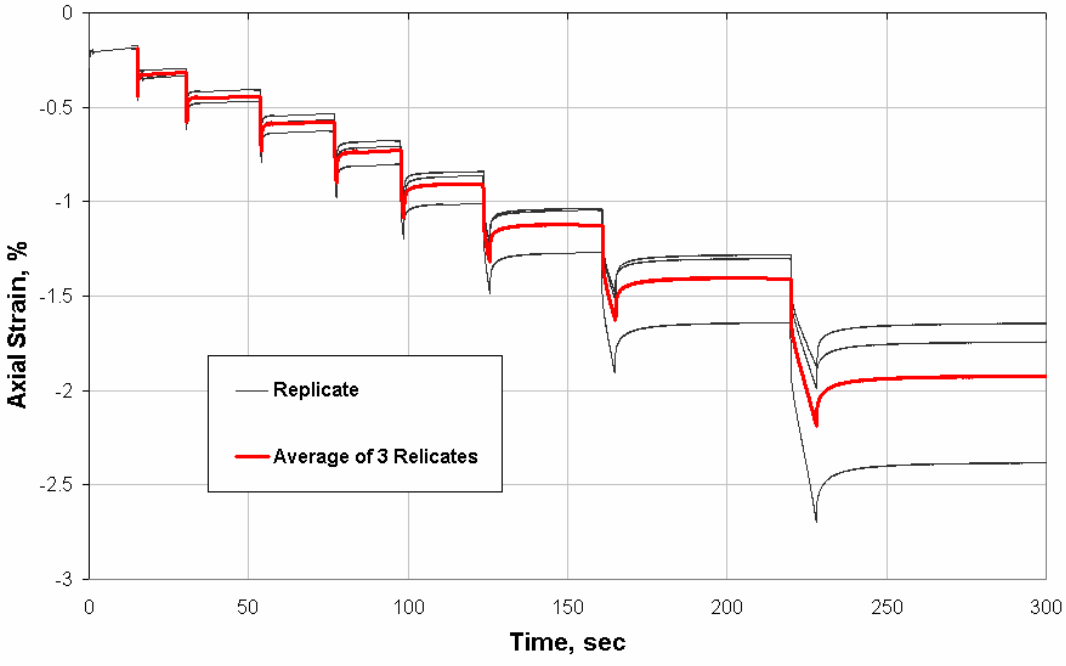

Figure 75. 45°C axial strain of three replicates for 35/45°C creep and recovery tests.

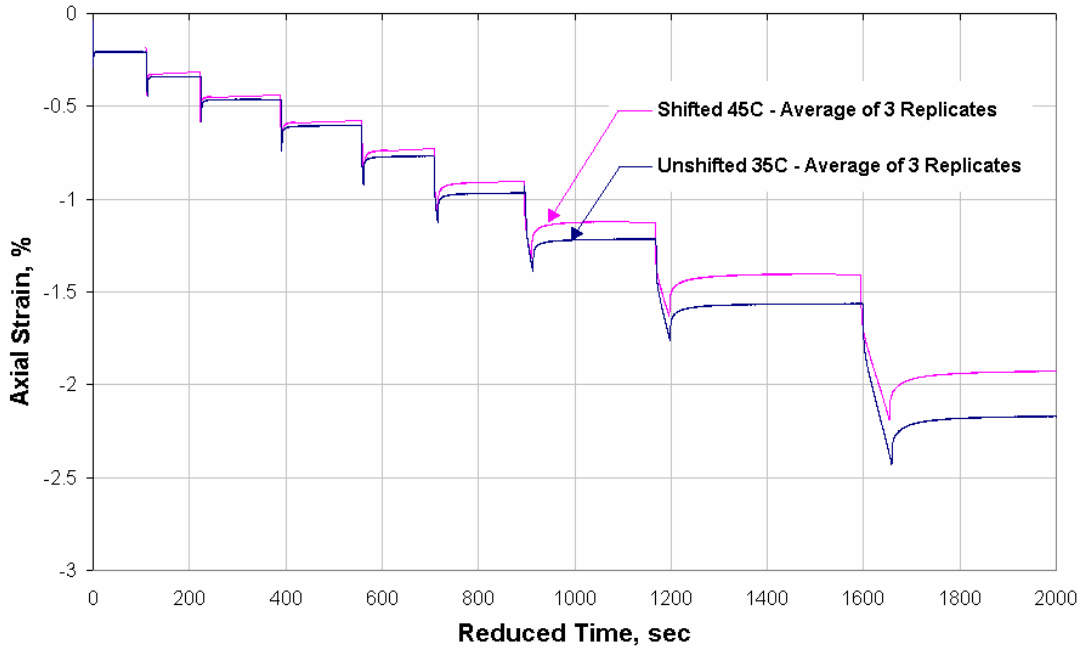

Figure 76. Shifted average of axial strain for 3 replicates for 35/45°C creep and recovery tests using large-strain temperature shift factors.

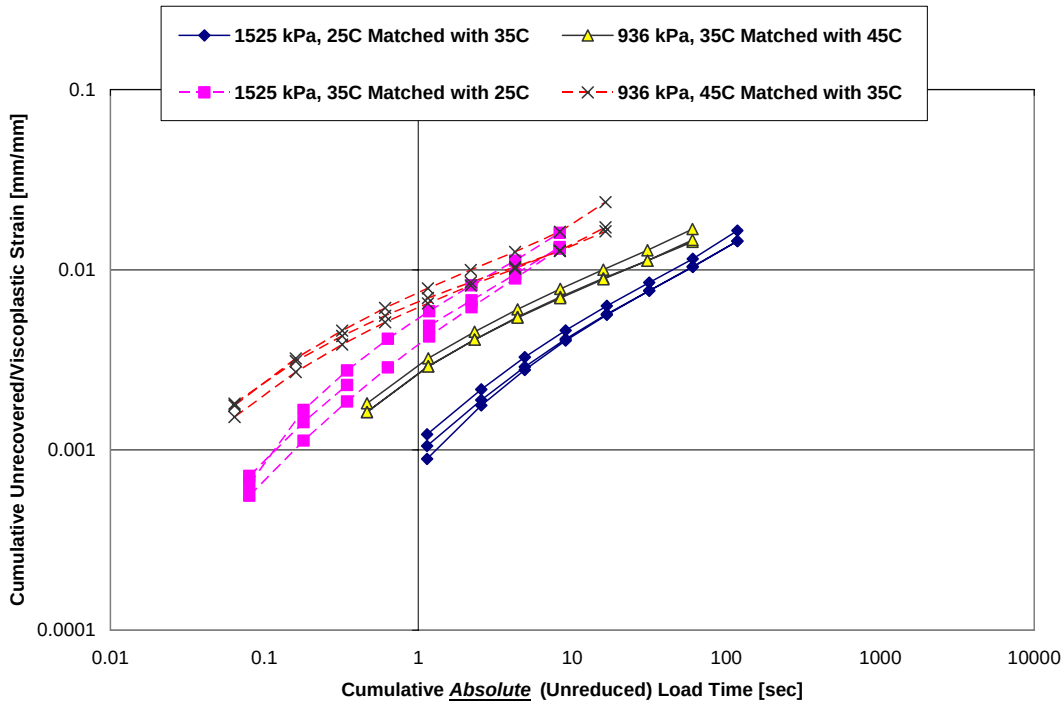

Figure 77. Alternate representation of un-shifted un-recovered strains from cyclic creep and recovery tests.

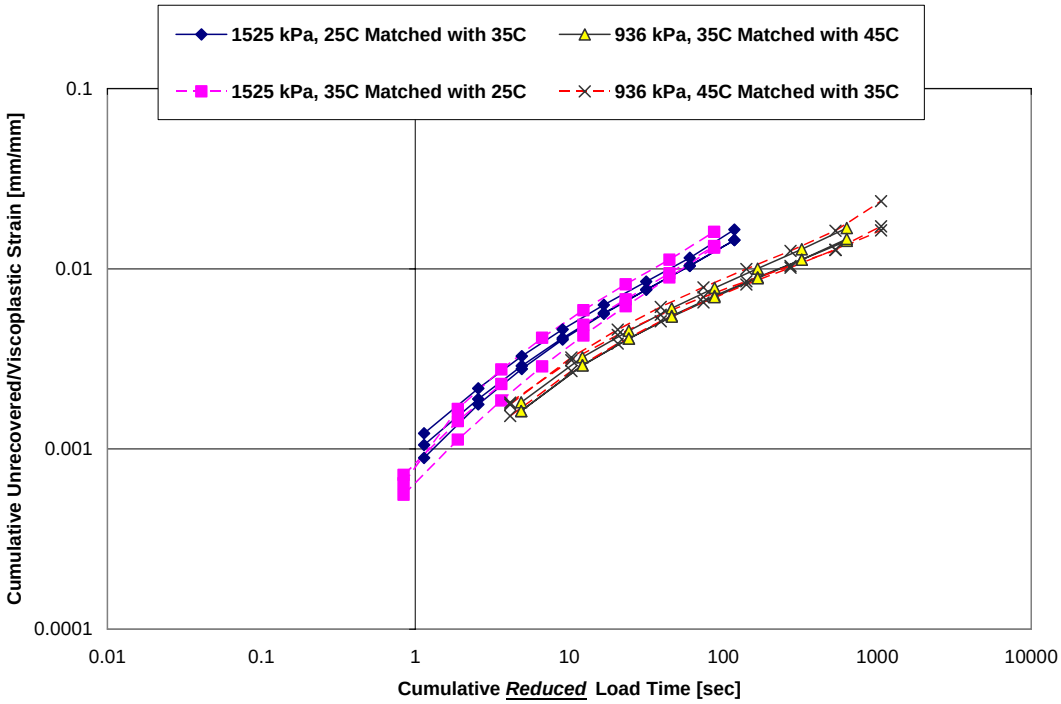

Figure 78. Alternate representation of shifted un-recovered strains from cyclic creep and recovery tests.

5.4.4 Limited Validation Under Triaxial Confinement

Confined triaxial testing was performed at a later date while studying the confined damage and viscoplastic responses of the material (Chapters 6 and 7). Since time-temperature superposition was shown to be valid at large strains under uniaxial conditions there was confidence that it would be valid for large strains under confined triaxial conditions because confinement would decrease the overall strain magnitude and suppresses a significant portion of material nonlinearity due to viscoplasticity and microstructural damage.

Nevertheless, time-temperature superposition under triaxial compression was checked by again designing equivalent loading schemes in reduced time at two different temperatures, but this time under confinement. To save time and effort, the confined 35^{o}C

fixed stress replicates performed to directly compare confined versus unconfined viscoplastic responses (described in Chapter 6) were recycled and only one new test was performed at a different temperature but with the same loading history in reduced time. The objective was to quickly check for any unexpected gross difference in confined responses at the two different temperatures. A fixed stress cyclic creep and recovery profile with constant deviatoric stress cycles of 1500 kPa was tested under 500 kPa of confinement, the highest level of confinement used in the confined viscoplastic study. The target temperature was 25^{o}C, but the specimens were tested at the 28^{o}C room temperature in the interest of time.

The results are shown in Figure 79. The 28^{o}C curve is one replicate and the 35^{o}C curve has two replicates. These tests compare the strain that is accumulated after the strains due to a hydrostatic stress portion of the tests have reached an acceptable steady state. Agreement between the two responses in reduced time is very close. This further verifies large-strain time-temperature superposition.

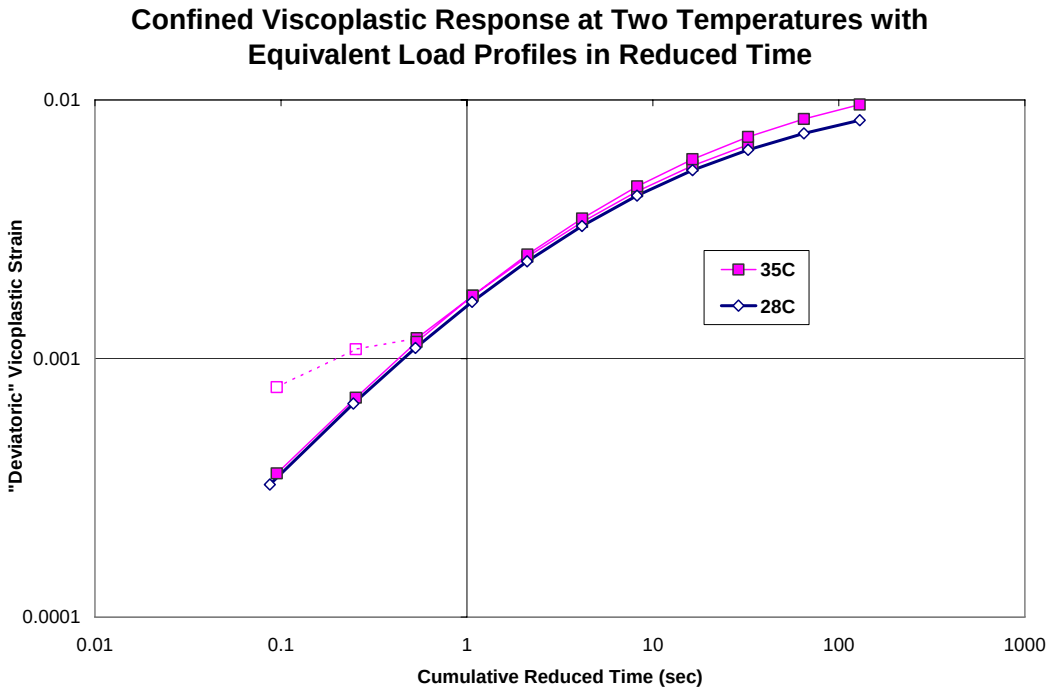

Figure 79. Confined triaxial cyclic creep and recovery.

5.5 Summary and Conclusions

Time-temperature superposition can be used for thermorheologically simple materials to interchange temperature and loading rate effects by means of simple temperature shift factors. Time-temperature superposition is reliable and widely used to interpret the results of small strain (< 100 με) asphalt concrete dynamic modulus tests. As described in Chapter 4, small-strain dynamic modulus tests were performed to obtain a master stiffness curve and temperature shift factors for a typical dense-graded asphalt concrete mixture using the time-temperature superposition principle.

These small-strain temperature shift factors were directly compared to shift factors determined from constant rate of strain tests at various large strain levels and at

multiple temperatures and loading rates. The shift factors determined at large strains were similar to the small strain results at low and intermediate temperatures and deviated slightly at the highest temperature.

Two sets of cyclic creep and recovery tests were performed at different temperatures to validate the results from the constant rate of strain tests. Using time-temperature superposition the tests were designed to have equivalent loading histories in reduced time although different loading histories in physical time (because of the different test temperatures). The agreement of the measured large strains at different temperatures supports the conclusion that time-temperature superposition is valid for asphalt concrete well beyond the conventionally accepted 100 με limit.

These findings and those from other researchers provide evidence that asphalt concrete is a thermorheologically simple material at small and large strains up to and including the immediate post peak region. The temperature shift factors derived from constant rate of strain tests appear to be weakly dependent upon strain level. However, for practical engineering purposes the difference among the temperature shift factors may be negligible. Reasonable explanations for the high temperature discrepancy were presented and support the findings from other research that there is perhaps less strain dependence and indeed a closer agreement between the compressive small- and large-strain temperature shift functions. The validation creep and recovery tests explored the use of small-strain and large-strain temperature shift factors to create equivalent loadings in reduced time. Again, time-temperature superposition was observed to be valid for large strains provided an appropriate temperature shift factor relationship is used.

One other important conclusion can be drawn from this study. The total response of asphalt concrete consists of multiple response components such as linear and nonlinear viscoelasticity, viscoplasticity, micro-structural damage, etc. These components are all present in some form in the large-strain constant rate of strain to failure and cyclic creep and recovery tests. The validity of the time-temperature superposition in these large-strain tests suggests that all of these response components follow the same or very similar temperature shift factors as for small-strain linear viscoelasticity. Therefore, the processes that govern these component responses for asphalt concrete must all derive from the same rate processes in the viscous asphalt binder.

Of considerable practical importance is the impact that time-temperature superposition can bring to material characterization programs. The results obtained in this study suggest that a single set of temperatures shift factors derived from small-strain dynamic modulus tests can be used to simplify material characterization testing for the other responses of asphalt concrete by eliminating the need for a full experimental factorial across multiple temperatures and loading rates.

6. Viscoplasticity Characterization

6.1 Introduction

The modeling formulation adopted for this research decomposes total strain as $\varepsilon_{Total} = \varepsilon_{Linear\ Viscoelastic} + \varepsilon_{Viscoplastic} + \varepsilon_{Damage}$. Viscoplasticity is logically treated before damage because viscoplastic strains must be removed from any test data that will be used to calibrate the damage model, expressed conceptually as $\varepsilon_{Damage} = \varepsilon_{Total} - (\varepsilon_{Viscoplastic} + \varepsilon_{Linear\ Viscoelastic})$. The large strain time-temperature superposition study (Chapter 5) found that the effects of loading time and temperature on viscoplastic strains can be interchanged using a generalized time-temperature superposition $t_R = {}^{t}\!/_{a(T)}$ where the temperature shift function $a(T)$ found from small-strain linear viscoelastic dynamic modulus tests is sufficient for practical engineering purposes. This permits considerable economies in the laboratory testing program needed to characterize the material parameters in the model.

6.2 Uniaxial Conditions

6.2.1 Model Form

Key aspects of the viscoplasticity model form given in Chapter 2 are repeated here for convenience. The theoretical background for the viscoplastic extension of the Schapery model starts with the assumption that the rate of change of viscoplastic strain for uniaxial constant stress loading follows a strain-hardening model of the form:

$$\dot{\varepsilon}_{vp} = \frac{d\varepsilon_{vp}}{dt} = \frac{g(\sigma)}{A\varepsilon_{vp}^{p}} \qquad \textbf{Equation 75}$$

in which $\dot{\varepsilon}_{vp}$ is the rate of change of viscoplastic strain in reduced time, ε_{vp} is the total viscoplastic strain level, $g(\sigma)$ is the uniaxial stress loading function and *A* and *p* are material constants. Equation 75 can be rearranged and integrated as:

$$\varepsilon_{vp}^{p+1} = \frac{p+1}{A}\int_0^t g(\sigma)dt \qquad \textbf{Equation 76}$$

or

$$\varepsilon_{vp} = \left(\frac{p+1}{A}\right)^{\frac{1}{p+1}}\left(\int_0^t g(\sigma)dt\right)^{\frac{1}{p+1}} \qquad \textbf{Equation 77}$$

For creep loading conditions where the stress is constant, $g(\sigma)$ is independent of time and Equation 77 becomes:

$$\varepsilon_{vp} = \left(\frac{p+1}{A}\right)^{\frac{1}{p+1}} g(\sigma)^{\frac{1}{p+1}} t^{\frac{1}{p+1}} \qquad \textbf{Equation 78}$$

Assuming a power law of the form $g(\sigma) = B\sigma^{q}$ in which B and q are material constants:

$$\varepsilon_{vp} = \left(\frac{p+1}{A} \right)^{\frac{1}{p+1}} \left(B\sigma^{q} \right)^{\frac{1}{p+1}} t^{\frac{1}{p+1}} \qquad \textbf{Equation 79}$$

or more simply:

$$\varepsilon_{vp} = \left(\frac{p+1}{Y} \right)^{\frac{1}{p+1}} \left(\sigma^{q} \right)^{\frac{1}{p+1}} t^{\frac{1}{p+1}} \qquad \textbf{Equation 80}$$

in which $Y = \frac{A}{B}$ is a material constant.

For cases in which stress is not constant with respect to time, the uniaxial stress loading function is a more generalized $g(\sigma) = B\left[\sigma(t_R)\right]^q$ and Equation 77 becomes:

$$\varepsilon_{vp} = \left(\frac{p+1}{Y} \right)^{\frac{1}{p+1}} \left[\int_0^t \left[\sigma(t)\right]^q dt \right]^{\frac{1}{p+1}} \qquad \textbf{Equation 81}$$

in which p, q and $Y = \frac{A}{B}$ again are material constants.

6.2.2 Uniaxial Viscoplastic Tests and Calibration

Various approaches may be used to calibrate a viscoplastic model. One involves simultaneous calibrating viscoplasticity and damage responses together using appropriate assumptions on each model formulation. The second, followed in this research, relies only on directly observed unrecovered strains from cyclic creep and recovery data. Two series of creep and recovery tests were conducted in uniaxial compression to evaluate the viscoplastic material behavior: constant stress creep and recovery tests at fixed stress level but varying time of loading denoted here as *Fixed Stress* tests (Figure 80a) and constant stress creep and recovery at varying stress levels denoted here as *Fixed Time*

tests (Figure 80b). The length or stress level of each cycle increased exponentially in subsequent pulses to ensure the model would be calibrated over a wide range of stress and load times. The creep aspect of the tests was selected for convenience because stress is constant over time. The cyclic aspect of the tests was not selected for convenience but as a necessity: a rest time is needed after the constant stress impulse to allow the other strain components to recover, leaving only the permanent viscoplastic strain as shown schematically in Figure 81. To ensure accurate measurement of the un-recovered viscoplastic strains the rest times were at least 10 times the length of the constant creep load pulse.

Results from both series of tests are used to determine the material parameters p, q, and Y for the viscoplastic model component given in Equation 81. As described previously in Chapter 5, the results from the Fixed Stress tests were also used to provide confirmation of the validity of time-temperature superposition into the large strain regime and therefore two sets these tests were performed at two different temperatures within each set and where the stress histories within each set were designed to be equivalent in reduced time – 35^{o}C complemented at 25^{o}C and 45^{o}C complemented at 35^{o}C. The increased number of tests has the added benefit of making the calibration of the viscoplasticity model component more robust. The Fixed Time tests were only carried out at one temperature, 35^{o}C, because validation of time temperature superposition was not one of the goals for this test series. Details of the stress histories for each test are summarized in Table 18. A small contact stress was also applied to maintain contact between the actuator and the specimen under nominal zero-stress conditions during the rest periods. Three replicates were tested for each condition.

The calibration procedure started with the total strain histories from each test shown in Figure 82 to Figure 84. The unrecovered strains are of principal interest for calibrating the viscoplastic model. These strains were obtained from the cumulative viscoplastic strain measured at the end of each cycle's recovery.

The most direct method for calibrating the viscoplastic model would be to use the Fixed Stress test data and Equation 80 for the cumulative viscoplastic strain versus cumulative load time plotted as a linear relation in log-log space. However, this ignores the Fixed Time tests. In addition, the Fixed Stress tests did not apply the constant stress instantaneously. A controlled stress ramp-up and ramp-down was used at the beginning and end of each cycle, with the length of each ramp fixed to the length for the first cycle. The ramp-up and ramp-down times for the 10-second Fixed Time cycles was 0.10 seconds. To include this ramp-up/ramp-down effect for the Fixed Stress tests and the results from the Fixed Time tests, all stress histories were simulated numerically using Equation 81 and trial values of the p, q, and Y model constants. Using nonlinear optimization techniques (Solver in MS Excel), optimal values of the p, q, and Y model constants were determined to minimize the least-squares difference between the logarithmic values of the measured and predicted viscoplastic strains. Graphical summaries of the calibration can be found in Figure 85 to Figure 89. The best fit constants are listed in Table 19. The values for the p and q exponents suggest that the viscoplastic strain rate is approximately proportional to stress and approximately inversely proportional to the square of the strain.

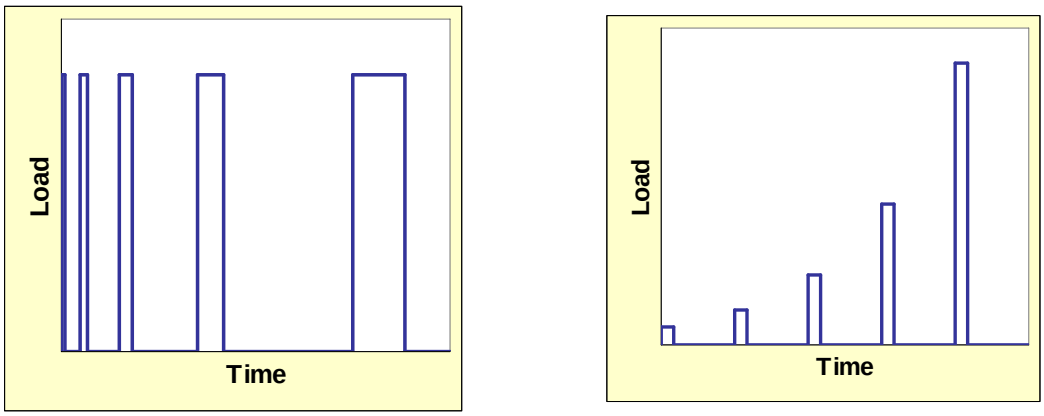

(a) (b)

Figure 80. Schematic of creep and recovery viscoplastic calibration tests.

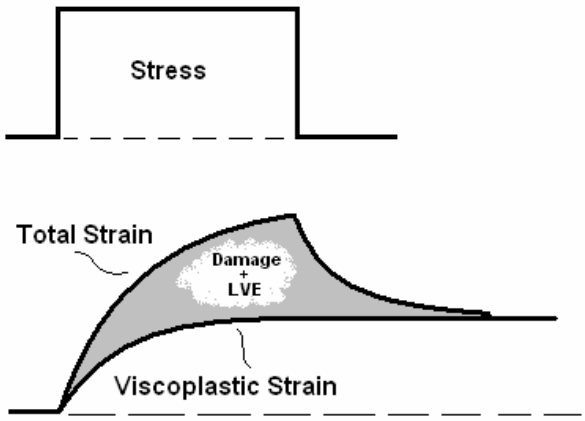

Figure 81. Rest times allow direct determination of un-recovered viscoplastic strain.

Table 18. Programmed stress history targets for viscoplastic cyclic creep and recovery tests.

Cycle	Fixed Stress Load Times (seconds) *Times are un-reduced*				35°C Fixed Time Stress Level @ 10 seconds each (kPa)
	25°C @ 1500 kPa	35°C @ 1500 kPa	35°C @ 963 kPa	45°C @ 963 kPa	
1	0.57	0.04	0.232	0.032	20
2	0.855	0.06	0.464	0.064	35
3	1.78	0.125	0.928	0.128	62
4	3.561	0.25	1.856	0.256	106
5	7.121	0.5	3.713	0.512	179
6	14.243	1	7.317	1.009	303
7	28.486	2	14.634	2.018	495
8	56.972	4	29.304	4.041	818
9	113.944	8	58.536	8.072	1354

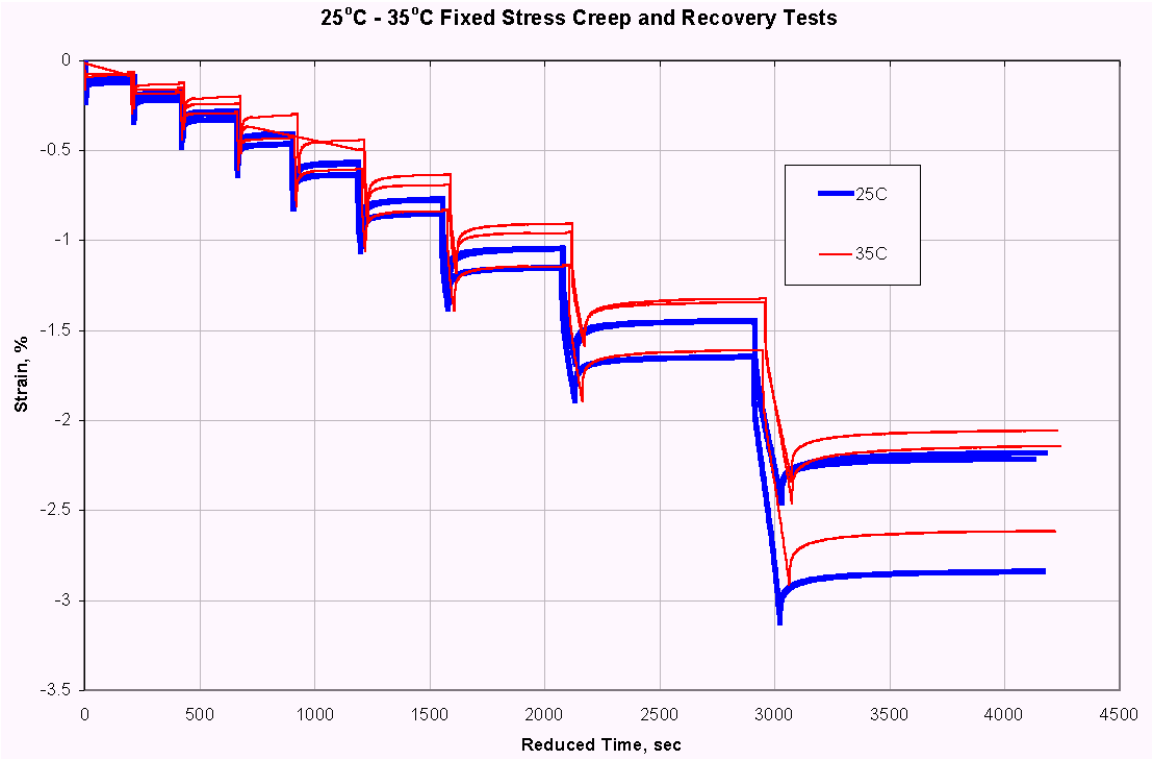

Figure 82. Measured total strain history from 25°C/35°C Fixed Stress tests.

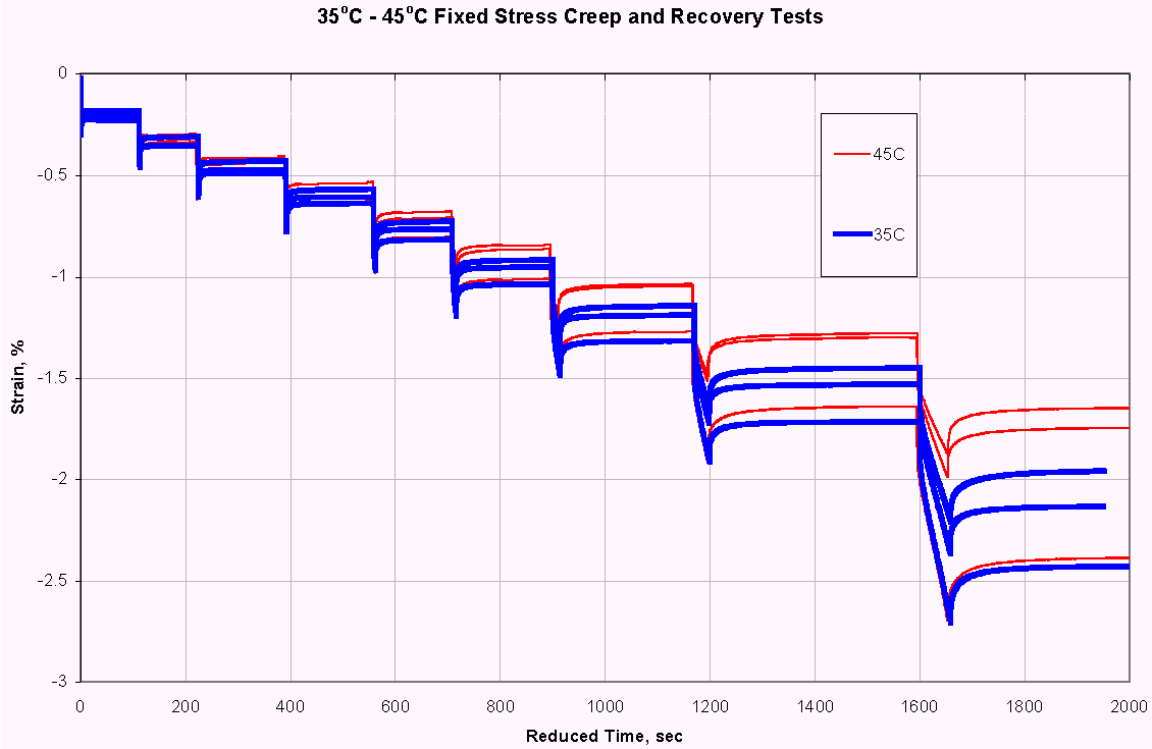

Figure 83. Measured total strain history from 35°C/45°C Fixed Stress tests.

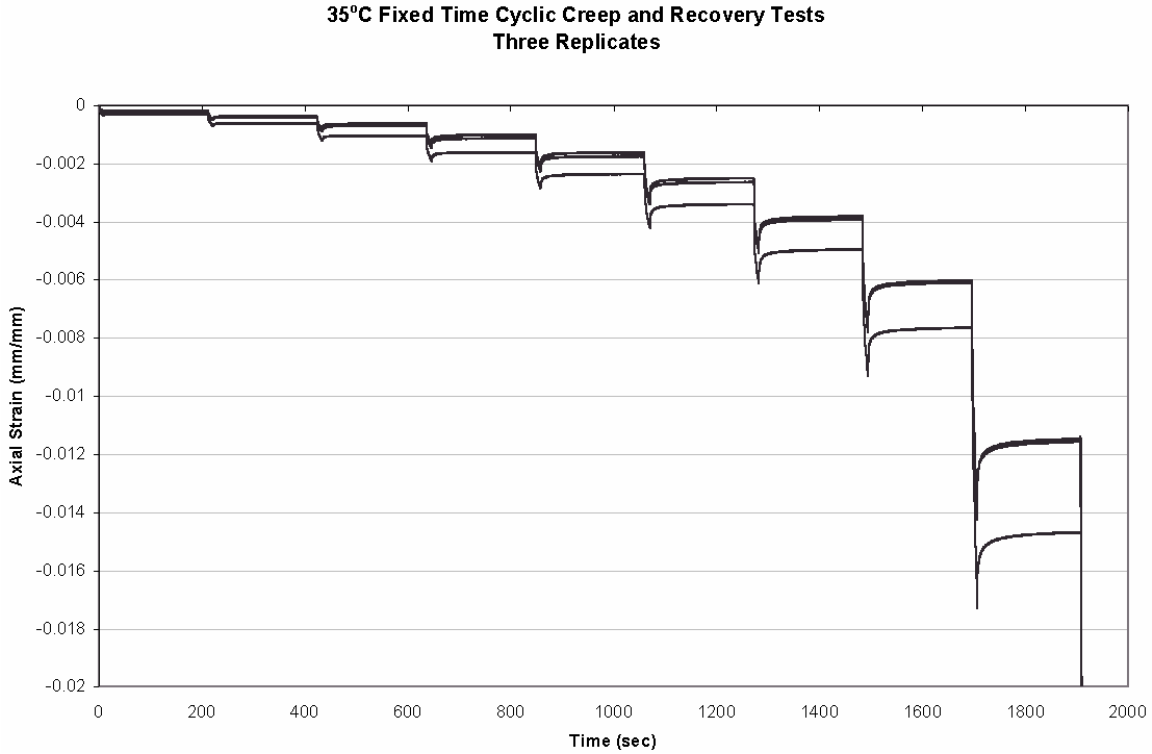

Figure 84. Measured total strain history from 35°C Fixed Time tests.

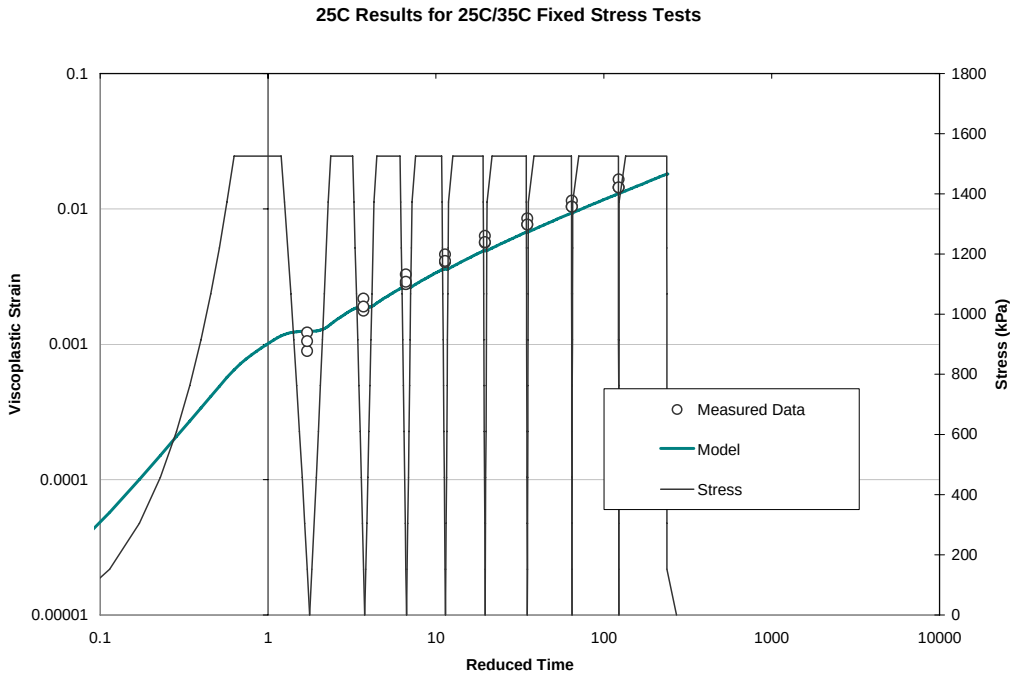

Figure 85. Viscoplastic model calibration with 25°C data from 25°C/35°C Fixed Stress test data.

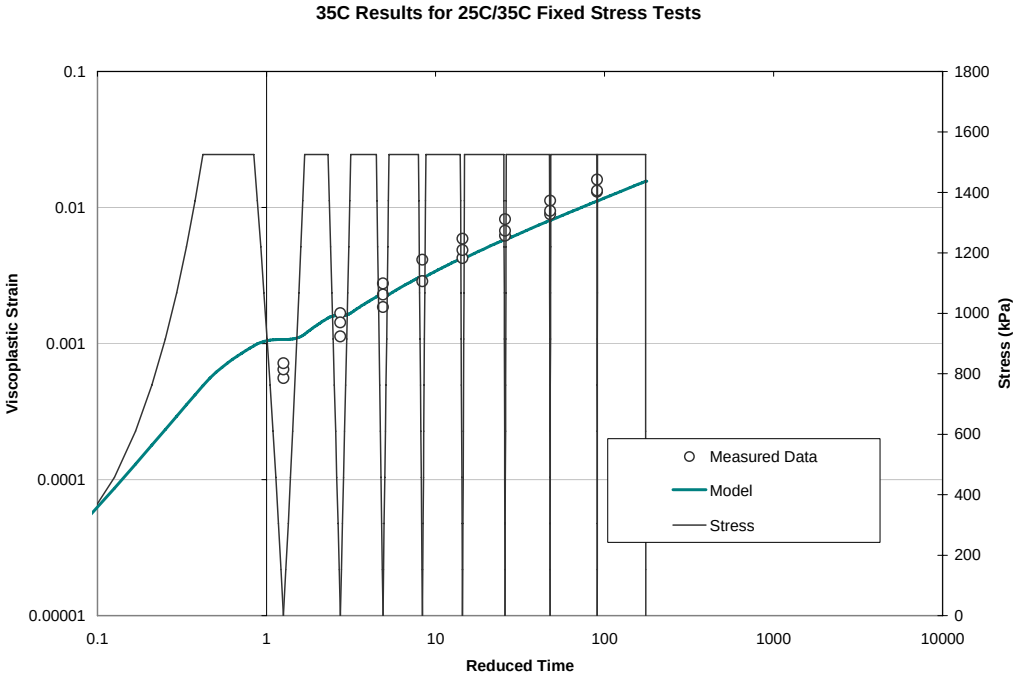

Figure 86. Viscoplastic model calibration with 35°C data from 25°C/35°C Fixed Stress test data.

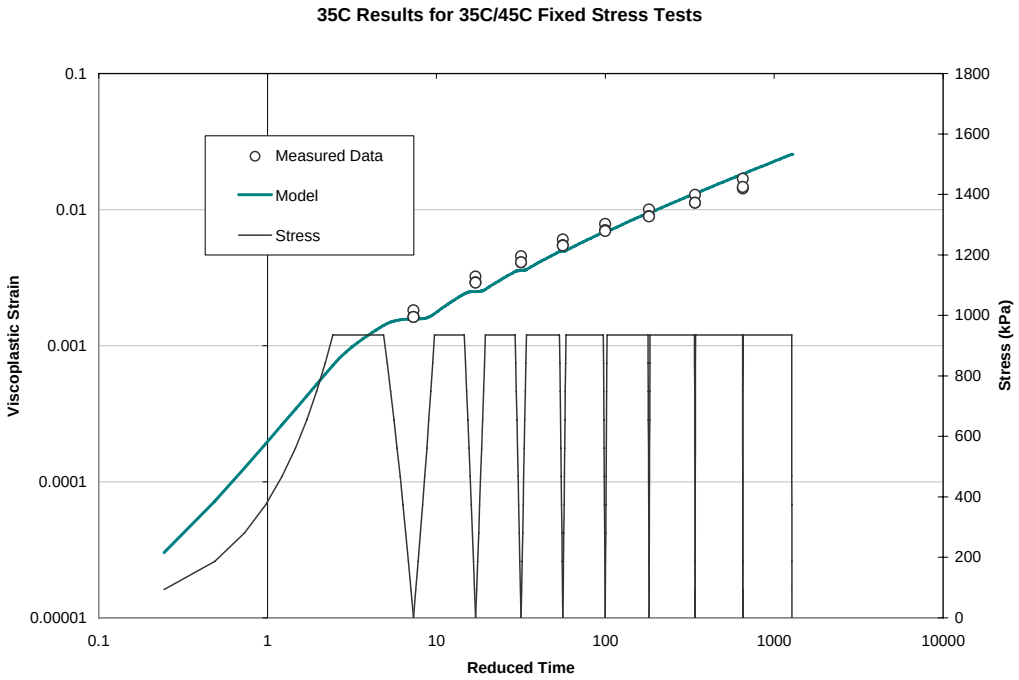

Figure 87. Viscoplastic model calibration with 35°C data from 35°C/45°C Fixed Stress test data.

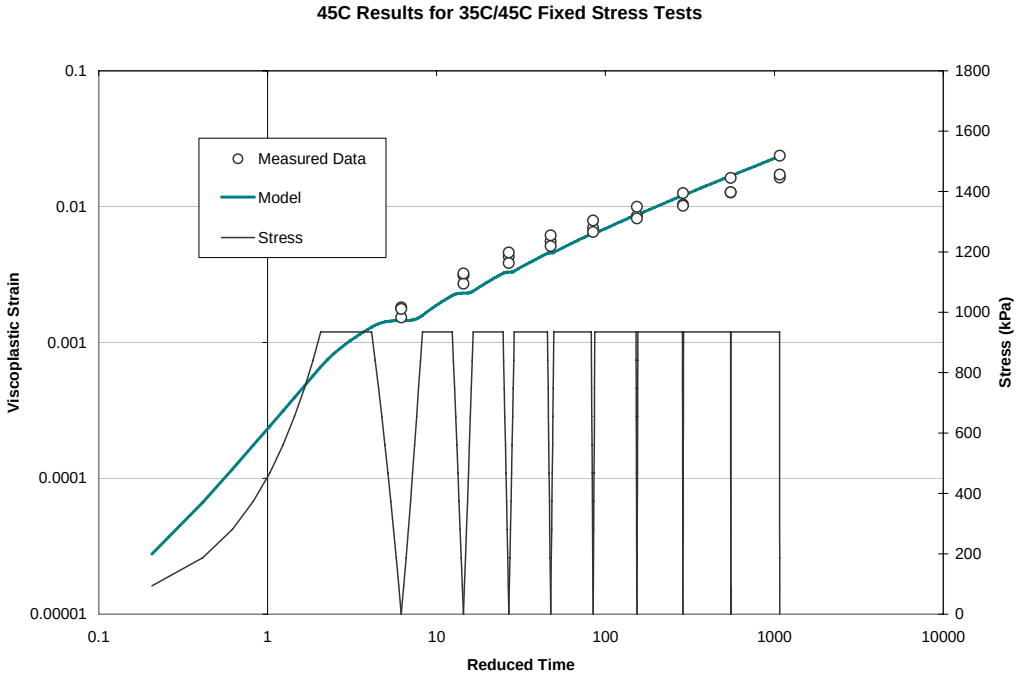

Figure 88. Viscoplastic model calibration with 45°C data from 35°C/45°C Fixed Stress test data.

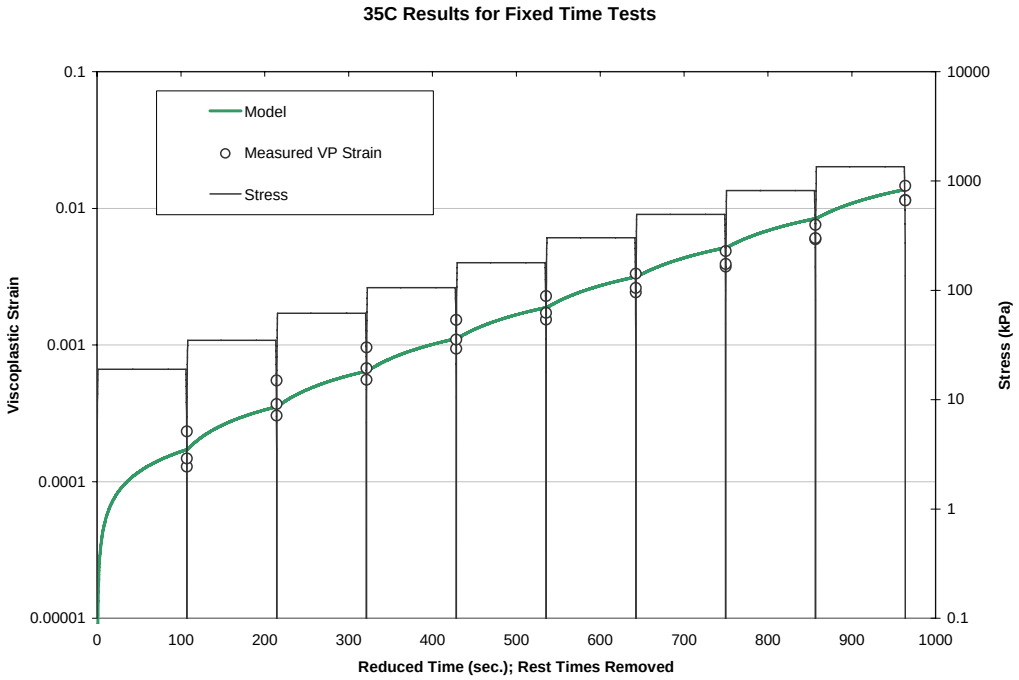

Figure 89. Viscoplastic model calibration with 35°C data from Fixed Time test data.

Table 19. Calibrated uniaxial viscoplastic model constants (stress in kPa, strain in mm/mm).

$\frac{d\varepsilon_{VP}}{dt_R} = \frac{1}{Y}\frac{\sigma^q}{\varepsilon_{vp}^p}$	
p	2.074
q	1.122
$\log Y$	12.982

6.3 Viscoplasticity under Confined Conditions

A universal viscoplastic model must have the ability to predict strain induced by multidimensional stress states. Deviatoric and hydrostatic triaxial compression viscoplastic tests were performed to quantify the effect of confining stress on the viscoplastic response of asphalt concrete.

6.3.1 General triaxial compression Tests

Cyclic triaxial compression tests at confining pressures of 250 and 500 kPa were performed to evaluate the effects of confinement on viscoplastic behavior. Only one temperature, 35^{o}C, was investigated; uniaxial tests had already shown that viscoplasticity is significant at this temperature.

Confining pressure was applied using air as the confining fluid. The maximum pressure for the UMD testing system is limited by the 'house' air supply of about 700 kPa (100 psi). The dynamic response of the pneumatic confinement system is relatively slow and requires a controlled ramp-up and ramp-down during pressurization and depressurization. Use of an incompressible fluid to apply confinement would enable faster loading and unloading rates, but this was beyond the capabilities of the UMD testing equipment. Exploratory tests determined that the quickest controllable pressurization time was about two minutes.

Before any deviatoric loads were applied, the hydrostatic stress was maintained to consolidate the material to a practical equilibrium. This was found to take about 30 minutes at 35^{o}C. After this point, the deviatoric stresses were applied. The deviatoric stress histories in the confined tests were identical to those in the unconfined cyclic creep and recovery tests. This permits direct comparison the induced strain response between unconfined and confined conditions. Figure 90 summarizes these concepts. After several confined tests were completed, it was observed that the variability between replicates was significantly decreased by the confining stress. Consequently, the third replicate was omitted for the later tests in the series.

Figure 91 shows typical results from one of the two confined Fixed Stress test replicates at the intermediate 250 kPa level of confinement. The axial and radial strain rates decrease during the consolidation period, eventually reaching a satisfactory steady state. The radial strains are slightly larger than the axial strains. The volumetric strains are computed from the measured strains as:

$$\varepsilon_{Vol} = \varepsilon_{Axial} + 2\varepsilon_{Radial} \qquad \textbf{Equation 82}$$

in which negative axial and radial strains correspond to a decrease in axial height and decrease in specimen diameter with corresponding effects on volumetric strain. Once the deviatoric loads begin the axial strain always decreases and the radial strain always increases as expected. The volumetric viscoplastic behavior was not isochoric (i.e., constant volume). The volumetric strain decreases (i.e., compression) during the early part of the deviatoric loading regime followed by increases (i.e., dilation) as loading proceeds further. Figure 92 shows similar results from the confined Fixed Stress test at 500 kPa of confinement. The total radial strains under hydrostatic stresses at this level of confinement are about twice as large as the axial strains, suggesting some initial anisotropy in this specimen. The volumetric strain from the consolidation period is about twice as large as in the 250 kPa case, suggesting some degree of linearity in the total strain consolidation response under hydrostatic stress. The volumetric strain during the deviatoric loading regime always decreases. No dilation was observed at the 500 kPa confining pressure, either because the deviatoric stresses were too small and or they were not applied long enough.

Typical results from a Fixed Time test at 250 and 500 kPa of confinement are shown in Figure 93 and Figure 94, respectively. The behavior in the Fixed Time tests was

similar to that observed under the Fixed Stress loading. The volumetric strain decreases (compression) and then increases (dilation) at 250 kPa, but at 500 kPa it barely goes into dilation because the stress history was not long or large enough. Again, there is some evidence of potential anisotropy, particularly for the 500 kPa specimen.

The volumetric strain responses from the unconfined Fixed Stress and Fixed Time tests are shown for comparison in Figure 95 and Figure 96**,** respectively. The data suggest that dilation occurs sooner at lower levels of confining stress. The unconfined Fixed Time tests (Figure 96) did not show any of the volumetric compression observed in the unconfined Fixed Stress tests and all of the confined tests. This was consistent for the other two replicates as well.

The unconfined and confined 'post-consolidation' axial viscoplastic strains were compared to investigate the relative effects of confinement on viscoplasticity. These viscoplastic strains were determined from the nonrecoverable strains at the end of the rest period before the start of the next load cycle. The results from the Fixed Stress tests are plotted against the cumulative amount of deviatoric load time in Figure 97. The magnitudes of the deviatoric stresses are slightly different between the unconfined and confined conditions because of testing difficulties. Nevertheless, it is clear from the figure that the effect of confinement is to significantly suppress the viscoplastic strain magnitude. In the early response at very short reduced times the suppression effect is less, but the divergence between the unconfined and confined results grows as the load duration increases, suggesting that confinement increases the strain hardening behavior. This is also shown in the more concave downward response curve for the confined test results. A hint of a slight bilinear or curvilinear response is seen as well. These results

suggest that the primary hardening region under confinement occurs over a larger range of time and strain than under the unconfined conditions. A single high confinement Fixed Stress replicate at a very large fixed stress from a preliminary shakedown test is included as well to demonstrate that confinement will not arrest tertiary flow at high deviatoric stress levels.

A similar comparison plot for the Fixed Time tests is given in Figure 98. It is less informative to plot viscoplastic strain vs. cumulative deviatoric load time as done for the Fixed Stress tests because of the different deviatoric stress magnitudes applied during the Fixed Time loading history. Instead, the confined and unconfined test results may be plotted as a function of the deviatoric stress level since the duration of each load cycle is the same. At small deviatoric stress levels, the viscoplasticity is suppressed by up to an order of magnitude. The divergence between the confined and unconfined cases then decreases at higher deviatoric stress levels, which is physically plausible.

To get a numerical insight as to how confining pressure affects the viscoplastic strain rate in terms of the stress and strain power law functions, the unconfined viscoplasticity model was fit to the confined creep and recovery test results to see which model parameters changed significantly and by how much. The model parameters as calibrated against the unconfined and confined test results are compared in Table 20. It is clear from these results that confinement affects all three model parameters, but the effect is most pronounced on the scaling constant term $\log Y$ and the stress exponent q. The increase in $\log Y$ is intuitively expected, since this corresponds to a reduction in viscoplastic strain rate as confining stress increases. The increase in q and the decrease in p corresponds to a counterintuitive increase in viscoplastic strain rate with increasing

confinement; however, this may be an artifact of a 'linear' power law formulation of the nonlinear hardening response. This issue is revisited in Chapter 8 in the context of model validation.

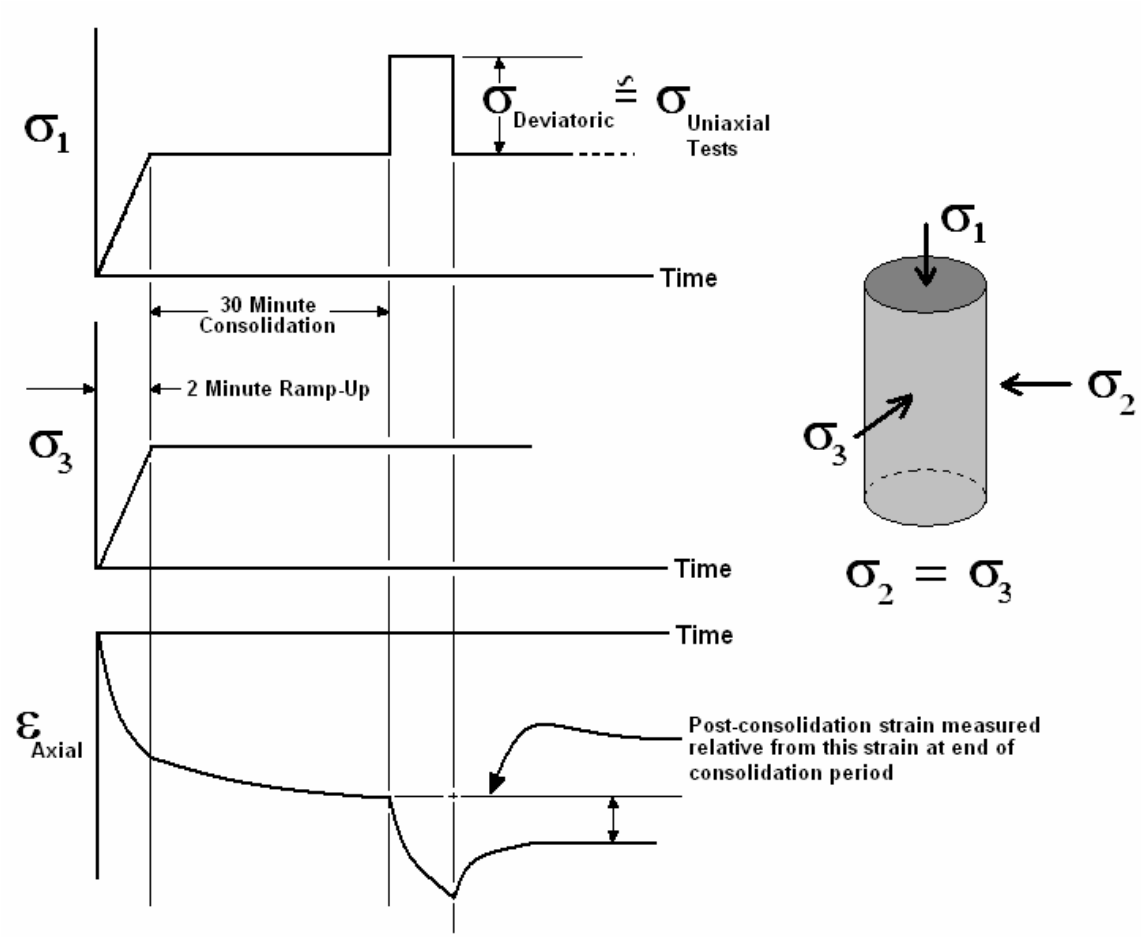

Figure 90. Schematic of confined viscoplastic test approach.

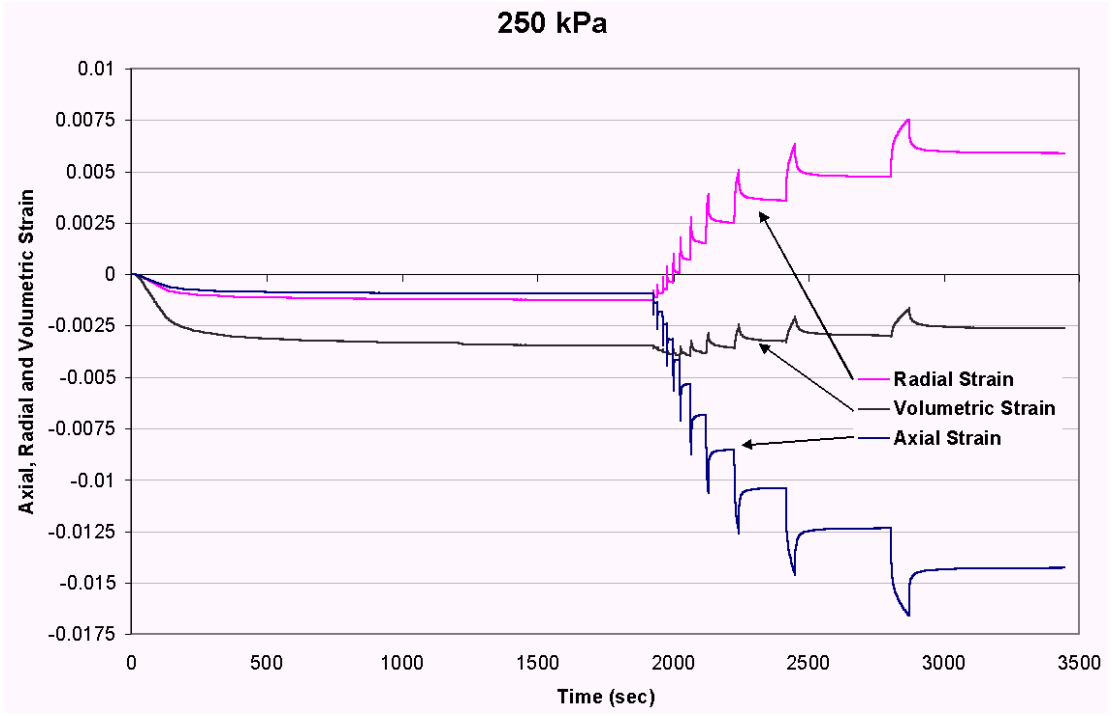

Figure 91. Axial, radial & volumetric response under confined Fixed Stress tests at 250 kPa.

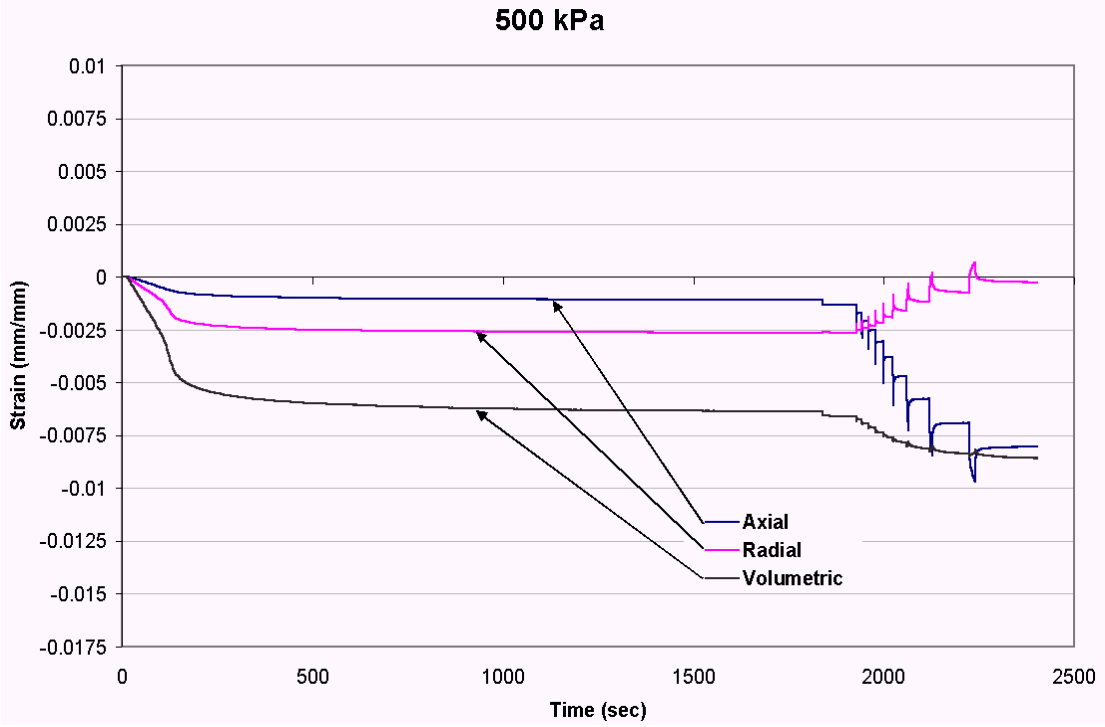

Figure 92. Axial, radial & volumetric response under confined Fixed Stress tests at 500 kPa.

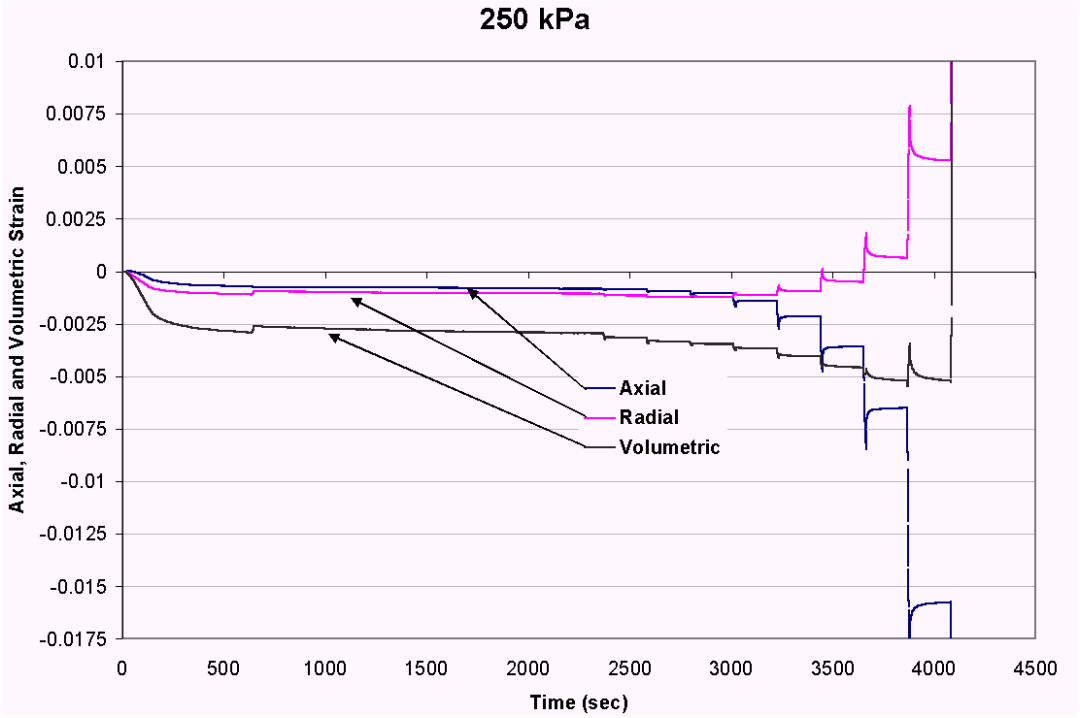

Figure 93. Axial, radial & volumetric response under confined Fixed Time tests at 250 kPa.

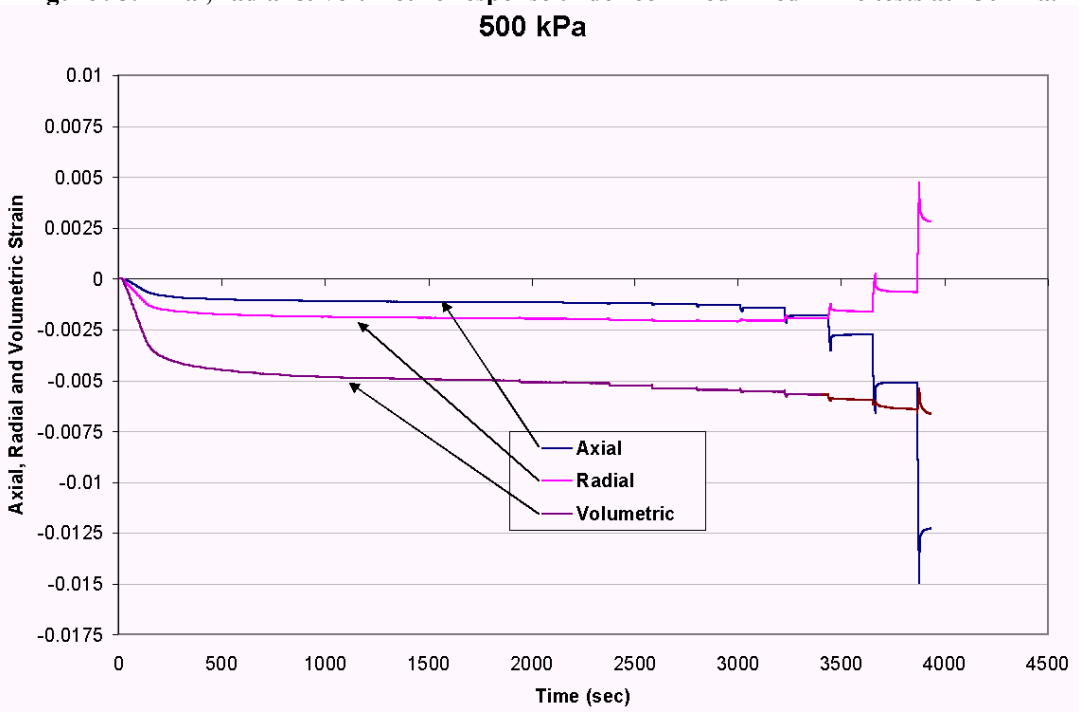

Figure 94. Axial, radial & volumetric response under confined Fixed Time tests at 500 kPa.

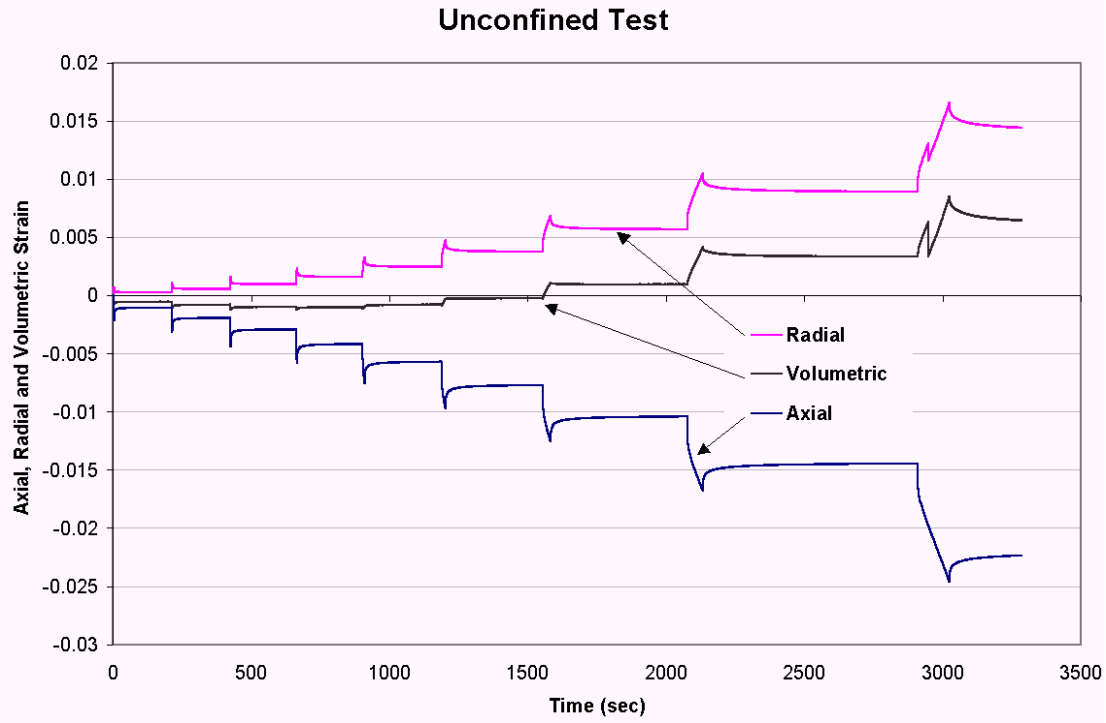

Figure 95. Axial, radial & volumetric response under uniaxial Fixed Stress tests.

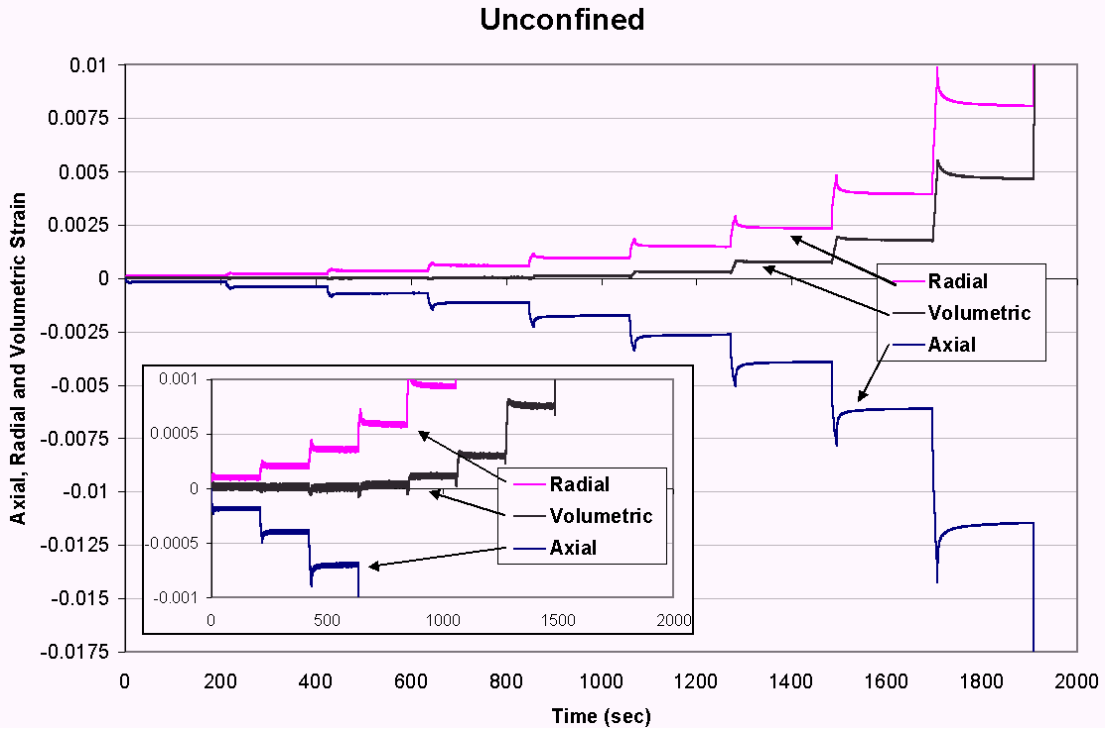

Figure 96. Axial, radial & volumetric response under uniaxial Fixed Time tests.

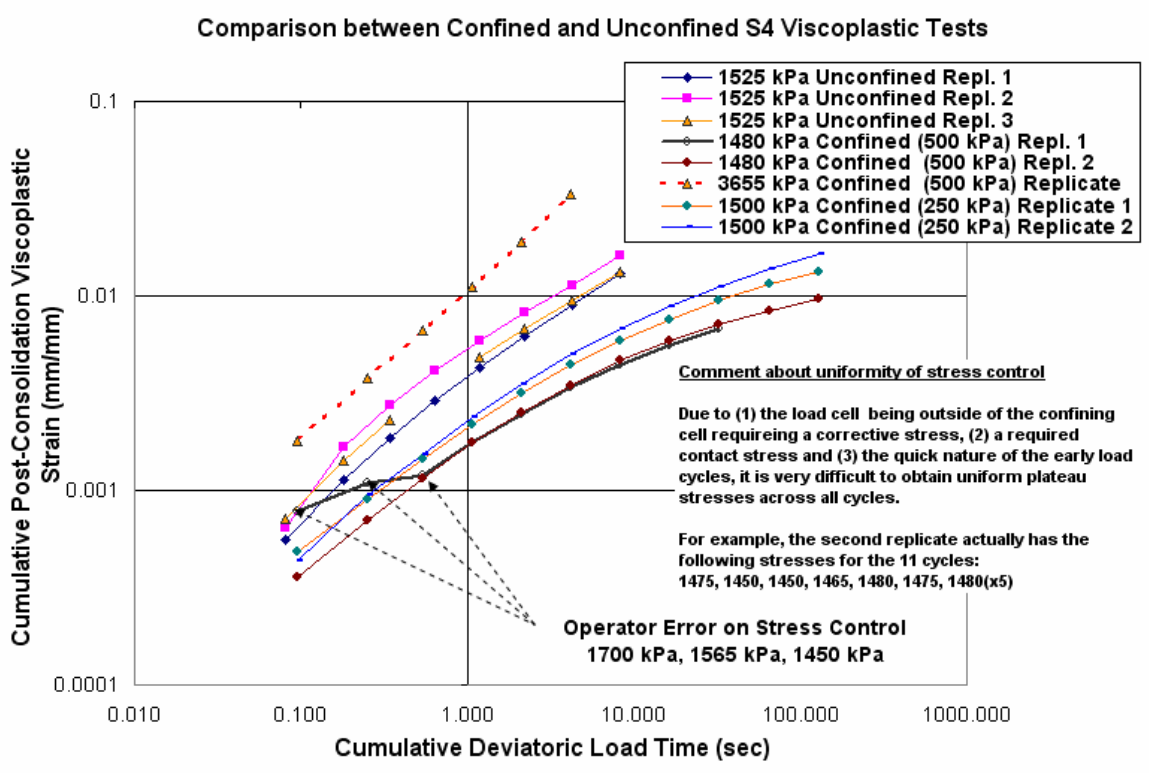

Figure 97. Comparison of unconfined and confined Fixed Stress test results.

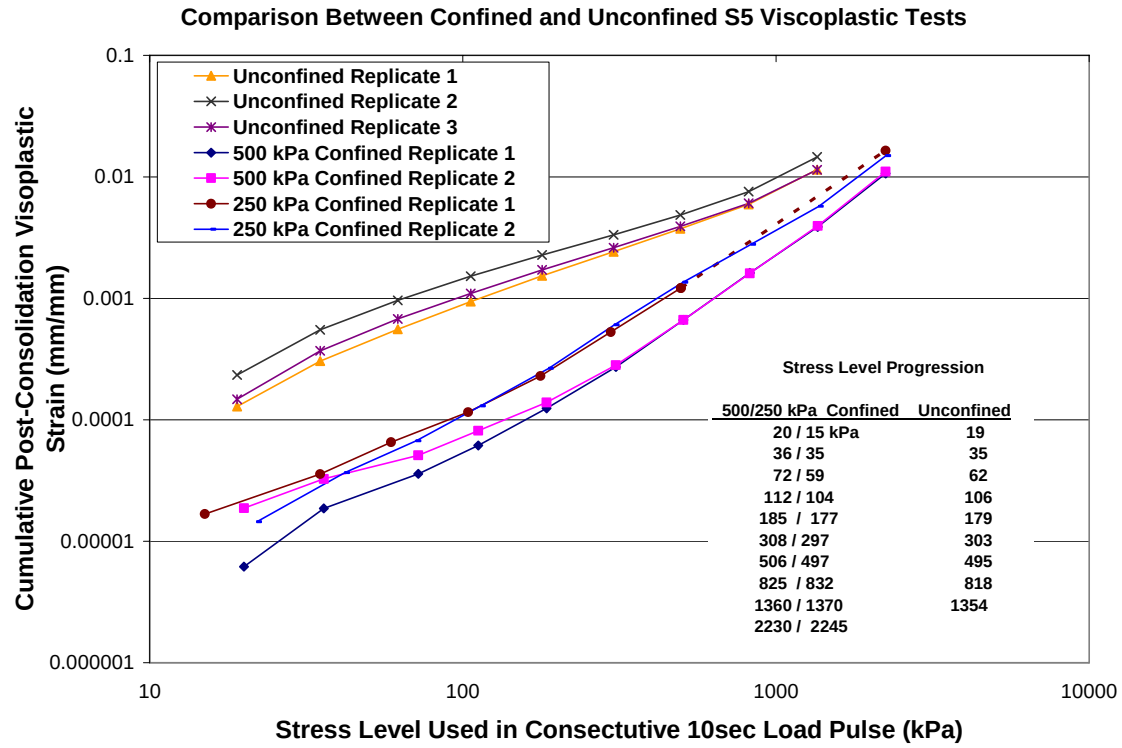

Figure 98. Comparison of unconfined and confined Fixed Time test results.

Table 20. Comparison of conventional uniaxial model parameters at different levels of confinement

Model Parameter	Unconfined	250 kPa Confined	500 kPa Confined
p	2.074	1.23	1.58
q	1.122	3.15	3.82
$\log Y$	12.982	17.40	20.70

6.3.2 Hydrostatic Creep and Recovery Tests

Hydrostatic creep and recovery tests were performed to assess viscoplastic strain induced from pure volumetric stresses. These tests will also give critical information regarding necessary capabilities of multiaxial models. The previous tests could not be used to assess this response because a volumetric depressurization is required in order to measure directly any viscoplastic volumetric strains. Two replicates at 35^{o}C and 250kPa were tested with a controlled ramp-up to a sustained hydrostatic creep cycle lasting 30 minutes followed by a ramp-down and a 45 minute recovery. This cycle was repeated for a second time and ended for a total creep time of about one hour. This length of time is approximates the duration of the longest confined viscoplastic test enabling a more complete picture of the total viscoplastic response.

The temperature of the cell air was monitored during filling and emptying of the confining cell to assess if significant temperature changes were occurring that might affect the response. The temperature at the center of the specimen was not observed, but shakedown tests indicate that there is a significant lag and difference in magnitude between changes in the peak cell air and center of specimen temperatures. Based on the

measurements illustrated in Figure 99, it was concluded that effect of any fluctuations in cell air temperature should be negligible because the air temperature change was relatively quick and only fluctuated about +/-2^{o}C about the mean temperature. The air temperature approaches equilibrium quickly once the air pressure reaches static pressurized or depressurized conditions.

Close attention was also paid to the individual LVDT readings during each test. Figure 100 and Figure 101 show the typical measured axial and radial deformations respectively, with positive deformations corresponding to tensile strains. With the exception of the top axial displacement signal in the beginning, the response is appropriate. The top LVDT signal shows axial extension during application of the hydrostatic pressure while the other three axial LVDTs behave as expected. The individual radial strain signals also exhibit erratic behavior, with one showing radial expansion and the other three showing varying degrees of radial compression under the hydrostatic loading. These variations in individual LVDT readings could be justified under deviatoric loading as the consequence of rigid body motion and/or specimen bending, but this argument is more difficult to make for hydrostatic loading. One possible explanation for this measured behavior is local variations in stiffness causing local variations in strain on the specimen.

Despite the erratic behavior of the individual LVDT signals, the averaged signal does behave ideally and smoothly, as shown in Figure 102 and Figure 103 for both replicates. Axial strains appear to be fully recoverable while radial strains show larger unrecoverable deformations that take place primarily under the very early initial loading.

The permanent volumetric strain is attributable to this radial deformation behavior with negligible contributions from the axial behavior.

The total volumetric strains measured in the 250 kPa confined Fixed Time and Fixed Stress tests replicates at the end of the 30-minute consolidation were 0.0035, 0.0041, 0.0029, 0.0029 with a mean of 0.00335 and standard deviation of 0.00057. The total volumetric strains, 0.0036 and 0.0038, measured in the hydrostatic tests at end of the first of two 30-minute consolidation periods are reasonable and within the mean plus one standard deviation from the Fixed Time and Fixed Stress tests. Thus, the viscoplastic component of the volumetric, axial and radial strain in the hydrostatic tests can be used to estimate the unrecovered quantities in the Fixed Time and Fixed Stress counterparts conducted at the same confinement and temperature where the confining stress was not removed before applying the deviatoric load. The axial consolidation strains in the confined Fixed Time and Fixed Stress tests should be fully recoverable because the axial strains in the hydrostatic tests were found to be fully recoverable. This in turn means that the unconfined axial viscoplastic strains and post-consolidation axial viscoplastic strains in Figure 97 and Figure 98 are directly comparable. However, anisotropy of the material as expressed in the unrecoverable radial strains—and thus the unrecoverable volumetric strains—should not be overlooked. The volumetric viscoplastic stain at the end of 30 minute 250 kPa hydrostatic stress is about 0.00165 or 80% of that at the end of the second 30 minute (total 60 minute) load cycle. This means during the deviatoric loading portion of the confined Fixed Time and Fixed Stress tests that the radial viscoplastic strains have not fully arrested, but are very close, specifically for this temperature and confining stress magnitude. The continued consolidation in the axial and radial directions

was extrapolated and removed so as not to influence the unrecovered strains caused by the deviator stress and not the hydrostatic stress.

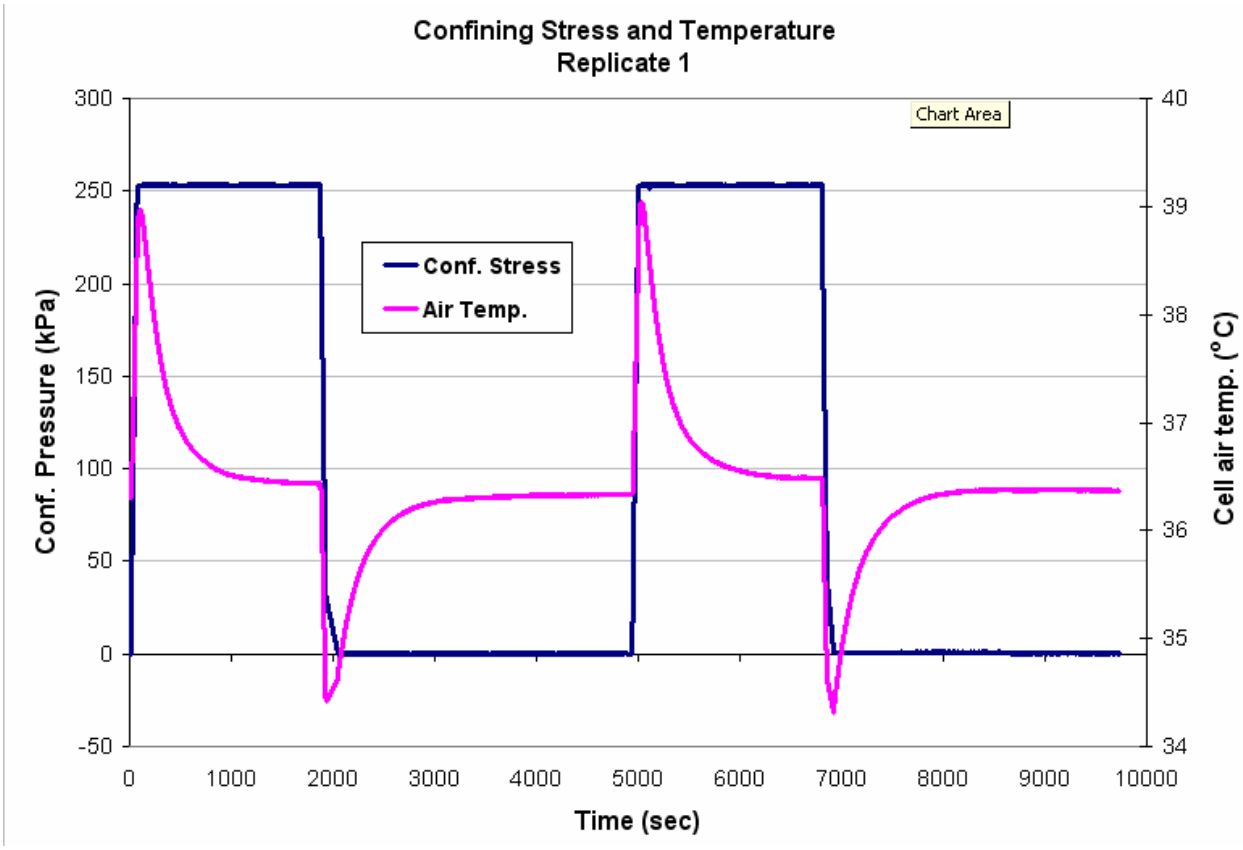

Figure 99. Variation in temperature during pressurization and depressurization.

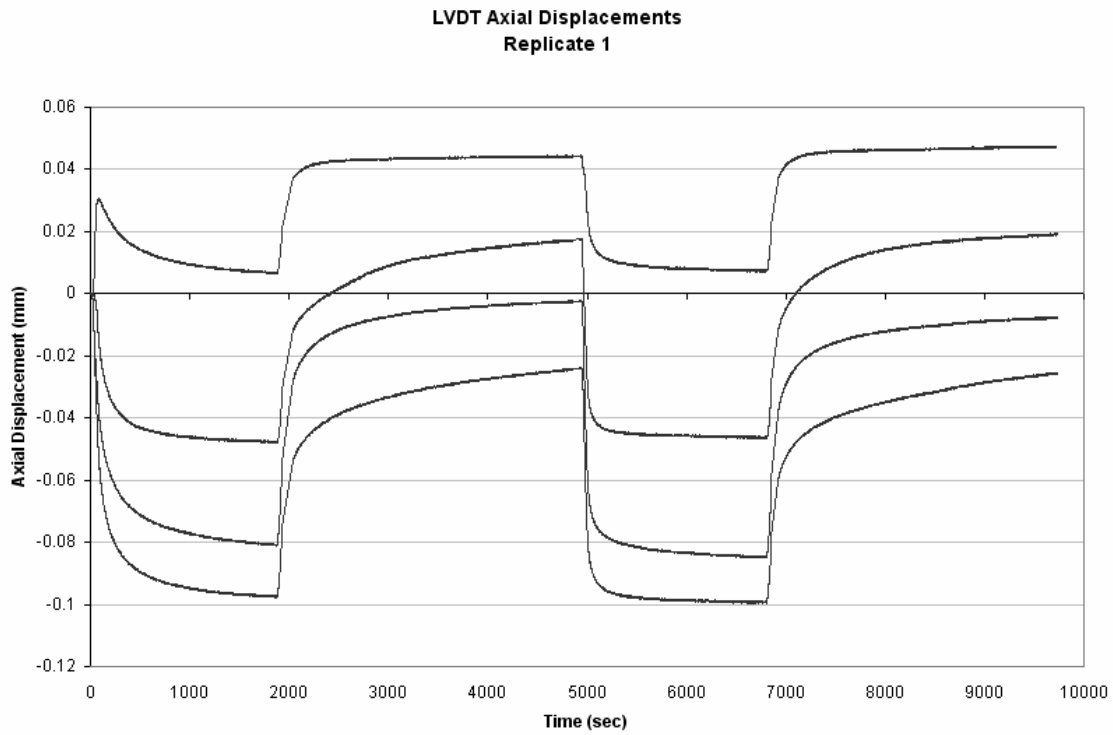

Figure 100. Typical individual axial LVDT response under consolidation.

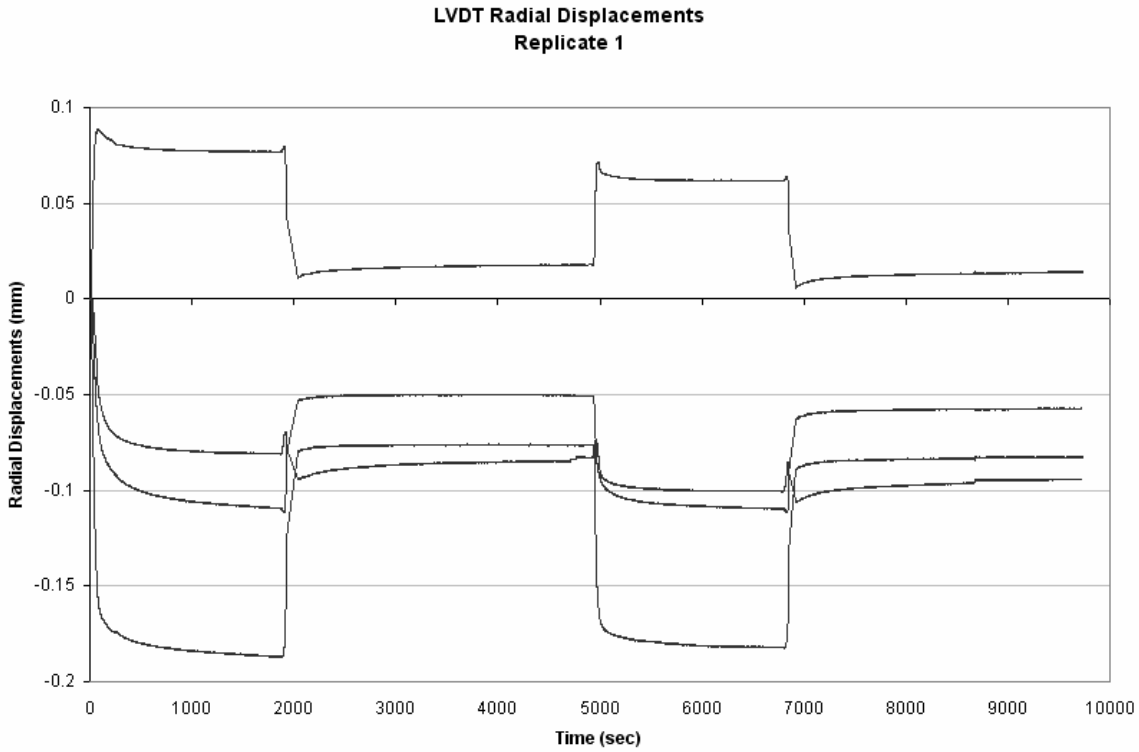

Figure 101. Typical individual radial LVDT response under consolidation.

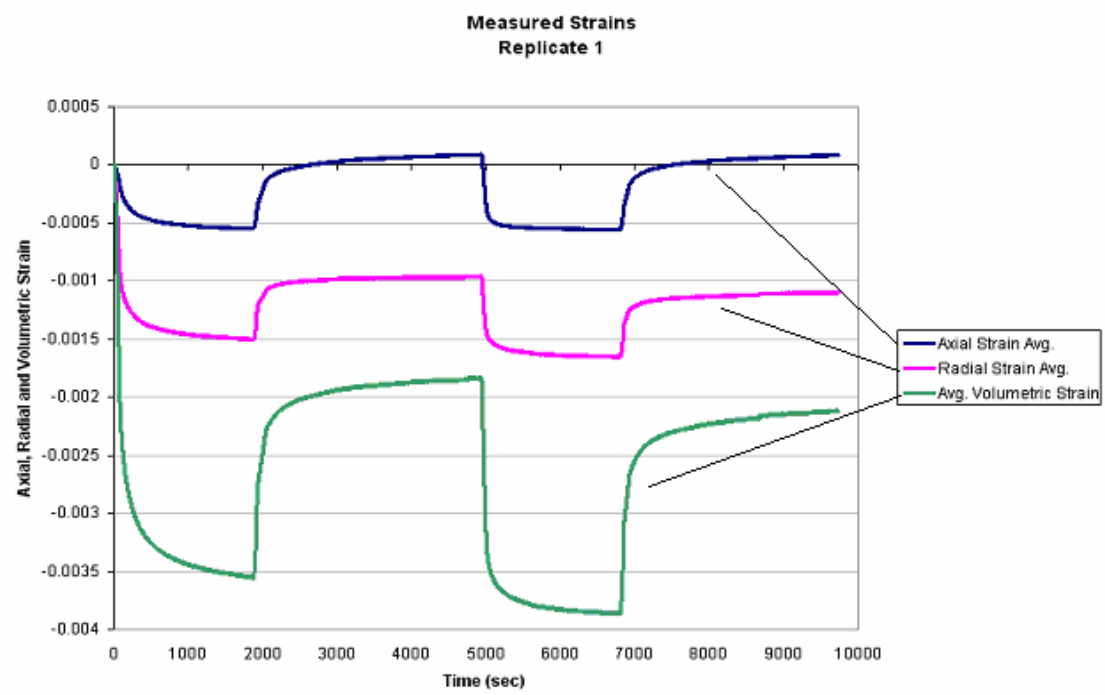

Figure 102. Replicate-1 average axial, radial and volumetric response under consolidation.

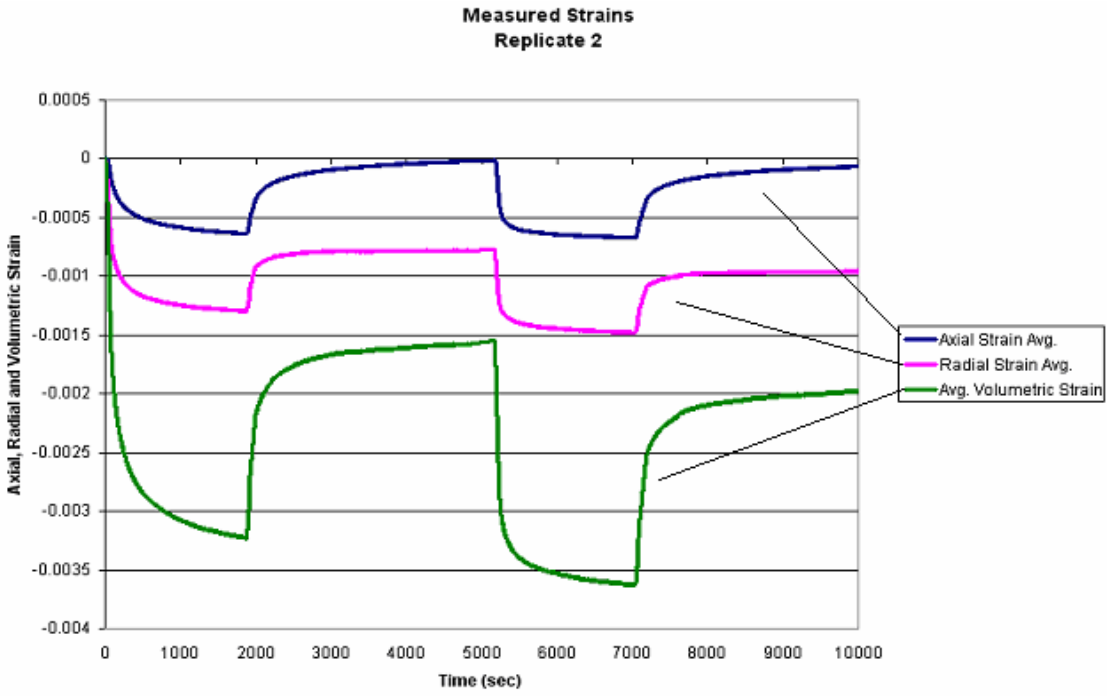

Figure 103. Replicate-2 average axial, radial and volumetric response under consolidation.

6.4 Summary and Conclusions

The experiments, analyses and model calibration in this portion of the study evaluated a variety of the compressive aspects of viscoplasticity in asphalt concrete. The time-temperature superposition principle was shown to be valid for large strains including the viscoplastic response (Chapter 5). This principle was used to calibrate the uniaxial strain hardening viscoplastic strain rate model. The behavior under Fixed Stress and Fixed Time cyclic creep loadings–two very different types of stress histories–were fit well by the calibrated model.

Viscoplasticity, like elasticity or any other material property, is truly a function of the three dimensional general state of stress and more than just uniaxial conditions. The effect of lateral confinement on measured viscoplastic response was quantified in a systematic manner with the same deviator stresses under different confining stresses. Confined viscoplastic tests were carried out to determine changes in behavior caused by confining stress. Confinement was found to significantly suppress viscoplastic strains, increase the hardening response, and extend the primary hardening region over a larger range of strains. Some viscoplastic anisotropy was evident under pure hydrostatic loading, with complete recovery of axial strains and unrecoverable radial viscoplastic strains.

These are all very important topics because the response can be complex due the aggregate movement and internal friction that develops. A data set is offered which is sufficiently comprehensive to calibrate a model more advanced and capable than the

uniaxial model. This calibration and validation is ultimately found in Chapter 9 motivated by some poor validation findings in Chapter 8 justified the extra efforts.

7. Damage Characterization

7.1 Introduction

The theoretical context for the damage model in this research is the Schapery continuum damage model (Park and Schapery, 1997; Ha and Schapery, 1998). Key conceptual components of this model include the use of elastic-viscoelastic correspondence principles, reduced time, and microstructural damage functions based on a thermodynamics formulation and expressed in terms of rate-dependent internal state variables. A simplified form of the basic Schapery continuum damage model has been applied in the past to asphalt concrete under cyclic and monotonic tension at moderate temperatures by Park et al. (1996) and Lee and Kim (1998a, 1998b). Damage behavior under compression is the focus of the present work.

Strain decomposition allows damage to be isolated conceptually as $\varepsilon_{Damage} + \varepsilon_{Linear\ \ Viscoelastic} = \varepsilon_{Total} - \varepsilon_{Viscoplastic}$. Calibration of the linear viscoelastic relaxation

modulus and temperature shift factors have already been described in Chapter 4, and calibration of the viscoplasticity model component has been described in Chapter 6. The findings from the large strain time-temperature superposition study (Chapter 5) validate the use of reduced time computed using temperature shift function to evaluate damage strains at varying temperatures.

7.2 Uniaxial Formulation

Key aspects of the viscoplasticity model form given in Chapter 2 are repeated here for convenience. The Schapery-based damage model is in actuality a nonlinear viscoelastic formulation with fully recoverable strains computed according to linear viscoelastic principles. Viscoelastic effects are taken into account in the damage model via the elastic-viscoelastic correspondence principle to remove time as an explicit variable. Pseudo strain ε^R is computed from the viscoelastic response via a convolution integral:

$$\varepsilon^R = \frac{1}{E_R}\int_0^{t_R} E(t_R - t'_R)\frac{\partial \varepsilon}{\partial t'_R}dt'_R \qquad \textbf{Equation 83}$$

in which $E(t_R)$ is the relaxation modulus master curve, E_R is an arbitrary reference modulus, and t_R is reduced time. Stress is then related to pseudo-strain via familiar stress strain expressions. For the simplest case of uniaxial loading:

$$\sigma = E_R \varepsilon^R \qquad \textbf{Equation 84}$$

in which σ is the uniaxial stress. Damage is incorporated by replacing the reference modulus E_R with a damage function $C(S)$ that is dependent upon an internal state variable S:

$$\sigma = C(S)\varepsilon^R \qquad \textbf{Equation 85}$$

The damage function $C(S)$ represents the degree of damage in the material. When the reference modulus is taken as unity for simplicity, $C(S)$ ranges between 1 for intact material to 0 for a completely damaged material.

A damage evolution law governs development of the damage internal state variable S :

$$\dot{S} = \frac{\partial S}{\partial t_R} = \left(-\frac{\partial W^R}{\partial S} \right)^{\alpha} \qquad \textbf{Equation 86}$$

in which W^R is the strain energy density based on the pseudo strain (i.e., the pseudo strain energy density):

$$W^R = \frac{1}{2} C(S) \left(\varepsilon^R \right)^2 \qquad \textbf{Equation 87}$$

The stress-strain relationship in Equation 85 can also be described in terms of the pseudo strain energy density using the standard definition:

$$\sigma \equiv \frac{\partial W^R}{\partial \varepsilon^R} = C(S)\varepsilon^R \qquad \textbf{Equation 88}$$

7.3 Uniaxial Calibration

The damage function $C(S)$ has been successfully found in the past using data from constant strain rate tests to failure (Lee and Kim, 1998a; 1998b). Cyclic tests can also be employed to determine $C(S)$. The constant strain rate testing approach[4] was used in the

[4] "Constant strain rate" is perhaps a misnomer. "Constant displacement rate" is perhaps more correct, as the actuator displacement rate was the controlled loading parameter in these tests. Because of start-up inertia

present study, using the 5°C tests from the large-strain time-temperature superposition validation study described in Chapter 5.

The low temperature of 5°C was selected to minimize viscoplasticity influences. The testing machine only had sufficient strength to fail the specimens at the slowest target nominal strain rate of 0.0005 ε/second. The machine load capacity was reached before failure at the next fastest target strain rate of 0.0015 ε/second. Faster rates were attempted until a catastrophic failure of one of the specimens damaged some of the equipment and instrumentation. Strain versus time and stress versus strain plots from the successful tests are shown in Figure 104 and Figure 105.

To ensure accurate calibration of the damage model, viscoplastic strains were removed using the calibrated viscoplasticity model (Chapter 6). The viscoplastic strain model was first applied to the prediction of the viscoplastic responses induced during the frequency sweep testing that took place before the monotonic loading to failure. The mean measured viscoplastic strain after the dynamic modulus tests was about 308$\mu\varepsilon$ as determined from the average of four LVDT readings 30 minutes after the frequency sweep test ended but before the start of the constant strain rate loading. The predicted strain from the viscoplasticity model was 573$\mu\varepsilon$. It may be hypothesized that the predicted viscoplastic strains are larger than the measured values because the 30 minute rest time after the frequency sweep was insufficient to achieve full recovery of the viscoelastic strain. However, both the measured and predicted viscoplastic strains are very small in absolute terms at the 5°C damage model calibration temperature (which is

---

and compliance in the loading system, constant actuator displacement rate does not translate to truly constant strain rate in the specimen, as described previously in Chapter 5.

to be expected, given the small stress and strain loading in the frequency sweep test) and substantially smaller than the strain magnitudes achieved in the constant strain rate to failure loading that followed. The model was then applied to the prediction of the viscoplastic strains induced during the constant strain rate tests. An example of the predicted viscoplastic strains for a constant strain rate test at 5°C is shown in Figure 106.

The elastic viscoelastic correspondence principle in Equation 83 was used to compute the pseudo strains from the measured physical strain vs. time history. The ratio between the pseudo strain and the measured stress yields the damage function values $C(S)$ at distinct points j in time (for a reference modulus E_R=1):

$$C(S)\Big|_j = \frac{\sigma_j}{\varepsilon_j^R} \qquad \textbf{Equation 89}$$

Although $C(S)$ can be directly determined from the test measurements using this method, the values of the damage internal state variable S cannot. However, values of S can be computed numerically at each time point j using the following discrete version of damage evolution law from Equation 86:

$$\dot{S}_j = \frac{\Delta S}{\Delta t_R} = \left(-\frac{\delta W_j^R}{\delta S} \right)^{\alpha} \qquad \textbf{Equation 90}$$

The approach employed here was to assume a functional form for $C(S)$, an initial estimate for α, and an arbitrarily small value of δS in order to evaluate Equation 90. An alternate method that does not require an assumed functional form for $C(S)$ is described by Park *et al*. (1996). The functional form for $C(S)$ assumed in the present study is an exponential series:

$$C(S) = \sum_{i=1}^{6} \frac{1}{i+3} e^{-a_i S} \qquad \textbf{Equation 91}$$

Values for S are then computed using the following finite difference relationships:

$$\delta W_j^R = \frac{1}{2}C(S_j + \delta S)\left(\bar{\varepsilon}_j^R\right)^2 - \frac{1}{2}C(S_j)\left(\bar{\varepsilon}_j^R\right)^2 \quad \textbf{Equation 92}$$

$$\bar{\varepsilon}^R{}_j = \frac{\varepsilon^R{}_j + \varepsilon^R{}_{j+1}}{2} \quad \textbf{Equation 93}$$

in which δS is a small perturbation of S (different from ΔS) and:

$$\Delta S_j = \left(-\frac{\delta W_j^R}{\delta S}\right)^{\alpha} \Delta t_j \quad \textbf{Equation 94}$$

$$S_{j+1} = S_j + \Delta S_j \quad \textbf{Equation 95}$$

The measured C versus reduced time (Equation 89) can then be fit to the predicted C versus reduced time by optimizing the series solution for $C(S)$ at an assumed α value. This process is then repeated for different values of the α exponent. The optimum α is the one for which the $C(S)$ curves computed at the different strain rates collapse to a common $C(S)$ relationship. After this optimum value for α is found, the computed $C(S)$ relationship is then recalibrated to the average of the computed $C(S)$ from the replicates.

Typical results of measured and computed C versus reduced time from a replicate that was loaded to failure are shown in Figure 107. This type of analysis was repeated for all replicates at all strain rates for values of α ranging between 1.25 and 2.25 in increments of 0.25. Results for α=2.00 and α=1.75 showed very similar collapses of the individual replicate results onto a common curve, as shown in Figure 108 and Figure 109 respectively. However, all replicates exhibited an abrupt drop in the very early part of the curves, as shown in the figure insets. Ideally, $C(S)$ decreases from an initial value of 1 (corresponding to a completely undamaged material) as damage begins to accumulate

during loading. In the limit, the measured C vs. reduced time curves appear to approach an intercept value less than 1 (between 0.7 and 0.9) as $S \rightarrow 0$ from the right. The fit $C(S)$ curves begin at 1.0 (0.9956 actually) but immediately jump down to some lower value before continuing to decrease gradually.

The abrupt drop-off of $C(S)$ at the beginning of the response in combination with the inherent variability in the replicate responses made it very difficult to determine an optimal value for α. It was hypothesized that some of these problems might be due to the effects of prior damage from the preceding frequency sweep loading—i.e., C was already less than 1 at the start of the constant strain rate loading. Damage from the preceding frequency sweep is a possibility. This hypothesis contradicts the conclusions during the back-to-back frequency sweep analyses (Figure 26 to Figure 28) and the adjustments to the upper shelf of the relaxation modulus in Chapter 4 (Linear Viscoelasticity Characterization).

It was hoped the variability in the $C(S)$ curves could be reduced if this effect was eliminated. The following iterative sequence was therefore employed:

1. Starting with the unadjusted fit [initial$C(0) = 1$] $C(S)$ curve, predict the S and corresponding C representing any mathematically predicted damage from the dynamic modulus frequency sweep stress history.
2. Substitute this "initial" S from the frequency sweeps into the beginning of each computation for each replicate and then determine an updated average $C(S)$ curve. This is intended to eliminate much of the abrupt drop in the initial portion of the $C(S)$ curve.
3. Repeat Steps 1 and 2 using the updated $C(S)$ curve computed in Step 2.

4. After each replicate is adjusted for the new estimate of the initial S value; a third and final average $C(S)$ is determined. The end results of this are shown in Figure 110.

As shown in Figure 111 for α =2.00, this process did produce the desired effects of increasing the smoothness of the very early response as evident in the fitted curves with and without the initial offset. Also, comparing this figure with Figure 108 shows that the variability among the curves is somewhat reduced. The optimal value of the α exponent remains about 1.75 to 2.00.

At this point it is still unclear as to which exponent is optimal and validation with both parameter sets shall determine final selection. As will be shown in Chapter 8 where both the viscoplastic and damage models are validated through a series of uniaxial tests, $\alpha = 1.75$ was ultimately determined as the optimal value. The discussion of the multiaxial damage calibration in the remainder of this chapter is based on this result, i.e., $\alpha = 1.75$. The calibrated coefficients for $C(S)$ for both damage evolution law exponents are summarized in Table 21.

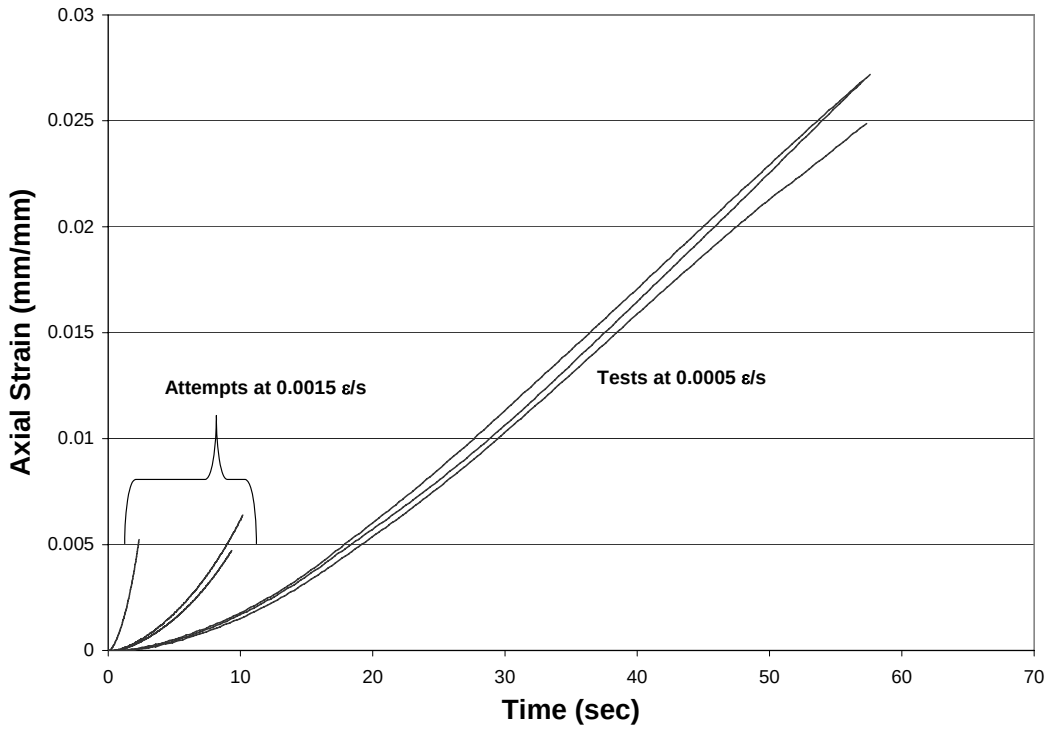

Figure 104. Strain versus time of the uniaxial 5°C damage calibration tests.

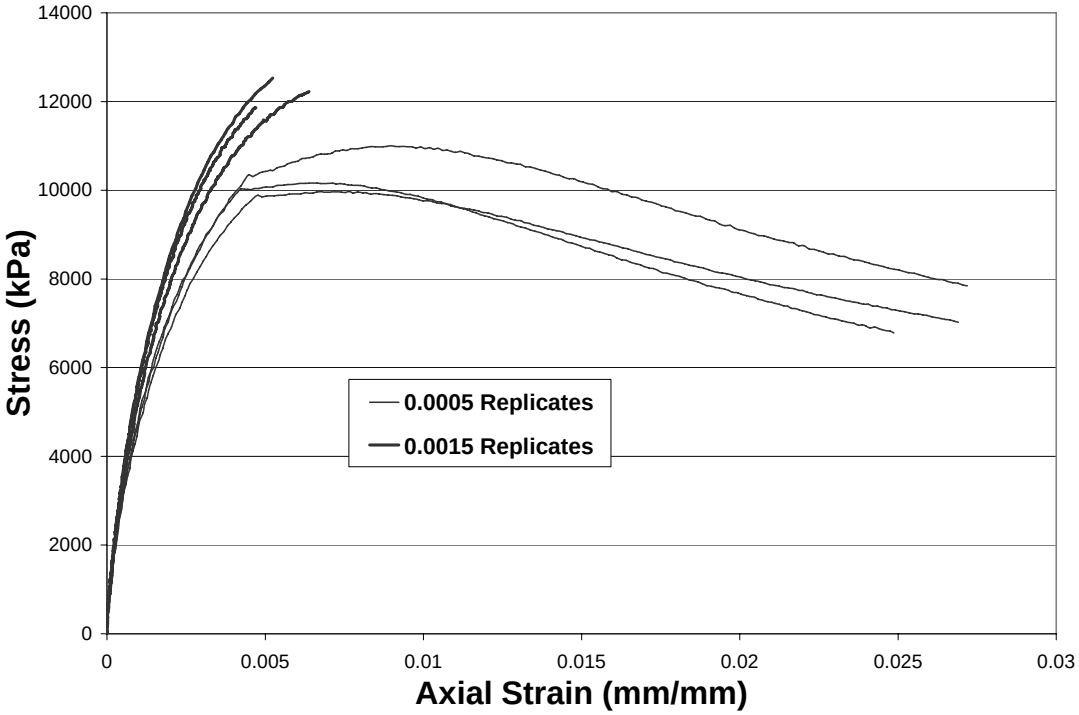

Figure 105. Stress versus strain of the uniaxial 5°C damage calibration tests.

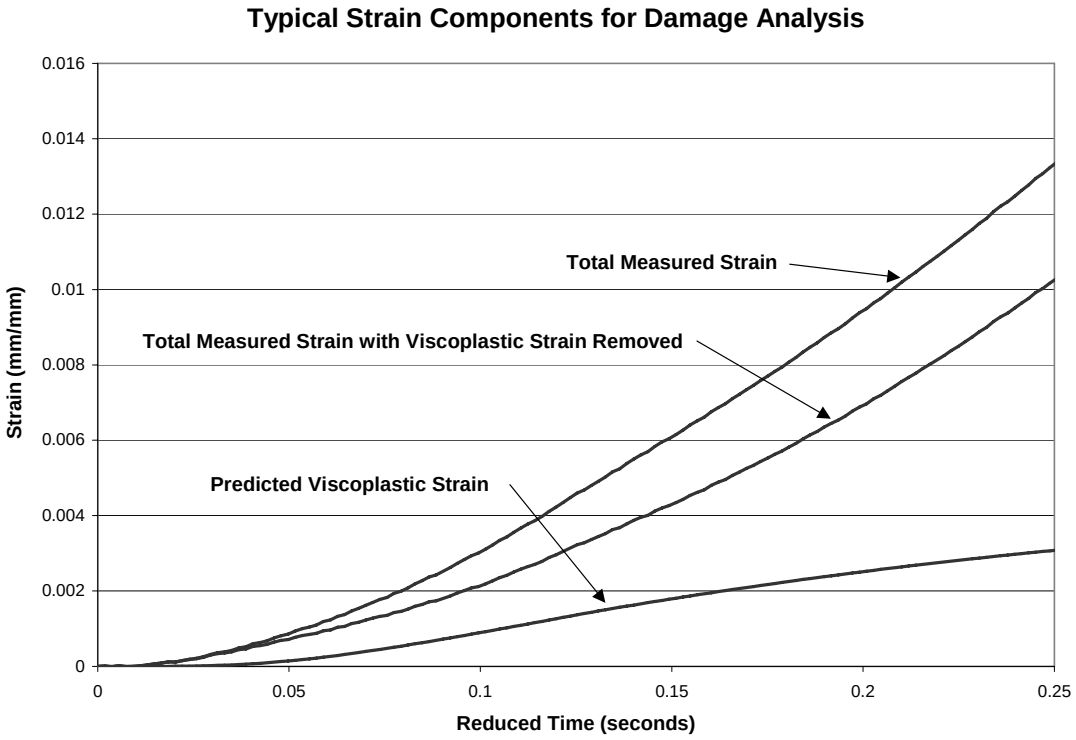

Figure 106. Computed viscoplastic strains for constant strain rate test at 5oC.

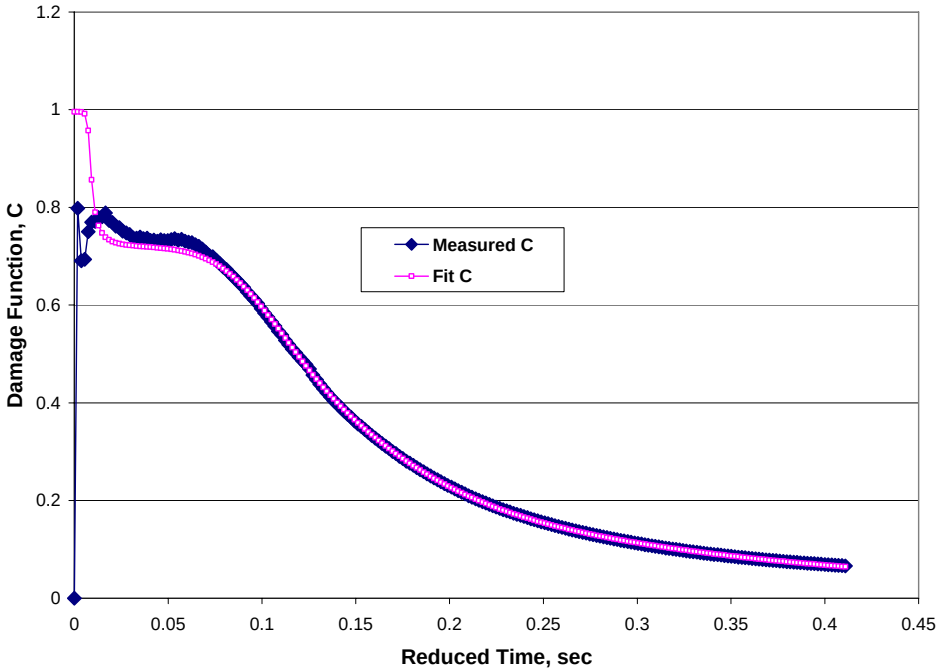

Figure 107. Typical computed and measured damage function C in reduced time, not the damage function C(S).

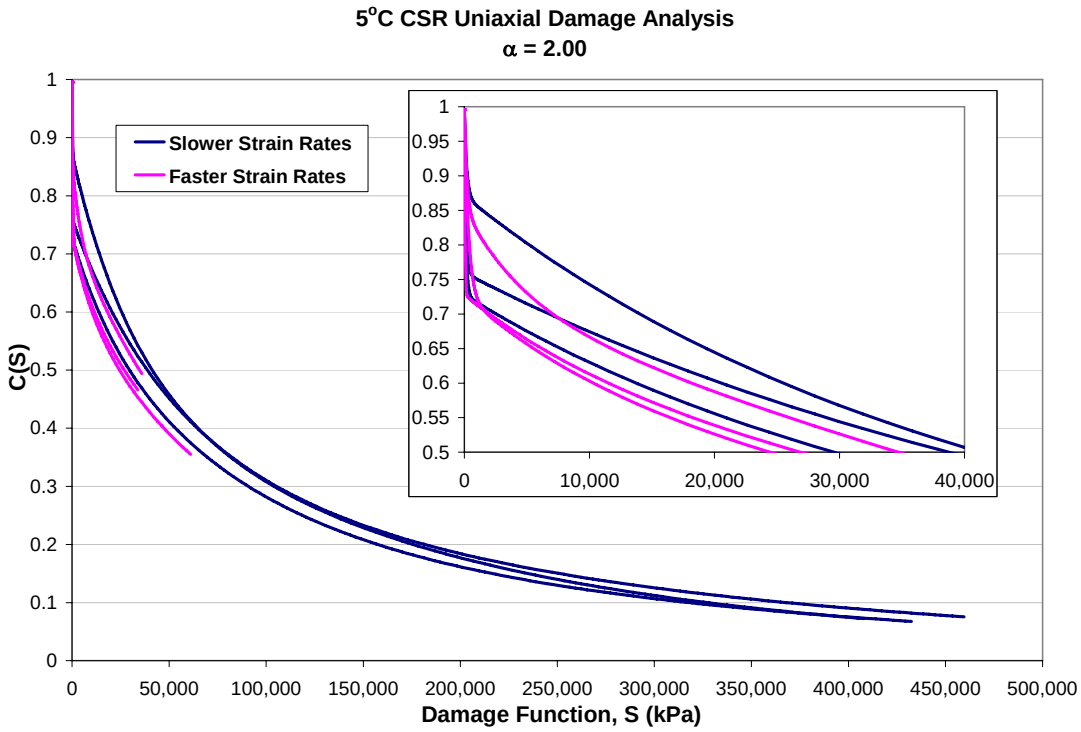

Figure 108. C(S) damage functions from 6 replicates for α=2.00.

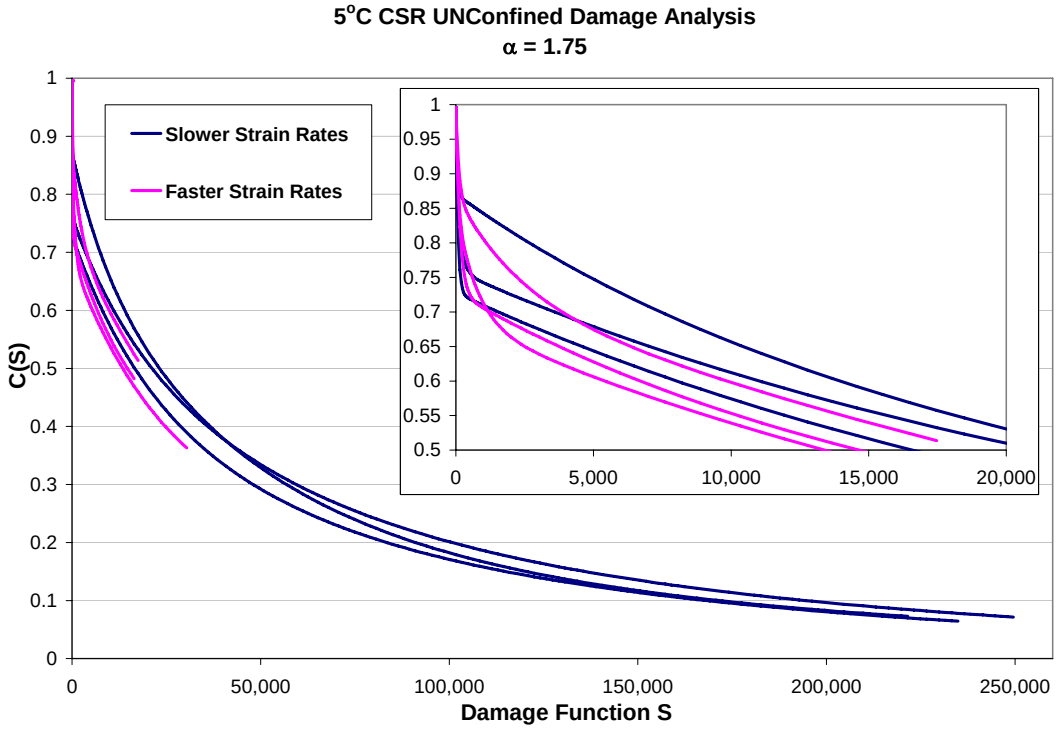

Figure 109. C(S) damage functions from 6 replicates for α=1.75.

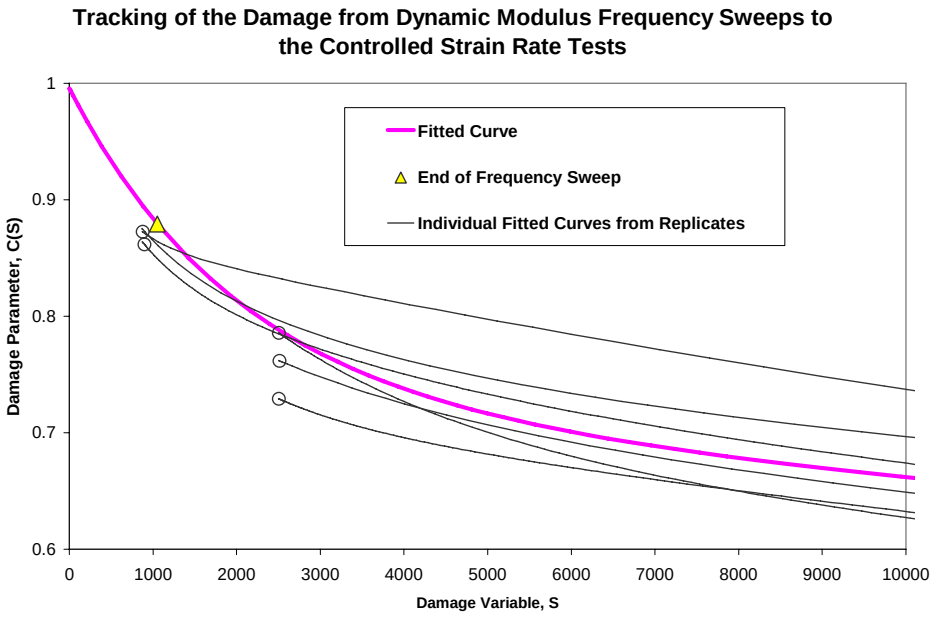

Figure 110. Adjustments of the initial portion of the replicate C(S) damage functions.

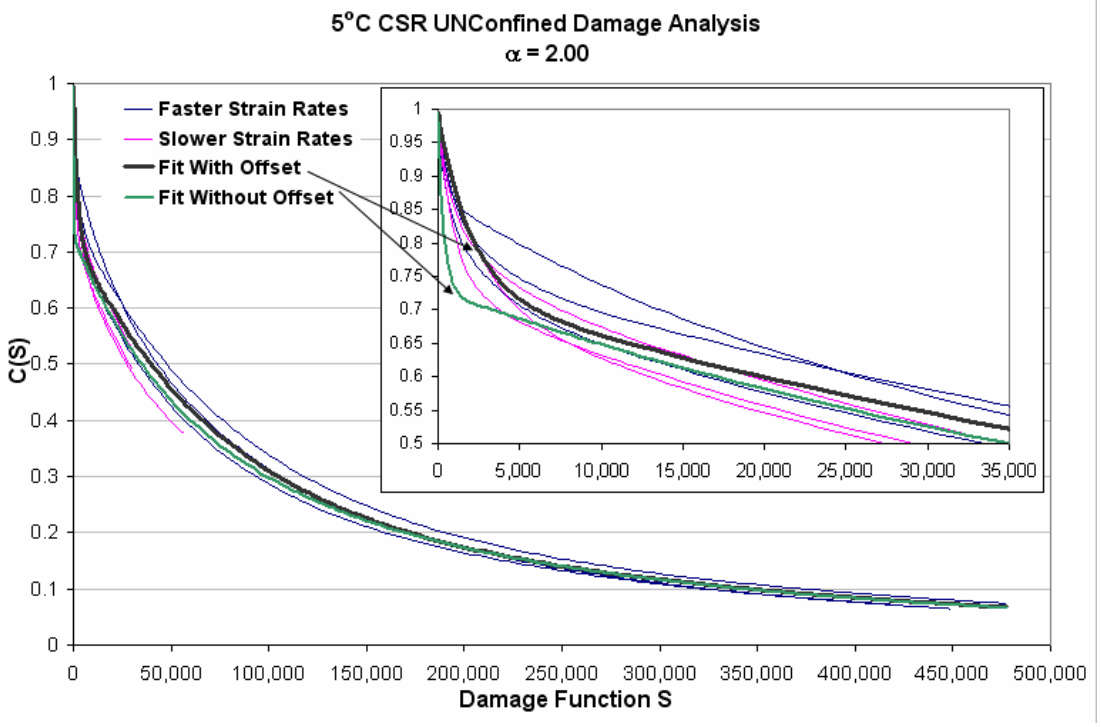

Figure 111. Adjusted and optimized C(S) damage function.

Table 21. Calibrated uniaxial damage function and coefficients.

$$C(S) = \sum_{i=1}^{6} \frac{1}{i+3} e^{-a_i S}$$

	Calibrated Coefficients a_i	
i	Damage Exponent α = 2.00	Damage Exponent α = 1.75
1	2.7630E-06	5.5574E-06
2	1.3759E-05	1.9607E-05
3	1.3758E-05	4.6669E-05
4	4.2359E-04	8.6808E-03
5	5.8286E-04	3.1604E-04
6	1.3748E-05	1.9608E-05

7.4 Three Dimensional Damage Formulation and Calibration

7.4.1 Model Form

The general form for the damage model under confined triaxial conditions can be stated as follows (Ha and Schapery, 1998). Starting from a dual pseudo strain energy density formulation in terms of the axial pseudo-strain ε_1^R and confining pressure p:

$$W_D^R = \frac{1}{2} C_{11}(S)(\varepsilon_1^R)^2 + C_{12}(S)\varepsilon_1^R p + \frac{1}{2} C_{22}(S) p^2 \qquad \textbf{Equation 96}$$

the constitutive relations for a damaged linear viscoelastic material can then be expressed as:

$$\Delta\sigma \equiv \frac{\partial W_D^R}{\partial \varepsilon_1^R} = C_{11}(S)\varepsilon_1^R + C_{12}(S) p \qquad \textbf{Equation 97}$$

$$\varepsilon_v^R \equiv \frac{\partial W_D^R}{\partial p} = C_{12}(S)\varepsilon_1^R + C_{22}(S) p \qquad \textbf{Equation 98}$$

in which W_D^R = dual energy density

$\Delta\sigma$ = deviator stress (tension positive)

p = confining pressure (compression positive; $p = -\sigma_3$ for triaxial loading conditions)

ε_1^R = axial pseudo strain (tension positive)

ε_v^R = volumetric pseudo strain (expansion positive)

$C_{ij}(S)$ = damage functions

S = damage internal state variable

The pseudo strain quantities are calculated using the correspondence principle via the hereditary convolution integrals:

$$\varepsilon_1^R = \int_0^{t_R} E(t_R - \tau_R) \frac{\partial \varepsilon_1}{\partial \tau_R} d\tau_R \qquad \textbf{Equation 99}$$

$$\varepsilon_v^R = \int_0^{t_R} E(t_R - \tau_R) \frac{\partial \varepsilon_v}{\partial \tau_R} d\tau_R \qquad \textbf{Equation 100}$$

in which $E(t_R)$ is the relaxation modulus and t_R is reduced time; the reference modulus E_R is taken as unity and omitted from the equations. The limiting case for Equation 97 and Equation 98 at $S \to 0$ corresponds to an undamaged linearly viscoelastic state. For isotropic conditions:

- $C_{11}(S) \to E_R$ as $S \to 0$, where E_R is the reference modulus in the stress versus pseudo strain relation (taken as unity in the present work)
- $C_{12}(S) \to (1 - 2\nu_0)$ as $S \to 0$, where ν_0 is the initial Poisson's ratio
- $C_{22}(S) \to -\frac{2}{E_R}(1 - 2\nu_0)(1 + \nu_0)$ as $S \to 0$

The most direct way to determine the $C_{12}(S)$ relation is to apply Equation 98 to the unconfined constant rate compression tests for which p =0, yielding:

$$C_{12}(S) = \frac{\varepsilon_v^R}{\varepsilon_1^R} \qquad \textbf{Equation 101}$$

Once both $C_{11}(S)$ and $C_{12}(S)$ are known, the remaining $C_{22}(S)$ damage function can be determined using the confined constant strain rate compression tests and Equation 98.

7.4.2 Viscoplastic Lateral Expansion

Unconfined constant rate tests at 5°C were used previously to determine $C_{11}(S)$, and these same tests are used now to determine $C_{12}(S)$ from Equation 99, Equation 100 and Equation 101. The volumetric strain ε_v in Equation 100 for the axisymmetric conditions in the test is simply $\varepsilon_v = \varepsilon_1 + 2\varepsilon_3$. Recall that the measured axial strain ε_1 at 5°C was corrected for viscoplasticity effects by removing the viscoplastic strain predicted by the viscoplasticity model, leaving only damaged linear viscoelastic strain component. A similar correction is required for the radial strain ε_3.

The approach adopted here is to estimate the radial viscoplastic strain based on the axial viscoplastic strain and a viscoplastic lateral expansion property like a Poisson's ratio, ν_{vp}, because viscoplasticity was found to be compressive and dilative. The unconfined Fixed Time (denoted S5 in figure legends) and Fixed Stress (denoted S4 in figure legends) viscoplastic test data (averaged across all replicates) were used to estimate ν_{vp}. The variation of the measured ν_{vp} versus axial viscoplastic strain for various temperatures is summarized in Figure 112. For the Fixed Stress tests, the variation of ν_{vp} with ε_{1vp} follows a power law that shifts vertically with temperature, giving an initial nonzero ν_{vp0} that is a function of temperature. The Fixed Time data

showed some deviations from this pattern, but principally only for the early low stress load cycles where significant viscoplastic strains have not yet accumulated. The initial ν_{vp0} is assumed to vary between 0.5 (incompressible) at high temperatures and 0.2 at cold temperatures and to follow a sigmoidal relationship at intermediate temperatures, as shown in Figure 113. Thus, the following equations are used to estimate the radial viscoplastic strain that is subtracted from the measured total radial strain to yield the damaged linear viscoelastic strain:

$$\nu_{VP}(\varepsilon_{1VP}, T) = k_1(\varepsilon_{1VP})^{k_2} + \nu_{VP0}(T) \quad \textbf{Equation 102}$$

$$\nu_{VP0}(T) = 0.5 + \frac{(0.2 - 0.5)}{1 + e^{c_3 T + c_4}} \quad \textbf{Equation 103}$$

$$\varepsilon_{3ve} = \varepsilon_3 - \varepsilon_{3vp}$$
$$\varepsilon_{3ve} = \varepsilon_3 - \left(\varepsilon_{vp}\right)\left(\nu_{vp}\right) \quad \textbf{Equation 104}$$

Equation 102 and Equation 104is used to compute the volumetric damaged viscoelastic strain, which in turn is used to determine the volumetric damaged viscoelastic pseudo strain in Equation 100.

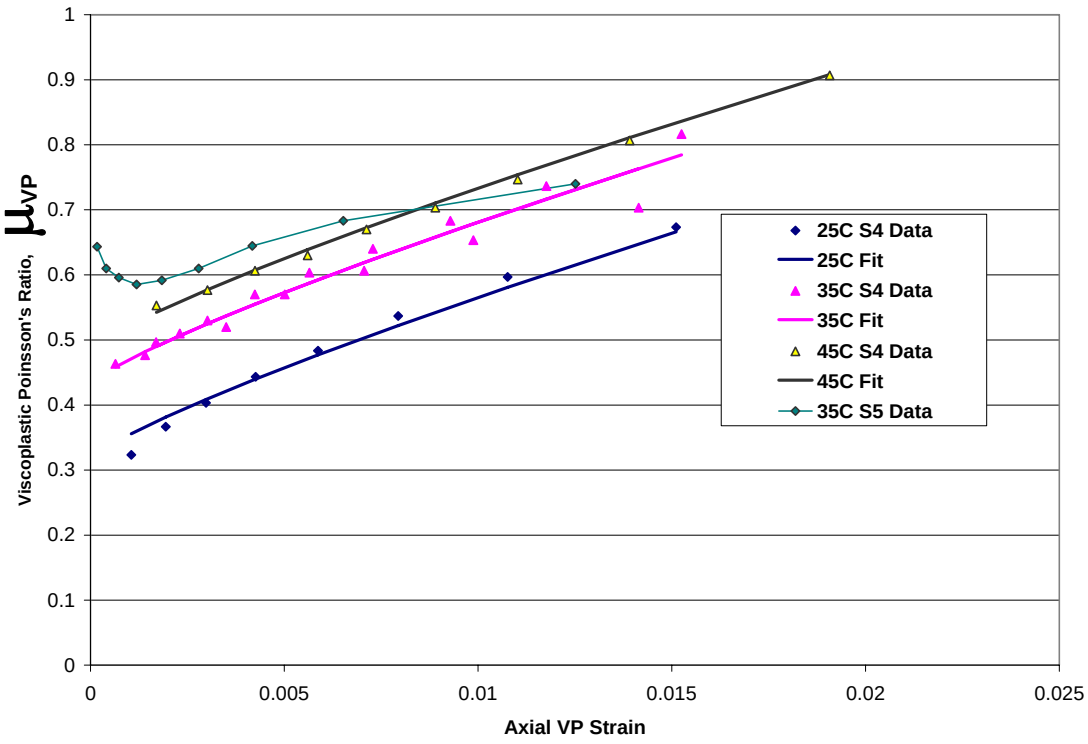

Figure 112. Viscoplastic Poisson's ratio versus axial viscoplastic strain. S4 denotes Fixed Stress and S5 denotes Fixed Time.

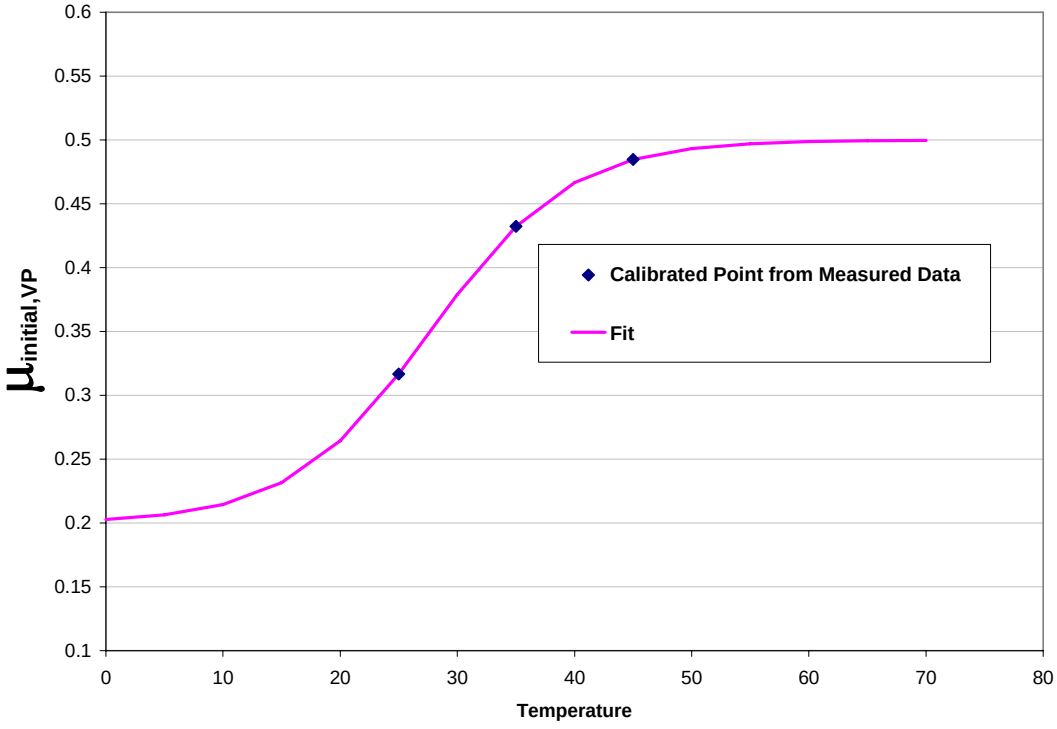

Figure 113. Assumed initial unloaded viscoplastic lateral expansion versus temperature.

7.4.3 Unconfined C_{12} Analysis

The typical response from the unconfined constant strain rate tests was increasing compressive axial strain and increasing tensile radial strain such that the resulting computed volumetric strain is initially compressive but then expansive, indicating dilation as seen in Figure 114 (note that a compression positive sign convention has been adopted for this figure).

The $C_{12}(S)$ relationship as computed using Equation 101 and the data from the unconfined constant rate tests at 5°C is shown in Figure 115. Two nominal strain rates were tested with three replicates per rate. The tests at the faster rates ended prematurely because the stress reached the load capacity of the testing machine, as can be seen in the figure. Three observations can be made regarding the behavior of the C_{12} relationship.

1. The curve fluctuates erratically at the very beginning of the test because of the small initial values for the strains. Similar behavior was observed in during the C_{11} analysis. This noise in the early response has been removed for the sake of clarity.
2. The initial $C_{12}(0)$ is positive because the axial pseudo strain and volumetric pseudo strain are both compressive as $S \to 0$. Considering the variability of the replicates and the noise in the data as $S \to 0$, it is difficult to determine directly the value for $C_{12}(0)$. The approach adopted here was to take the smoothed measured viscoelastic Poisson's ratios for $t_R > 0$ and extrapolate back to an initial undamaged value at $t_R = 0$ (see Figure 116). The estimates of the initial

undamaged viscoelastic Poisson's ratio ν_{ve0} ranged between 0.1 and 0.35 with an average value of 0.22, which is a reasonable number for asphalt concrete at 5°C. This initial Poisson's ratio is described in the relation determined in the limiting case discussions above, such that $C_{12}(0) = (1 - 2\nu_0) = 0.56$ using $\nu_0 \approx 0.22$. This intercept was constrained to this value in the curve fitting procedure.

3. The C_{12} curves in Figure 115 all tend to decrease with increasing damage, as expected. A decreasing C_{12} curve reflects an increase in the Poisson's ratio due to growing damage. There are only slight differences between the different loading rates, suggesting that the estimates of the radial viscoplastic strain values are reasonable.

The functional form and coefficients for the $C_{12}(S)$ damage function are summarized in Table 22.

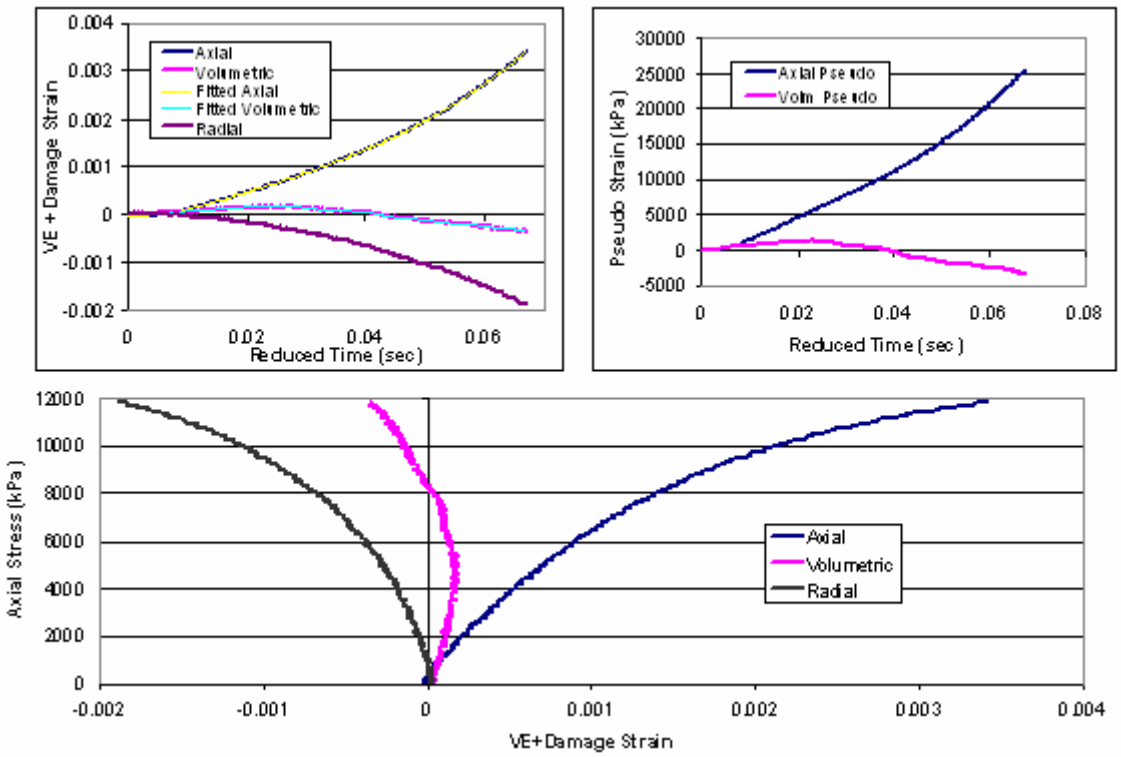

Figure 114. Typical unconfined strain and pseudo strain behavior.

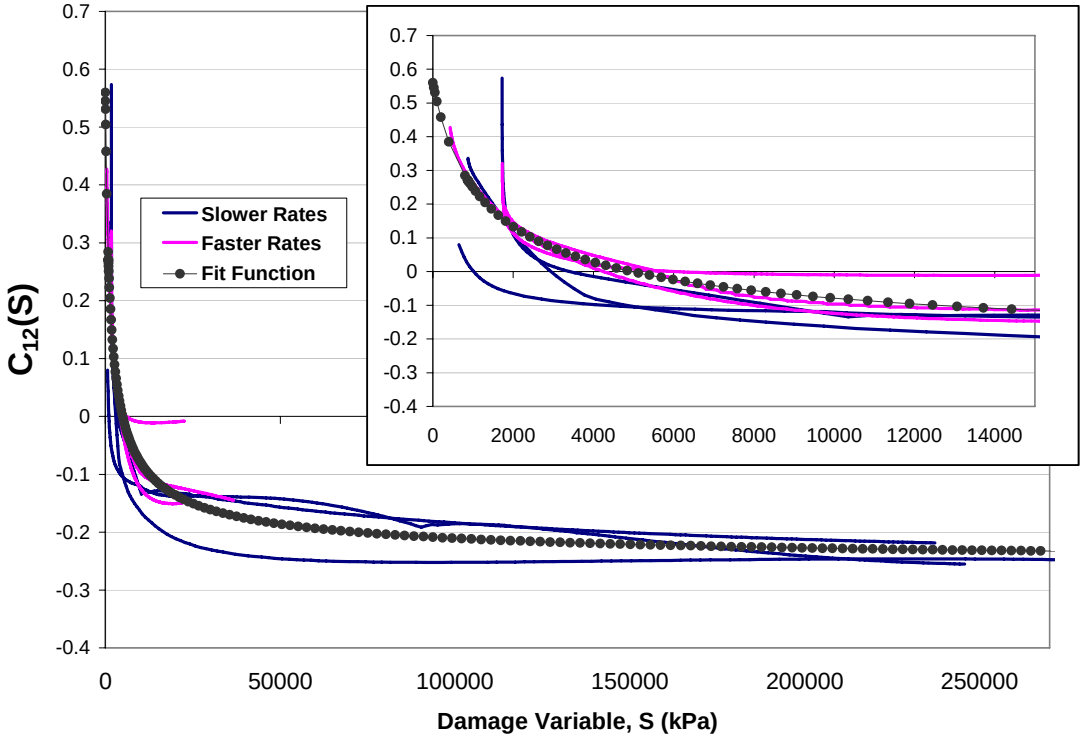

Figure 115. $C_{12}(S)$ computed from unconfined constant strain rate replicates.

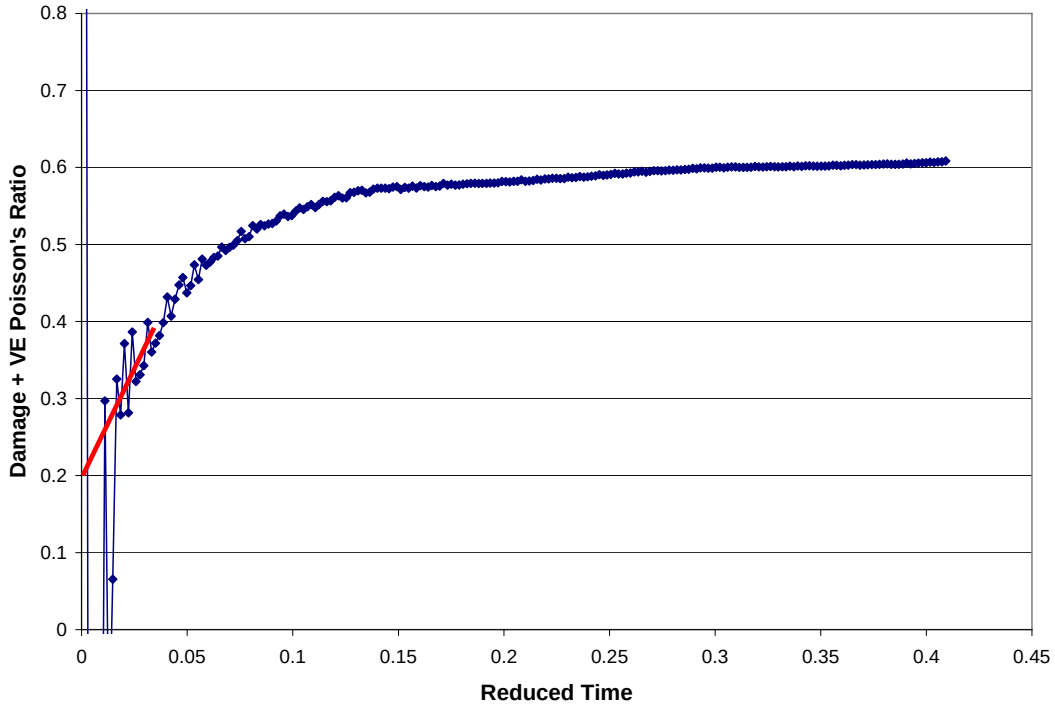

Figure 116. Typical damage plus viscoelastic Poisson's ratio.

Table 22. Calibrated $C_{12}(S)$ damage function and constants, α=1.75.

$C_{12}(S) = c_1 + \frac{c_2}{1+e^{c_3(\log S + c_4)+c_5}}$	
c_1	-0.262
c_2	162.634
c_3	1.304
c_4	753.676
c_5	1.530

7.4.4 Confined C_{22} Analysis

The remaining damage function $C_{22}(S)$ required testing under confining pressure p in order to utilize Equation 100. Two series of confined triaxial compression tests were conducted at 250 and 500 kPa at a cool temperature of 10°C. At each confining

stress there were two replicates and two strain rates. A temperature of 10^{o}C was chosen for several reasons. The first was to avoid reaching the testing machine capacity before failure. Recall this happened during the unconfined 5^{o}C compression test; confining stress increases the stiffness and chances of running out of load capacity prematurely. Time-temperature superposition was employed because the unconfined damage functions were calibrated at 5^{o}C.

Most importantly, viscoplasticity was assumed to be reduced to a negligible level by the combination of a cool temperature and confining stress, at least in the axial direction. The confined viscoplastic tests showed that viscoplasticity was reduced by up to one-half to a full order of magnitude at 35^{o}C. These strains would be expected to be reduced even further at the significantly colder temperature of 10^{o}C.

The tests followed a loading sequence similar to that in the confined viscoplasticity tests (Chapter 6), with a hydrostatic pressure applied via a controlled two-minute ramp-up to the confining stress with measured volumetric strains. The duration of the hydrostatic creep loading was extended from 30 minutes to one hour even though the creep does not need to come to equilibrium or near-equilibrium since the constitutive equations are applicable under dynamic conditions. Typical results from these tests are shown in Figure 117 and Figure 118; note that the constant strain rate to failure portion of the loading is very short compared to the hydrostatic creep. The LVDTs did go out of range at times, which manifests as abrupt changes in the strain response. The radial LVDTs tend to go out of range before the axial as a consequence of the inevitable small rigid body motions permitted by the lubricated ends of the cylindrical specimen. During the hydrostatic creep portion of the loading, the magnitude of the radial strain is much

larger than the axial strain, which may be indicating anisotropy or possibly some viscoplasticity in the radial direction. The latter would be consistent with the observations from the viscoplasticity tests at warmer temperatures (Chapter 6) where the axial strains were found to be fully recoverable but the radial strains were not.

The two types of pseudo strains ε_1^R and ε_V^R were computed based on the measured strains with Equation 99 and Equation 100 and the assumption of negligible viscoplasticity influences. The unknown $C_{22}(S)$ damage function was then backcalculated. Some iteration is required because this function is a component of the pseudo strain energy density W_D^R in Equation 96, which is in turn is used in the damage evolution law:

$$\dot{S} = \frac{\partial S}{\partial t_R} = \left(-\frac{\partial W_D^R}{\partial S} \right)^{\alpha} \qquad \textbf{Equation 105}$$

that determines the internal state variable S based on the loading history. However, because $C_{11}(S)$ and $C_{12}(S)$ are known from the previous calibrations, preliminary estimates of the pseudo strain energy density W_D^R and thus the internal state variable S can be calculated. The initial backcalculated $C_{22}(S)$ damage functions from each replicate are shown in Figure 119 and are computed using the following relation:

$$C_{22}(S) = \frac{\varepsilon_v^R - C_{12}(S)\varepsilon_1^R}{p} \qquad \textbf{Equation 106}$$

The curves from the replicates in the figure do not collapse as nicely as desired, but it is encouraging that one pair each of fast and slow replicates are in agreement. The curves also appear to have an intercept that is less than zero, which agrees with the theory because the limiting case discussion above states that as $S \to 0$,

$C_{22}(S) \to -\frac{2}{E_R}(1-2\nu_0)(1+\nu_0)$ meaning $C_{22}(0) = -1.37$ using $\nu_0 \approx 0.22$ and $E_R = 1$ from the unconfined tests. A second order polynomial was fit to each initial backcalculated $C_{22}(S)$ replicate curve while forcing an intercept of -1.37.

In the second iteration, the estimated functional form for $C_{22}(S)$ enables inclusion of its contributions to the pseudo strain energy density and damage evolution law. The backcalculated results from the second iteration are shown in Figure 120 based on polynomial fits to the initially backcalculated replicate responses. The later portions of the curve are virtually unaltered by the iteration, but the initial behavior of the backcalculated $C_{22}(S)$ curves are changed dramatically with the appearance of an unreasonable near-horizontal extension of the intercept indicating a calculated rapid growth of damage, i.e. large ΔS. This behavior is physically implausible, as damage functions should be naturally smooth. The portion of the test history responsible for the horizontal offset is the hydrostatic creep, which in the first iteration did not contribute to any significant damage growth since $C_{22}(S)$ was ignored. Mathematically, the source for this behavior must be the actual damage variable S in the $C_{12}(S)$ term in Equation 106 because it is the only term that can vary. The $C_{12}(S)$ function is fixed and the two pseudo strain and confining pressure are predetermined and fixed as well. This is obviously incorrect and the actual behavior of $C_{22}(S)$ must lie between the initial and second back calculated responses. Thus, the final form of the $C_{22}(S)$ damage function was found by fitting a simple polynomial through the second iteration results while holding the intercept value fixed at -1.37. The calibrated parameters for this function are found in Table 23 below.

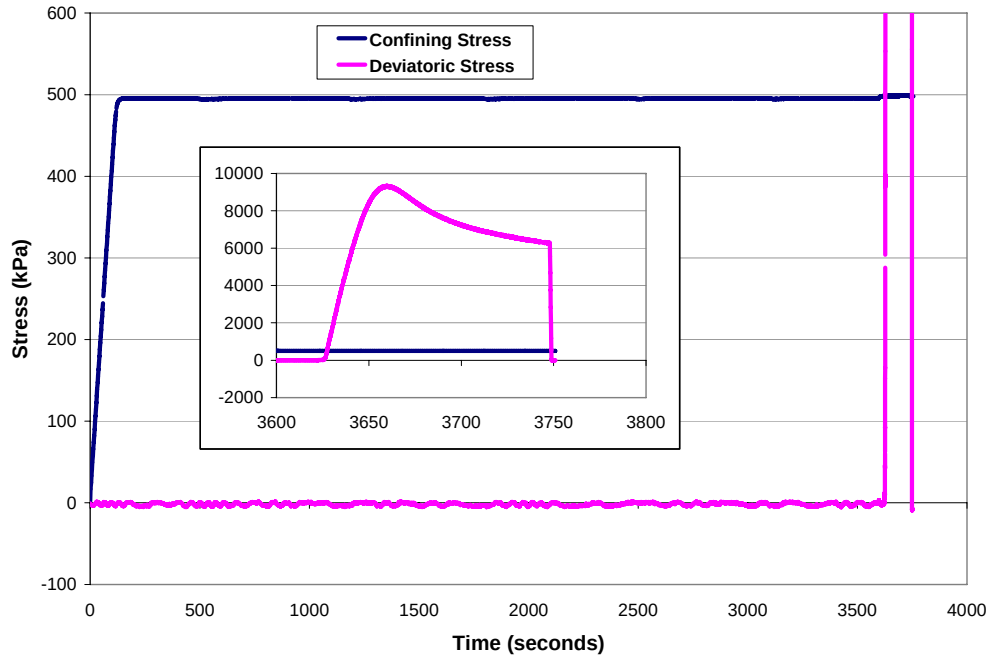

Figure 117. Typical stress history from 500 kPa confined constant strain rate tests at 10°C.

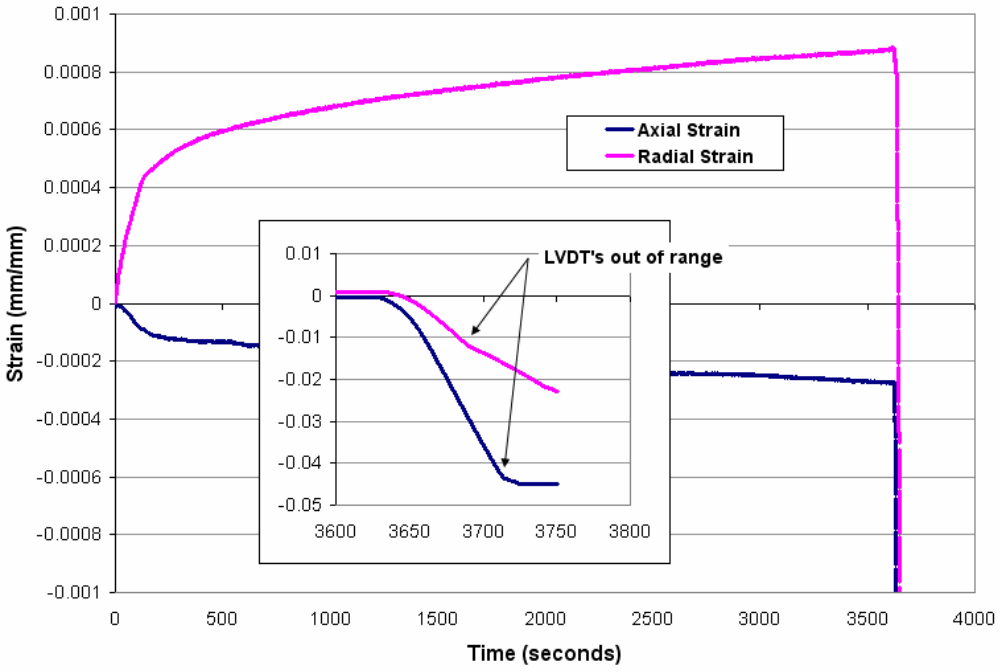

Figure 118. Typical strain history from 500 kPa confined constant strain rate tests at 10°C.

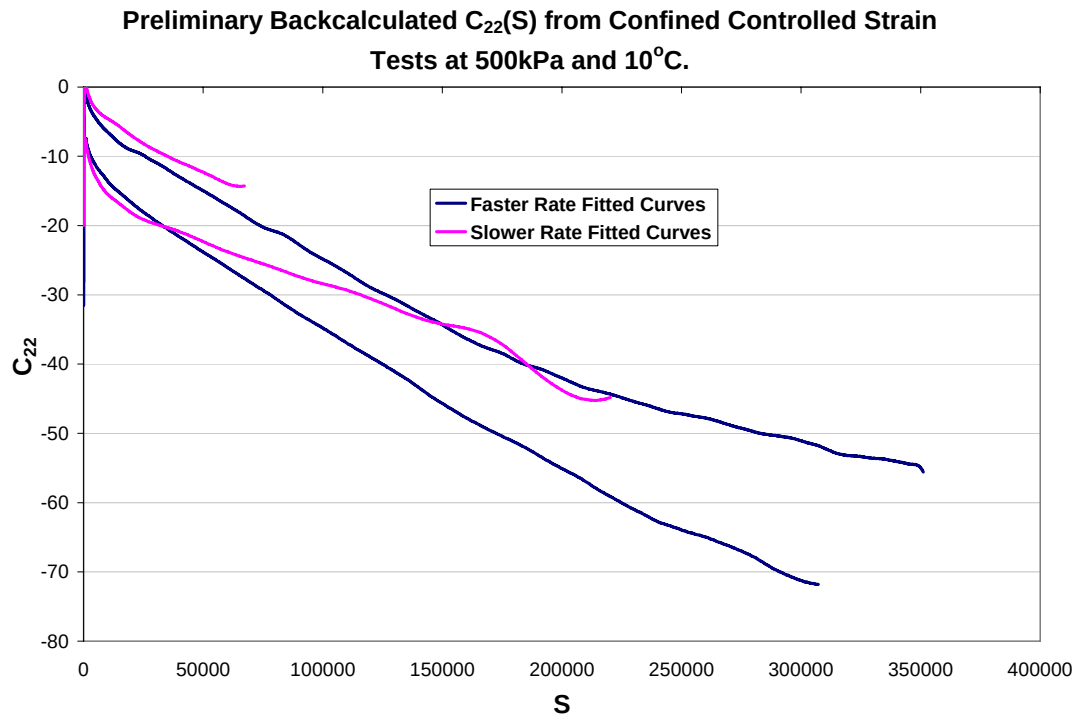

Figure 119. Initial backcalculation of damage function $C_{22}(S)$.

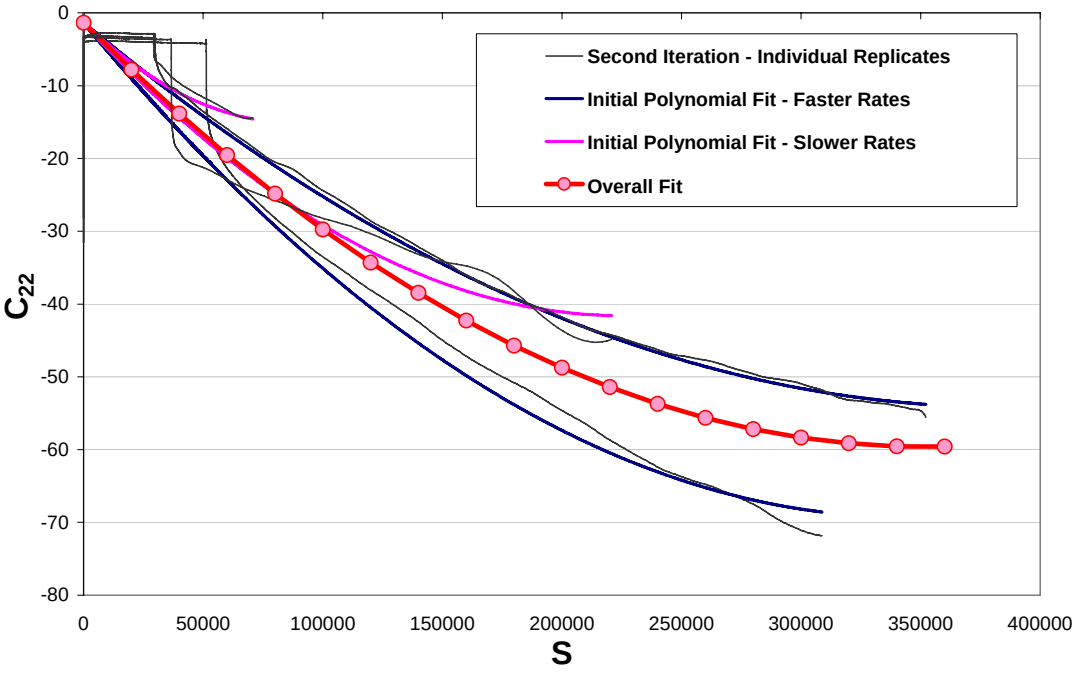

Figure 120 Overall $C_{22}(S)$ behavior

Table 23. Calibrated $C_{22}(S)$ damage function and constants, α=1.75.

$$C_{22}(S) = a + bS + cS^2$$

a	-1.3700E+00
b	-3.3085E-04
c	4.6979E-10

7.5 Three Dimensional Damage Validation

Validation at 10°C and 250 kPa of confinement is presented here and not in Chapter 8 in part because this is a validation only of the damage model component and not a comprehensive validation of all model components including viscoplasticity. Recall that 500 kPa confining pressure and 10°C test temperature values were used for calibration of the multiaxial damage model. Both calibration and validation at 10°C are more susceptible to viscoplastic effects because they are warmer than the 5°C uniaxial calibration tests which had viscoplasticity removed with the calibrated uniaxial model. However, confinement still justifies neglecting viscoplastic effects based on the suppression of viscoplasticity observed in the confined vs. unconfined comparisons of viscoplasticity in Chapter 6.

This validation offers the opportunity to evaluate the performance of the calibrated damage functions C_{12} and C_{22}, which were fit to very unwieldy and unsmooth backcalculated initial responses during calibration. The intent here is to ensure that radial strain predictions using those smooth-fit functions yield reasonable predictions. Furthermore, this exercise also validates the use of the linear viscoelastic relaxation modulus determined from unconfined tests in the context of confined conditions. Recall

that the comparisons of confined and unconfined tension and compression dynamic modulus in Chapter 4 showed no meaningful effect of confinement on the linear viscoelastic relaxation modulus.

Once the $C_{ij}(S)$ damage functions were calibrated, physical strains that are a combination of damage and linear viscoelasticity in the axial and radial directions may be predicted from any general deviatoric and volumetric stress history using the three dimensional constitutive equations. The corresponding axial and volumetric strains from two replicates at two controlled rates were predicted and compared to the measured counterparts to judge the performance of the model.

The first task in the validation was to predict the damage internal state variable S and all corresponding $C_{ij}(S)$ damage functions based solely on the measured stresses. To do so, the first constitutive Equation 97 was solved for axial pseudo strain ε_1^R to yield:

$$\varepsilon_1^R = \frac{\Delta\sigma - C_{12}p}{C_{11}} \qquad \textbf{Equation 107}$$

Equation 107 is substituted into the pseudo strain energy Equation 96 to yield:

$$\begin{aligned} W_D^R &= \frac{1}{2}C_{11}\left(\varepsilon^R\right)^2 + \frac{1}{2}C_{22}\left(p\right)^2 + C_{12}\varepsilon^R p \\ W_D^R &= \frac{1}{2}C_{11}\left(\frac{\Delta\sigma - C_{12}p}{C_{11}}\right)^2 + \frac{1}{2}C_{22}\left(p\right)^2 + C_{12}\left(\frac{\Delta\sigma - C_{12}p}{C_{11}}\right)p \\ W_D^R &= \frac{\left(\Delta\sigma\right)^2 - \left(C_{12}p\right)^2}{2C_{11}} + \frac{C_{22}\left(p\right)^2}{2} \end{aligned} \qquad \textbf{Equation 108}$$

Then the same incremental formulation in Equation 92 to Equation 95 may be used to compute S and $C_{ij}(S)$ throughout the tests, allowing the pseudo strains to be computed using the two constitutive relations:

$$\varepsilon_1^R = \frac{\Delta\sigma - C_{12}p}{C_{11}} \qquad \textbf{Equation 109}$$

$$\varepsilon_V^R = C_{12}\varepsilon_1^R + C_{22}p \qquad \textbf{Equation 110}$$

Now the computation of the physical axial and volumetric strains follows the reverse of the hereditary integrals used in the forward calculation procedure:

$$\varepsilon_1 = E_R \int_0^{t_R} D(t_R - \tau_R)\frac{d\varepsilon_1^R}{d\tau_R} d\tau_R \qquad \textbf{Equation 111}$$

$$\varepsilon_V = E_R \int_0^{t_R} D(t_R - \tau_R)\frac{d\varepsilon_V^R}{d\tau_R} d\tau_R \qquad \textbf{Equation 112}$$

The verification results for the axial and radial directions are shown in Figure 121. The predicted deviatoric stress versus axial and radial strain shows remarkably well behaved behavior and excellent agreement with the measured response. Similar to the unconfined validation tests, there is very reasonable agreement in the pre-peak and peak stresses and divergence in the post-peak region. The inset shows strains beginning at the point after the hydrostatic stress sequence at the start of application of the deviatoric stresses for the constant strain rate portion of the loading. The isotropic nature of the model and the anisotropic nature of the material are reflected by the measured radial strains being larger than the axial strains at the end of the hydrostatic loading. However, the predicted axial and radial strains at this point are equal because the calibration procedure averages the anisotropic response into a representative isotropic response. Nonetheless, the isotropic model does very well in predicting the overall response, especially under stress conditions where the deviatoric stress is much larger then the confining stress.

The volumetric strains are compared to the measured strains in Figure 122 through Figure 125 for each of the four replicates. In each figure, the volume change

during the hydrostatic portion is shown in the main plot while the inset magnifies the controlled-strain-rate-to-failure portion. The magnitudes of the predicted volumetric strains during the consolidation are about one half of the measured values. The calculated amount of damage (ΔS) during this part of the tests was very, very small. Therefore, the discrepancies in the predicted consolidation behavior are most probably due to aggregate skeleton anisotropy and perhaps very small amounts of viscoplasticity, especially in the radial response early in the loading. No attempt was made to correct for potential viscoplastic strains in the measured response.

Although the magnitudes of the predicted consolidation strains appear to be predicted not so well, the shape of the consolidation and, most importantly, the predicted compression followed by dilation under the deviatoric loads is realistically captured by the model. A peak occurs in the measured volumetric compression as the material becomes very damaged under the deviatoric stresses and then subsequently dilates. The predicted magnitude of the incremental amounts of compression and expansion relative to the beginning of the deviatoric loads reasonably agree with the measured response, especially when noise in the LVDT signals is considered. Capturing these qualitative characteristics responses is paramount in validating the realism of the modeling formulation. Improvements in the magnitudes of the predicted strains may be improved by considering anisotropy and viscoplasticity.

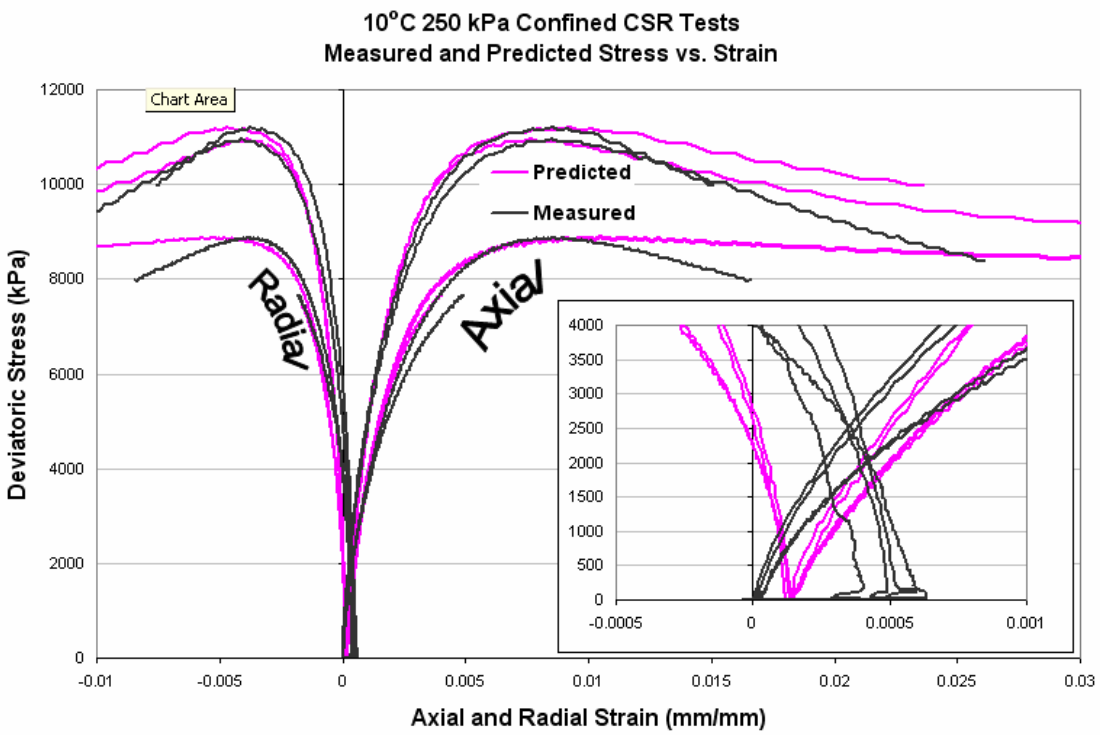

Figure 121. Measured and predicted axial and radial strain versus deviatoric stress from 250 kPa confined constant strain rate tests at 10°C.

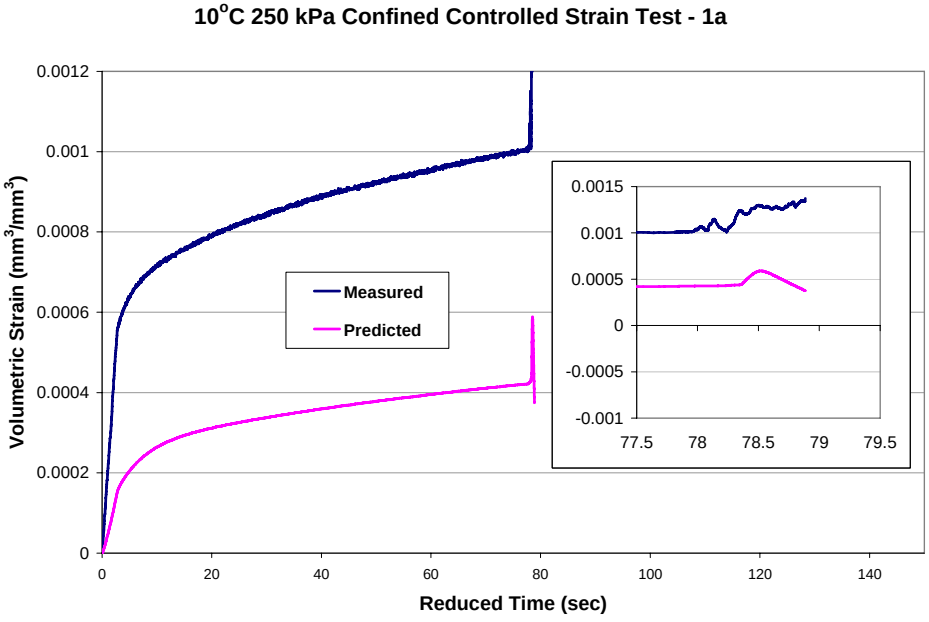

Figure 122. Measured and predicted volumetric strain versus reduced time from 250 kPa confined constant strain rate tests at 10°C; Slower rate Replicate A. Main plot – hydrostatic creep; Inset – deviatoric constant strain rate to failure.

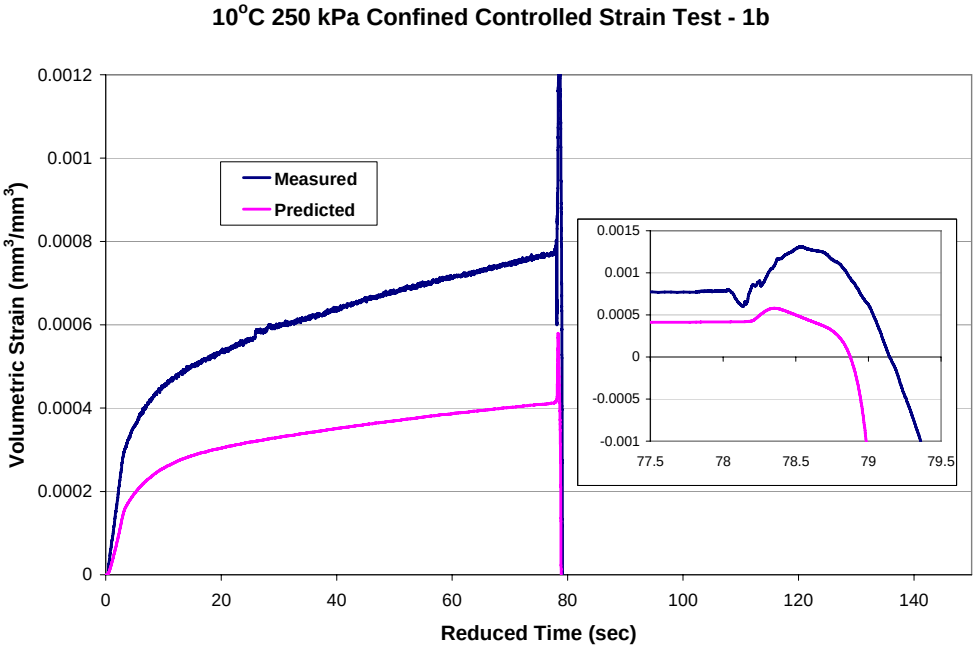

Figure 123. Measured and predicted volumetric strain versus reduced time from 250 kPa confined constant strain rate tests at 10°C; Slower rate Replicate B. Main plot – hydrostatic creep; Inset – deviatoric constant strain rate to failure.

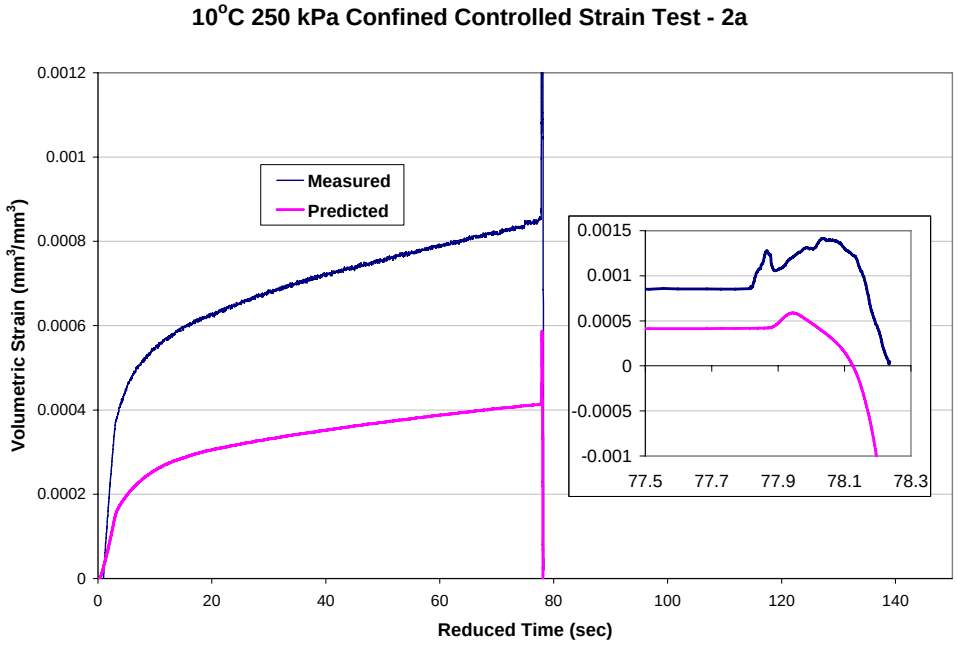

Figure 124. Measured and predicted volumetric strain versus reduced time from 250 kPa confined constant strain tests at 10°C; Faster rate Replicate A. Main plot – hydrostatic creep; Inset – deviatoric constant strain rate to failure.

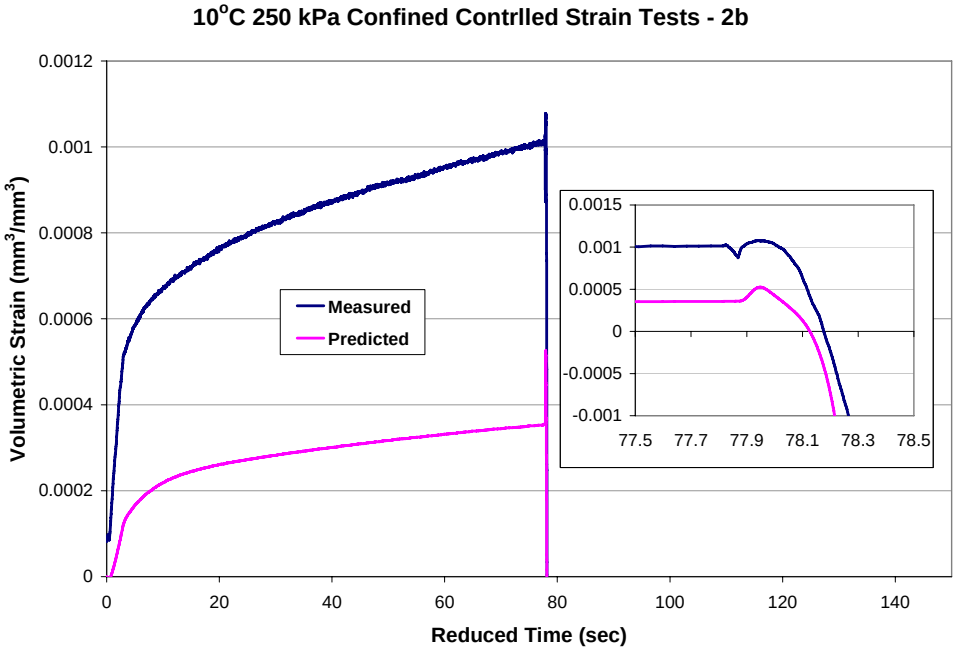

Figure 125. Measured and predicted volumetric strain versus reduced time from 250 kPa confined constant strain rate tests at 10°C; Faster rate Replicate B. Main plot – hydrostatic creep; Inset – deviatoric constant strain rate to failure.

7.6 Summary and Conclusions

The Schapery viscoelastic continuum damage model originally investigated by Park et al. (1996) and Lee and Kim (1998a, 1998b) in tension was calibrated in this study for compressive conditions and validated under uniaxial and confined stresses. This type of calibration faithfully removed any viscoplastic effects predicated by the model.

The required laboratory tests are fairly simple monotonic to failure protocols for both the uniaxial and confined multiaxial constitutive equations. The most computationally demanding calculation is the evaluation of the hereditary convolution integrals.

There was some difficulty in the calibration due to a suboptimal number of strain rates, the limited excursion into the post-peak region at the fastest achievable rate, assumptions on multiaxial viscoplasticity and being forced to consider initial damage for numerical reasons. Determining the optimum value for the α exponent in the damage evolution law was problematic because only two strain rates were available; four or more strain rates over a wide range would have enabled better estimation of this model parameter. In the future, fresh undisturbed specimens should be used in constant strain rate tests because calibrating $C_{11}(S)$ damage function was found to be very sensitive to the initial condition of the backcalculated responses.

A simplified estimate of the unconfined radial strains was used to calibrate $C_{12}(S)$ and $C_{22}(S)$. As a practical matter, reduction of potential viscoplasticity by testing at colder temperatures is preferred to post-test analytical corrections, assuming a testing machine of sufficient capacity is available. The 100 kN capacity testing machine with 100 mm diameter specimens at the University of Maryland could not fail the specimens at medium to high strain rates at 5^{o}C, which is not a particularly cold temperature.

Despite these hurdles, the uniaxial monotonic calibration results provide evidence that the multiaxial damage functions for asphalt concrete are unique, inherent material properties independent of temperature and loading rates through the use of reduced time. In other words, the $C_{11}(S)$ and $C_{12}(S)$ functions were fit at 5^{o}C uniaxial conditions and the and $C_{22}(S)$ function was fit at 10^{o}C triaxial conditions; a remarkable use of reduced time. The calibrated damage evolution law and single internal state variable S were shown to satisfactorily account for the growth of damage. The multiaxial validation test that exercised all $C_{ij}(S)$ damage functions showed agreement comparable to the unconfined

model for both the axial and radial strains for cases where the deviatoric stresses are large in relation to the confining stress. The model is less accurate under pure hydrostatic loading conditions, perhaps because the material anisotropy is more pronounced.

8. Model Validation

Some validation of individual model components has already been presented in earlier chapters. Specifically, Chapter 5 in general and Section 5.4 in particular summarize validation testing for the extension of time-temperature superposition concepts to large strains, while Chapter 7 and Section 7.5 in particular describe some limited validation of the multidimensional damage model component. The present chapter describes testing and results used to validate all components of the model simultaneously. Although each of the validation test series described in this section exercised the entire model, some were designed to emphasize individual components more than others—e.g., damage vs. viscoplasticity.

8.1 Uniaxial Monotonic Tests to Failure

Both the uniaxial damage and viscoplastic model were validated by predicting the 25^{o}C and 40^{o}C constant strain rate tests at nominal strain rates of 0.0005, 0.0015, 0.0045, and 0.0135 *ε/s***.** Although these tests were used in the large-strain time-temperature superposition study described previously in Chapter 5, they were not used to calibrate any

of the material properties for the linear viscoelastic (Chapter 4), viscoplastic (Chapter 6), or damage (Chapter 7) model components. In other words, the validation tests described here are different from the calibration tests used to determine the model parameters.

The stress versus strain predictions are shown in Figure 126 and Figure 127 for two temperatures and two values of α (the exponent in the damage evolution law). Figure 126 (a) and (b) shows the predictions for 25^{o}C and α =1.75 and 2.00 respectively while Figure 127 (a) and (b) shows similar results at 40^{o}C. Consistent with the calibration procedures, the validation predictions included any damage and viscoplasticity accumulated during the prior dynamic modulus frequency sweep loadings, although all strain components are re-zeroed at the start of the constant strain rate responses plotted in the figures. Predictions using both values of α show generally good agreement with the overall measured response, with a slight overprediction of total strains prior to the peak response. However, the predictions using α=1.75 are closer in the pre-peak range and better behaved after the peak response than the predictions using α=2.00, which tend to be slightly high over the entire measured range. This suggests that the optimal value for the uniaxial damage model is α=1.75 (see also Chapter 7). Continuum damage theories are no longer applicable once macro cracks develop in the post-peak region. Some macro cracking of the specimens was observed, but it typically occurred well into the post peak region. The fixed gage length LVDT instrumentation used in all University of Maryland (UMD) tests cannot determine the precise point at which macro cracking occurs. Direct tension tests at the North Carolina State University (Chehab et al., 2003) using LVDTs with varying gage lengths in combination with Digital Image Correlation (Chehab et al.,

2003 and Seo et al., 2002) were able to pinpoint localization of damage and formation of macro cracks occurring after the peak stress.

The predictions of the individual strain components versus time are shown in more detail in Figure 128 to Figure 131 for the case α=1.75. It is evident from these plots that the viscoplastic component is the most likely cause of the overprediction of total strain, since at 40^{o}C the viscoplastic strain is at times larger than the total measured strain. Nonetheless, the overall conclusion to be drawn from these validation results is that the Schapery-based strain decomposition approach and calibrated viscoelastic-viscoplastic damage model predicts well the material response at temperatures and strain rates that are different from the calibration conditions.

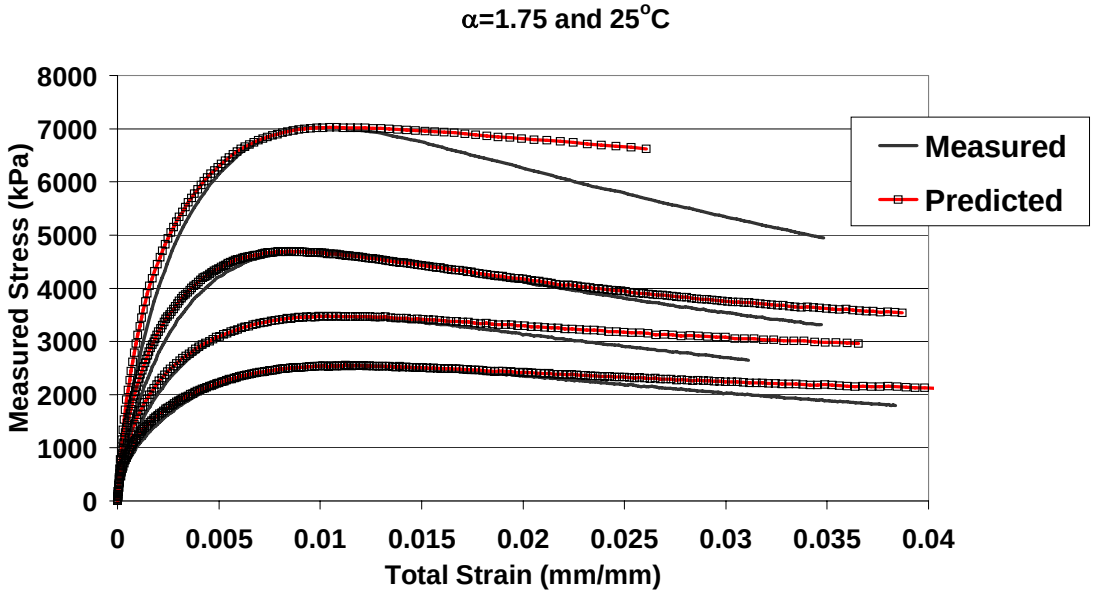

(a)

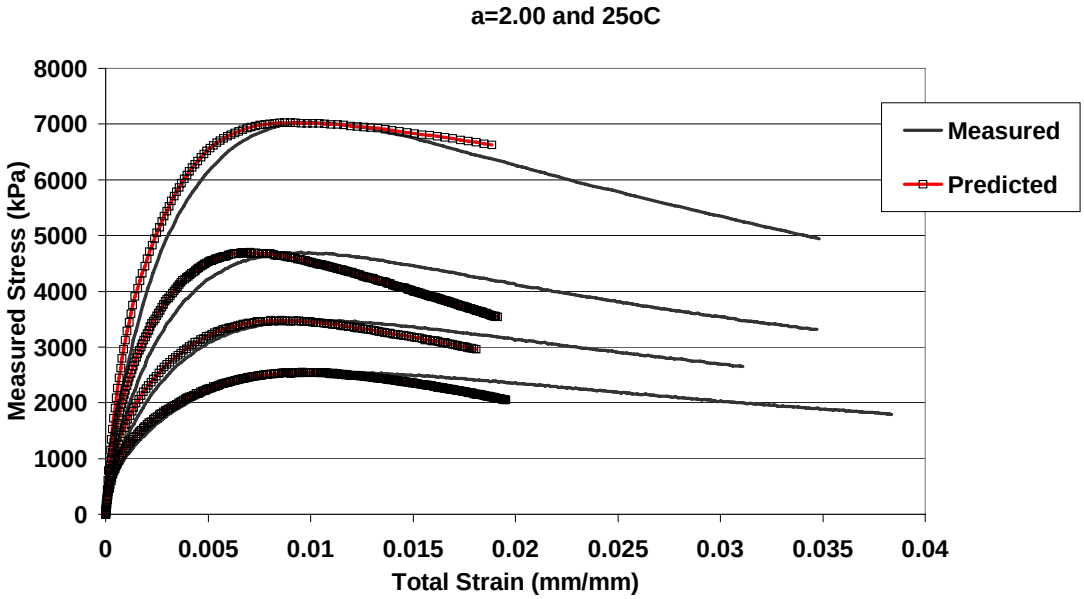

(b)

Figure 126. Measured stress versus predicted and measured total strain at 25°C for different damage evolution law exponents, (a) α=1.75 and (b) α=2.00.

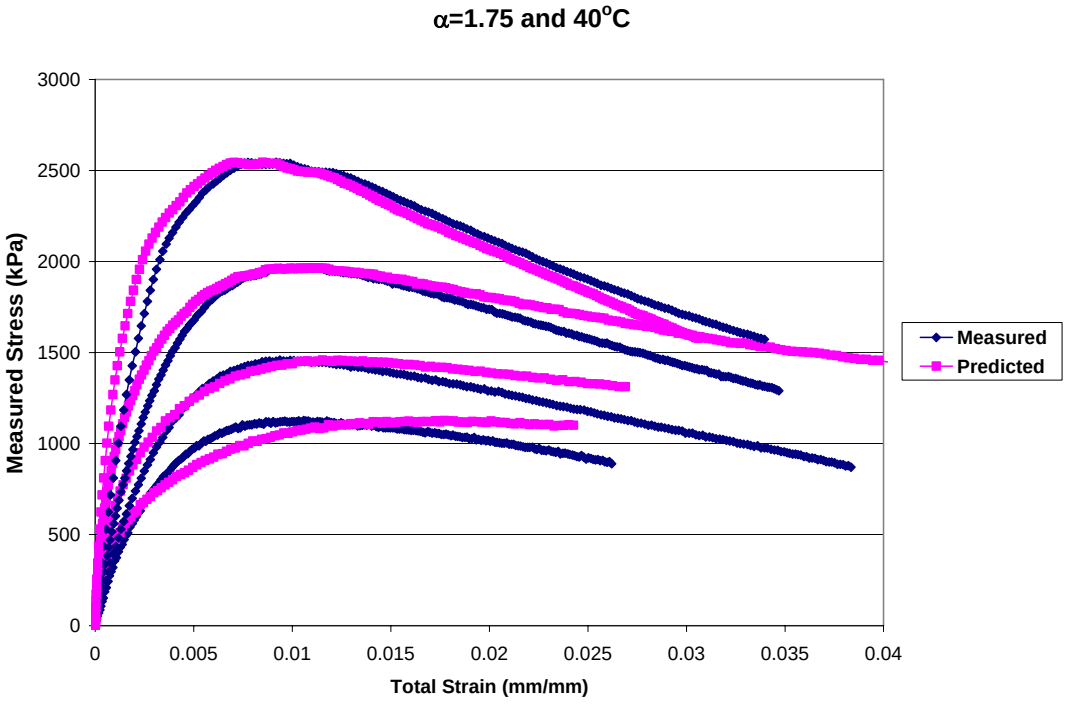

(a)

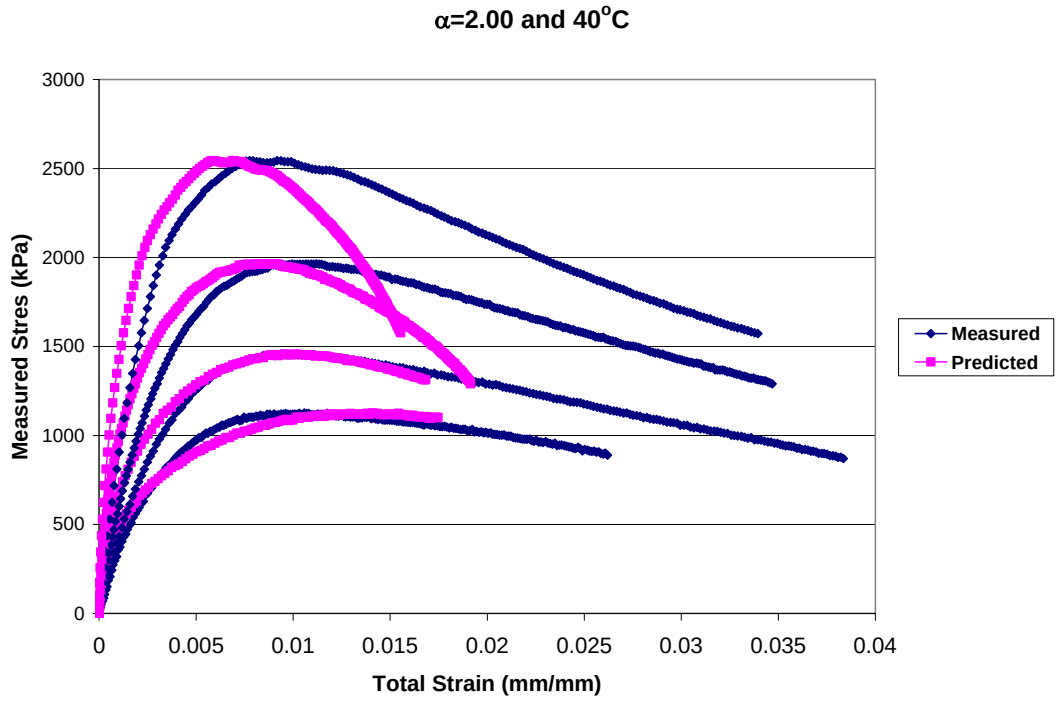

(b)

Figure 127. Measured stress versus predicted and measured total strain at 40°C for different damage evolution law exponents, (a) α=1.75 and (b) α=2.00.

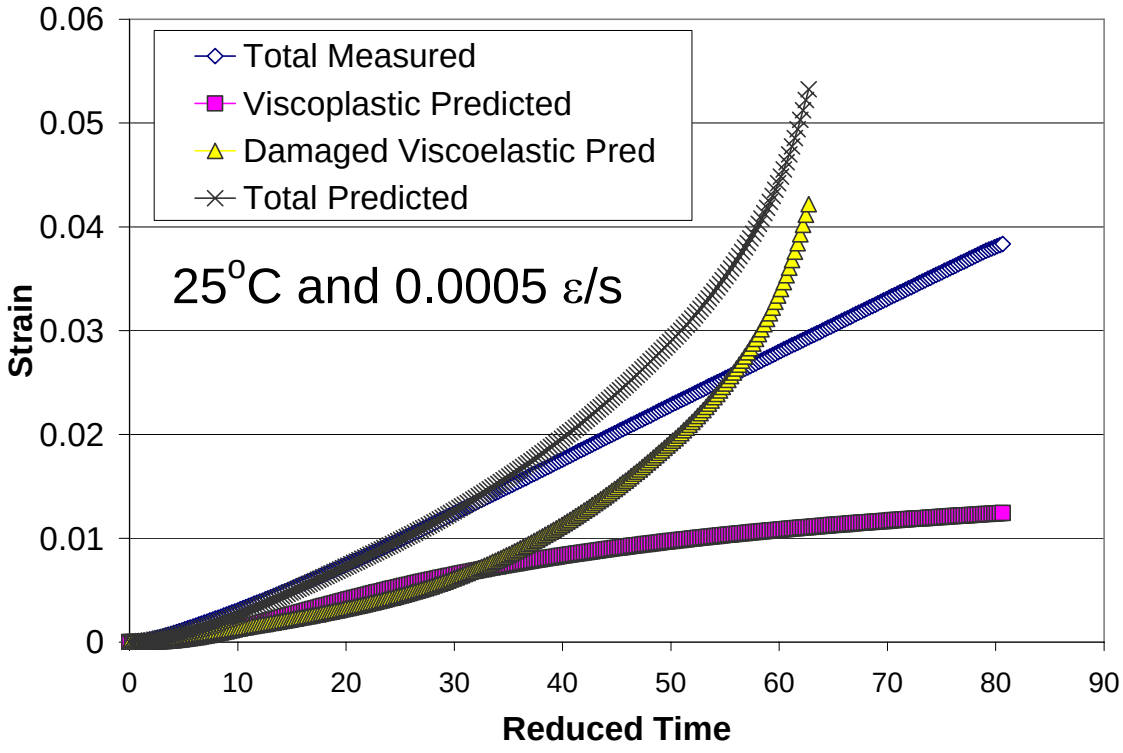

(a)

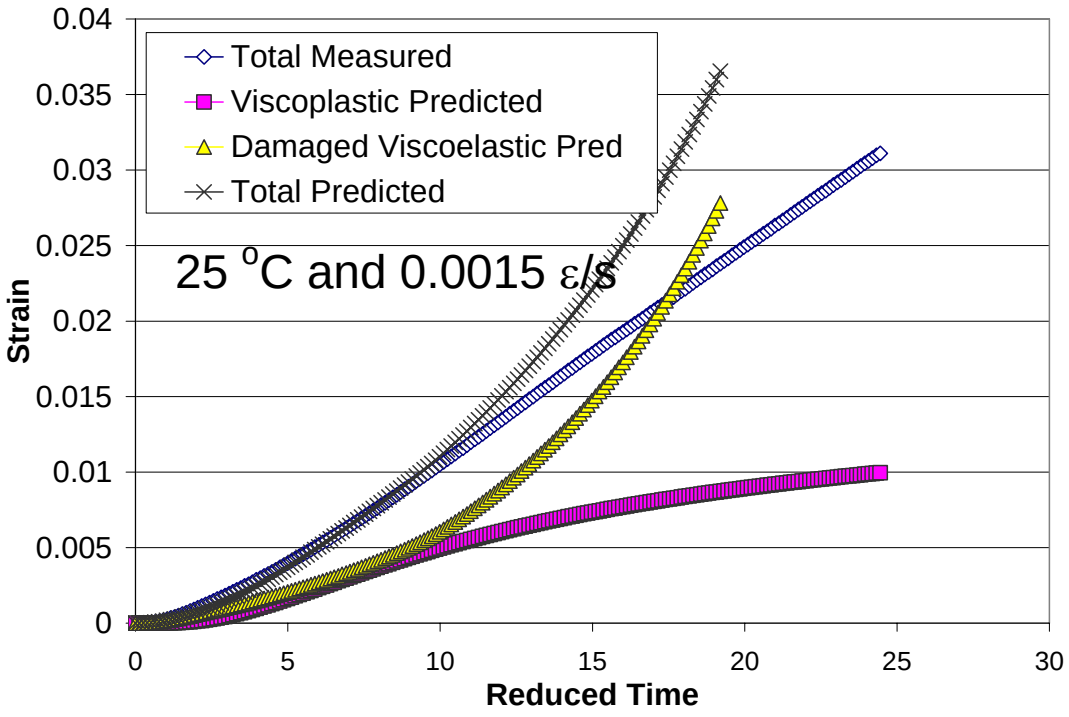

(b)

Figure 128. Individual predicted strain components from uniaxial constant strain rate tests at 25°C – two slowest strain rates.

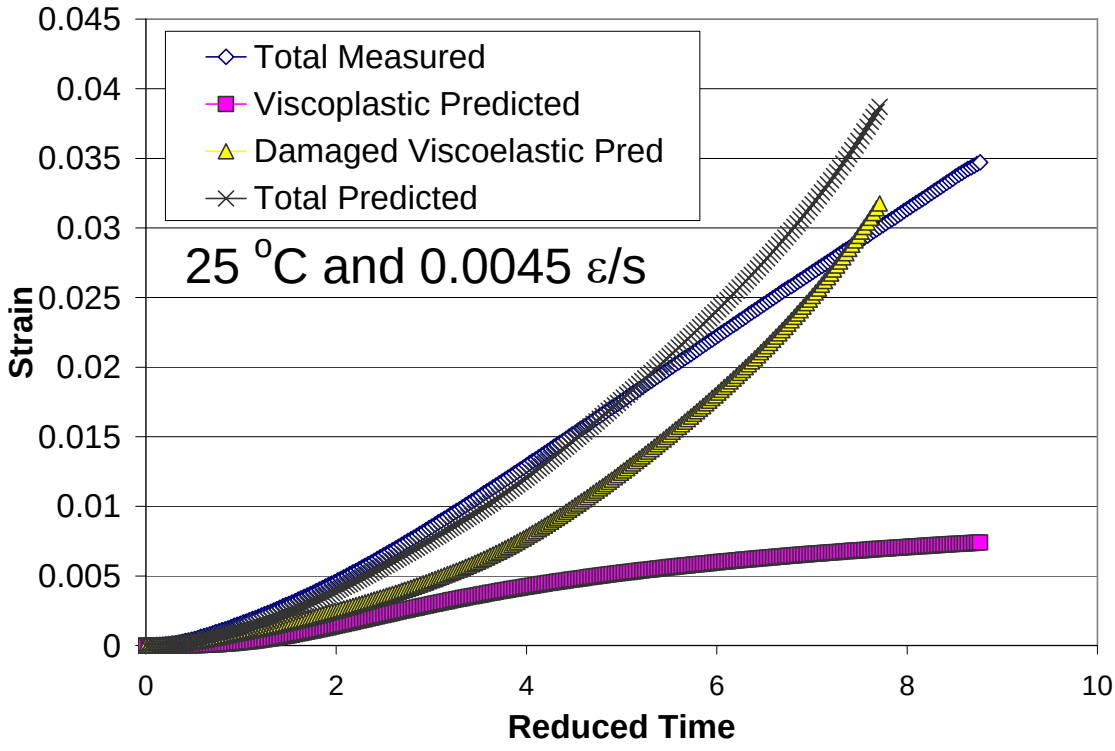

(a)

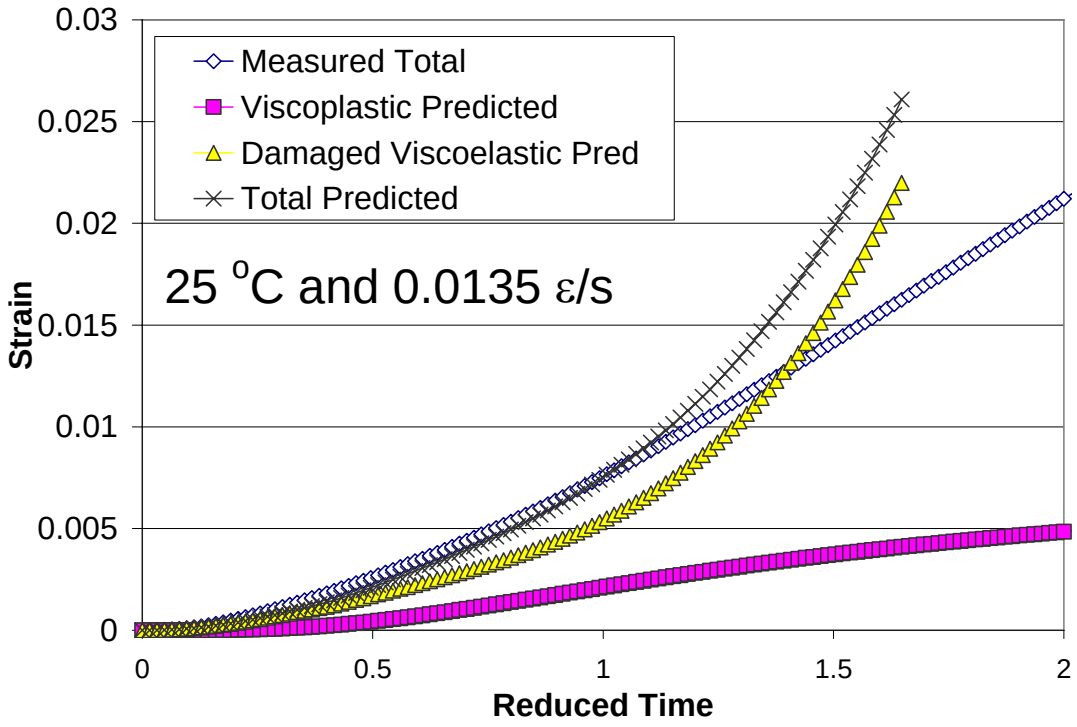

(b)

Figure 129. Individual predicted strain components from uniaxial constant strain rate tests at 25°C – two fastest strain rates.

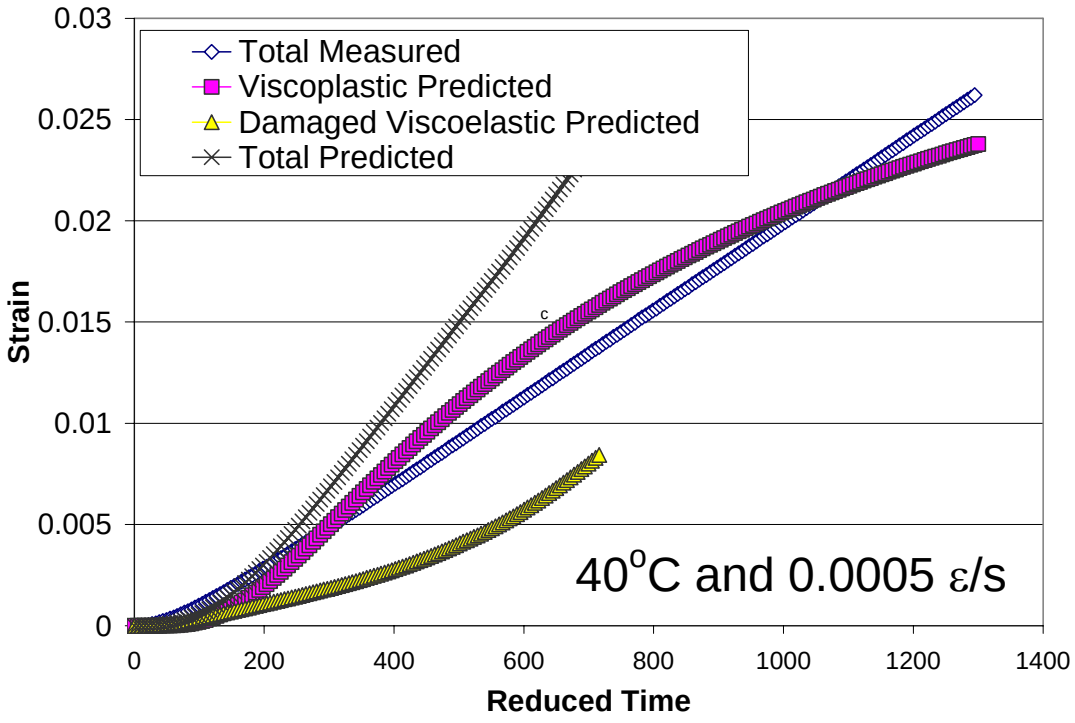

(a)

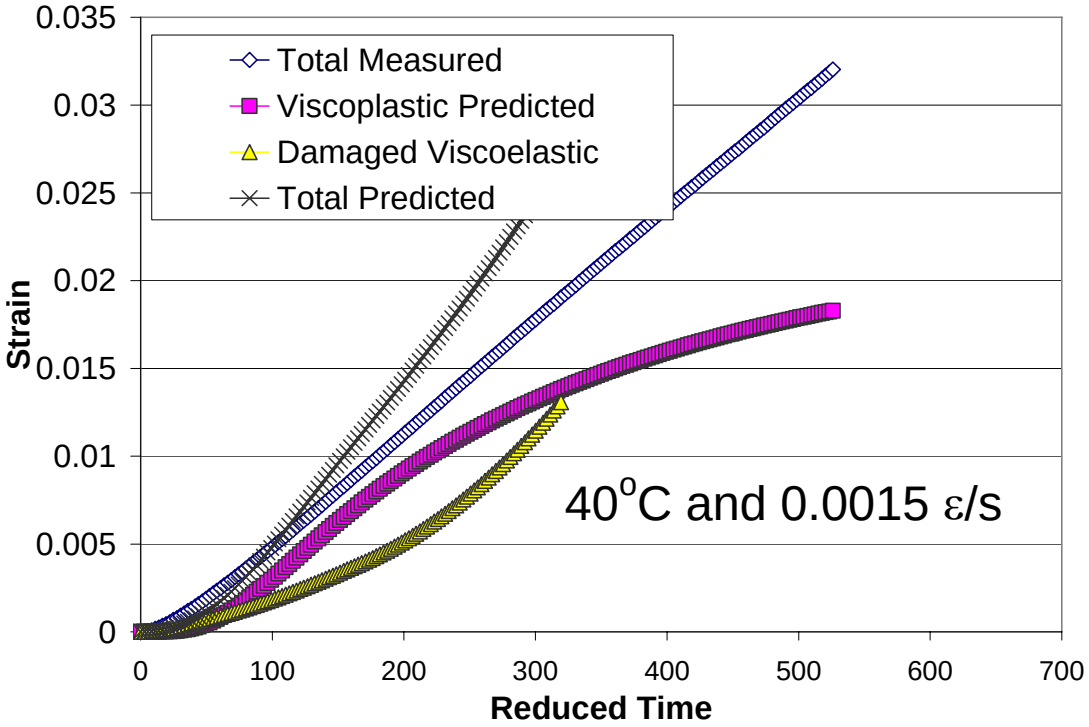

(b)

Figure 130. Individual predicted strain components from uniaxial constant strain rate tests at 40°C – two slowest strain rates.

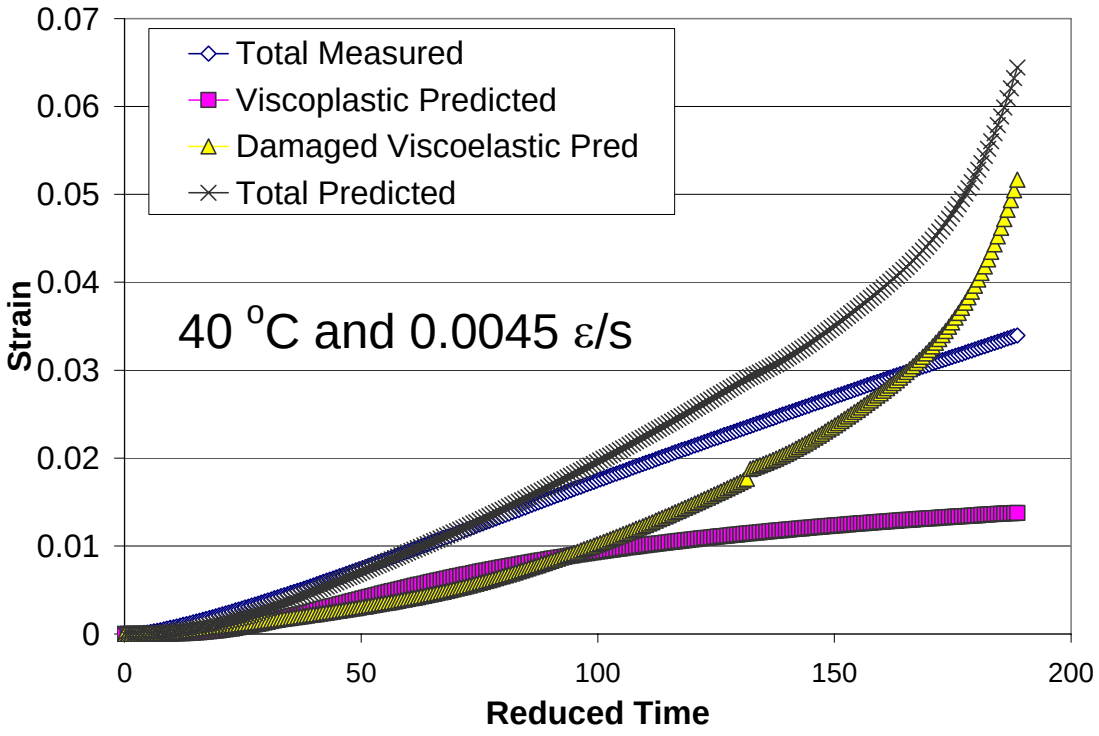

(a)

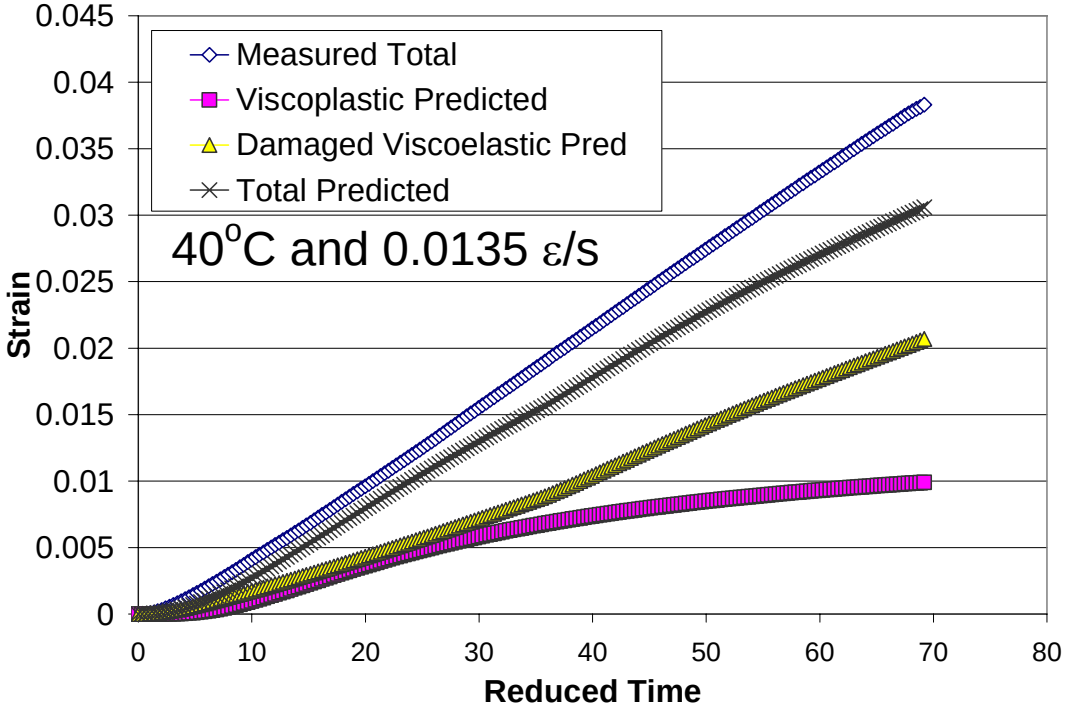

(b)

Figure 131. Individual predicted strain components from uniaxial constant strain rate tests at 40°C – two slowest strain rates.

8.2 Uniaxial Sensitivity

An abbreviated sensitivity analysis was completed to complement the model calibration and validation. Key model parameters considered included the viscoelastic creep compliance $D(t_R)$ and temperature shift factor $a(T)$, the viscoplasticity parameters p, q, and Y, and the α exponent for the damage model. The point of comparison was taken as the strain predicted at 75% of the peak measured stress for a monotonic constant strain rate test at the intermediate strain rate 0.0045ε/s and the two constant strain rate verification temperatures of 25 and 40°C. The average strain change $\Delta\varepsilon_{Avg}$ due to $\pm$20% perturbations of each model parameter is expressed in terms of a normalized sensitivity index $S.I.$ (see Figure 132 for notation):

$$\Delta\varepsilon_{Avg} = \frac{|\Delta\varepsilon_1| + |\Delta\varepsilon_2|}{2} \qquad \textbf{Equation 113}$$

$$S.I. = \frac{\Delta\varepsilon_{Avg}}{\varepsilon_{Calibrated}} \qquad \textbf{Equation 114}$$

These values are ranked by order of importance in Table 24. The predicted strains are clearly most sensitive to the viscoplastic model parameters, and of these, log$Y$ has the greatest effect on the predictions. The sensitivity of predictions to the other model parameters is dependent on the temperature and thus should also be dependent on strain rate via time-temperature superposition considerations.

Table 24. Sensitivity ranking of the individual model parameters.

Parameter Adjusted	Sensitivity Index $S.I.$	
	25°C 0.0045 ε/s	40°C 0.0045 ε/s
$\log Y$	2.700	4.01
q	1.014	1.275
p	0.178	0.233
α exponent	0.160	0.070
$D(t_R)$	0.135	0.110
$\log a(T)$ *	0.045	0.176

* $\log a(T)$ could not be adjusted at 25°C because it was the reference temperature so the actual t_R itself was adjusted

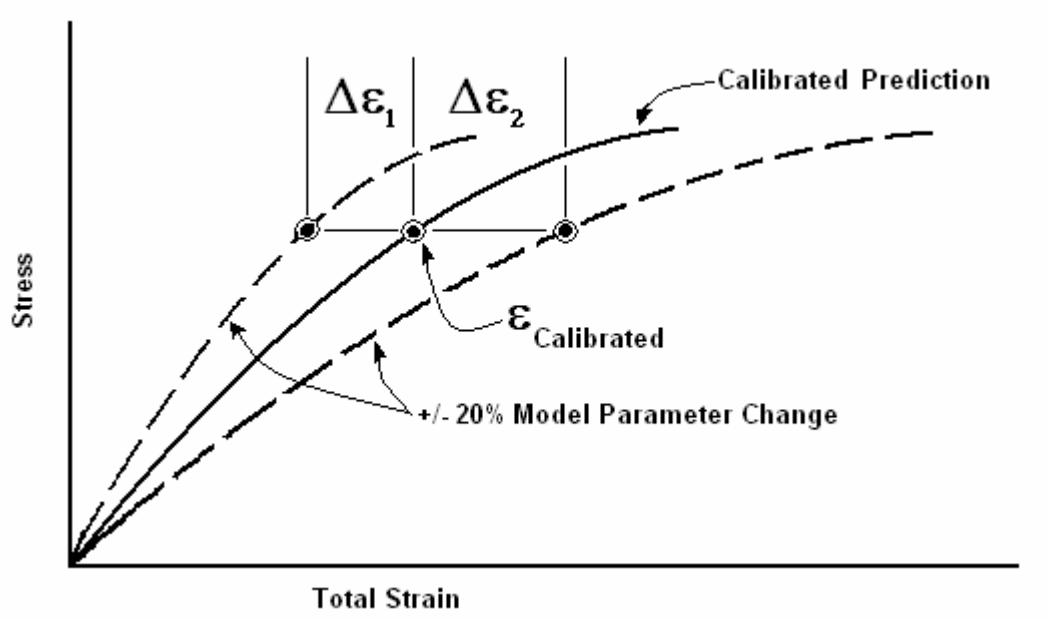

Figure 132. Schematic of total strain sensitivity to model parameter changes.

8.3 Independent Validation Tests

Four sets of independent validation tests were performed at the Arizona State University (ASU) asphalt material laboratories (Witczak and Sullivan, 2001; 2002). All of these tests used the same asphalt mixture that was used for the development and

calibration of the material model in the present study. Two of these tests, a standard repeated load permanent deformation and a random repeated load permanent deformation, strongly exercise the viscoplastic model under compressive loading. The specimen geometry and instrumentation employed in these independent validation tests were similar to those used at the University of Maryland in the calibration testing.

8.3.1 Repeated Load Permanent Deformation Tests

The repeated load permanent deformation test is a standard test performed on asphalt concrete mixtures to gauge resistance to rutting. The tests performed at ASU applied a 0.1 sec haversine load pulse followed by a 0.9 sec rest period at two cyclic stress and temperature combinations: 69 kPa at 37.8^{o}C (100^{o}F) and 30 kPa at 54.4^{o}C (130^{o}F). Recall the stresses are much higher in the calibration tests for the uniaxial viscoplastic model, which applied 1500 kPa at 25^{o}C and 35^{o}C and 936 kPa at 35^{o}C and 45^{o}C in the Fixed Stress tests and between 20 kPa and 1354 kPa at 35^{o}C in the Fixed Time tests.

The haversine load pulse induces a recoverable viscoelastic and a nonrecoverable viscoplastic deformation. The long rest period allows for recovery of the viscoelastic strain; any remaining strain at the end of the rest period is assumed to represent the nonrecoverable or permanent viscoplastic component. The comparisons of the predicted viscoplastic strains from the model against the permanent strains measured during the tests are the focus of the validation. A Matlab algorithm was used to calculate the predicted strain response over a measured stress history of 12,000 load cycles. The actual reported contact and pulsed stresses in the database for the independent tests were used in

the predictions. The measured stress histories at each temperature were converted from absolute to reduced time using the corresponding temperature shift factor from the large strain *a(T)* relation.

Comparisons of predicted vs. measured permanent strain for the repeated load permanent deformation tests are shown in Figure 133 and Figure 134 for 100^{o}F and 130^{o}F respectively. The model tends to under predict permanent strains slightly at 100^{o}F and over predict slightly at 130^{o}F. The 100^{o}F model predictions generally follow the measured response and lie within the minimum and maximum bounds. However, the measured response clearly shows an increase in strain hardening (flattening of the slope) with increasing load cycles while the model predicts a pure power law rate of strain hardening, linear log-log. The 130^{o}F model predictions again generally follow the measured response but are just inside the maximum bound for the measured data. The measured data also suggest a primary-secondary-tertiary permanent strain transition with increasing (flatter slope) and then decreasing (steeper slope) strain hardening; this behavior is not captured by the model. However, the overall trends between the model predictions and the measured test data are similar over the range of comparison.

Closer examination of the evaluation test data revealed some questions regarding the quality of the 130^{o}F test data, particularly at the higher *N* values. Figure 135 compares the measured ε_p versus *N* response in arithmetic space for each replicate at both 100 and 130^{o}F. The results at 100^{o}F are reasonable, albeit with a considerable amount of scatter among the replicates. Many of the individual replicate results at 130^{o}F show anomalous behavior, however. Considering each replicate in turn:

- *Specimen 506*: There is a sharp discontinuity in slope at about 4000 cycles, followed by an essentially linear increase in ε_p with *N*.
- *Specimen 510B*: Similar to A, but with the sharp discontinuity in slope occurring at about 2000 cycles. (Note: This specimen is not included in Figure 134.)
- *Specimen 516*: No evident anomalies in the data, but the curve falls along the average of the 100^{o}F tests. This suggests that the test may have been incorrectly labeled in the database and that it was performed at 100^{o}F instead of 130^{o}F.
- *Specimen 512*: Expected behavior. No evidence of tertiary failure.
- *Specimen 510*: Expected behavior. There is a moderately large change in slope at about 9000 cycles, but this may correspond to the onset of tertiary failure.
- *Specimen 511*: Expected behavior. Tertiary failure begins at around 9000 to 10000 cycles.

Based on these evaluations of the individual replicate data, Figure 136 compares the model predictions with measurements from the good test specimens only. Note that the spread between the minimum and maximum measured permanent strains is remarkably small after removing the poor quality data. The model predictions now closely match the primary stage of the response but still do not capture the increasing strain hardening (flatter slope) in the secondary stage or the decreasing strain hardening (steeper slope) in the tertiary stage.

Finally, Figure 137 compares the average measured response from the 100 and 130^{o}F repeated load permanent deformation tests. These tests were performed at different target deviatoric stresses as well as different temperatures, so the magnitudes of the permanent strains measured in each set of tests will be different. However, Figure 137

clearly shows that the initial strain hardening (slope of $\log\varepsilon_p$ versus $\log N$) is similar at both 100°F and 130°F. Both sets of data show a transition to increased strain hardening in the secondary stage. The 130°F data appear to have a slightly higher slope in the secondary stage, but the significance of this is difficult to evaluate because the 130°F data almost immediately transition to the tertiary stage. The conclusions drawn from these examinations are as follows:

1. The model provides predictions that are well within the ballpark of the measured response at both test temperatures.
2. The test data at both temperatures clearly indicate a transition from primary to secondary permanent deformation stages, with a subsequent (nearly immediate) transition to tertiary stage failure for the 130°F data. The model predictions do not mirror this behavior, nor can they given the current formulation of the model.
3. Strain hardening does not appear to be a function of temperature during the primary permanent deformation stage. This is consistent with the assumption of time-temperature superposition validity in the viscoplasticity formulation.

It is unclear whether strain hardening is a significant function of temperature during the secondary and tertiary permanent deformation stages. The secondary stage is very short in the 130°F tests, while the 100°F tests never reach the tertiary stage.

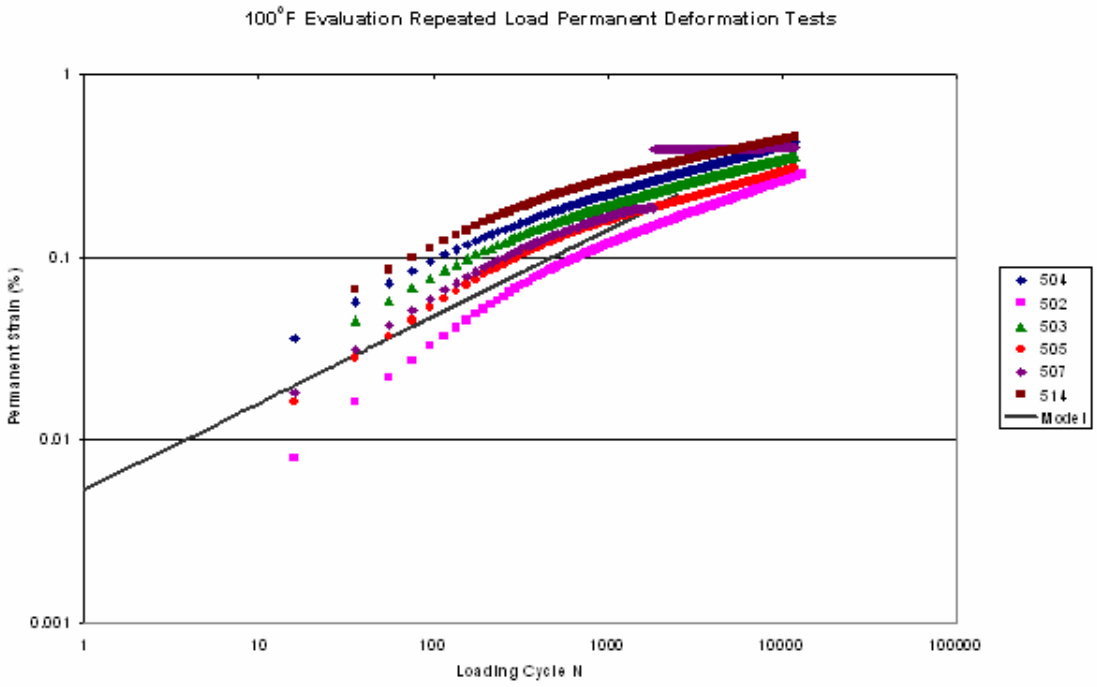

Figure 133. Comparisons between model predictions and measured response for repeated load permanent deformation tests at 100°F.

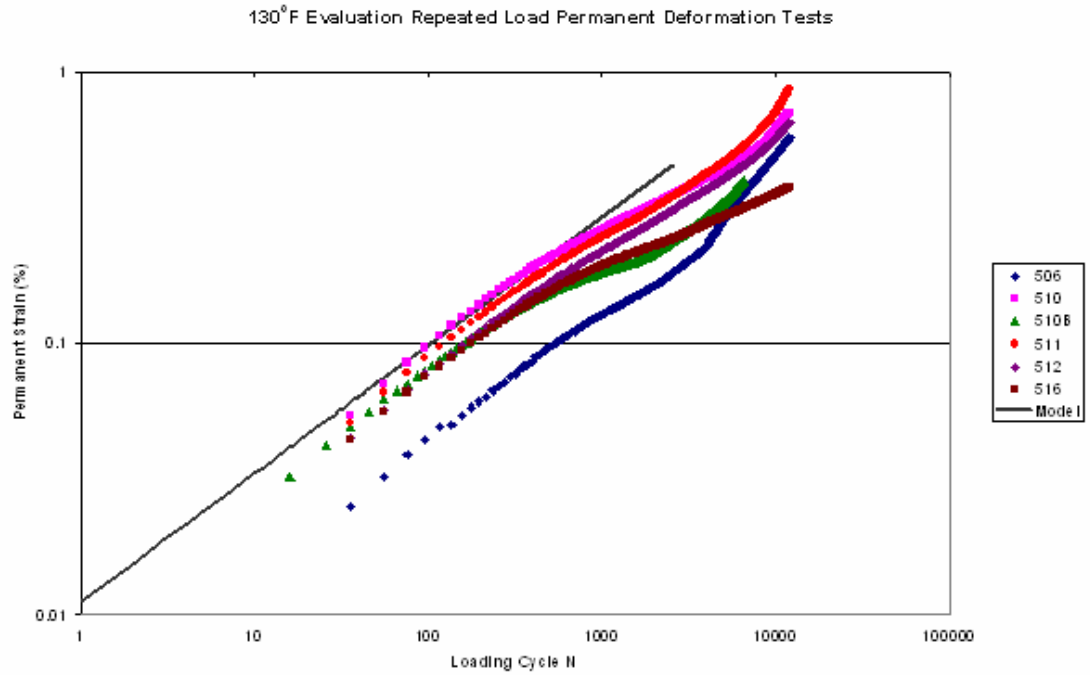

Figure 134. Comparisons between model predictions and measured response for repeated load permanent deformation tests at 130°F.

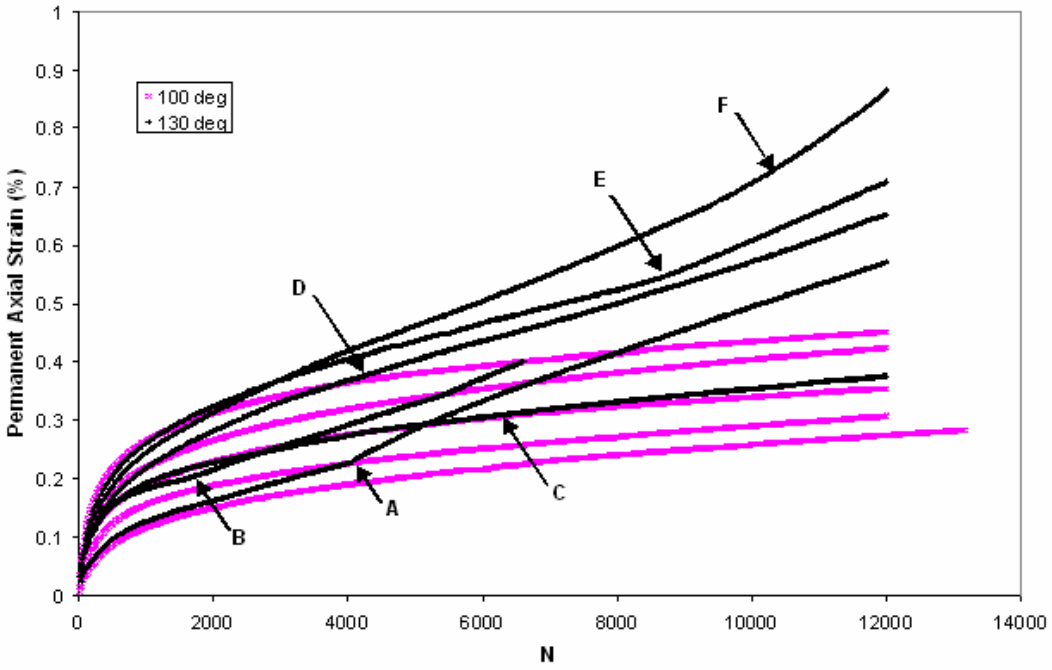

Figure 135. Individual replicate results for ^{100oF} and 130°F repeated load permanent deformation tests (arithmetic strain axis)

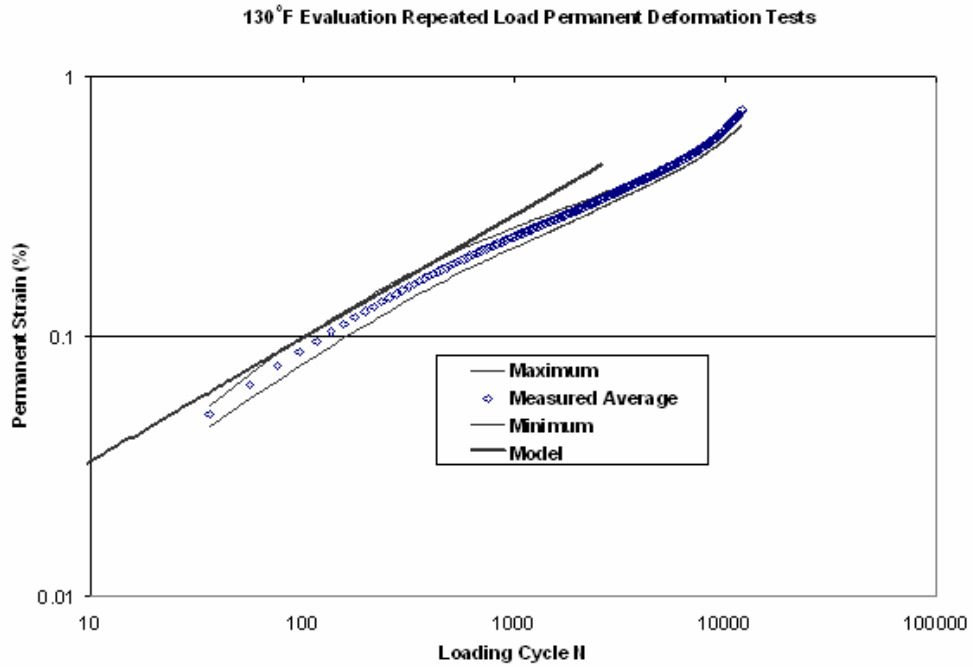

Figure 136. Measured and predicted permanent strains for 130°F repeated load permanent deformation tests (Specimens E/510, F/511, D/512 only).

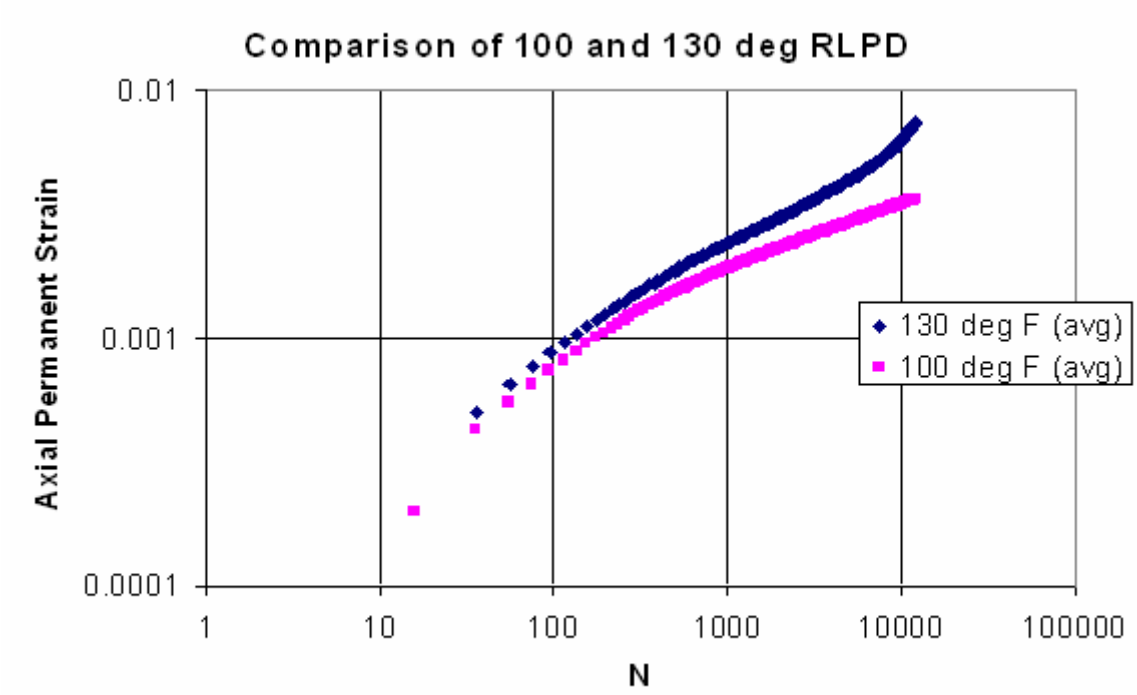

Figure 137. Comparison of average measured response from the 100°F and 130°F repeated load permanent deformation tests.

8.3.2 Random Repeated Load Permanent Deformation Tests

This series of uniaxial tests was performed at ASU at temperatures of 54.4°C (130°F) and 37.8°C (100°F). Loading consisted of three separate haversine stress histories followed by a recovery period. Table 25 summarizes the different load frequencies, stress levels and rest periods.

A typical measured total strain vs. time history for the three load cycles and rest periods from one of these tests is shown in Figure 138. A small viscoelastic recovery can be seen at the beginning of each rest period. Predicted strains were computed with the

same Matlab algorithm and material model calibration as for the conventional repeated load permanent deformation tests, but as evident in Figure 139 and Figure 140 the agreement between the predicted and measured values was much worse. The model consistently over predicted the viscoplastic strain except in the first load group at 37.8°C. These results clearly suggest that hardening in the model is insufficient under these conditions.

Table 25. Random Repeated Load Test Loading Cycles.

Load Group	Duration	Rate	Axial Stress (kPa)	
			54.4°C	37.8°C
1	630 cycles	10 Hz	34.5	69.0
2	5 min	Rest	0	0
3	500 cycles	0.1 Hz	86.2	172.4
4	10 min	Rest	0	0
5	2500 cycles	1.0 Hz	51.7	103.4
6	15 min	Rest	0	0

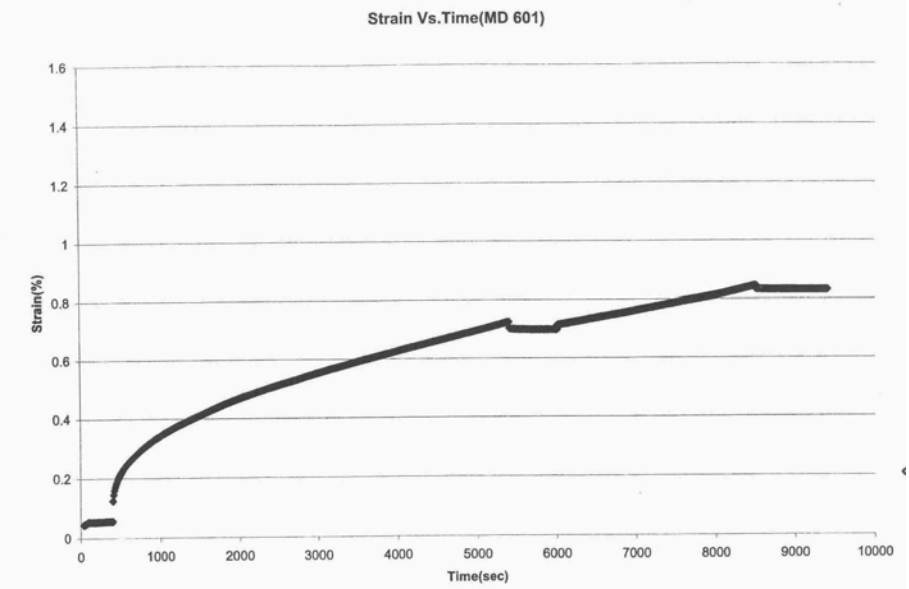

Figure 138. Typical measured tests result in random repeated load permanent deformation tests, 54.4°C.

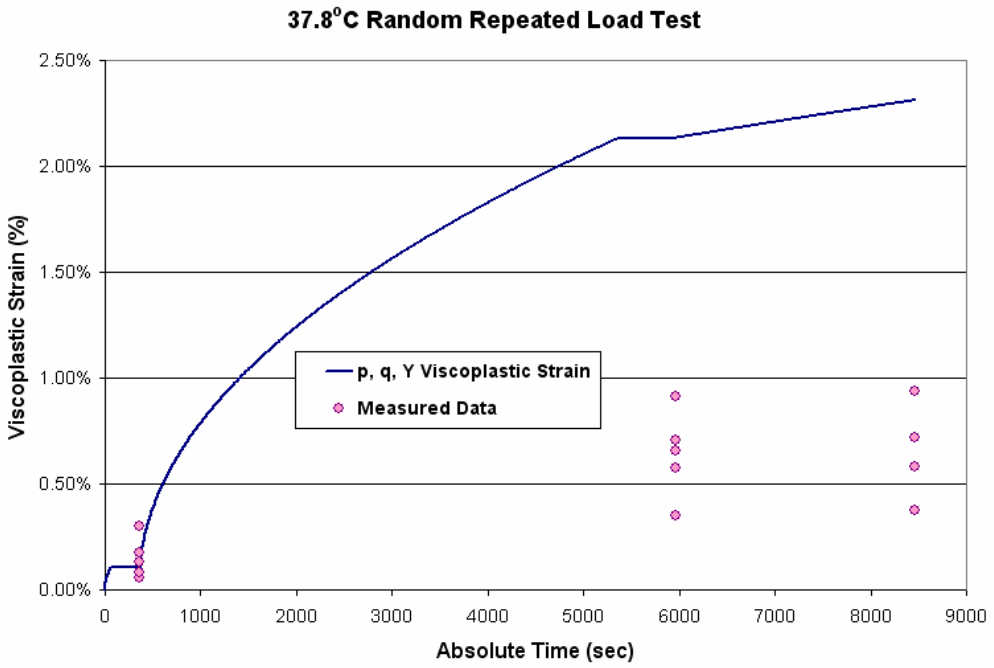

Figure 139. Viscoplastic prediction of 37.8°C random repeated load permanent deformation tests with measured results.

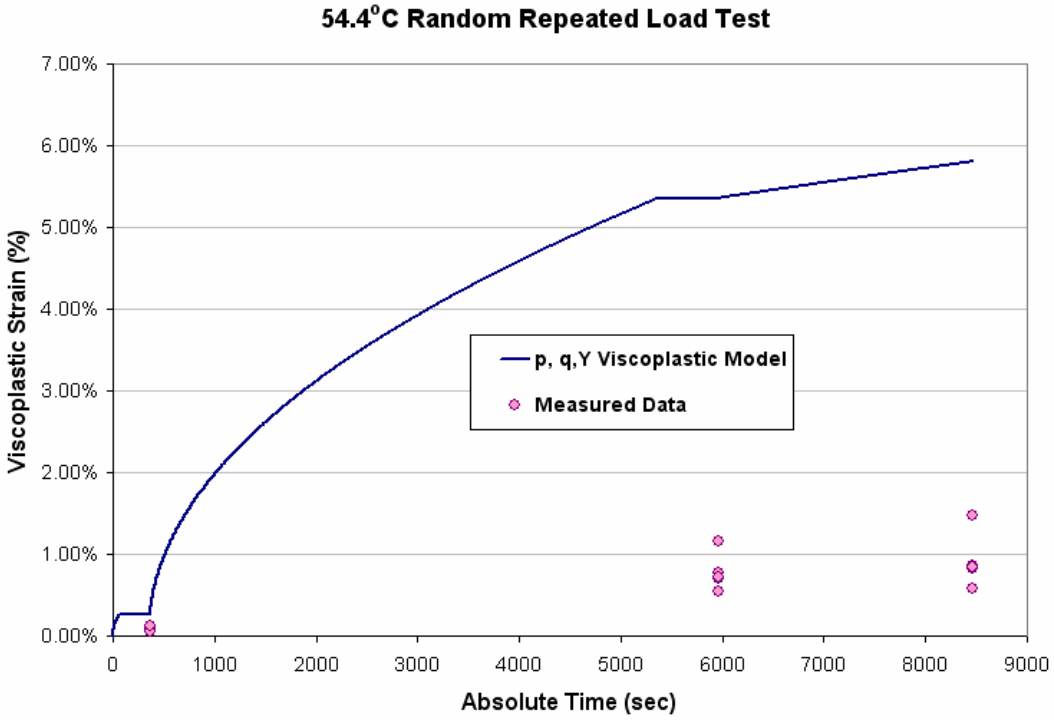

Figure 140. Viscoplastic prediction of 54.4°C random repeated load permanent deformation tests with measured results.

8.4 Summary and Conclusions

Two distinct types of comprehensive validation tests were performed to evaluate the ability of the model to predict asphalt concrete response over a wide range of loading characteristics. The first type, monotonic uniaxial controlled strain rate tests to failure, exercised all model components in the pre-peak, peak, and post-peak failure regions. The controlled strain rate tests at 25^{o}C emphasized the continuum damage component of the model. This component will be largely responsible for predicting cracking distresses, specifically fatigue. It is designed to capture the distributed microstructural damage that occurs before the initiation of macro cracking. Accurate prediction of the significant viscoplasticity that is also present in these tests was also required for a complete validation.

The 45^{o}C controlled strain rate tests push the viscoelastic continuum damage model to its limits. This temperature is probably the warmest of any relevance for cracking; at higher temperatures, the damage response becomes secondary to viscoplasticity. The power law based strain hardening and stress dependent viscoplasticity model provided realistic predictions of the material response in these high temperature tests.

The second type of validation tests focused on the abilities of the model to predict response under cyclic loading conditions more similar to field rutting. Two variations of these cyclic loading tests were performed: conventional repeated load permanent deformation tests, and random repeated load tests. Both types were conducted at

generally warmer temperature and lower stress conditions than used in the calibration tests.

The model predictions for the conventional repeated load permanent deformation tests were well within a very reasonable ballpark of the measured response and lie inside the measured variability at 100^{o}F and just at the upper boundary of the 130^{o}F variability. The model predictions from this stress history follow a power law and are thus linear in log-log space whereas the actual measured response from the validation tests showed a bilinear primary-secondary hardening. The model predictions essentially matched the measured slope in the primary hardening region; which was independent of temperature consistent with time-temperature superposition, but could not reproduce the secondary hardening.

Unfortunately, the model consistently and significantly overpredicted the measured strain response in the random repeated load tests. The poor validation results for the random repeated load test and need for more flexible primary-secondary hardening behavior in the conventional repeated load permanent deformation tests identifies areas where the model—specifically the viscoplastic model component—lacked the ability to simulate asphalt concrete realistically. The next chapter describes changes to the model in order to improve the viscoplastic strain prediction.

9. Continued Development of the Viscoplastic Model

The validation tests in Chapter 8 demonstrated the ability of the viscoelastic continuum damage model to predict asphalt concrete response under low and moderate temperatures under both uniaxial and multiaxial conditions. Unfortunately, the viscoplastic model exhibited flaws under some situations, most notably in the high temperature low stress repeated load permanent deformation tests. This chapter describes modifications to the existing uniaxial model that were made in an attempt to remedy these problems. In the end, the original, uniaxial model was judged to be inadequate, and a new alternative model based on Perzyna viscoplasticity theory was adopted. The formulation, calibration, and validation of this new viscoplastic model component is documented in this chapter.

9.1 Bilinear Enhancement of Viscoplastic Hardening Law

Based on the analyses of the independent validation tests, attempts were made to modify the viscoplasticity hardening law to better capture the transition from primary to secondary (and ideally tertiary) permanent deformation behavior. Additional potential changes to allow the strain hardening rate (i.e., slope of the $\log\varepsilon_p$ vs. $\log N$ curve) to vary

with temperature were disregarded, in part because of the inconclusive experimental evidence (Figure 137) and in part because of the other results in the overall study that indicated the validity of time-temperature superposition for the viscoplastic response (Chapter 5).

The simplest hardening model enhancement that incorporates a transition from primary to secondary behavior is a bilinear form (in $\log\varepsilon_p$ vs. $\log N$ space):

$$\dot{\varepsilon}_{vp} = \frac{\sigma^q}{Y_1 \varepsilon_{vp}^{p_1}} \quad \varepsilon_{vp} \le \varepsilon_{vpt} \qquad \textbf{Equation 115}$$

$$\dot{\varepsilon}_{vp} = \frac{\sigma^q}{Y_2 \varepsilon_{vp}^{p_2}} \quad \varepsilon_{vp} > \varepsilon_{vpt} \qquad \textbf{Equation 116}$$

in which ε_{vpt} is the accumulated plastic strain at the transition from primary to secondary permanent deformation response. Note that Equation 115 and Equation 116 can be easily generalized to include the transition from secondary to tertiary response. Equation 115 and Equation 116 also assume that the stress exponent q is the same for the primary and secondary stage response. This too can be easily generalized, and it might be one way to incorporate an increase in the $\log\varepsilon_p$ vs. $\log N$ secondary stage slope with temperature should additional test data prove this to be a desirable additional enhancement.

A simple relation was found to backcalculate strain-related hardening law parameters p_1 and p_2 in Equation 115 and Equation 116 from the estimated $\log\varepsilon_p$ vs. $\log N$ slopes in the repeated load permanent deformation tests:

$$p_i = \frac{1}{slope_i} - 1 \qquad \textbf{Equation 117}$$

This is shown schematically in Figure 141, where the values prior to the transition and after were averaged to get an overall composite between the 100°F and 130°F tests. The

remaining model parameters to be found are the transition strain level ε_{vpt}, stress exponent q, and bilinear scaling constants Y_1 and Y_2. These model parameters were calibrated using the Fixed Stress cyclic creep and recovery tests. In reality, the transition strain level ε_{vpt} is not directly calibrated but is determined by q, Y_1, and Y_2. The backcalculated and calibrated values for all parameters are summarized in Table 26. As shown in Figure 142 and Figure 143, the quality of the calibrations was good for the 25/35°C, σ = 1525 kPa Fixed Stress test set and quite good for the 35/45°C, σ = 936 kPa test set.

Table 26. Bilinear model parameters found from mixture between 100°F and 130°F repeated load permanent deformation tests and Fixed Stress tests.

ε_{vpt}	q	p_1	p_2	$\log Y_1$	$\log Y_2$
0.00764	1.88	0.734	2.38	11.32	15.10

Recall that the corresponding values originally determined from the Fixed Stress and Fixed Time creep and recovery tests were p = 1.122, q = 2.074 and $\log Y$ = 12.982. The new stress exponent of 1.89 in the bilinear model is very close to the conventional linear exponent of 2.00 suggesting viscoplastic hardening in this approach is less sensitive to stress effects.

Figure 144 shows the predictions of the repeated load permanent deformation test with the conventional (dashed line) and enhanced (solid line) bilinear viscoplastic models. The enhancement brings the model predictions only slightly closer to the actual behavior by reducing the under predictions early in the response. The backcalculated transition strain is only achieved in the 130°F predictions and not at 100°F. One practical complication in calibrating the bilinear viscoplastic hardening model is that the transition

between primary and secondary (and tertiary) permanent deformation response is not as well defined in the Fixed Stress and Fixed Time viscoplastic creep and recovery tests as it is in the repeated load permanent deformation tests. Consequently, repeated load permanent deformation tests may need to be added to the set of model characterization tests, either to supplement Fixed Stress and Fixed Time tests or perhaps as a partial replacement.

A further analysis was done for two purposes. The first was to fully reverse the model calibration and obtain all bilinear model parameters from the repeated load permanent deformation tests (except q being fixed at 2.074) and then validate these parameter values using predictions of the Fixed Stress cyclic creep and recovery tests. The second purpose was to check the viscoplastic strain prediction algorithm using both the conventional and bilinear models. Only data from the 100^{o}F repeated load permanent deformation tests were used. The calibration parameters determined from the repeated load permanent deformation tests are summarized in Table 27. Note that the transition strain from the reverse calibration procedure is about five times smaller then previous. The exact agreement between the bilinear predictions in Figure 145 from the two linear fits verifies the viscoplastic algorithm, however the poor predictions for the cooler Fixed Stress test results in Figure 146 exhibit magnified over prediction and then under prediction and demonstrate that the bilinear enhancement is still insufficient to accurately describe universal viscoplastic behavior. Therefore, a revised strain hardening formulation was investigated as an alternative to the power law based linear and bilinear laws.

Table 27. Bilinear model parameters found from 100°F repeated load permanent deformation data only.

ε_{vpt}	q	p_1	p_2	$\log Y_1$	$\log Y_2$
0.00162	2.074	0.953	3.402	12.01	19.20

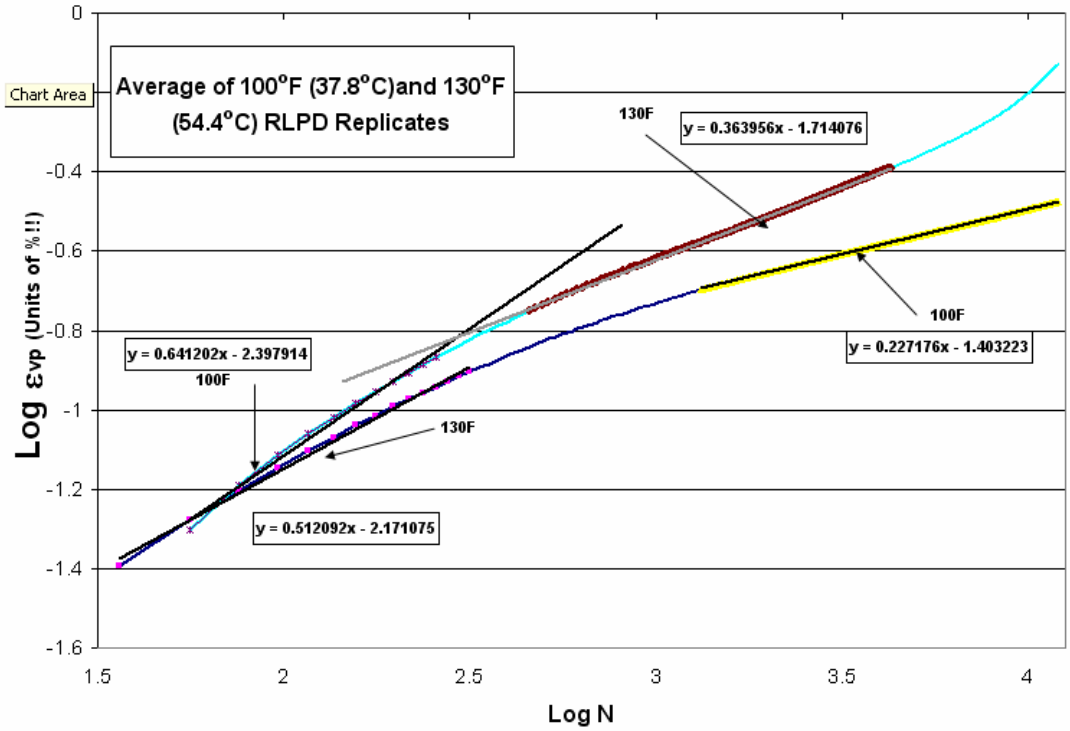

Figure 141. Schematic of method for extracting p exponent values from slopes of repeated load permanent deformation tests.

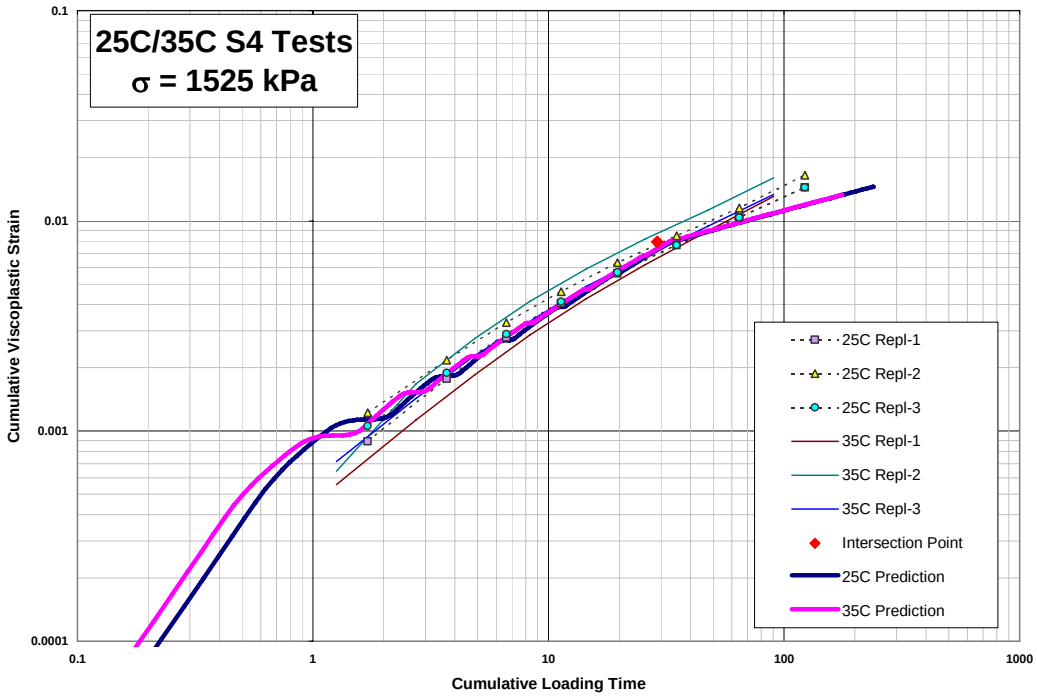

Figure 142. Enhanced bilinear calibration with Fixed Stress creep and recovery tests at 25/35°C and 1500 kPa.

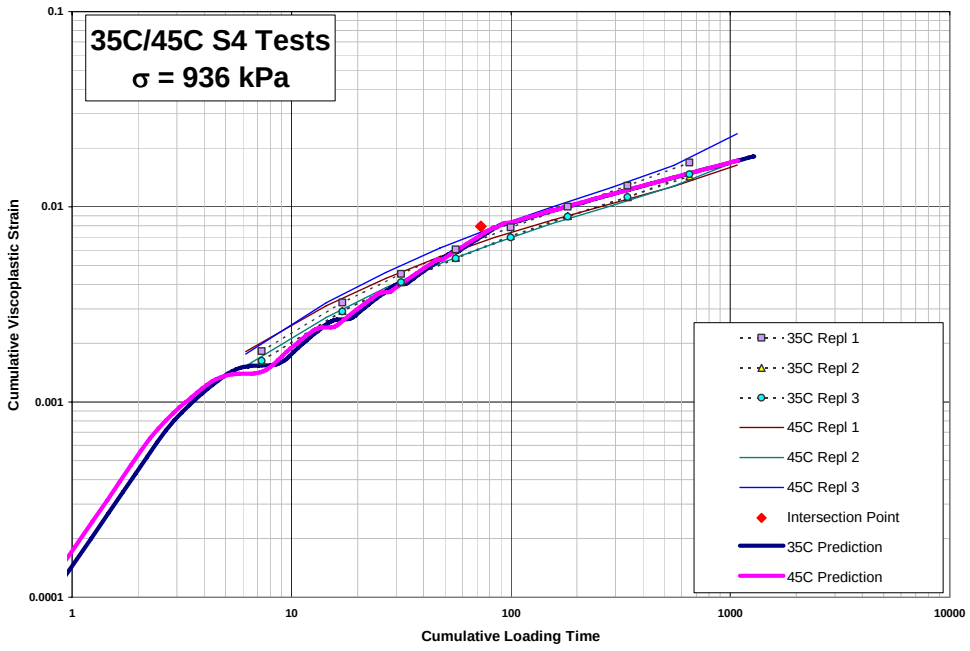

Figure 143. Enhanced bilinear calibration with Fixed Stress creep and recovery tests at 35/45°C and 936 kPa.

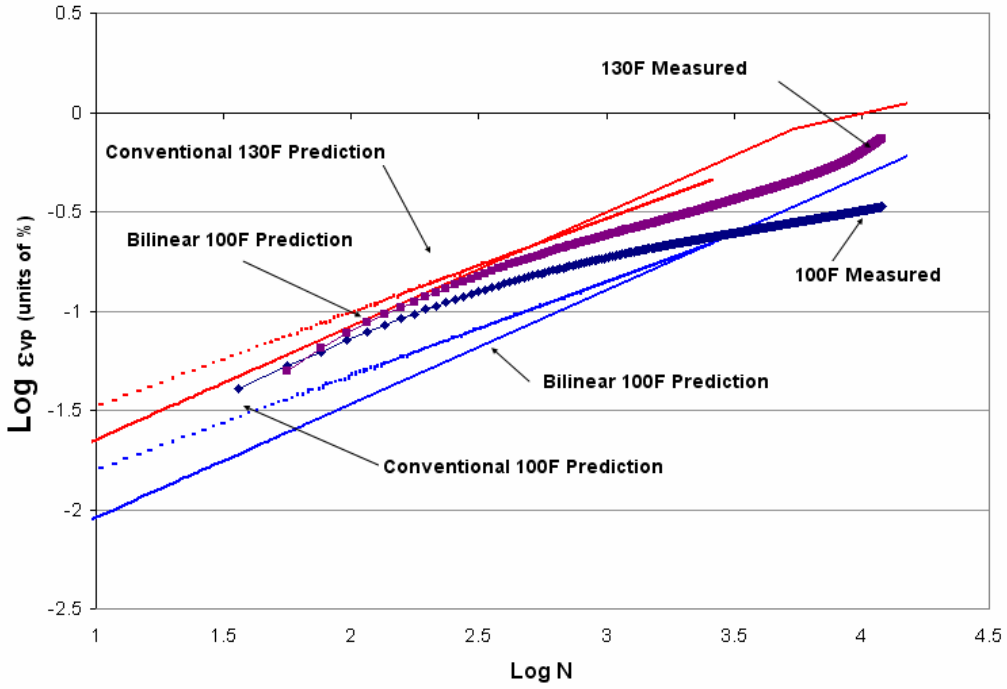

Figure 144. Repeated load permanent deformation predictions with enhanced bilinear hardening law.

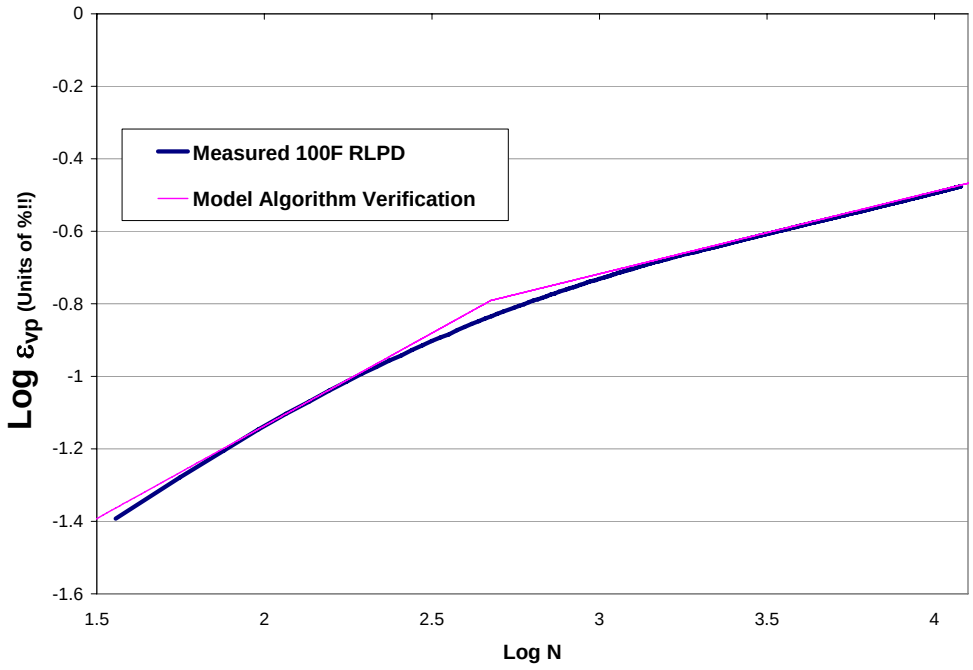

Figure 145. Verification of viscoplastic model algorithm with all enhanced model constants determined with primary and secondary slope and intercept from repeated load permanent deformation tests.

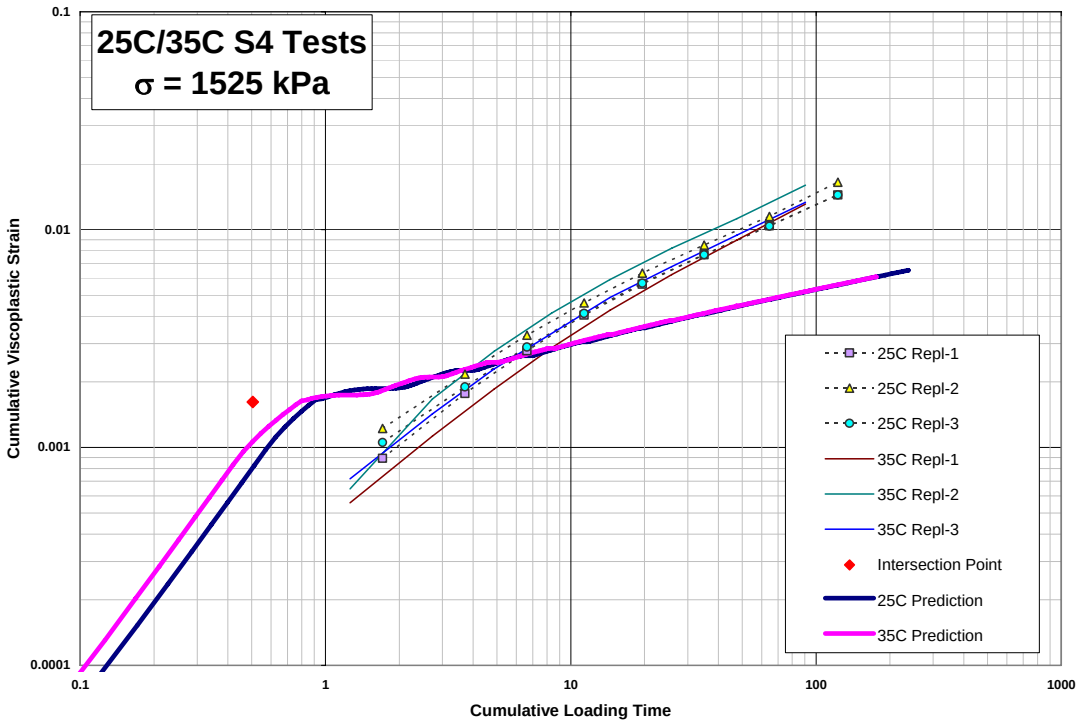

Figure 146. Fixed Stress test prediction with bilinear model fully calibrated from 100°F repeated load permanent deformation test data.

9.2 Cross Plotting to Derive Hardening Functions

The original viscoplastic strain rate model has been shown to have difficulty capturing some of the behavior typically observed in repeated load permanent deformation tests. Kim and Chehab (2002) based on suggestions by Schapery outlined an approach for evaluating the viscoplastic response more generally in an effort to extract the correct functional form for the numerator and denominator of viscoplastic rate model. Recall that the original viscoplastic strain rate relation employed in this study is of the following form:

$$\dot{\varepsilon}_{vp} = \frac{B\sigma^{q}}{A\varepsilon_{vp}^{p}} \qquad \textbf{Equation 118}$$

This relation can be expressed more generally as:

$$\dot{\varepsilon}_{vp} = \frac{f(\sigma)}{g(\varepsilon_{vp})} \qquad \textbf{Equation 119}$$

in which $f(\sigma)$ captures the nonlinear stress dependence of the viscoplastic response and $g(\varepsilon_{vp})$ is the strain hardening relation. Note that Equation 119 makes no assumption regarding the functional form of the stress dependence and strain hardening other than that their effects are separable. Both $f(\sigma)$ and $g(\varepsilon_{vp})$ can be inferred from constant strain rate monotonic tests as shown schematically starting in Figure 147, where each curve i corresponds to a different rate.

Assuming that the viscoelastic damage portion of the model has already been calibrated, the damaged viscoelastic strains ε_{ve} can be subtracted from the total strains measured in the constant rate tests to permit plotting of viscoplastic strain ε_{vp} versus reduced time ξ (alternative symbol for t_R) and stress σ versus viscoplastic strain ε_{vp} as shown in Figure 148. For each strain rate at a given viscoplastic strain level $\bar{\varepsilon}_{vp}$, corresponding values of viscoplastic strain rate $\dot{\varepsilon}_{vp}$ and stress σ can be determined.

Equation 119 can be rearranged as follows:

$$f(\sigma) = \dot{\varepsilon}_{vp} g(\varepsilon_{vp}) \qquad \textbf{Equation 120}$$

At any particular viscoplastic strain level $\bar{\varepsilon}_{vp}$, $g(\varepsilon_{vp})$ is a constant and the pairs of corresponding $\dot{\varepsilon}_{vp}$ and σ values (Figure 148) can be plotted as in Figure 149. Various $f(\sigma)$ can be developed corresponding to different levels of $\bar{\varepsilon}_{vp}$. These curves can all be

inverted and plotted in log-log space as shown in Figure 150. If the curves in Figure 150 are geometrically similar and can be shifted horizontally, the resulting master curve is the inverse of $\log f(\sigma)$ and the shift factors are equal to $\log g(\varepsilon_{vp})$ in Figure 151 at the various viscoplastic strain levels $\bar{\varepsilon}_{vp}$.

The analysis approach described above has been applied to the unconfined compression tests at 40°C and 25°C discussed in Chapter 5 for the time-temperature superposition study and in Chapter 8 as validations of the viscoplastic and damage models. As an example, the 40°C data are shown in Figure 152 after damage and viscoelasticity have been removed. Some liberties must taken with this approach in that the original viscoplastic model was used to calibrate the damaged viscoelastic response which is then used to separate damaged viscoelastic response from the total response at 25°C and 40°C to yield viscoplastic data for the present analysis. However, viscoplasticity is much smaller at the low temperature used for calibrating the damage model, so there is some confidence in the accuracy of the remaining viscoplastic strains computed in this analysis.

There is an initial viscoplastic strain of about 0.006 that was predicted with the original viscoplastic model as induced from the preceding dynamic modulus frequency sweeps. The average measured permanent strain from the 40°C frequency sweeps was 0.0048 and a standard deviation of 0.0015. At 25°C there was an initial viscoplastic strain of 0.003 predicted by the original model. The average measured permanent strain measured from the 25°C frequency sweeps was 0.0042 and a standard deviation of 0.0006.

The 25°C and 40°C unshifted plots of $\log\sigma$ versus $\log\dot{\varepsilon}_{vp}$ strain rate (Figure 150) at various viscoplastic strain levels from these tests are shown in Figure 153; Figure 154 shows these plots after shifting with the shift factors (Figure 151) in the inset. Key observations from these figures include the following:

- Smooth master curve and shift functions were developed, but unfortunately neither the stress nor strain function master curves at each temperature aligned well.
- The linear trend (in log-log space) for the $f(\sigma)$ relation in Figure 154 suggests that the power law form originally assumed for this term in Equation 118 is justified.
- The nonlinear trend (in log-log space) for the $g(\varepsilon_{vp})$ relation in the inset of Figure 155 suggests that the power law form originally assumed for this term in Equation 118 is not justified. However, the concave downward relation suggests decreasing strain hardening with increasing viscoplastic strains, which is just the opposite of what is commonly observed in repeated load permanent deformation tests.

It could be possible that the initial viscoplastic strain masks the expected concave upward stain function shift factor, causing both the shifted stress and strain functions to be non-colinear. The analysis was repeated with a different initial viscoplastic strain representing the average unrecovered strain measured from the frequency sweeps, 0.0048 at 40°C and 0.0042 at 25°C. These results are shown in Figure 155 and Figure 156. Although this method did not align the stress master curves at the two temperatures, they are closer than the previous analysis. The strain function (shift factors) also improved.

These results suggest there is probably an initial strain at each temperature different from the predicted and averaged measured that will make the stress and strain function collapse.

In light of the initial disturbances in the constant strain rate test data from the frequency sweeps and the apparent effect on the master curve analysis, a complementary calibration of the Fixed Stress and Fixed Time tests was performed based on the second and third observations above. The numerator term in the hardening law (Equation 119) was fixed as a power law with coefficients from the average of the slope and intercepts from the log-log linear fits in Figure 155. A different functional form for the denominator was implemented and then fit to the data assuming that perhaps the concave-up behavior did occur in Figure 156 before the subsequent concave down behavior. A sigmoid function having characteristics of concave up then concave down was used. There was extreme difficulty in finding an acceptable fit to both measured Fixed Time and Fixed Stress data with this approach. When only one type of test data was included in the optimization and the fit was satisfactory, the resulting prediction of the other test type was very poor. The most these analyses can offer is that independent stress functions and strain functions cannot be used. In other words, stress and strain cannot be separated from one another in order to accurately model viscoplastic deformations in asphalt concrete at large and small stresses with the same *pqY* model.

In conclusion, the original *pqY* viscoplasticity model formulation was the "best" of the variations investigated in that it adequately captured the viscoplastic response in the cyclic creep and recovery and controlled strain rate to failure validation tests. Nevertheless, this "best" formulation was still unable to capture key aspects of the

repeated and random load permanent deformation validation tests, in particular the complex hardening observed in these high-cycle low-stress tests. None of the enhancements examined for the original *pqY* model were able to address this deficiency. Consequently, a completely different viscoplastic model formulation was explored. This is described in the next section.

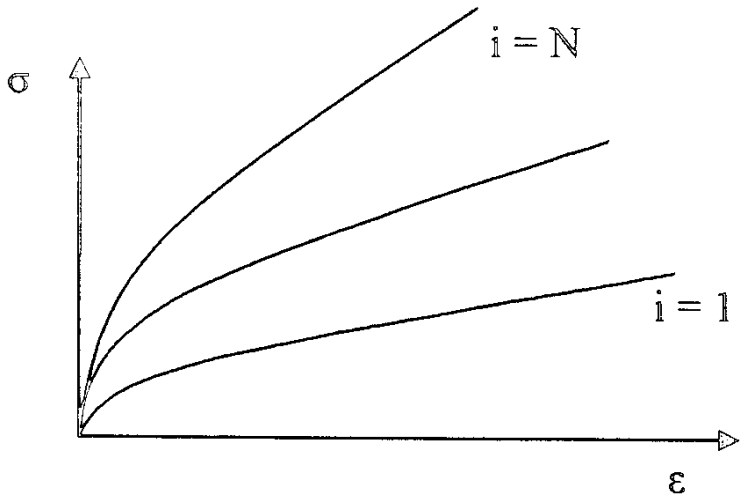

Figure 147. Schematic of stress versus viscoplastic strain results from constant rate tests.

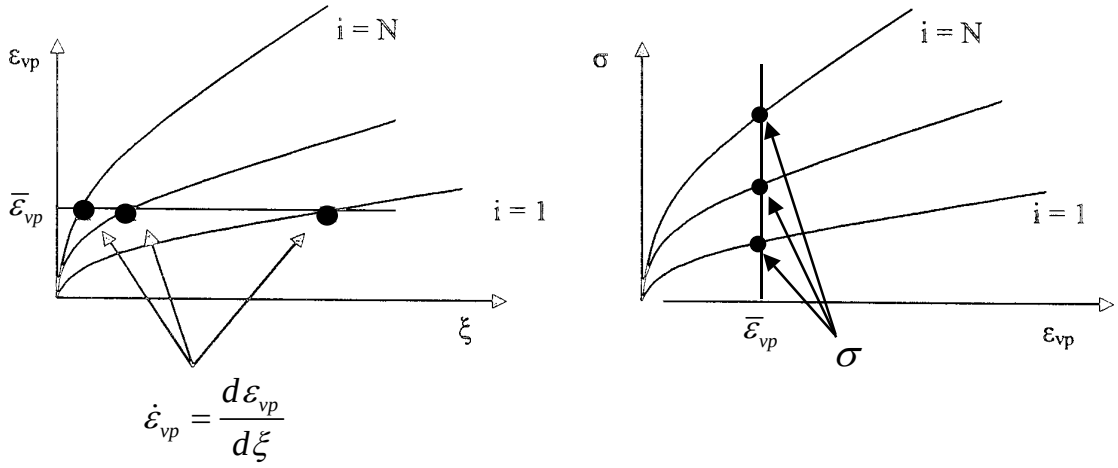

Figure 148. Viscoplastic strain versus reduced time and stress.

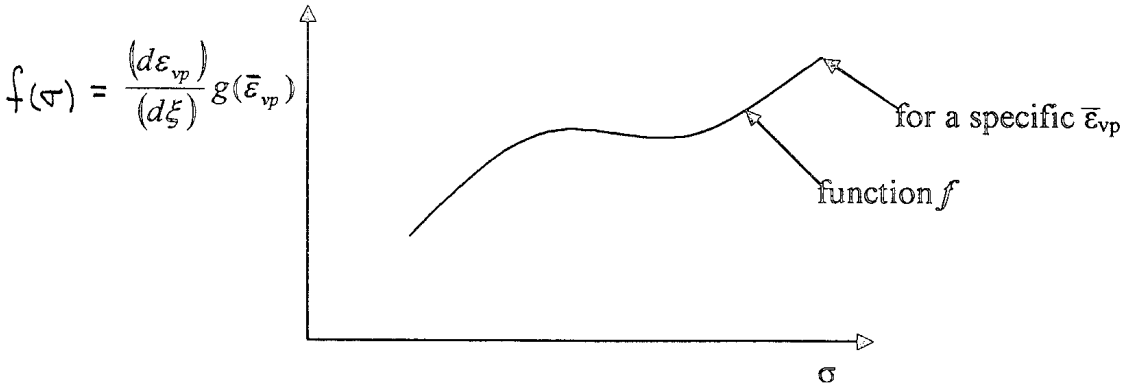

Figure 149. Plot of $f(\sigma)$ versus σ at given viscoplastic strain level (from data in Figure 148).

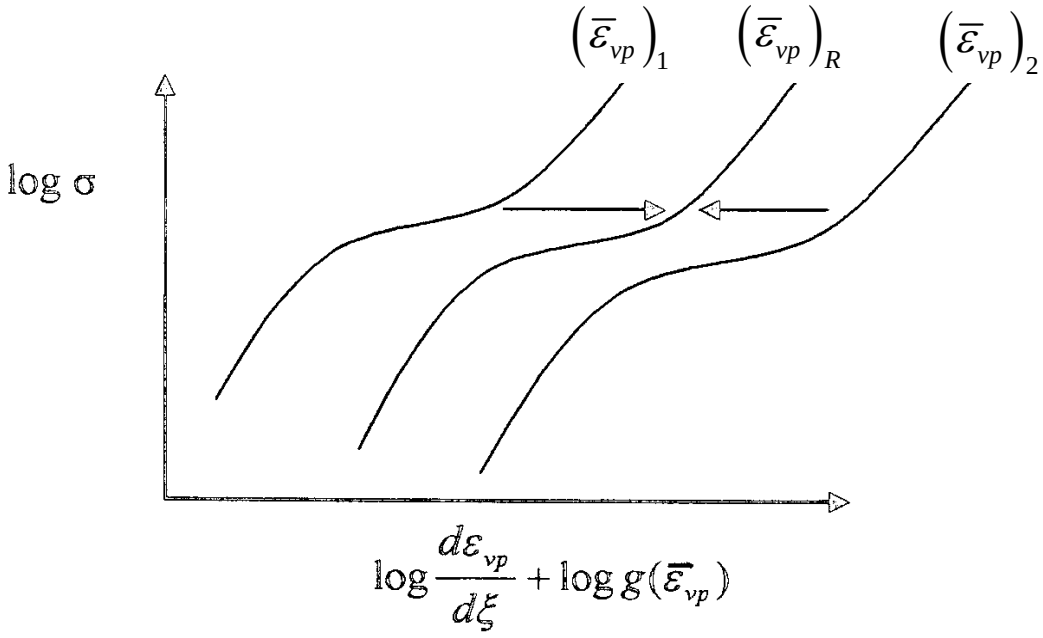

Figure 150. Inversion of f(σ) versus g(ε) relation (log-log space).

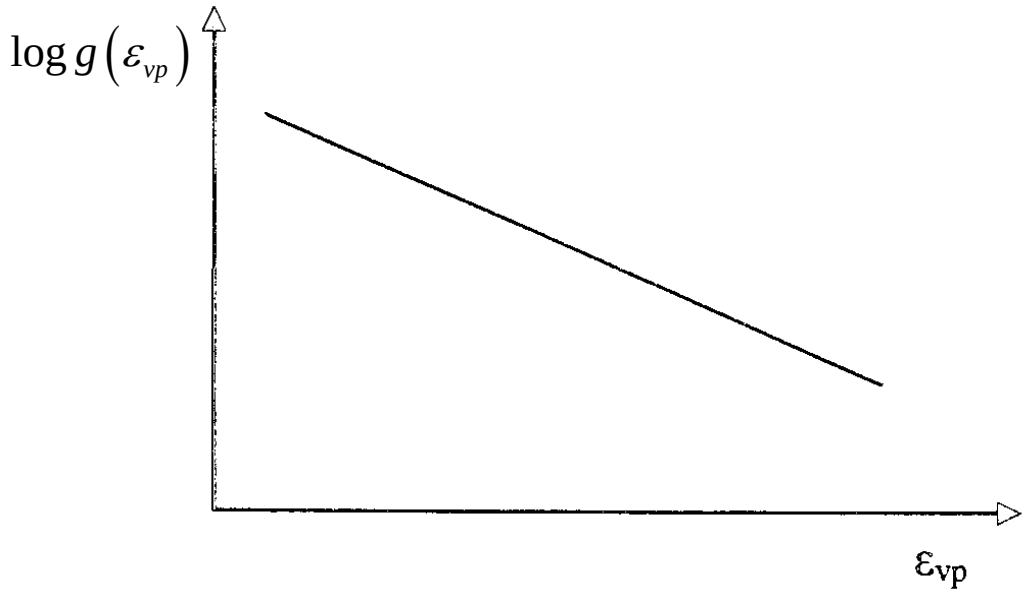

Figure 151. Strain hardening function $g(\varepsilon_{vp})$ expressed as a shift factor.

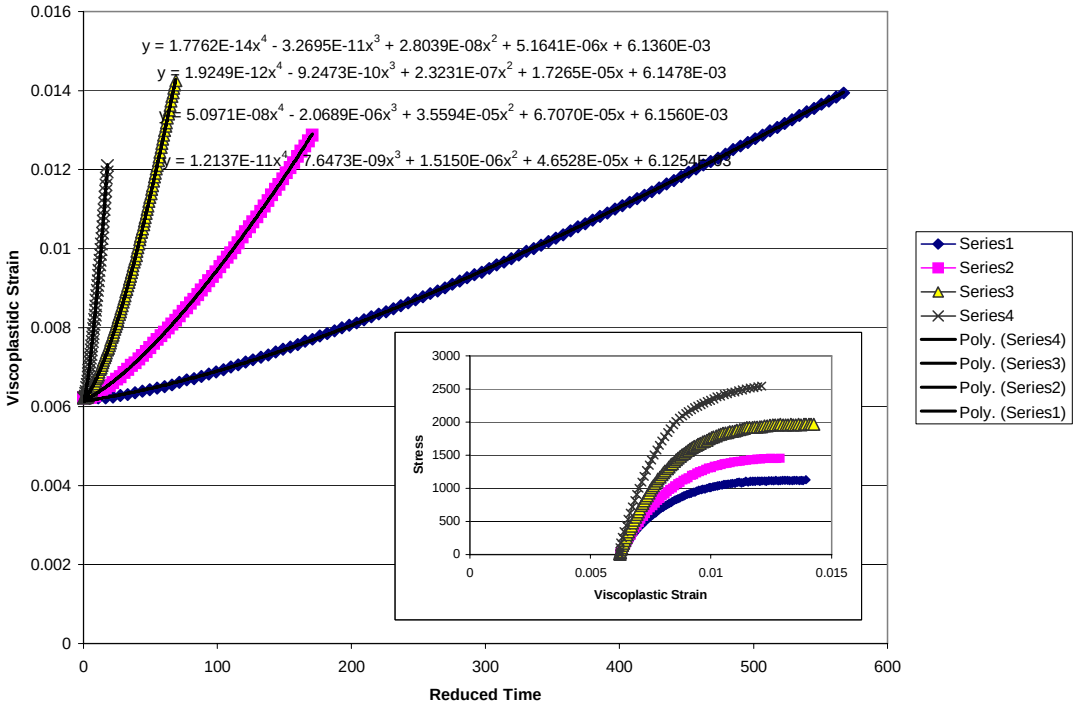

Figure 152. Example of viscoplastic strain versus time and stress remaining after damage and viscoelasticity are removed from the total measured strain.

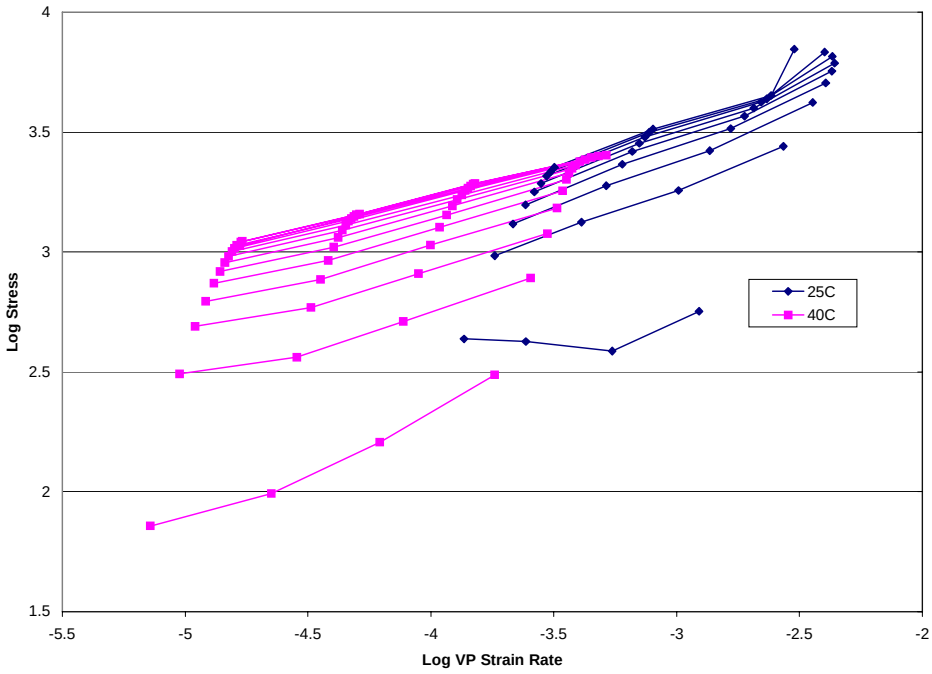

Figure 153. Unshifted data from unconfined compression fixed stress creep and recovery tests.

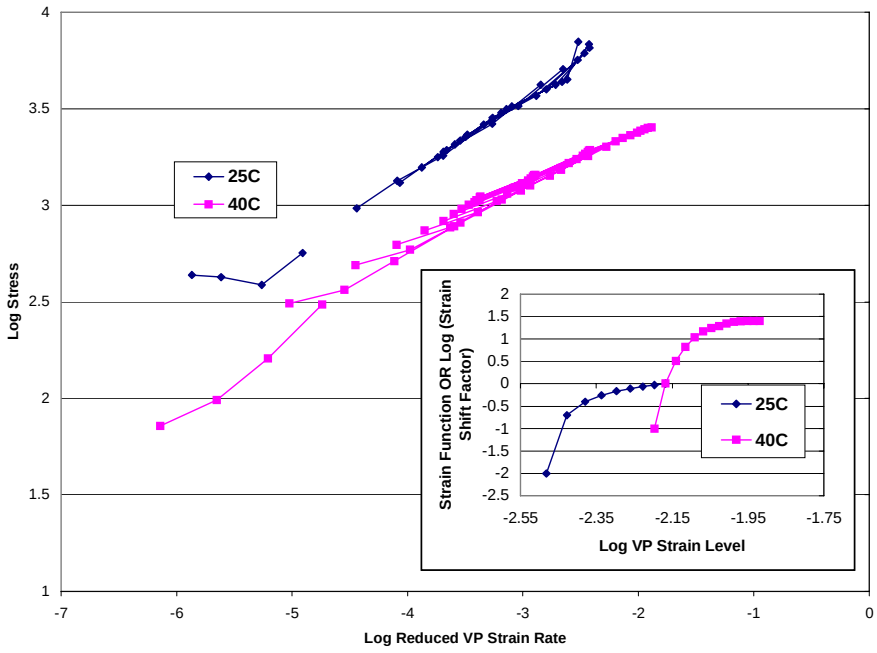

Figure 154. Shifted stress and strain functions from unconfined compression tests using stress-strain function master curve approach with predicted initial viscoplastic strain.

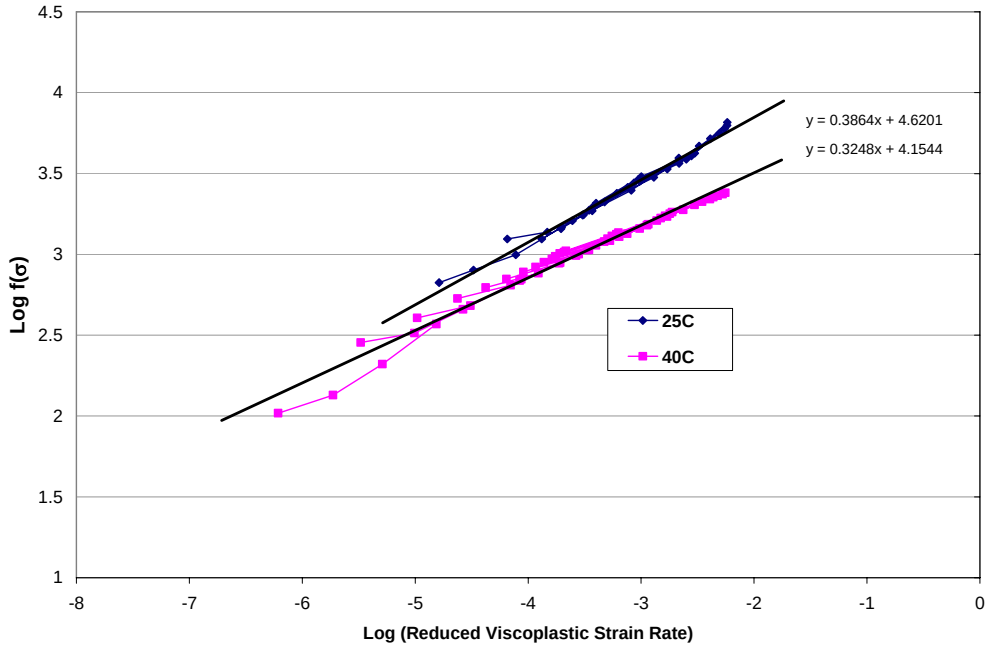

Figure 155. Shifted stress function from unconfined compression tests using stress-strain function master curve approach with measured initial viscoplastic strain.

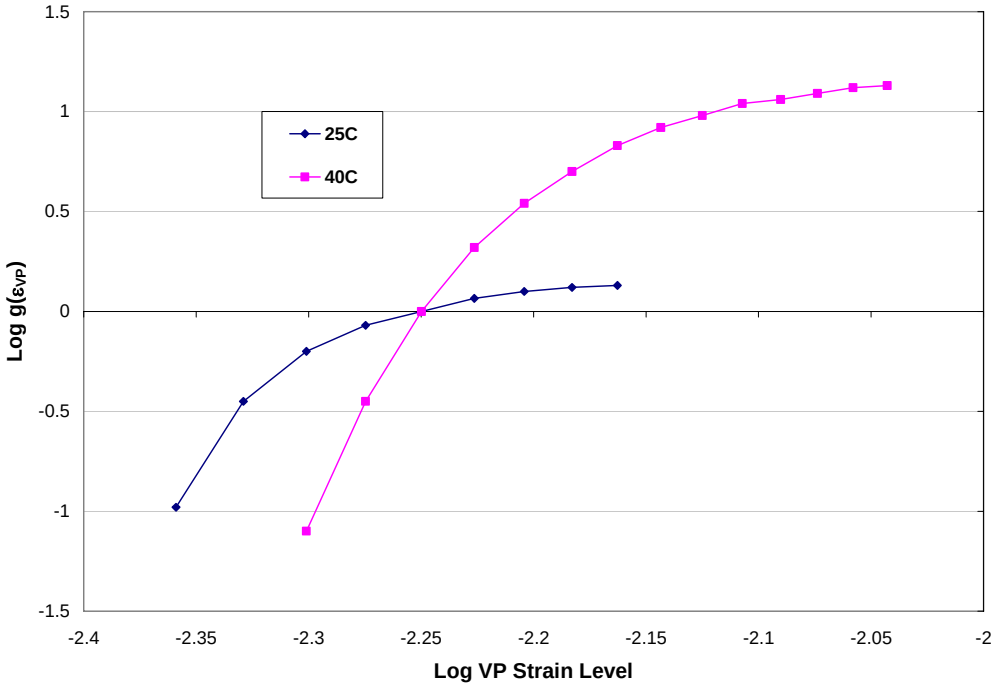

Figure 156. Shifted strain function from unconfined compression tests using stress-strain function master curve approach with measured initial viscoplastic strain.

9.3 Re-development of the viscoplastic model

9.3.1 Introduction

The calibrated uniaxial *pqY* was unable to capture with realism the secondary hardening in the repeated and random load permanent deformation tests, and consequently the model tended to over predict permanent strains, as illustrated in Figure 133 and Figure 136. Furthermore, could the uniaxial *pqY* model cannot be easily generalized to multidimensional loading conditions. A more robust model is clearly needed to describe the permanent deformation behavior. Key features required for this more robust model include the following:

- Three-dimensional applicability
- Asymptotic arrest of viscoplastic strain (rate) for a fixed stress state (i.e. creep)
- Enhanced hardening sensitivity to stress magnitude and path
- Suppression of viscoplasticity with confining stress
- Calibration and validation with existing data and extended time-temperature superposition

While tertiary softening and flow leading to failure is a real phenomenon in asphalt concrete, it is not included in the model.

9.3.2 Review of Existing Models and Theories

Various approaches for modeling permanent deformations in asphalt concrete have been suggested in the literature over recent years. Erkins (2002) developed a comprehensive model for asphalt concrete, ACRe, which incorporated a rate-dependent plasticity formulation. A conventional plasticity model was modified to have model parameters that are dependent on temperature and loading rate. The capped Hierarchical Single Surface, HiSS, developed by Desai (Desai and Zhang, 1987) for geomaterials is used to address compressive yielding. This model was calibrated using monotonic tests in tension and in compression at a variety of temperatures and loading rates. Since the model is not a true viscoplasticity formulation, it is not capable of simulating constant stress viscoplastic creep, cyclic creep and recovery, or repeated load permanent deformation behavior. For example, for repeated load permanent deformation response the model fully deforms upon application of the first load cycle, and subsequent cycles do not produce any additional incremental permanent strains.

Huang et al. (2002) present an elastic-viscoplastic model with temperature dependent material properties. Perzyna's viscoplasticity theory (Perzyna 1966) is used. Compressive yielding is modeled using the HiSS surface similar to Erkens. Monotonic tests were employed for calibration.

Work by Tashman et al. (2004a) and Park et al. (2004) shares some similarities with Huang's model, except that compressive yielding is addressed with a simpler, uncapped Drucker-Prager surface. Temperature is also an explicit model variable. Continuum damage is incorporated via an effective stress that considers micro cracking; anisotropy and hardening due to the microstructural damage are also considered.

Levenberg and Uzan (2004) followed a different approach for a viscoplastic model by using the theories proposed by Chaboche (1997) instead of Perzyna. Yielding and hardening formulations are not used; instead, a phenomenological 'back stress' provides the underpinnings for the time-dependent nonlinear response. Interaction between tension and compression are implemented, but only for very small strains (i.e., a few hundreds of micro strains).

9.3.3 The Perzyna Theory for Viscoplasticity

Perzyna offered a seminal theory for viscoplasticity in the 1960's (Perzyna 1966) that follows cues from rate-independent plasticity theory. The Perzyna theory for viscoplasticity is attractive for the model reformulation in the present study for the following reasons:

- It is truly three-dimensional.
- It predicts a viscoplastic strain rate that can be easily modified into a reduced viscoplastic strain rate like the *pqY* model using the extended time temperature superposition.
- The theory is general enough to accommodate a wide variety of hardening functions.

The Perzyna formulation predicts the rate of viscoplastic strain as follows:

$$\frac{d\varepsilon_{ij}^{vp}}{dt} = \Gamma\left\langle f(G)\right\rangle \frac{\partial F}{\partial \sigma_{ij}} \qquad \text{Equation 121}$$

In Equation 121, Γ is a fluidity parameter that is conceptually similar to a viscosity term. The function $\left\langle f(G)\right\rangle$ is an overstress function that governs the magnitude of viscoplastic

flow. The brackets $\langle\ \rangle$ are used to denote the value is zero if $f(G) \le 0$ and equal to $f(G)$ when $f(G) > 0$. G can be represented as a surface $G(\sigma_{ij}) = 0$ in multidimensional stress space. The term $F(\sigma_{ij}) = 0$ is a potential function in multidimensional stress space; the $\frac{\partial F}{\partial \sigma_{ij}}$ gradient term requires that the viscoplastic strain increments are normal to the potential function. Generalized viscoplasticity models make a distinction between the overstress function $G(\sigma_{ij}) = 0$ and the potential function $F(\sigma_{ij}) = 0$. For simplicity, the same function—usually termed the flow function or flow surface—is used for both *G* and *F*, resulting in what is known as associated flow viscoplasticity.

Simply stated, Equation 121 specifies that viscoplastic strains develop only when the applied stress state lies outside the flow surface. In contrast, plasticity theories do not allow the applied stress state to lie outside the yield surface. In viscoplasticity, however, the magnitude of the strain rate is proportional to how far the stress state is outside the flow surface. Materials such as metals may be realistically represented by flow surfaces that depend only on shear stresses, e.g. Von-Mises theory. Asphaltic materials usually take their cue from granular geo-materials, which gain strength from confining pressure and exhibit dilation. Realistic modeling of these behavior aspects requires flow surfaces that depend on both shear and confining stresses, e.g. Drucker-Prager or generalized Mohr-Coulomb theories. Erkins (2002) provides a more in-depth discussion of flow surfaces vs. observed behavior. Strain hardening (and softening) materials like asphalt concrete can be simulated with these theories by changing the size and shape of the flow surface as a function of internal state variables that track deformation history.

9.3.4 Adaptation to the Project Material and Data

Employing the extended time-temperature superposition concepts described previously, the reduced viscoplastic strain rate is expressed as:

$$\frac{d\varepsilon_{ij}^{vp}}{dt_R} = \Gamma\langle f(G)\rangle \frac{\partial F}{\partial \sigma_{ij}} \qquad \text{Equation 122}$$

where reduced time t_R is given as:

$$t_R = \frac{t}{a(T)} \qquad \text{Equation 123}$$

and where $a(T)$ is the temperature shift function. Associated flow is assumed, thus $F=G$.

Damage adjustments are not incorporated in the formulation to keep the model as simple as possible. Tashman et al. (2004b) have studied this topic using x-ray tomography in a 12.5mm dense graded mixture at 56^{o}C under 0, 103, and 206 kPa of confinement. A slight decrease in bulk specimen voids was found at 1% axial strain. At 2% axial strain, the bulk specimen voids were about 0.5% larger than initial conditions. A large increase in bulk specimen voids was observed at 4% and higher axial strains. For comparison, a 2.2% axial viscoplastic strain was the largest encountered in this study. This agrees with the volumetric strains measured for the mixture in this study, where the small induced volumetric viscoplastic strains were first compressive and later dilational but close to a zero volume change condition for all practical purposes until tertiary flow.

The Perzyna theory using the HiSS flow surface (Desai and Zhang, 1987) was adopted. The HiSS flow surface can be expressed compactly in terms of stress invariants as:

$$F = 0 = J_{2D} - [\gamma(I_1 + R(\xi))^2 - \alpha(\xi)(I_1 + R(\xi))^n] \qquad \text{Equation 124}$$

in which

- J_{2D} and I_1 are the usual shear and bulk stress invariants.
- γ and n are fixed parameters that govern the size and shape of the growing flow surface.
- $\xi = \varepsilon_1^{vp} + \varepsilon_2^{vp} + \varepsilon_3^{vp}$ is the viscoplastic strain trajectory; which is a very simple quantification of deformation used as the hardening internal state variable.
- $R(\xi)$ and $\alpha(\xi)$ are parameters that govern the size and nature of the capped surface. They are adjusted as hardening accumulates, thereby reducing the potential for viscoplastic flow. These parameters are assumed to follow simple exponential relationships $R(\xi) = R_0 + R_A \xi^{k_2}$ and $\alpha(\xi) = \alpha_0 e^{\xi k_1}$. A small, initial, undisturbed surface must be assumed as a starting point in this formulation.

Representations of the HiSS surface can be found in Figure 157 and Figure 158. As can be seen from the surface, viscoplastic flow requires more shear stress ($\sqrt{J_{2D}}$ direction) as confinement increases (I_1 direction). The capped surface intersects the hydrostatic axis, allowing yielding under pure hydrostatic stress.

Recall the flow rule, $\langle f(G) \rangle$, in Equation 121. Since associated flow has been assumed, $\langle f(G) \rangle$ is equivalent to $\langle f(F) \rangle$. Through trial and error the optimal functional form for $f(F)$ was determined as:

$$f(F) = A\left(\frac{F}{F'_0} - 1\right)^N \qquad \text{Equation 125}$$

in which F is taken as the distance in principal stress space from the applied stress to the hydrostatic axis in the direction normal to the current flow surface, F'_0 is taken as the portion of that distance from the hydrostatic axis to the current flow surface. Both are

determined at the beginning of the current time step. The terms A and N are material parameters. As can be seen from the schematic shown in Figure 159, the potential for viscoplastic flow diminishes asymptotically as the flow surface expands because of hardening. This is precisely what is observed in experiments such as constant creep loading. A Newton-Raphson technique is employed to search for the points P_i in principal stress space where the outward normal to the instantaneous flow surface points through the applied stress point. This is the point on the flow surface at which the gradient in Equation 122 is evaluated.

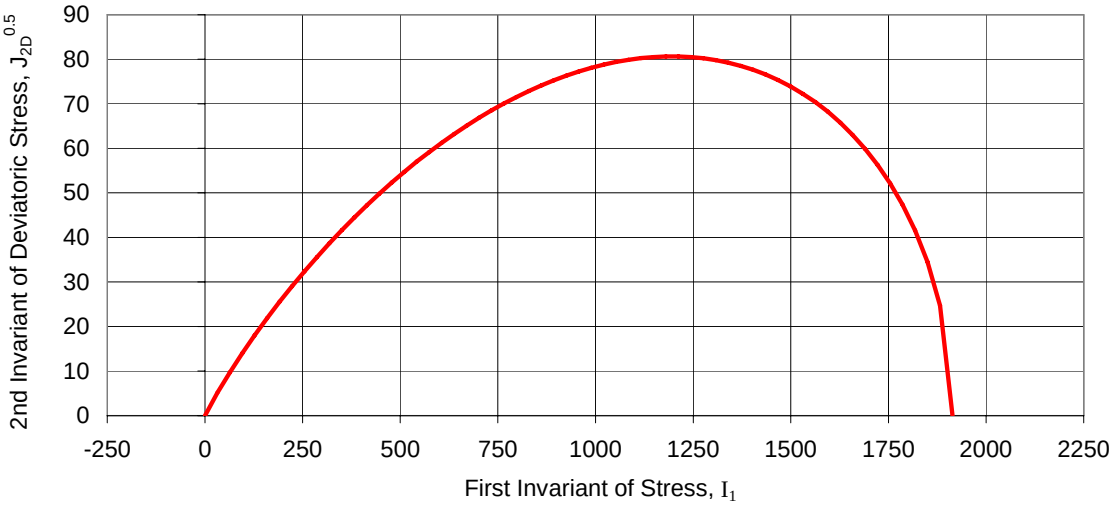

Figure 157. Representation of the HiSS surface in familiar two-dimension stress invariant space.

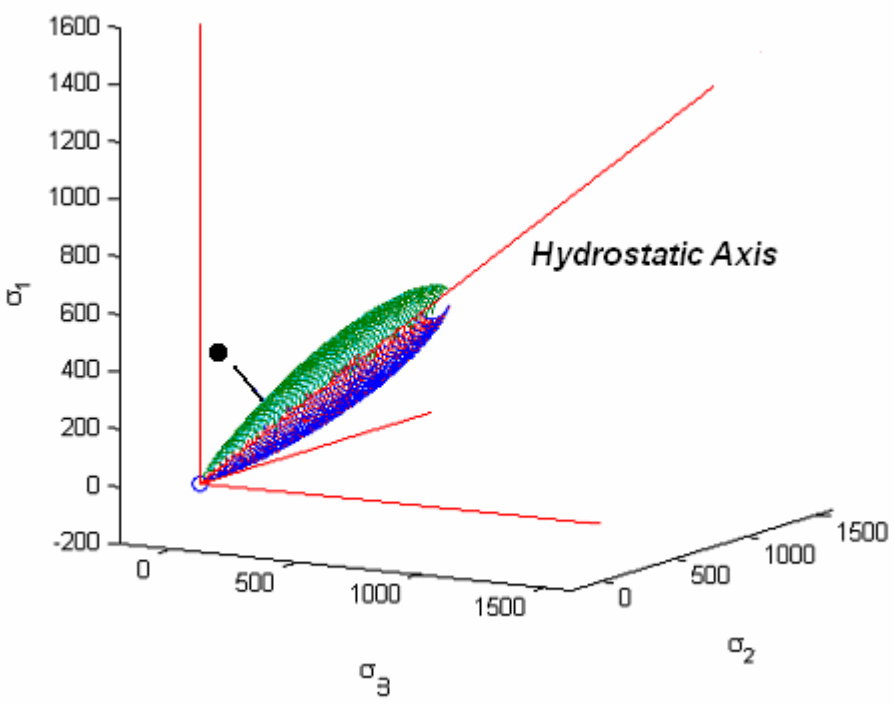

Figure 158. Three-dimensional representation of the HiSS surface in principal stress space

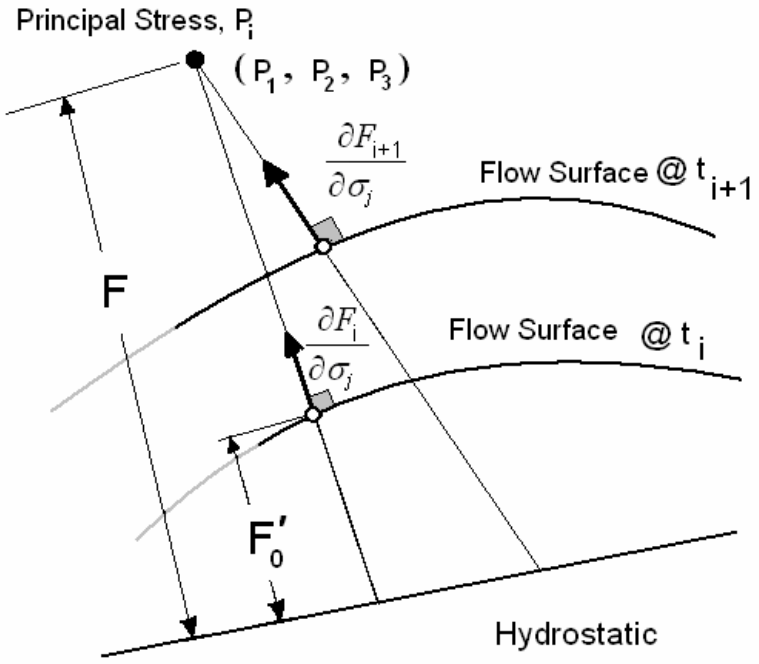

Figure 159. Schematic of Flow Rule and Surface Hardening

9.3.5 Calibration

The Fixed Time cyclic creep and recovery tests were again used for the model calibration because these enable a more direct determination of the unrecovered viscoplastic strain after the recovery period. Confinement stresses of 0, 250 and 500 kPa were applied. The post consolidation axial and radial strains determined with the methods described in Chapter 6, Figure 90. Test temperature was 35^{o}C, which is sufficiently high to expect significant viscoplasticity.

The applied triaxial stress vs. time histories from the tests were simulated in Excel. Using the nonlinear optimization and a set of initial estimates for the model parameters in Equation 124 and Equation 125, the model constants were iteratively adjusted until the summed squared errors between measured and predicted axial and radial strains were minimized.

During calibration, it was determined that *A* in the flow rule (Equation 125) needed to be modified to increase the amount by which confinement suppresses viscoplasticity. The *A* parameter was therefore defined as the following function:

$$A = \left(\frac{\theta}{\theta_{REF}} \right)^{k3} \qquad \text{Equation 126}$$

The θ angles can be interpreted as the inclination of the current stress vector in I_1 vs. $\sqrt{J_{2D}}$ space; the reference angle θ_{REF} corresponds to a uniaxial stress path angle and has a value of 0.528 radians. Ideally, the flow rule and inherent geometry of the HiSS surface should account for confinement effects akin to a Mohr-Coulomb surface, and it did this satisfactorily for later times of the calibration tests. At very early times, however,

the original model predicted slightly greater deformations with confinement than without. The formulation in Equation 126 suppresses this physically unrealistic behavior.

Figure 160 through Figure 162 show the graphical results of the calibrations. The goodness-of-fit statistics for the model vs. measured axial strains from the calibration tests were quite good, with R2 = 0.97, 0.93 and 0.96 for the 0, 250 and 500 kPa confined tests respectively. The corresponding goodness-of-fit values for radial strains were R^2 = 0.97, 0.98 and 0.82 for the 0, 250 and 500 kPa confined tests respectively. The calibrated model parameters are summarized below in Table 28.

Table 28. Calibrated Model Parameters

Parameter	Γ	γ	N	N	α_0
Value	10^ -7.5190	0.039525	2.25982	2.5533	0.0055485
Parameter	k_1	R_0	R_A	k_2	K_3
Value	-38.5093	23.0031	3756.6	0.54361	4.7736

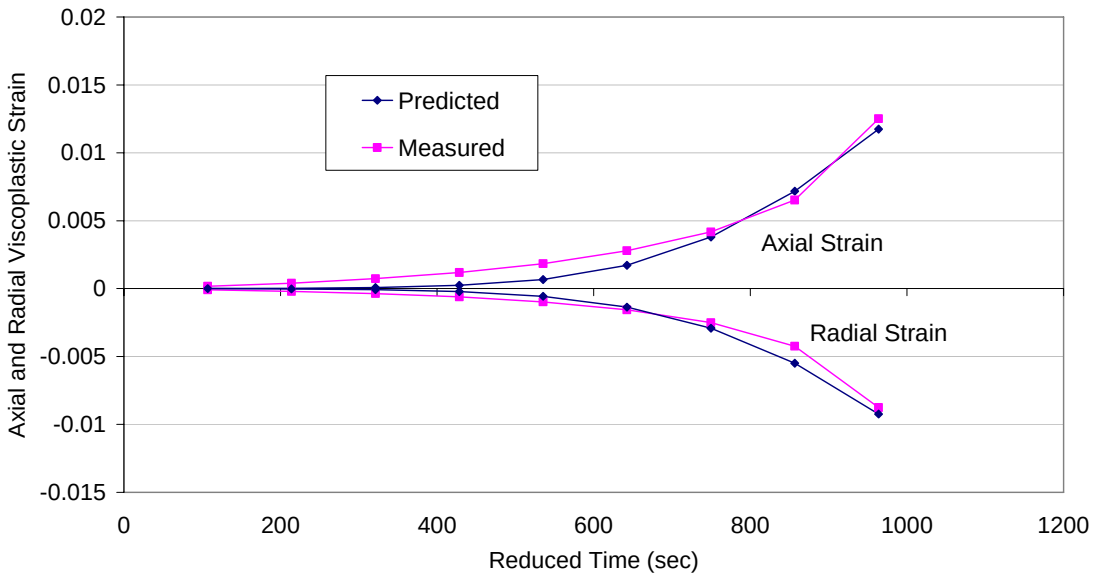

Figure 160. Unconfined Fixed Time Calibration Results

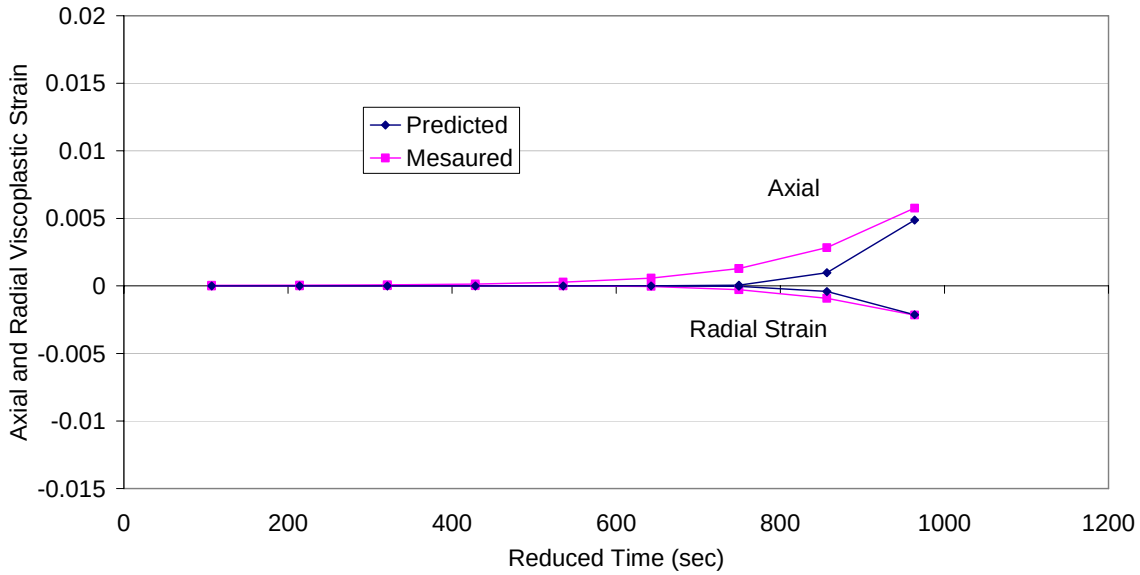

Figure 161. 250 kPa Confined Fixed Time Calibration Results

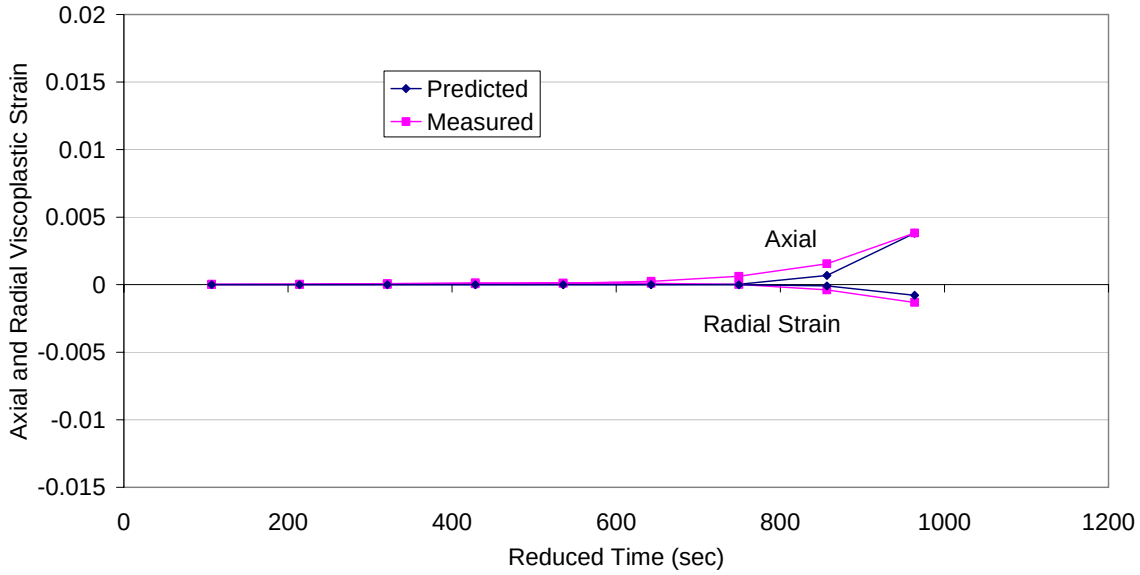

Figure 162. 500 kPa Confined Fixed Time Calibration Results

9.3.6 Validation Results

Three types of tests were used to validate the calibrated model; all have been described in preceding Chapters. The first type is the Fixed Stress cyclic creep at 0, 250

and 500 kPa of confinement at 25°C, 35°C and 45°C. The second validation set was the regular and random repeated load permanent deformation tests. Even though these latter tests are all unconfined, they are important validation tests because they were independently performed at the Arizona State University and because the uniaxial pqY model had difficulties tracking the secondary hardening in the response at small stresses. Finally, the third type of validation test was the monotonic controlled strain to failure loading at 25°C and 40°C (Chapter 8). Although the original pqY model was able to predict the viscoplastic strains in these tests quite successfully, they were nevertheless revisited with the enhanced Perzyna-HiSS model reformulation.

Graphical comparisons of the validation responses are summarized in Figure 163 to Figure 175. Figure 163 shows excellent agreement between predicted and measured axial and radial viscoplastic strains from the cyclic creep tests at three different confining stress levels - unconfined, 250kPa, and 500kPa. Note that the confined results are included with the unconfined values in Figure 163 for comparison; the deviator stress levels in the confined tests matched those in the unconfined test, and the suppression of viscoplasticity due to confinement is clearly evident. The unconfined tests were conducted at 25°C while the confined tests were performed at 35°C; however the results are all plotted in terms of the unifying reduced time. Validation for the set of 35°C/45°C Fixed Stress cyclic creep and recovery tests are shown in Figure 166 and Figure 167; in addition to the warmer temperatures, these unconfined tests were conducted at smaller stress levels.

The validation results for the conventional and random repeated load permanent deformation tests shown in Figure 168 to Figure 172 demonstrate the improved hardening

response from the Perzyna-HiSS formulation. The mean measured permanent strain and the +/- 1 standard deviation bounds for all of the replicates is shown for the conventional repeated load tests while all measured replicates are shown for the random tests to highlight the large variability in the measured data. The 37^{o}C results plotted in log-log space in Figure 168 exhibit the characteristic 'bend over' hardening behavior (see Figure 163) that the uniaxial pqY model was unable to replicate. The corresponding predictions for the individual replicates in the random loading permanent deformation tests are summarized in Figure 171 and Figure 172. While the agreement between predicted vs. measured strains is not as strong for these tests as compared to the cyclic creep tests, the major trends in the response are faithfully captured, most notably the complex, aggregate-related, secondary hardening.

Figure 173 plots the predicted axial strains against the radial strains for the triaxial creep and recovery tests along with a line which divides the responses into compressive (above line) and dilation (below line). This figure demonstrates the model's ability to predict the complex three-dimensional volumetric strain growth as a function of the applied stress state.

Finally, Figure 174 and Figure 175 show the measured and predicted total strains for the controlled strain rate to failure tests as calculated using the previously calibrated viscoelastic continuum damage model component combined with both the uniaxial pqY and the revised Perzyna-HiSS viscoplasticity model formulations. The predicted response is similar for both the original and revised model. This is to be expected, since the comparisons are now based on total strains, the original uniaxial pqY model had already been shown to adequately predict these tests, and the tests were conducted at

temperatures and loading rates for which the viscoplastic strains will not necessarily be the dominant component of total strains. The agreement between predicted and measured strains is closest at the warmer temperatures and slower loading rates, with increased divergence observed in the post-peak portion of the response at cooler temperatures and faster rates. This in part is because the faster and cooler validation tests are subjected to stresses that are well outside range of stresses in the calibration tests. As a practical matter, the divergence of results in the post-peak region occurs at stress levels that will not be encountered in realistic pavement systems and within the regime in which coalescence of micro cracks will convert the material response into a macro crack fracture mechanics problem.

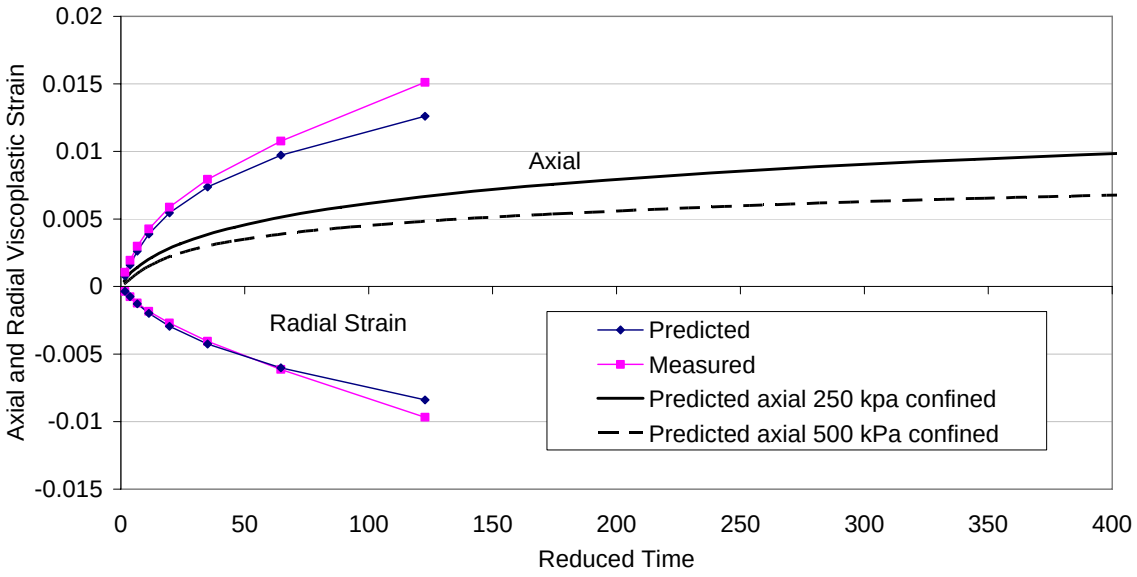

Figure 163. Measured and predicted viscoplastic strains for Fixed Stress cyclic creep with equivalent deviator-stress (1500 kPa) confined test predictions for comparison

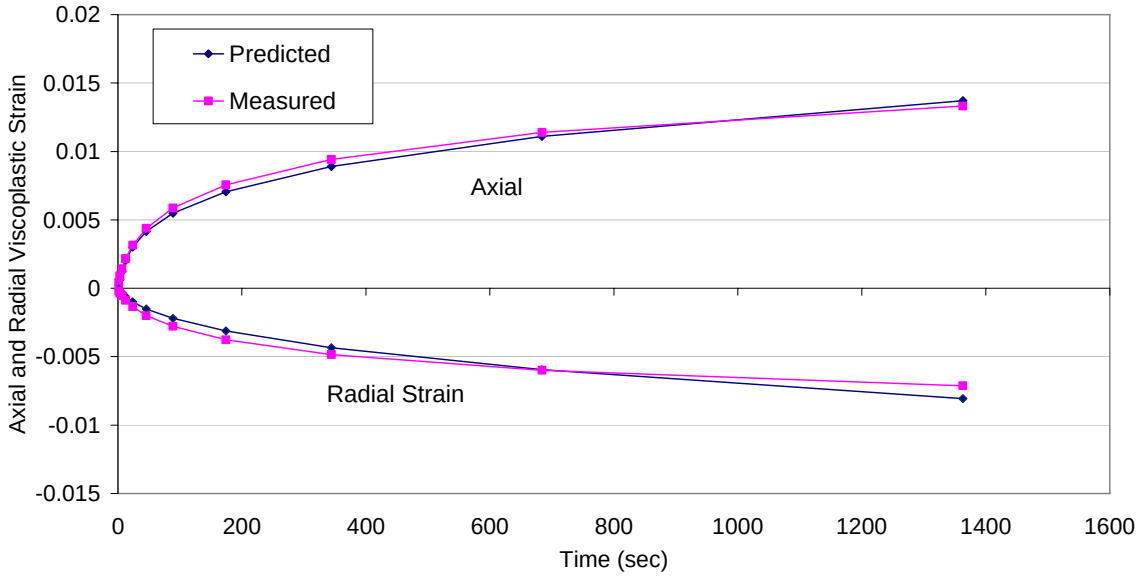

Figure 164. Measured and predicted viscoplastic strains 250 kPa confined Fixed Stress (1500 kPa deviator)

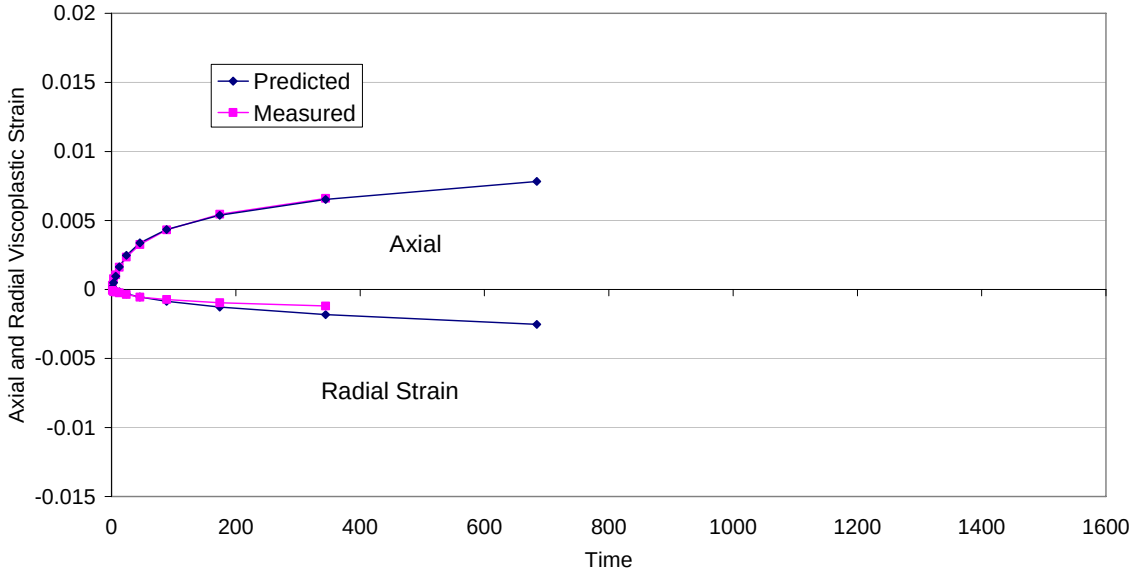

Figure 165. Measured and predicted viscoplastic strains 250 kPa confined Fixed Stress (1500 kPa deviator)

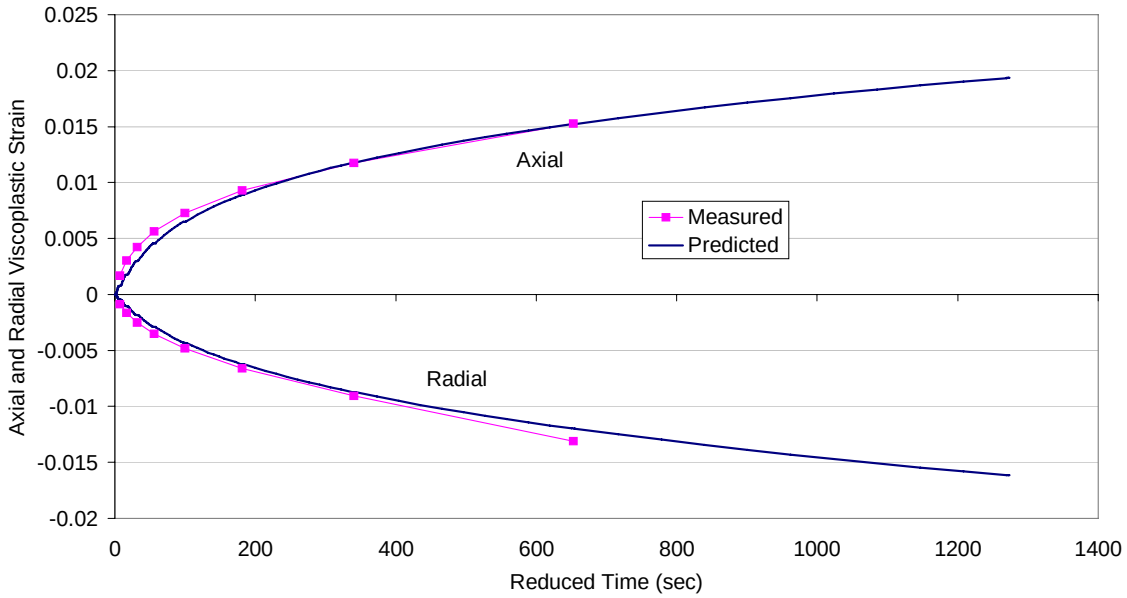

Figure 166. Additional unconfined 35°C cyclic creep validation (936 kPa deviator)

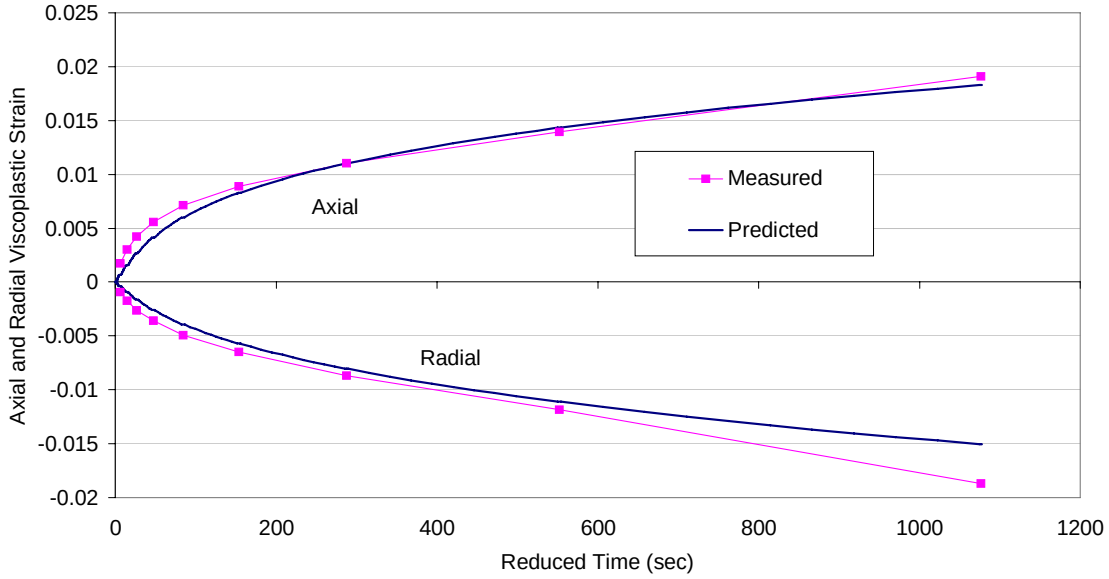

Figure 167. Additional unconfined 45°C cyclic creep validation (936 kPa deviator)

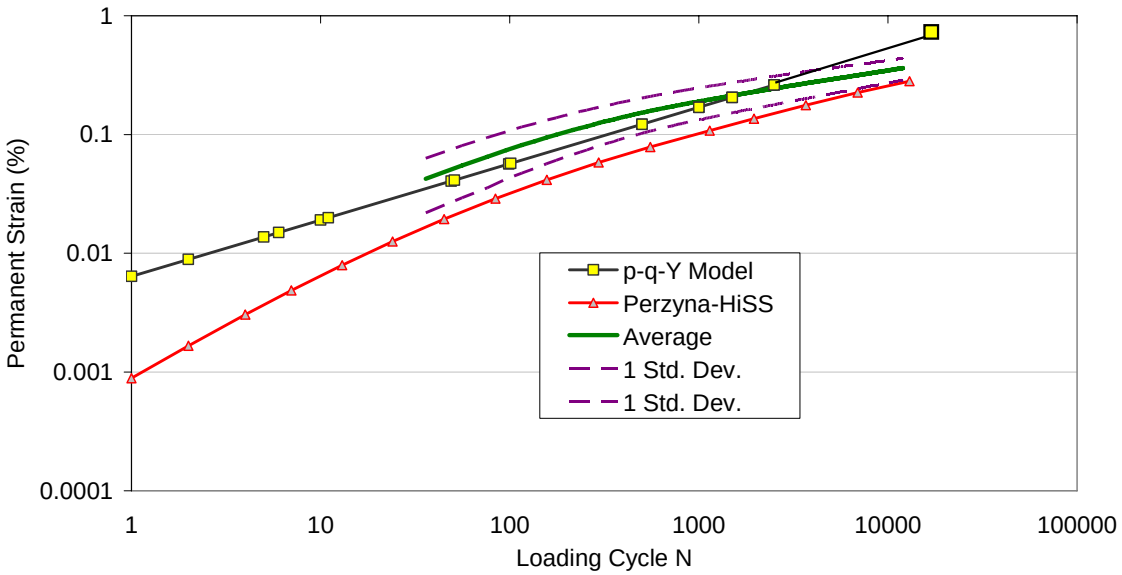

Figure 168. Log-log space - 37°C Regular repeated load permanent deformation test validation

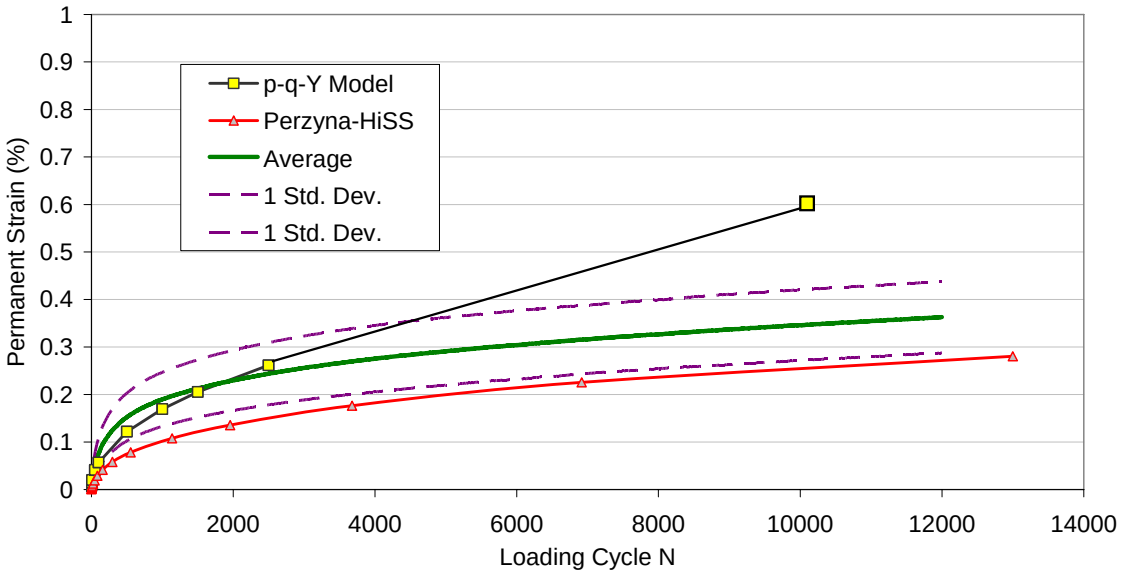

Figure 169 Arithmetic space - 37°C Regular repeated load permanent deformation test validation

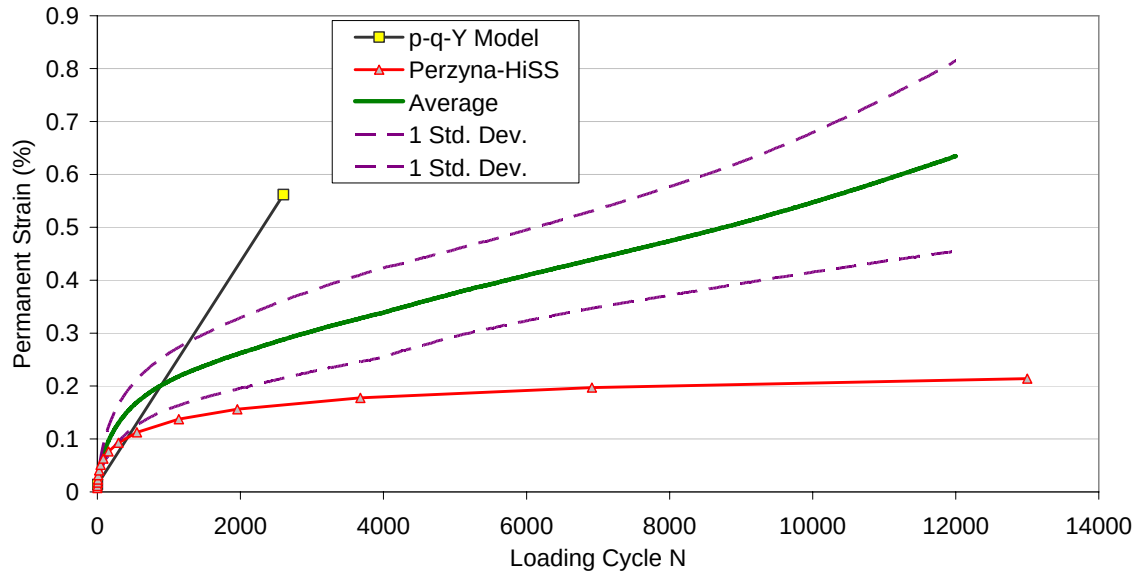

Figure 170. Arithmetic space - 54°C Regular repeated load permanent deformation test validation

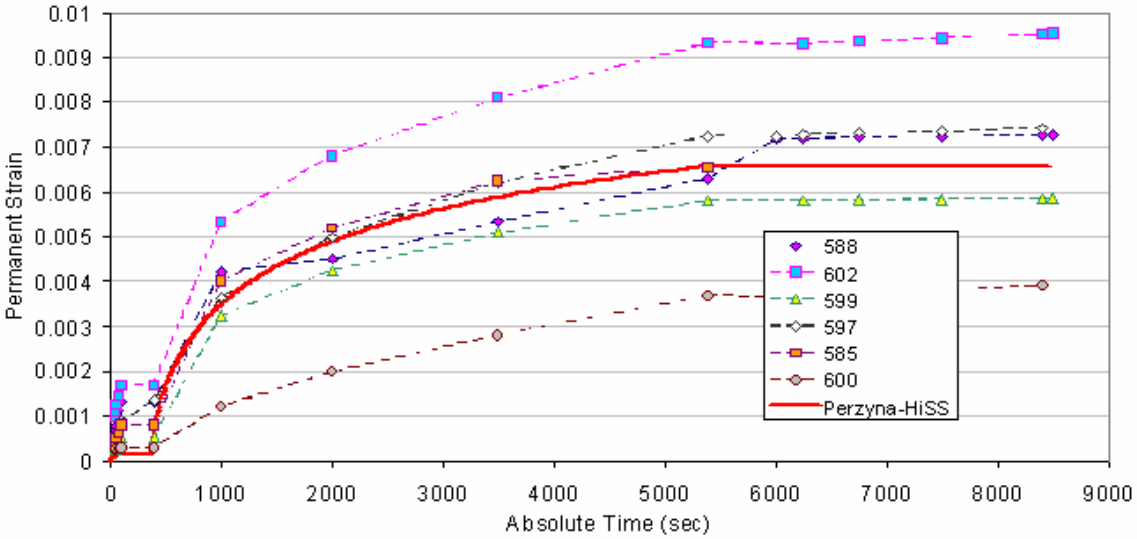

Figure 171. Random repeated load permanent deformation validation at 37°C

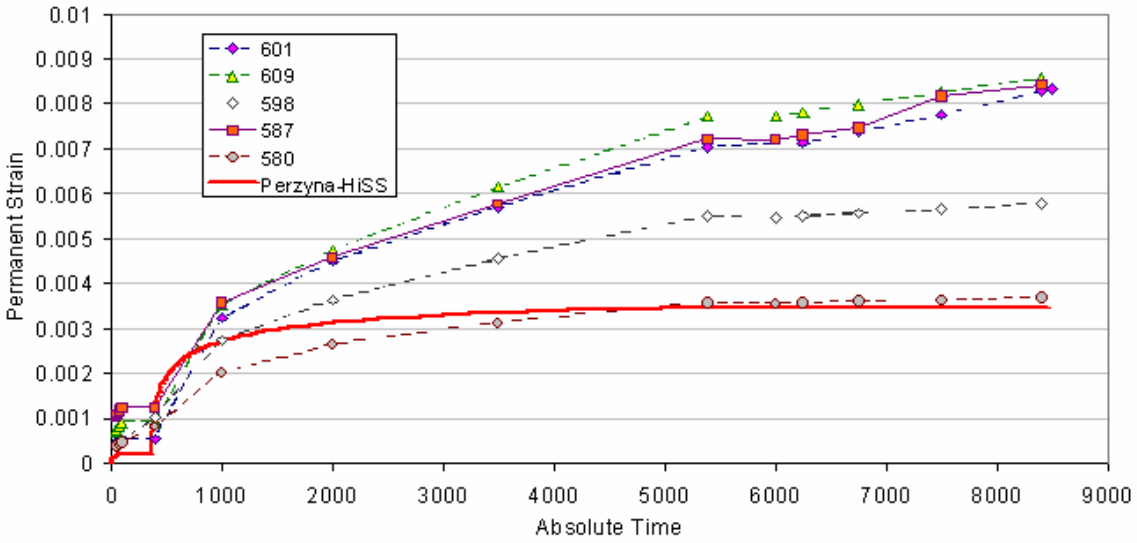

Figure 172. Random repeated load permanent deformation validation at 54°C.

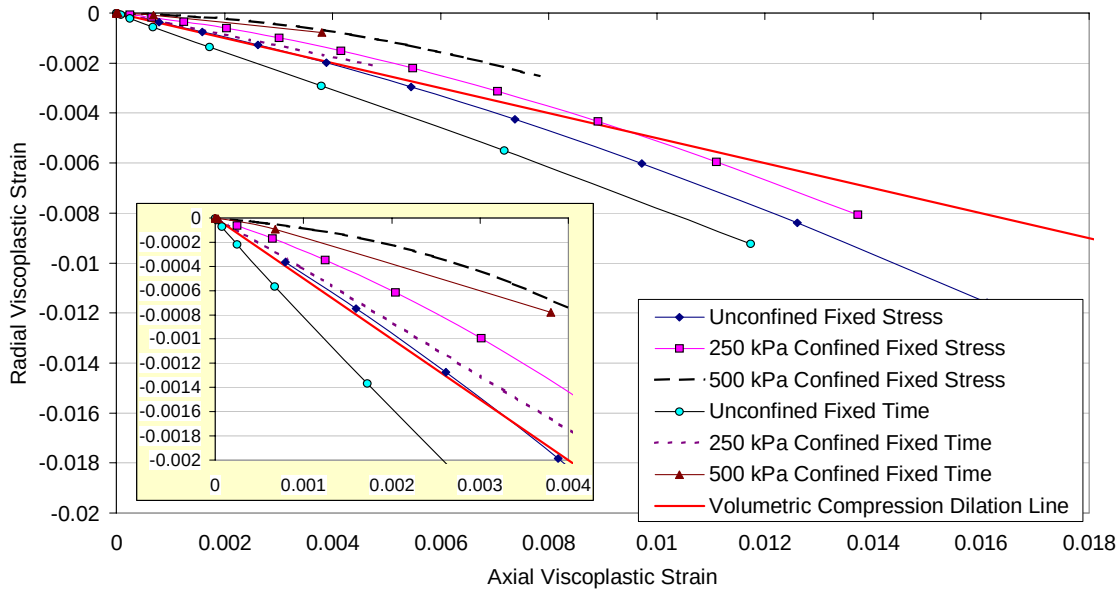

Figure 173. Compressive and dilative responses of Perzyna-HiSS Viscoplastic Model

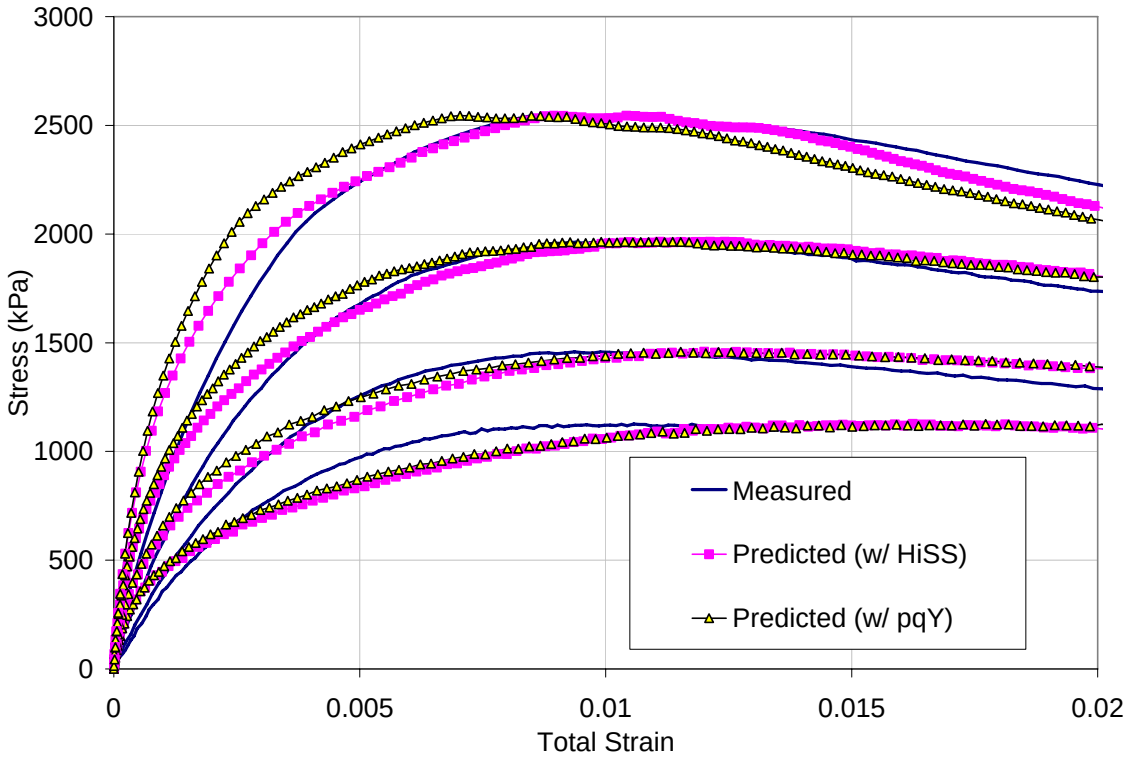

Figure 174. 40°C monotonic test validation results

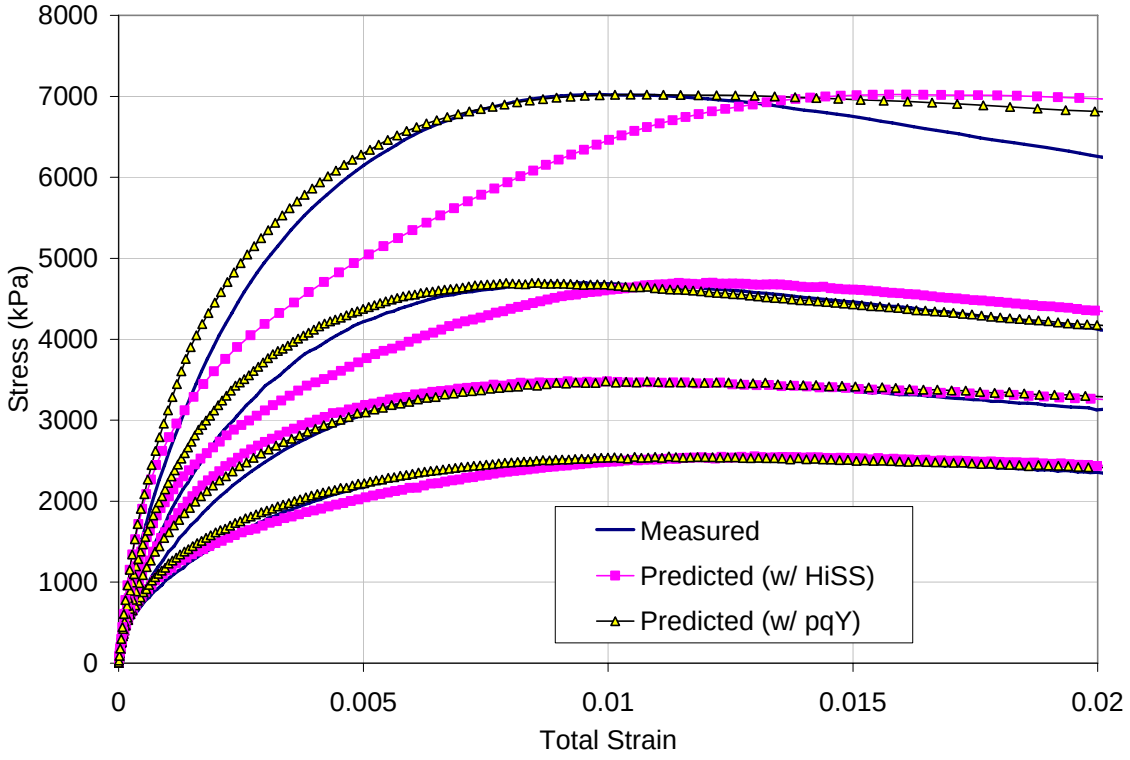

Figure 175. 25°C monotonic test validation results

9.4 Viscoplastic Model Revision Conclusion

This chapter has documented three different approaches aimed at addressing the deficiencies of the original uniaxial viscoplasticity model, specifically the lack of realistic hardening and multidimensionality. Ultimately, a completely new model had to be formulated to address these issues.

A bilinear hardening law was attempted by modifying the original uniaxial viscoplasticity model to transition from a higher-sloped primary to a lower-sloped secondary response at a prescribed strain level. The modification was calibrated using two methods. Composite model parameters first determined from the previous validation and calibration tests produced predictions that generally overestimated the measured strains before the transition strain had been reached. The transition strain between primary and secondary hardening is not a fixed value, but depends on the test conditions and is more apparent in small stress repeated load tests. The second method was a reverse calibration of the model using the repeated load validation tests, but this yielded very poor reverse predictions of the calibration tests.

A novel method of cross plotting was attempted to separate the viscoplastic strain rate dependence into functions of stress and viscoplastic strain. Constant strain rate test data at 25^{o}C and 40^{o}C were used to separate the stress and strain functions. These results confirmed the validity of a power law dependence of viscoplastic strain on stress but identified the need a more complex strain function. Based on these observations it is

evident that viscoplasticity and hardening is highly complex and requires a very robust model formulation.

Ultimately, a new enhanced viscoplastic model specifically designed for multidimensional, time-dependent irrecoverable deformations was formulated. This model is a significant improvement over the uniaxial pqY model. The enhanced model is based on Perzyna viscoplasticity theory incorporating Desai's Hierarchal Single Surface (HiSS) with hardening as the flow rule. The calibration was completed using both the axial and radial strains from cyclic creep and recovery tests with and without confinement. To test the model's capabilities it was validated against an independent set of cyclic creep tests, repeated load permanent deformation tests (two types), and monotonic constant strain rate to failure tests. The validation was quite successful; very good agreement was found between predicted and measured strains in all cases. While it is recognized that secondary aspects such as material anisotropy remain to be incorporated, the enhanced model provides reasonably robust and faithful predictions for asphalt concrete behavior within a familiar and relatively simple and easy to calibrate formulation.

Viscoplasticity in asphalt concrete was found to be a very challenging phenomenon to model. The first uniaxial pqY viscoplastic model did support the successful development and calibration of the viscoelastic continuum damage model component using calibration tests that exhibited some small levels of viscoplasticity. Although the original pqY viscoplasticity model is quite simple and was able to successfully predict response under relatively large stresses and short duration monotonic tests, it failed to faithfully reproduce the response of the repeated and random load

permanent deformation tests. These flaws were substantially remedied by the more sophisticated and general Perzyna-HiSS theory.

10. Summary and Conclusions

Mechanistic approaches for pavement design and performance prediction employ theories of mechanics to relate pavement structural behavior and performance to traffic loading and environmental influences. A key element of this approach is the accurate prediction of the response of the pavement materials—and thus of the pavement itself. Consequently, adequate and accurate characterization of material behavior is vital if pavement performance is to be predicted with realism.

This dissertation documents the development, calibration, and validation of a comprehensive, fundamental material model for asphalt concrete. The model, which is based on an extended form of the Schapery continuum damage formulation considers the viscoelastic, viscoplastic, and damage component behavior over the full range of temperatures, loading rates, and stress levels of interest in pavement engineering. Key conceptual components of this model include the use of viscoelastic correspondence principles, microstructural damage functions based on a thermodynamics-based formulation and expressed in terms of rate-dependent internal state variables, and a strain

hardening viscoplasticity relation. The model has been calibrated and validated for a typical dense graded Superpave mixture under a range of unconfined and confined compression loading conditions. Although only one specific dense graded asphalt mixture was employed in this study, the comprehensive mechanistic nature of the model makes it applicable to other asphalt concrete materials as well.

The Schapery model explicitly separates the total strain ε_t into linear viscoelastic ε_{lve}, microstructural damage ε_d, and viscoplastic ε_{vp} components. Note that the damage strain ε_d is actually included as a part of the viscoelastic strain ε_{ve} in the formal Schapery model. The following sections summarize key findings and conclusions for each of the model components and for the overall validity of the model when applied to a variety of laboratory test configurations.

10.1 Linear Viscoelasticity

Viscoelasticity is one of the most recognized properties of asphalt concrete. The linear viscoelastic relaxation modulus or creep compliance of asphalt concrete is relatively easy to calibrate using simple small-strain dynamic modulus tests and mathematical principles.

A large set of small-strain dynamic modulus tests were performed under uniaxial compression loading conditions during the course of this study. The small strain loading conditions are intended to ensure that only the viscoelastic component of the model response is excited and that the viscoplastic and damage components remain negligible. These tests, which are assumed to cause no damage to the specimen, were typically

performed as the first step of a destructive test sequence—e.g., a small-strain frequency sweep at a given test temperature prior to a constant strain rate to failure loading at the same temperature. A storage modulus master curve was fit to the full set of measured dynamic modulus test data, and this storage modulus master curve was then transformed mathematically into Prony series approximations to the linear viscoelastic relaxation modulus and creep compliance relationships needed for the model formulation.

It is important to note that the dynamic modulus tests performed here for advanced modeling purposes did not conform to the standard dynamic modulus testing protocol as developed for the Simple Performance Test portion (Task C) of the NCHRP 9-19 project. In particular, the dynamic modulus tests performed here typically did not include very cold temperatures, since the subsequent testing steps (e.g., constant strain rate to failure, cyclic creep and recovery to failure) at coldest temperatures were either impossible to achieve or irrelevant to the model calibration. As a consequence, it was somewhat difficult to determine the cold temperature upper shelf of the dynamic modulus master curve. These difficulties reinforce the need for dynamic modulus test data in the very cold temperature glassy modulus range on the upper shelf, e.g. less than 0^{o}C. The material behavior in this range is particularly important for accurate prediction of the instantaneous or short time response at the very start of test loading.

Comparisons of the compression-only dynamic modulus data measured at the University of Maryland against the companion tension and tension/compression dynamic modulus data collected at the North Carolina State University show little difference in the storage modulus values in the overlapping measured temperature/frequency range; the storage modulus master curves are generally within one standard deviation. For locations

other than the lower shelf, all of the viscoelastic properties—storage modulus, relaxation modulus, creep compliance, phase angle, and temperature shift—are practically insensitive to the mode of loading. Confinement stress effects in the moderately high temperature region approaching the master curve lower shelf were examined using some exchanged confined tension/compression data from the North Carolina State University. The practical conclusion drawn from the data in this study is that linear viscoelastic properties of asphalt concrete may be assumed largely insensitive to confining stress up to 500 kPa of confinement. There is a virtually no effect of confining stress on the storage modulus in the measured range, although some influence may exist in the lower shelf at the highest temperature/slowest loading rate region.

10.2 Extended Time-Temperature Superposition

One of the most significant findings from this project was that conventional time-temperature superposition principals for asphalt concrete remain valid at large strain conditions up to peak failure and beyond into the post peak region. Time-temperature superposition for asphalt concrete has traditionally been thought to apply only for very small strain—i.e., linear viscoelastic—conditions. The temperature shift factors determined at large strains at low and intermediate temperatures were nearly identical to those measured at small strains for the same conditions. Large strain temperature shift factors at the highest temperatures deviated only slightly from the small strain values. The discrepancies at the highest temperatures can be attributed to a variety of causes, many of them related to the difficulties of performing dynamic modulus tests at the

highest temperatures (e.g., load control at very small loads, signal noise, etc.). The extended validity of the time-temperature superposition at large strains suggests that all of these response components are governed by the same rate processes.

The finding that time-temperature superposition applies to both small and large strain conditions with similar temperature shift relations is of considerable practical importance. For example, the single temperature shift relation can be conveniently measured using conventional small strain dynamic modulus testing and then applied to larger strain conditions. The material calibration testing program can also be greatly economized and simplified. For example, calibration testing can be performed at a single critical temperature and loading condition rather than at a factorial of temperatures and loading rates.

10.3 Viscoplasticity

The extended time-temperature superposition principle was employed to calibrate the uniaxial viscoplastic strain rate model. The model was calibrated using Fixed Stress and Fixed Time cyclic creep and recovery loadings at a single temperature. The test temperatures were high enough that viscoplasticity is expected to dominate the response; running the tests in a creep and recovery mode allows direct measurement of the nonrecoverable viscoplastic strain component (recall that the nonlinear damage strains in the Schapery model are assumed to be fully recoverable). The viscoplastic model component was then separately validated against Fixed Stress and Fixed Time cyclic creep tests performed at other temperatures. The Fixed Stress and Fixed Time tests also

provided additional confirmation of the validity of time-temperature superposition at large strain levels.

The calibrated uniaxial viscoplastic model and the extended time-temperature superposition were also critical to the calibration of the damaged nonlinear viscoelastic model component. Calibration of the damage model component was based on uniaxial constant strain rate to failure tests performed at 5^{o}C, a relative cool temperature but not cool enough to suppress all viscoplastic strain. Determination of the damage functions for the material therefore hinged upon accurate predictions of viscoplastic strains from the uniaxial viscoplastic model so that these strains could be subtracted from the damage calculations.

Confinement of 250 kPa and 500 kPa was found to significantly suppress viscoplastic strains by up to an order of magnitude and to increase the nonlinearity of the hardening response over a larger range of strains. Some viscoplastic anisotropy was evident under pure hydrostatic loading, with complete recovery of axial strains and some nonrecoverable radial viscoplastic strains.

Ultimately, a second viscoplasticity model needed to be developed in order to address deficiencies of the original model, specifically the poor validation results for the two types of repeated load permanent deformation tests and the difficulty in generalizing the original model to multidimensional stress conditions. The enhanced viscoplastic model is based on Perzyna viscoplastic flow theory combined with the Hierarchical Single Surface (HiSS) flow function from geomechanics. The improved multiaxial strain hardening inherent in this model addressed the key deficiencies of the original pqY

model and produced much better predictions of the problematic repeated and random load permanent deformation validation tests.

10.4 Continuum Damage

The Schapery theoretical model framework for viscoelastic material with damage was successfully calibrated with a sequential calibration approach that separated the viscoplastic strain from the total strain. In the absence of viscoplasticity, this study assumed the remaining response consists of linear viscoelasticity and nonlinear viscoelasticity due to very small-scale damage and cracking. This nonlinear viscoelasticity is still fully recoverable.

Calibration of the damage relationships for the material requires laboratory tests at multiple controlled strain rates and cold temperatures. The purpose of the cold temperatures is to suppress the viscoplastic component of the response; the measured response therefore consists primarily of linear viscoelastic (which can be computed using the already-calibrated linear viscoelastic model component) and damage components. The most computationally demanding calculation is the evaluation of the hereditary convolution integrals for the viscoelastic response. Some difficulties were encountered during calibration due to a sub-optimal number of strain rates (due to testing equipment limitations), inability to completely suppress all viscoplastic response, unavoidable assumptions regarding multiaxial viscoplasticity, and the suggestion of initial damage that may have occurred during the prior frequency sweep loading. Future tests should use fresh undisturbed specimens in the constant strain rate tests (i.e., no prior frequency sweep) given the sensitivity of the damage function calibration to any initial damage.

Despite these hurdles, adjustments and steps were made to utilize the acquired data as best as possible and yielded a numerical model that predicts continuum damage strain in three dimensions. In the end, the physical damage and the laws and functions that predict that damage in asphalt concrete were effectively demonstrated to be unique, inherent material properties independent of temperature and loading rates through the use of reduced time. In other words, the uniaxial $C_{11}(S)$ and $C_{12}(S)$ functions were fit at 5^{o}C uniaxial conditions and the $C_{22}(S)$ function was fit at 10^{o}C triaxial conditions, a remarkable use of reduced time. The multiaxial validation test that exercised all damage functions showed agreement between predictions and measurements that was comparable to if not better than the corresponding comparisons for unconfined conditions.

10.5 Validation

As described in the preceding sections, the viscoelastic, viscoplastic, and damage components of the complete material model were each calibrated separately using tests optimized for each type of response. The complete material model was then validated using a series of uniaxial constant strain rate tests to failure at strain rates and temperatures that were substantially different than any employed in the calibration testing. The pre-peak, peak, and immediate post-peak responses were captured very well by the model for nearly all of the constant strain rate validation tests. The distant post-peak response—i.e., after the stress has dropped by more than about 10% from the peak value—was less well predicted, but this was expected because this is the regime in which macro cracks begin to coalesce and the material transitions from a continuous to

discontinuous system. Fracture mechanics theories should be employed after damage has localized and macro cracks have begun to coalesce.

Special attention was focused on validating the viscoplastic model component, as this was the new capability added to the Schapery model as part of this project. The viscoelasticity and damage components of the Schapery continuum damage model had received more attention in the past and had already been demonstrated as suitable for asphalt concrete at low to moderate temperatures. The uniaxial *pqY* viscoplastic model was validated against repeated load permanent deformation tests performed at conditions having generally warmer temperatures and lower stresses than employed in the calibration tests. The model predictions agreed well with measured strains in the initial hardening region but showed increasing discrepancies in the secondary hardening region at larger permanent strains.

Several model enhancements were investigated to improve the predictions from the viscoplastic model component in the secondary hardening region. A bilinear hardening law was attempted, but this proved inadequate in capturing the change in hardening slopes between the initial and secondary hardening regions. A novel cross plotting method was attempted to separate the hardening strain rate dependence into functions of stress and viscoplastic strain. However, this too proved unsuccessful in improving the model predictions.

Ultimately, a new formulation for the viscoplasticity model component had to be developed. This new formulation adapted the multidimensional Desai HISS model into a Perzyna-type viscoplasticity formulation. The model formulation was developed and calibrated using a subset of the cyclic creep and recovery tests then validated against the

same tests for which the initial *pqY* viscoplasticity model had performed poorly. The validation results for the new model formulation are extremely promising.

The overall conclusion is that the material modeling and calibration approach developed in this project can very successfully capture the full range of relevant material response for asphalt concrete under compressive loading. It directly incorporates the inherent viscoelastic, viscoplastic, and microstructural damage components of asphalt concrete constitutive behavior. It thus provides an excellent foundation for subsequent advances in the fully mechanistic modeling of flexible pavement systems.

Additional work is of course required before realistic mechanistic modeling of complete pavement systems becomes a reality. The work described in this report describes only an essential but very important first step. However, it very clearly illuminates the path for future advances.

11. Recommendations

11.1 Calibration Tests

Linear viscoelastic characterization tests should remain unchanged with multiple temperature and frequencies at very small dynamic strains. Enough data at the extreme temperatures and frequencies should be obtained for reliable very short and very long loading time accuracies in the resultant master creep compliance or relaxation modulus. The inter-conversion method outlined by Schapery to take data from the frequency domain to the time domain worked well as is evident from the validation. No temperatures warmer than 60^{o}C are needed, but at least temperatures as cool as –10^{o}C is required to define the master curve upper shelf.

There is the potential for heavily polymer-modified binders to be non-thermorheologically simple materials and violate time temperature superposition. Mixtures with these binders should be checked for time-temperature superposition in frequency sweeps and double-checked for extended time-temperature superposition at large total strains. The controlled multiple strain rate procedure outlined in this project seems sufficient, but fresh unloaded specimens should always be used. These will verify

if there are any difference between large and small strain temperature shift functions and guide researchers which to use and when.

Cyclic creep and recovery tests are recommended for calibrating the viscoplastic model parameters. These tests enable direct measurement of the viscoplastic strains that are in the focus of the viscoplastic model. Ambitious researchers may want to supplement the controlled strain rate validation tests with two or three Fixed Stress cyclic creep and recovery tests. The results in the present study suggest that different recommended stress states and magnitudes for cyclic creep and recovery calibration tests may produce better results. Unconfined tests should be performed at a fairly low stress around 100 kPa, while the 250 kPa confined test should have deviator stresses somewhat larger than in the unconfined loading but smaller than in the 500 kPa confined tests, and so on. Reasonable estimates for the maximum deviator stress levels in the confined creep and recovery tests are 400 kPa and 1500 kPa for the 250 kPa and 500-kPa confinement conditions respectively. These are based on a simple analysis of I_1 and $\sqrt{J_{2D}}$ stress invariant ranges induced in a multilayer elastic pavement model. The recommended temperature for viscoplastic calibration testing is 45^{o}C.

In addition, some smaller critical stress states can be used to augment the above test recommendation. About 30% of the initial load cycles should be performed at about 25% of maximum deviatoric stress level. The remaining cycles can then be performed at the target stress levels. The objective should be to search for the point of viscoplastic saturation, which will require some sacrificial specimens. A schematic of this recommendation is shown in Figure 176. Recall that viscoplastic saturation occurs when the growing flow surface meets or envelops the applied state of stress. Viscoplastic

saturation was predicted by the model during the early portions of the confined Fixed Time calibration tests and was also measured and modeled in the later portions of the random repeated load permanent deformation validation tests. This revised testing procedure permits a more strategic approach toward calibrating the hardening of the HiSS flow surface. The points of viscoplastic saturation provide necessary constraints in the model parameter optimization routine.

Confinement up to 500 kPa in this research indicated that axial viscoplastic strains are fully recoverable, but full recovery of the radial strains after hydrostatic equilibrium was not always observed. Hydrostatic preconditioning to full radial strain saturation, while requiring extra steps and time, should be used before both unconfined and confined tests such that the material starts from the same mechanistic state. Future research into possible initial anisotropy effects is needed. Another reason for hydrostatic preconditioning is that the constraints for the “nose” of the HiSS surface where it intersects the compressive hydrostatic stress axis could be directly determined. However, it is expected hydrostatic stresses greater than 800 kPa may be required to fully mobilize the material viscoplastically in all three dimensions.

For validation, repeated load permanent deformation tests with haversine pulses and rests are ideal because they represent an important distress mode observed in asphalt pavements. Confined versions of these tests should also be included to make the validation more robust.

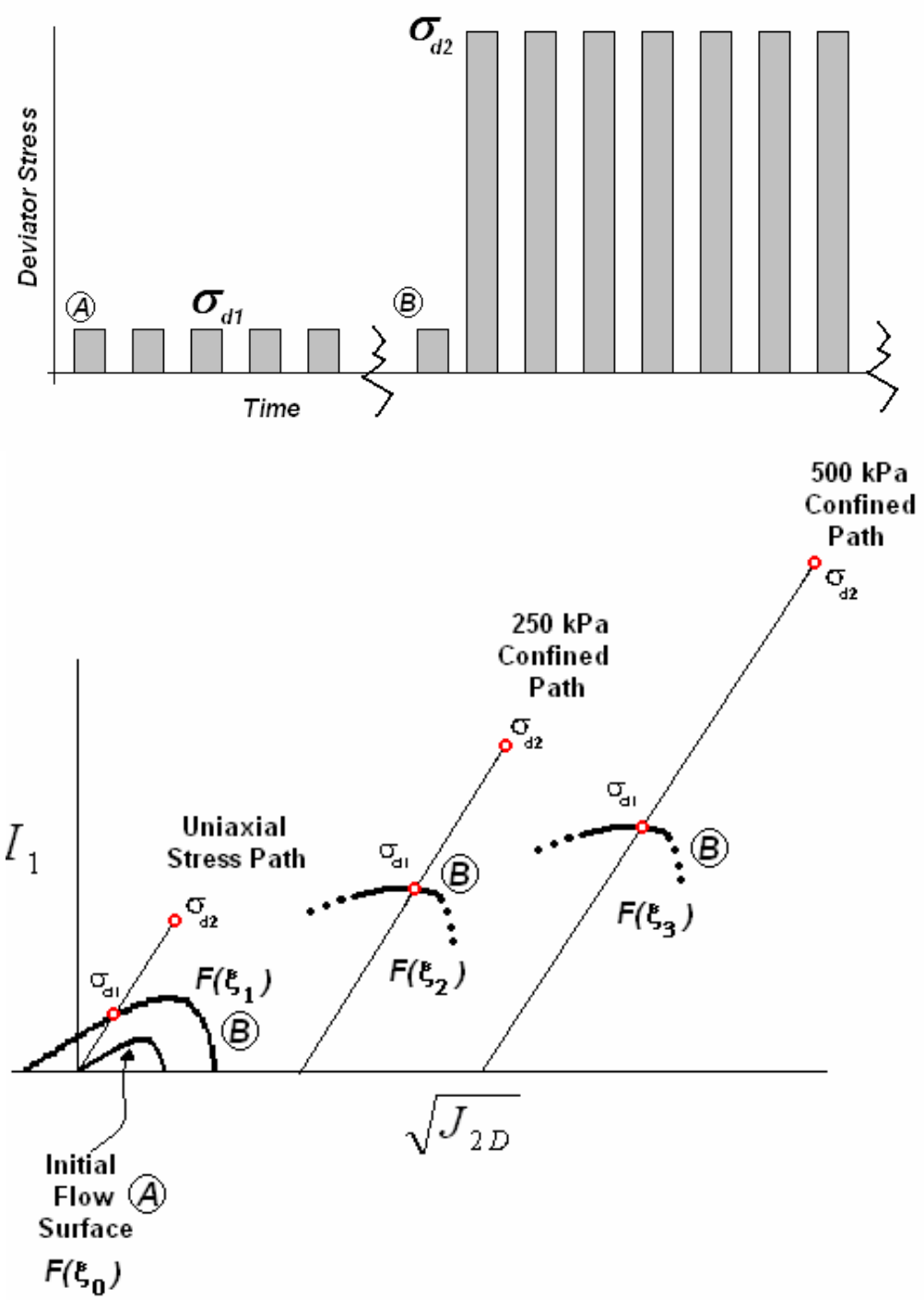

Figure 176. Schematic of viscoplastic saturation test modification

The original uniaxial pqY model proved adequate for removing any viscoplasticity from the low temperature controlled strain rate tests used for calibrating the viscoelastic continuum damage model component. It may be desirable to employ confined monotonic tests for this purpose because increasing confinement tends suppress viscoplastic effects more than does than decreasing temperature. Load system capacity may be the limiting factor, however.

Another alternative is to conduct compression tests using 75mm diameter specimens (not violating representative volume requirements) rather than 100 mm diameter. The smaller specimens allow higher stresses to be reached at a given load magnitude. The test can then be performed at cooler temperatures to further suppress viscoplasticity while still remaining within the load capacity of servo hydraulic testing machines commonly available at research institutions. At least four widely different rates should be used to ensure confidence in the damage evolution law exponent. The fastest in these experiments, 0.0135ε/s, is more than sufficient. It may also be beneficial to sacrifice two specimens at the slowest rate by halting loading at 33% and 67% of the peak stress and allowing the specimens to recover in order to confirm the low levels of viscoplasticity in these tests.

11.2 Recommended Areas of Further Research

Some specific additional recommendations for future research beyond those already mentioned in the preceding sections include the following:

- Additional studies should be conducted to confirm the validity of time-temperature superposition into the large strain region for different asphalt mix types. Modified

binder mixtures, in particular, should be studied. The discrepancies/agreement between small vs. large strain temperature shift relations as determined from controlled strain rate tests vs. cyclic creep and recovery tests should also be investigated.

- The effects of initial material anisotropy should be evaluated more thoroughly for all of the model components.
- The desirability of hydrostatic preconditioning during the viscoplastic model calibrations to ensure the same initial mechanistic (strain) state for all conditions should be more thoroughly examined.
- The discrepancies between observations of no damage in small-strain |E*| frequency sweeps vs. initial damage predicted from the fully calibrated viscoelastic continuum damage model need better resolution.
- Future research should explore whether any viscoelastic continuum damage localization accompanies significant viscoplasticity.

Finally, and most difficult, separately developed compressive and tensile damage and viscoplastic models need to be unified in order to be able to predict the true reversed tensile and compressive loading in real pavement systems. This will include unified damage evolution and strain hardening laws.

12. References

Bonaquist, R.R., D.W. Christensen and B. Stump, *Simple Performance Tester for Superpave Mix Design: First-Article Development and Evaluation*, National Cooperative Highway Research Program, National Academy Press, 2003, Washington, D.C.

Chaboche, J.L., "Thermodynamic Formulation of Constitutive Equations and Application to the Viscoplasticity and Viscoelasticity of Metals and Polymers," *International Journal of Solids and Structures*, Vol. 34, No. 18, 1997, pp. 2239-2254.

Chehab, G.R., Y.R Kim, R.A. Schapery, M.W. Witczak, and R. Bonaquist, "Time Temperature Superposition Principle for Asphalt Concrete Mixtures with Growing Damage in Tension State," *Asphalt Paving Technology*, Association of Asphalt Paving Technologists, Vol. 71, 2002, pp. 559-593.

Chehab, G.R., Y.R Kim, R.A. Schapery, M.W. Witczak, and R. Bonaquist, "Characterization of Asphalt Concrete in Uniaxial Tension using a Viscoelastoplastic Continuum Damage Model," *Asphalt Paving Technology*, Association of Asphalt Paving Technologists, Vol. 72, 2003, pp 315-355.

Desai, C.S, S. Somasundaram G. and Frantziskonis, "A Hierarchical Approach for Constitutive Modeling of Geologic Materials", *International Journal of Numerical and Analytical Methods in Geomechanics*, Vol. 10, 1986, pp. 225-257.

Desai, C.S. and D. Zhang, "Viscoplastic Model for Geologic Materials with Generalized Flow Rule," *International Journal for Numerical and Analytical Methods in Geomechanics*, Vol. 11, 1987, pp. 603-62.

Erkins, S.M.J.G., A.A.A. Molenaar, A. Scarpas, "A Better Understanding of Asphalt Concrete Response," *Proceedings of the 16th ASCE Engineering Mechanics Conference*, July 16-18, 2003, University of Washington, Seattle, WA.

Erkins, S.M.J.G., *Asphalt Concrete Response (ACRe) – Determination, Modeling, and Prediction*, Ph.D. Dissertation, Technical University-Delft, 2002, The Netherlands.

Findley, W.N., J.S. Lai, and K. Onaran, *Creep and Relaxation of Nonlinear Viscoelastic Materials*, 1989, Dover, New York.

Gibson, N., C.W. Schwartz, R. Schapery and M.W. Witczak, "Viscoelastic, Viscoplastic and Damage Modeling of Asphalt Concrete in Unconfined Compression," *Transportation Research Record*, TRR 1860, Transportation Research Board, 2003a, pp. 3-15.

Gibson, N.H., C.W. Schwartz, R.A. Schapery and Witczak, M.W., "Confining Pressure Effects on Viscoelasticity, Viscoplasticity, and Damage in Asphalt Concrete," *Proceedings, 16th ASCE Engineering Mechanics Conference*, 2003b, Seattle, WA.

Gillespie, T.D. , S. M. Karimihas, D. Cebon, M. Sayers, M. A. Nasim, W. Hansen, N. Ehsan., *Effects of Heavy-Vehicle Characteristics on Pavement Response and Performance*, Appendix-C, NCHRP Report No. 353, National Cooperative Highway Research Program, National Academy Press, 1993, Washington, D.C.

Ha, K. and R.A. Schapery, "A Three-Dimensional Viscoelastic Constitutive Model for Particulate Composites with Growing Damage and Its Experimental Verification," *International Journal of Solids and Structures*, Vol. 35, No. 26-27, 1998, pp. 3497-3517.

Huang, B., L. Mohammad, W. Wathugala and H. Paul, "Development of a Thermo-Viscoplastic Constitutive Model for HMA Mixtures," *Asphalt Paving Technology*, Association of Asphalt Paving Technologists, Vol. 71, 2002, pp. 594-618.

Kim, Y.R. and G.R. Chehab, Communication during quarterly NCHRP Project 9-19 meeting, 2002.

Krarup, J., "Measured and Calculated Pavement Response in the Danish Road Testing Machine," *Vehicle-Road Interaction*, ASTM STP 1225, B.T. Kulakowski, Ed., American Society of Testing and Materials, Philadelphia, 1994, pp. 89-104.

Lee, H.J., and Y.R. Kim, "Viscoelastic Constitutive Model for Asphalt Concrete Under Cyclic Loading," *Journal of Engineering Mechanics*, ASCE, Vol. 124, No. 1, 1998a, pp. 32-40.

Lee, H.J., and Y.R. Kim, "Viscoelastic Continuum Damage Model for Asphalt Concrete with Healing," *Journal of Engineering Mechanics*, ASCE, Vol. 124, No. 11, 1998b, pp. 1224-1232.

Levenberg, E. and J. Uzan, "Triaxial Small-Strain Viscoelastic-Viscoplastic Modeling of Asphalt Aggregate Mixes," *Mechanics of Time Dependent Materials*, Vol. 8, No. 4, 2004, pp. 365-384.

Lytton, R.L., J. Uzan, E.G. Fernando, R. Roque, D. Hiltunen, and S.M. Stoffels, *Development and Validation of Performance Prediction Models and Specifications for Asphalt Binders and Paving Mixes*. Report SHRP A-357, Strategic Highway Research Program, National Research Council, 1993, Washington, DC.

Mehta, Y.A., and D.W. Christensen, "Determination of the Linear Viscoelastic Limits of Asphalt Concrete at Low and Intermediate Temperatures," *Asphalt Paving Technology*, Association of Asphalt Paving Technologists, Vol. 69, 2000, pp. 281-312.

Monismith, C.L., R.L. Alexander, and K.E. Secor, "Rheological Behavior of Asphalt Concrete," *Asphalt Paving Technology*, Association of Asphalt Paving Technologists, Vol. 35, 1966, pp. 400-450.

National Research Council, Highway Research Board, *The AASHO Road Test*, Special Reports, 1962, Report 73.

Park, D.W., A. Epps-Martin and E. Masad, "Simulation of Permanent Deformation Using an ElasticViscoplastic Constitutive Relation," *Proceedings of the Second International Conference on Accelerated Pavement*, 2004, Minneapolis, MN.

Park, S.W. and R.A. Schapery, "Methods of Interconversion between Linear Viscoelastic Material Functions. Part I – A Numerical Method Based on Prony Series," *International Journal of Solids and Structures*, Vol. 36, 1999, pp. 1653-1675.

Park, S.W. and R.A. Schapery, "Viscoelastic constitutive model for particulate composites with growing damage," *International Journal of Solids and Structures*, Vol. 34, No. 8, 1997, p 931-947.

Park, S.W., Y.R. Kim, and R.A. Schapery, "A Viscoelastic Continuum Damage Model and Its Application to Uniaxial Behavior of Asphalt Concrete," *Mechanics of Materials*, Vol. 24, 1996, pp. 241-255.

Pellinen, T.K., *Investigation of the Use of Dynamic Modulus as Indicator of Hot-Mix Asphalt Performance*, Ph.D. Dissertation, Department of Civil and Environmental Engineering, Arizona State University, 2001, Tempe, AZ.

Pellinen, T.K. and S. Xiao, "Relationship Between Triaxial Shear Strength and Indirect Tensile Strength of Hot Mix Asphalt." *Asphalt Paving Technology*, Association of Asphalt Paving Technologists, Vol. 74, 2005, pp. 347-379.

Perzyna, P., "Fundamental Problems in Viscoplasticity," *Adv. Appl. Mech*., 9, 1966, pp. 243-377.

Scarpas, A., J. Blaauwendraad, R. Al-Khoury, and C. van Gurp, "Experimental Calibration of a Viscoplastic-Fracturing Computational Model," *Proceedings of the*

International Conference on Computational Methods and Experimental Measurements, CMEM, 1997, p 643-652.

Schapery, R. A., "Correspondence Principles and Generalized J Integral for Large Deformation and Fracture Analysis of Viscoelastic Media," *International Journal of Fracture*, Vol. 25, No. 3, 1984, p 195-223.

Schapery, R.A. (1999). "Nonlinear Viscoelastic and Viscoplastic Constitutive Equations with Growing Damage," *International Journal of Fracture*, Vol. 97, pp. 33-66.

Schapery, R.A. "A Micromechanical Model for Non-Linear Viscoelastic Behavior of Particle-Reinforced Rubber with Distributed Damage," *Engineering Fracture Mechanics*, Vol. 25, No. 5-6, 1985, p 845-867.

Schapery, R.A. *A Simple Collocation Method for fitting Viscoelastic Models to Experimental Data*. Report No. SM 61-23A, Graduate Aeronautical Laboratories, California Institute of Technology, 1961, Pasadena, CA.

Schapery, R.A., "Analysis of Damage Growth in Particulate Composites Using a Work Potential," *Composites Engineering*, Vol. 1, No. 3, 1991, pp. 167-182.

Schwartz, C.W., N. Gibson, and R. Schapery, "Time-Temperature Superposition for Asphalt Concrete at Large Compressive Strains," *Transportation Research Record*, TRR 1789, Transportation Research Board, 2002, pp. 101-112.

Seo, Y., Kim Y.R., M.W. Witczak, and R. Bonaquist, "Application of Digital Image Correlation Method to Mechanical Testing of Asphalt-Aggregate Mixtures," *Transportation Research Record*, No. 1789, Transportation Research Board, 2002, pp. 162-172.

Superpave Models Team, *Task F.1 – Advanced AC Mixture Characterization, Team Report SLS-3.* SUPERPAVE Support and Performance Models Management, NCHRP 9-19, Department of Civil and Environmental Engineering, Arizona State University, 199b, Tempe, AZ.

Superpave Models Team, *Volumetric Design of Standard Mixtures Used by the University of Maryland Models Team, Internal Team Report*. SUPERPAVE Support and Performance Models Management, NCHRP 9-19, Department of Civil Engineering, University of Maryland, 1999a, College Park, MD.

Tashman, L., E. Masad, D. Little and R. Lytton, "Damage evolution in Triaxial Compression Tests in HMA at High Temperatures," *Asphalt Paving Technology*, Association of Asphalt Paving Technologists, Vol. 73, 2004b, pp 53-87.

Tashman, L., E. Masad, H. Zbib, D. Little and K. Kaloush, "Anisotropic Viscoplastic Continuum Damage Model for Asphalt Mixes," *Recent Advances in Materials*

Characterization and Modeling of Pavement Systems, ASCE Geotechnical Special Publication, No. 123, 2004a, pp. 111-125.

Witczak, M.W. and B. Sullivan, B., *Repeated Load (ep/er) Deformation Tests, NCHRP 9-19, Subtask F6.Evaluation Tests*. SUPERPAVE Support and Performance Models Management, Department of Civil Engineering and Environmental Engineering, Arizona State University, 2001, Tempe, AZ.

Witczak, M.W. and B. Sullivan, *Random Repeated Load Permanent Deformation Tests, NCHRP 9-19, Subtask F6.Evaluation Tests*. SUPERPAVE Support and Performance Models Management, Department of Civil Engineering and Environmental Engineering, Arizona State University, 2002, Tempe, AZ.

Witczak, M.W., H.L. Von Quintus, and C.W. Schwartz, "Superpave Support and Performance Models Management: Evaluation of the SHRP Performance Models System," *Proceedings of the 8th International Conference on Asphalt Pavements*, Seattle, WA, 1997, pp. 175-195.

Zafir, Z., R. Siddharthan, P. Sebaaly, "Dynamic Pavement Strain Histories from Moving Traffic Load," *Journal of Transportation Engineering*, Vol. 120, No. 5, 1994, pp. 821-842.

Zhao, Y. and Y.R. Kim, "Time-Temperature Superposition for Asphalt Mixtures with Growing Damage and Permanent Deformation in Compression," *Transportation Research Record*, No. 1832, Transportation Research Board, 2003, p 161-172.